Reduced-Order Modelling and Observations of Geological Carbon Dioxide Storage

Kieran A. Gilmore

A dissertation submitted for the degree of
Doctor of Philosophy
at the University of Cambridge

St Catharine's College
February 2022

Declaration

This dissertation describes my original work except where acknowledgement is made in the text. It does not exceed the page limit and is not substantially the same as any work that has been, or is being submitted to any other university for any degree, diploma or any other qualification.

Kieran A. Gilmore
February 2022

Reduced-Order Modelling and Observations of Geological Carbon Dioxide Storage

Kieran A. Gilmore

Worldwide carbon dioxide (CO_2) emissions targets are unlikely to be met without large scale geological CO_2 storage, with much of the storage capacity found in saline aquifers. The key aim of carbon sequestration is the long-term or permanent storage of CO_2 within the sub-surface, minimising the potential for CO_2 leakage back to the surface. When CO_2 is injected into a saline aquifer, it rises until it reaches an impermeable horizon, known as a caprock, where it subsequently spreads out due to buoyancy forces. While the CO_2 is spreading, the chance of encountering potential leakage pathways increases and the potential rates of trapping also increase. In this dissertation, I combine reduced-order fluid models and geophysical data to understand the controls on the rate of trapping and CO_2 leakage in saline aquifers. Chapter 1 outlines the broader context of CO_2 sequestration, both in terms of physical processes, observations, and policy implications. In Chapter 2, I investigate the rate at which CO_2 dissolves when injected into heterogeneous saline aquifers. As CO_2 dissolves into brine, the density of the brine is increased, thereby acting as a mechanism for the stable trapping of CO_2. CO_2 injected into heterogeneous geological formations results in preferential migration along high permeability pathways, thus increasing the CO_2-water interfacial area and enhancing dissolution rates. I analyse the rate at which free-phase CO_2 propagates in layered reservoirs and the quantity of CO_2 dissolved, showing that for reservoirs with finely bedded strata, over 10% of the injected CO_2 can dissolve in a year. In Chapter 3, I investigate the potential for fault zones, which are localised planes of brittle deformation, to act as leakage pathways which transect low permeability structural seals. I develop an analytical model to describe the dynamics of leakage through a fault zone cross-cutting multiple aquifers and seals. This is tested against a set of porous media tank experiments and applied to a naturally occurring CO_2-charged aquifer system at Green River, Utah. In Chapters 4 and 5, I combine seismic observations of a carbon sequestration project with numerical modelling to investigate the extent to which reduced-order models can accurately predict CO_2 movement in heterogeneous aquifers at the Otway CO_2 sequestration project in Victoria, Australia. I analyse seismic measurements of the motion of CO_2 in the stage 2C trial, in which 15,000 tonnes of CO_2-rich gas was injected into a saline aquifer at $\sim 1.5\,\mathrm{km}$ depth. The geometry of the reservoir and extent and thickness of the CO_2 current is extracted from a series of time-lapse seismic surveys. I solve a gravity current model which accounts for topographic gradients in the caprock and incorporates residual trapping of CO_2 numerically to model the observed spreading. This vertically-integrated model is inverted to find bulk reservoir properties that best match the modelled and measured CO_2 distributions. The sensitivity of the model to changes in bulk properties and topographic gradients is investigated. In the concluding Chapter 6, I review the use of reduced-order physical modelling in describing the movement, trapping and leakage behaviour of CO_2 in geological porous media, with application to field scale CO_2 sequestration projects.

Publications arising from this dissertation

Chapter 2

Gilmore, K. A., Neufeld, J. A., and Bickle, M. J., (2020), CO_2 dissolution trapping rates in heterogeneous porous media, *Geophysical Research Letters*, Vol. 47(12), e2020GL087001

Chapter 3

Gilmore, K. A., Sahu, C. K., Benham, G. P., Neufeld, J. A., and Bickle, M. J., (2022), Leakage dynamics of fault zones: experimental and analytical study with application to CO_2 storage, *Journal of Fluid Mechanics*, Vol. 931, A31, doi.org/10.1017/jfm.2021.970

Planned publications arising from this dissertation

Chapter 4 and 5

Gilmore, K. A., Butler, A., Neufeld, J. A., and Bickle, M. J., (in preparation), Vertically-integrated CO_2 flow simulations of the Otway Stage 2C injection, *International Journal of Greenhouse Gas Control*

Acknowledgements

I would like to start by thanking my supervisors, Jerome Neufeld and Mike Bickle. Jerome has been a wonderful mentor throughout this PhD, and his encouragement, patience and generosity with his time has given me the confidence to learn to solve problems for myself. Mike has been an endless source of interesting discussion and ideas, and his exuberance and dry humour are a perfect reminder to never take life too seriously.

Bullard has been a great place to do a PhD, largely thanks to the people. Chunendra Sahu, Adam Butler and Graham Benham have been excellent colleagues, collaborators and friends. Thanks to Nicky White and Ben Conway-Jones for teaching me the ropes of seismic interpretation. The interesting discussions at CCS coffee with JP, Alex, Zhong and Duncan were a highlight of every week. The idle chatter at Bullard coffee with Fergus, Paddy, Conor, Hannah, Stephen, Camilla, Zhi, Leo, Patricia, Jenny, Clare, Aisling and Simon has been no less entertaining. Thomasina Ball patiently taught me many things about fluid dynamics. Thanks to Laurence Cowton for getting me up to pace. Ian and Dave have been invaluable in helping fix various computer problems, and my experiments would not have gone ahead without help from Andrew Pluck and Lotty.

I would like to thank the whole sub-surface containment team at Shell for being so welcoming during my placement, with special thanks to Niko Kampman, Jeroen Snippe, Kevin Bisdom and Marcella Dean for their excellent guidance. I thank Max Watson and Hadi Nourollah at CO2CRC for their help in accessing the seimsic reflection data sets.

I have been lucky enough to have gone through the whole process with my two house mates, Matt and Matyas. Who knows how much more we would have all achieved if we had not been living together. Thanks to all my CUHC teammates throughout the years, who have offered a welcome distraction from research. Finally, I would like to thank my parents, Eddie and Yimsoon, for their constant love and support and Charlotte, who has been there with me all the way.

Contents

List of Figures

List of Tables

Chapter 1

Introduction

1.1 The Climate Crisis

In recent years, the climate crisis has come to the forefront of mainstream political, economic and social issues, gaining regular, widespread media coverage with numerous countries and companies around the world announcing net zero emissions targets. Global temperatures are rising, with average surface temperatures 1.09 [0.95 to 1.20] °C higher in 2011-2020 than 1850-1900 (IPCC, 2021). The observed warming is driven by anthropogenic greenhouse emissions, which increase the amount of heat trapped by the atmosphere. Levels of carbon dioxide (CO_2) in the atmosphere are rising at an increasing rate (Keeling *et al.*, 2001). In 2019, atmospheric CO_2 concentrations were higher than at any time in the last two million years, and concentrations of the greenhouse gases CH_4 and N_2O higher than any time in the last 800,000 years (IPCC, 2021).

Global temperature rise caused by human behaviour is a major problem as it results in increases in extreme weather events, sea level rise, as well as harsher livable climates across

much of the world. The extra energy in the atmosphere causes more frequent and stronger storms, which put human lives and infrastructure directly at risk, and more intense rainfall events which lead to increased flooding (Trenberth, 2011). Heatwaves have also increased in frequency and intensity since the 1950s (Perkins *et al.*, 2012), which increases the likelihood of droughts and wildfires. The higher global temperatures also contribute towards global sea level rise, through thermal expansion of seawater, mass loss from glaciers and ice sheets, primarily the Greenland and Antarctic ice sheets, and changes in land water storage (IPCC, 2021). Studies have estimated that over a billion people globally are at risk of climate related displacement, mostly due to flooding caused by sea level rise and increased rainfall, and water stress due to drought (IEP, 2020). These people are mostly found in Africa, the Middle East and parts of Central Asia, but their displacement will cause mass migration, triggering a climate refugee crisis with global consequences.

An important approach to limiting the effects of global warming is to eliminate net anthropogenic greenhouse gas emissions as quickly as possible. A landmark report by the Intergovernmental Panel on Climate Change said that to limit total warming relative to pre-industrial times to 1.5°C, global emissions would have to reach net zero by 2050 (IPCC, 2018), meaning that the greenhouse gases going into the atmosphere are balanced by removal of CO_2 from the atmosphere. Although some impacts of climate change will still be felt with 1.5°C of warming, the effects are predicted to be much less severe than with 2°C or higher levels of warming. However, reaching net zero emissions by 2050 requires rapid and far-reaching transitions across the global economy.

1.2 The Role of Carbon Capture and Storage in Net Zero Strategies

Some sectors have clear road-maps to decarbonisation, and supportive policy as well as increased economic input are required to transition these sectors as fast as possible. An example of this would be decarbonisation of light passenger vehicle fleets by replacing all internal combustion engine vehicles with battery powered alternatives charged using a clean electricity grid powered by renewable sources. However, some large emitting sectors still do not have a clear pathway to net zero emissions. For example, the cement industry emits 2.2

$GtCO_2$ (billion tonnes of CO_2) per year, equating to around 5% of global emissions (ETC, 2018). Over half of these emissions are a by-product of the chemical reaction required to produce cement and are largely unavoidable (the other half coming from heat generation in the production process). Carbon capture and storage (CCS) is a potential solution to decarbonising these hard-to-abate sectors. CCS is the process whereby CO_2 is captured and then stored over long timescales in underground reservoirs, as a means of mitigating CO_2 emissions. Anthropogenic CO_2 is captured using chemical solvents at the point of formation, typically large industrial plants or power stations. The CO_2 is then compressed and transported through pipelines into deep (>800 m depth) geological reservoirs suitable for storing the CO_2 permanently. Taking the example of cement production, a CO_2 scrubber could be fitted onto existing cement kilns to capture both the process emissions and the emissions produced from heat generation.

Another variation of carbon capture that is receiving a lot of interest is direct air capture. Direct air capture pulls CO_2 directly out of the air using a chemical filter (Beuttler *et al.*, 2019; Keith *et al.*, 2018). Since CO_2 only makes up a small fraction of the composition of the atmosphere, large volumes of air need to be processed to extract significant amounts of CO_2, a process which is extremely energy intensive. If the captured CO_2 is subsequently stored in the subsurface, this results in a net decrease of atmospheric CO_2 concentrations. This technology could have important implications for offsetting remaining emissions from hard-to-abate sectors of the economy. Recent net zero scenarios have 2.4 $GtCO_2$ per year removed from the atmosphere by 2050, through direct air capture and bioenergy with CCS technologies (IEA, 2020, 2021). However, the technology is currently still in the early stages of deployment, with only 13,000 tonnes of CO_2 captured per year.

Currently, 40 $MtCO_2$ (million tonnes of CO_2) is captured and stored per year (IEA, 2021), which amounts to just under 0.1% of global emissions. The CO_2 storage sites range from scientific projects injecting small volumes of CO_2 for monitoring purposes, to larger commercial projects injecting millions of tonnes a year. There are 26 operating commercial CCS facilities worldwide with a further 34 in development (Global CCS Institute, 2020). Most scenarios for reaching net zero emissions assume a major role for CCS, with estimates of 7-8 $GtCO_2$ per year sequestered by 2050 (ETC, 2017; IEA, 2021). The majority of this storage

capacity comes from large estimates of carbon dioxide removal technologies such as direct air capture with CCS (DACCS) and bioenergy with CCS (BECCS), to balance remaining emissions from other sectors. The likelihood of these technologies reaching these scales by mid-century remains a controversial topic (Hansson *et al.*, 2021). However, there is still an important role for CCS in the full decarbonisation of the industrial sector, namely the three biggest industrial emitters: steel, cement and petrochemicals (ETC, 2018), which would require around 2 $GtCO_2$ sequestered per year (IEA, 2019). Hydrogen is also likely to play a key role in the decarbonisation of shipping, heavy-duty transport and industrial heating. Currently the cheapest and most scalable method of clean hydrogen production is by steam methane reformation with CCS used to remove and store the CO_2 by-product.

1.3 Sub-surface Storage of CO_2

One the CO_2 is captured, it is transported in pipelines and stored in geological reservoirs, at depths of 800 - 3000 m below the Earth's surface. Possible reservoirs for CO_2 storage include depleted oil and gas fields (Godec *et al.*, 2011; Jenkins *et al.*, 2012), unmineable coal seams (Busch *et al.*, 2003), igneous rocks such as basalts (Gislason & Oelkers, 2014), or saline aquifers (Bentham & Kirby, 2005). The latter accounts for around 90% of the total potential storage volume (Michael *et al.*, 2010). It is estimated that there is 13,500 $GtCO_2$ of effective global storage capacity (Bachu *et al.*, 2007; Dooley, 2013), which suggests that a lack of geological CO_2 storage capacity is unlikely to be an obstacle for the commercial adoption of CCS technologies.

The key aim of carbon sequestration is the long-term, or better still, permanent storage of CO_2 within the subsurface, minimising the potential for CO_2 leakage back to the surface. When CO_2 is injected into the reservoir, it is buoyant with respect to the surrounding reservoir fluid and will rise until it reaches an impermeable horizon, known as a caprock, where it subsequently spreads out due to buoyancy forces. As the CO_2 spreads out underneath the caprock, the chances of encountering a potential leakage pathway increase. However, as the CO_2 permeates into the reservoir, it undergoes further processes such as dissolution, mineralisation and capillary trapping, which act to immobilise the CO_2 and render it per-

manently trapped within the reservoir. This highlights some important areas which must be understood to ensure the safe, long-term storage of CO_2 in geological reservoirs. Firstly, what governs the spreading of CO_2 on injection into a reservoir. Secondly, what are the secondary trapping mechanisms that occur within the reservoir which contribute towards the permanent storage of CO_2. Thirdly, where are the potential leakage pathways for CO_2 to escape through and what determines how much CO_2 will leak. And finally, how can we observe the CO_2 once it is within the reservoir to ensure that it remains securely trapped and is not leaking.

1.3.1 CO_2 Flow in the Sub-Surface

CO_2 is usually injected into aquifers at depths $> 800\,\mathrm{m}$, which given typical geothermal and hydrostatic pressure gradients implies that it is in a supercritical state, with properties between those of a gas and a liquid. The movement of CO_2 following injection is dependent on the relative densities and viscosities of the CO_2 and the ambient interstitial fluid phase, which is often a high-concentration salt solution, or brine, in saline aquifers (Huppert & Neufeld, 2014). The properties of CO_2 are temperature and pressure dependent, and so vary according to the aquifer depth and the magnitude of the geothermal gradient. For shallow aquifers, at depths around $1000\,\mathrm{m}$, the density of CO_2 is $\rho_{CO_2} = 266\text{-}714\,\mathrm{kg\,m^{-3}}$ and the density of brine is $\rho_{br} = 998\text{-}1230\,\mathrm{kg\,m^{-3}}$ (note upper limits are for very saline fluids which are rare). For deeper aquifers, at depths around $3000\,\mathrm{m}$, $\rho_{CO_2} = 479\text{-}733\,\mathrm{kg\,m^{-3}}$ and $\rho_{br} = 945\text{-}1202\,\mathrm{kg\,m^{-3}}$ (Nordbotten *et al.*, 2005). The viscosity of CO_2 is $\mu_{CO_2} = 0.023\text{-}0.0611\,\mathrm{mPa\,s}$, while for brine it is $\mu_{br} = 0.195\text{-}1.58\,\mathrm{mPa\,s}$, giving viscosity ratios which range from $\mu_{CO_2}/\mu_{br} = 0.026\text{-}0.22$ (Nordbotten *et al.*, 2005). The density difference $\Delta\rho$ is important for driving fluid motion by buoyancy forces, and the viscosity ratio has important implications for the dynamics of the flow.

The velocity of a fluid travelling through a porous media can be evaluated using Darcy's equation which relates the fluid flux or Darcy velocity with the driving pressure gradient and buoyancy forces (Bear, 1988),

$$\mathbf{u} = -\frac{k}{\mu}(\nabla p - \rho g \hat{z}), \tag{1.1}$$

where $\mathbf{u}$ is the Darcy or transport velocity, k is the permeability of the porous medium which is a function of the size and shape of the grains as well as the structure and packing of the porous medium (Woods, 2015), μ is the viscosity of the CO_2, ∇p is the applied pressure gradient and $\rho g\hat{z}$ is the buoyancy force, where $\hat{z}$ is a unit vector in the vertical direction. On injection, the buoyant CO_2 rises through the reservoir at the natural buoyancy velocity, $u_b = \Delta\rho g k/\mu$, which is its velocity through a porous medium driven by the gravity acting on the density difference, $\Delta\rho$, between the CO_2 and the water. The CO_2 will rise until it reaches a low permeability structural seal or caprock, under which it ponds and subsequently spreads as a buoyancy-driven gravity current. An example of this behaviour is seen at the Sleipner field in the North Sea, where CO_2 is injected into a 200 - 300 m thick sandstone formation. Injected CO_2 rises and ponds beneath 9 distinct shale horizons (Arts *et al.*, 2004; Bickle *et al.*, 2007; Cowton *et al.*, 2016). The spreading of CO_2 current is mostly driven by buoyancy, consisting of diffusive slumping of the current and advection up topographic gradients. Pressures gradients due to injection may also contribute towards the movement of CO_2, particularly in less permeable and more confined aquifers, but these effects are typically limited to regions close to the injection location.

One feature of the observed spreading at many CO_2 sequestration sites is that the current is long and thin. There are a suite of mathematical models which describe the behaviour of buoyancy-driven gravity currents in porous media where the current thickness is much smaller than the lateral extent (e.g. Huppert & Woods, 1995; Pegler *et al.*, 2014a; Vella & Huppert, 2006). In these models, as the aspect ratio of the current is large, the flow is predominantly lateral, and so the pressure within the current can be treated as hydrostatic. These models are sharp-interface models, as they assume that the phases are distinct from each other. The flow of the current can be treated as confined or unconfined. In confined flows, the thickness of the current is comparable to the thickness of the aquifer and return flow of the ambient brine affects the flow of CO_2 (Pegler *et al.*, 2014a). In unconfined flows, the thickness of the current is much smaller than the thickness of the aquifer and the flow of ambient brine has no effect (Hesse *et al.*, 2007; Huppert & Woods, 1995).

Supercritical CO_2 and water are largely immiscible fluids and so surface tension effects between the fluids will mean that each phase will occupy a fraction of the pore space within

a rock. This changes the behaviour of the CO_2-water system in two ways. Firstly, the effective pore space available for the CO_2 to move through is reduced by the remaining saturation of the water phase. Secondly, the effective permeability of the porous medium is dependent on the saturations of the phases present. Experimental studies on rock samples can be used to determine the effect of CO_2 saturation on capillary pressures and the relative permeability of the rock (Bennion & Bachu, 2005; Jackson *et al.*, 2018; Krevor *et al.*, 2012). Capillary forces tend to thicken the current, as increased capillary forces reduce the CO_2 saturation which results in a reduced effective porosity and permeability of the rock (Golding *et al.*, 2011). Studies incorporating capillary effects in confined (Gasda *et al.*, 2009) and unconfined (Golding *et al.*, 2011, 2013) aquifers find the extent of the current thickening is dependent on the pore size distribution of the rock, the strength of the capillary forces and the relative permeability of the two phases. However, the rate of CO_2 propagation is found to be insensitive to capillary effects.

Another factor that can affect the spreading of CO_2 on injection into a reservoir is the geological structure of the reservoir, particularly variations in permeability. The injected CO_2 will preferentially travel down high permeability pathways, an effect that is enhanced by capillary forces (Sathaye *et al.*, 2014). When large gradients in capillary pressure exist due to geological heterogeneities, capillary forces tend to rearrange the CO_2 saturation into high permeability regions, thereby accelerating plume migration through these channels.

1.3.2 CO_2 Trapping Mechanisms

While the CO_2 spreads throughout the aquifer, there are a number of processes that occur which result in the CO_2 becoming permanently immobilised before it has the chance to encounter a potential leakage pathway. These processes, referred to as secondary trapping mechanisms, are capillary trapping of CO_2 within pore spaces, known as residual trapping, mineralisation of the CO_2 into carbonate minerals, known as mineral trapping, and dissolution of the CO_2 into the ambient brine, known as solubility or dissolution trapping. Understanding the time and length scales over which these trapping mechanisms occur is important for determining when and where the CO_2 will no longer be in the mobile free phase and at risk of leakage.

Residual trapping is where CO_2 is permanently trapped at the receding interface of the CO_2 current by capillary forces during imbibition of brine (Krevor *et al.*, 2015). There are two primary length scales at which this process occurs. At the pore scale, imbibition of brine causes ganglia of CO_2 to snap off the main plume, becoming trapped in the pore spaces (Iglauer *et al.*, 2011; Karpyn *et al.*, 2010). At a slightly larger scale (around 1 mm for sandstones (Pini & Madonna, 2016)), capillary barriers with high capillary entry pressures trap CO_2 during imbibition and isolate pockets of CO_2 filling many pores from the main CO_2 plume (Krevor *et al.*, 2011; Saadatpoor *et al.*, 2010). These capillary barriers act in a similar manner to a CO_2 plume under a caprock. The amount of residually trapped CO_2 is dependent on the reservoir volume contacted by the CO_2 current, as well as the fraction of CO_2 that is residually trapped, which is controlled by a range of properties of the rock and the fluids, including pore size distribution and connectivity (Geistlinger *et al.*, 2014; Herring *et al.*, 2013), wettability (Chaudhary *et al.*, 2013; Huang *et al.*, 1996) and petrophysical properties (Ni *et al.*, 2019). Empirical evidence suggests the residual saturation depends on the historical maximum CO_2 saturation before imbibition (Pentland *et al.*, 2010). Due to the many factors affecting the residual trapping potential of a rock, it is difficult to predict the magnitude of residual trapping in advance without the use of measurements (Krevor *et al.*, 2015). Trapping rates can be determined experimentally by fitting empirical trapping relationships to measured initial-residual saturation curves (Perrin & Benson, 2010; Suzanne *et al.*, 2003; Spiteri *et al.*, 2008). Perhaps the simplest model of the effect of residual trapping on the propagation of a CO_2 current is a constant saturation of residually trapped CO_2 left at the receding interface of the current as it propagates, causing the total volume of the active current to reduce over time (Hesse *et al.*, 2008; Kochina *et al.*, 1983).

Mineral trapping is the precipitation of CO_2 as minerals, usually carbonate minerals or clay minerals. The precise chemical reactions that occur and the timescales that they happen over vary between aquifers (Baines & Worden, 2004). In general, when CO_2 is injected into siliciclastic rocks such as sandstones, the feldspar group minerals may react with CO_2 dissolved in the formation brine to form carbonates and clays over 100 year timescales or longer (Land *et al.*, 1987). Mineralisation rates estimated from a natural CO_2-rich gas field shows only $\sim$2.4% of the CO_2 is stored in the mineral phase after tens of millions of years (Wilkinson *et al.*, 2009). Geochemical modelling of the Sleipner CO_2 site suggests that

mineral trapping is only a minor contributor to CO_2 storage over 10,000 years (Audigane *et al.*, 2007). This is because CO_2 quickly establishes a new chemical equilibrium with the in-situ pore waters post-injection, and subsequent reaction rates are very slow (Ringrose *et al.*, 2021). However, these examples represents a conservative end-member for reactions rates as North sea sandstones have high quartz contents and hence are very unreactive. In contrast, on injection of CO_2 into basaltic rocks, as demonstrated by the CarbFix project in Iceland, 80% of the CO_2 is observed to mineralise within one year (Aradóttir *et al.*, 2011; Gislason & Oelkers, 2014). Basaltic reservoirs will likely be a small fraction of the total storage capacity but where saline reservoirs are interbedded with volcanic rocks, mineral trapping of CO_2 could play a larger role, as in the case in natural CO_2 reservoirs in the Otway basin in Australia (Watson *et al.*, 2004).

Dissolution trapping is the dissolution of injected CO_2 into the ambient brine within a saline aquifer. As the CO_2 dissolves into water, the density of the water increases (Teng & Yamasaki, 1998), eliminating the buoyancy of free-phase CO_2 and reducing the risk of leakage to the surface. The rate of CO_2 dissolution in formation waters is controlled by the diffusive transport of dissolved CO_2 away from the CO_2-water contact, as well as the total contact area. In a static system, diffusion of CO_2 into water is slow as the CO_2 diffusion coefficient is small and diffusive fluxes decrease as the square-root of time. The size of the CO_2-enriched brine boundary layer will grow to $\sim$10 cm thick in 1 year or $\sim$4 m in 100 years (Lindeberg & Wessel-Berg, 1997). Density differences within the brine due to concentration gradients of dissolved CO_2 can lead to convection of the CO_2-saturated brine. This results in fresh brine being brought into contact with the free-phase CO_2, dramatically enhancing the rate of CO_2 dissolution (Ennis-King & Paterson, 2005; Neufeld *et al.*, 2010; Riaz *et al.*, 2006). At the Sleipner CO_2 site, it is estimated that roughly 10% of the annually injected mass would be trapped by convective dissolution (Neufeld *et al.*, 2010). However, this effect is substantially reduced in reservoirs with more highly anisotropic permeability structures (Green & Ennis-King, 2014). Sathaye *et al.* (2014) constrained dissolution rates at a natural CO_2 field and found that 22% of the emplaced CO_2 dissolved over 1.2 million years, with dissolution rates post emplacement exceeding the amount expected from diffusion and providing field evidence for convective CO_2 dissolution. It is clear that the relative movement of water and CO_2 will exert an important control on CO_2 dissolution rates. During injection and flow, the lower

viscosity of the CO_2 will result in fingering (Saffman & Taylor, 1958) which will be strongly enhanced by reservoir heterogeneities. For CO_2 injection into horizontally layered reservoirs comprising alternating higher and lower permeability layers, free-phase low viscosity CO_2 flow will preferentially be confined to the higher permeability layers. This will likely lead to increased dissolution rates due to an increase in interfacial area between the CO_2 and reservoir fluid. In Chapter 2, I use an analytical approach to estimate the quantity of CO_2 dissolved and the rate of propagation of free-phase CO_2 in heterogeneous layered reservoirs.

1.3.3 CO_2 Leakage Pathways

As the CO_2 current spreads underneath the caprock, there is potential for defects within the seal to allow stored CO_2 to leak into overlying aquifers and eventually to the surface. There are two main mechanisms by which this may happen. Firstly, CO_2 may leak slowly through the low permeability caprock (Acton *et al.*, 2001; Pritchard *et al.*, 2001; Pritchard & Hogg, 2002). For this to occur, the hydrostatic pressure in the underlying CO_2 current must overcome the finite capillary entry pressure of the caprock (Woods & Farcas, 2009). Increased pressure due to injection or background pressure gradients between multiple aquifers may also contribute to overcoming the capillary entry pressure (Pegler *et al.*, 2014b). If the pressure within the current is less than the entry pressure, no leakage occurs and the CO_2 remains trapped under the caprock. Secondly, the impermeable caprock may contain discrete fractures or other permeable defects that allow leakage of CO_2. The leakage flux through these fractures is driven by the pressure gradient across the fracture, which may comprise of the hydrostatic pressure of the underlying fluid (Pritchard, 2007), the buoyancy of fluid in the fault (Neufeld *et al.*, 2009), and increased pressures due to background pressure gradients or injection pressures.

Faults, which are localised zones of brittle deformation caused by tectonic activity, are a common feature in geological reservoirs, and may act as discrete leakage pathways for trapped fluids (Caine *et al.*, 1996; Faulkner *et al.*, 2010; Nicol *et al.*, 2017). As faults can cut through multiple aquifers and caprocks, they have the potential to act as significant leakage pathways from depth all the way to the surface, and so it is important to understand what controls their flow dynamics, as well as how they may affect how much CO_2 remains trapped within

the aquifer. In Chapter 3, I present an analytical model which describes the dynamics of leakage through a fault zone and apply the model to a CO_2-charged aquifer system at Green River, Utah to calculate the CO_2 leakage rates and fluid distribution across multiple aquifers.

1.3.4 Post-injection Monitoring of CO_2

Monitoring of the CO_2 post-injection is important for confirmation that the CO_2 is remaining securely trapped within the subsurface, as well as giving prior warning of any potential leaks. Site operators of CO_2 storage projects are legally required to show that the injected CO_2 is migrating as predicted within the predefined lease area, and that it remains safely contained with no risk of negative impact to the environment (Chadwick *et al.*, 2008; Davis *et al.*, 2019). The most widely used technique for post-injection monitoring of stored CO_2 is repeat seismic imaging, also known as time-lapse seismic or 4D seismic (Furre *et al.*, 2017; Ringrose *et al.*, 2013; Huang *et al.*, 2018; Tanase & Tanaka, 2021; Bourne *et al.*, 2014; White *et al.*, 2017). Here, a controlled seismic source is used to image velocity and density contrasts within the reservoir over time due to the presence of CO_2. Other monitoring techniques that have been used include time-lapse resistivity logging (Nakajima & Xue, 2013), time-lapse gravity surveys (Wilkinson *et al.*, 2017), direct CO_2 saturation measurements through pulsed neutron logging (Ivanova *et al.*, 2012; Marsh *et al.*, 2018), and the use of geochemical tracers (Bickle *et al.*, 2017; Roberts *et al.*, 2017).

The aim of time-lapse seismic imaging is to characterise the spatial extent and thickness of the CO_2 layer as a function of time. The presence of CO_2 within the pore spaces of a rock dramatically reduces its seismic velocity and this changes the properties of the reflected seismic wavelets. The seismic surveys taken after CO_2 injection can be compared to a seismic survey taken prior to injection to ascertain the location of the CO_2. However, there are two major challenges to overcome when using seismic imaging to detect CO_2. Firstly, there is a seismic resolution below which it is difficult to resolve the thickness of the CO_2 layer. An approximation for the minimum resolvable layer thickness is one quarter of the wavelength of the seismic wavelet. By analysing different features of the seismic trace that are controlled by the thickness of the CO_2 layer, it is possible to obtain estimates of CO_2 thickness below the seismic resolution. This includes the peak frequency (Huang *et al.*, 2016; White *et al.*,

2018; Williams & Chadwick, 2012), peak amplitudes (Arts *et al.*, 2004; Cowton *et al.*, 2016) and the time-shift of the peaks and troughs (Cowton *et al.*, 2016; Furre *et al.*, 2015; Ghaderi & Landrø, 2009). However, these methods require high signal-to-noise ratios and a relatively homogeneous injection interval with well defined structure and geology. Secondly, seismic imaging detects impedance contrasts between layers in the subsurface, which is a product of the density and velocity of each layer. The velocity of a CO_2 layer behaves nonmonotonically with increasing CO_2 saturation (Gassmann, 1951; Smith *et al.*, 2003), which introduces uncertainty into the CO_2 saturation within the reservoir. Nevertheless, seismic imaging has delivered important insight into the behaviour of CO_2 in the subsurface, as well as enabling benchmarking and vertification of dynamic flow models which allows better prediction of future injections (Cowton *et al.*, 2018; Chadwick & Noy, 2010; Williams & Chadwick, 2017; Williams *et al.*, 2018).

1.4 Aims and Approaches

In this dissertation, I investigate three important aspects of carbon dioxide storage security in the sub-surface: CO_2 trapping rates due to dissolution in heterogeneous reservoirs, CO_2 leakage rates through fault zones, and the flow of CO_2 within a heterogeneous reservoir with comparison to time-lapse seismic reflection surveys. Reduced-order analytical and numerical models are used to explore these problems, with the focus on understanding the key physical parameters that affect the behaviour of these systems.

The rate of CO_2 dissolution in saline aquifers is the least well-constrained of the secondary trapping mechanisms enhancing the long-term security of geological carbon storage. CO_2 injected into a heterogeneous saline reservoir will preferentially travel along high permeability layers, increasing the CO_2-water interfacial area which increases dissolution rates. An analytical approach is used to provide a conservative, first-principles analysis of the quantity of CO_2 dissolved and the rate at which free-phase CO_2 propagates in layered reservoirs. Fault zones have the potential to act as leakage pathways through low permeability structural seals in geological reservoirs. An analytical model is presented that describes the dynamics of leakage through a fault zone cutting multiple aquifers and seals. This combines current

analytical models for a buoyant plume in a semi-infinite porous media and a model for a leaking gravity current with a new model to account for increased pressure gradients within the fault due to an increase in Darcy velocity directly above the fault. A series of analogous porous media tank experiments are used to verify the results. Finally, a numerical model is used to investigate the flow of CO_2 through a reservoir at the Otway CCS site in Australia. The effects of residual trapping on the plume are modelled, and results compared to observations from time-lapse seismic imaging. The sensitivity of the flow model to variations in reservoir permeability and caprock topography are also explored.

1.5 Dissertation Structure

In the remainder of the dissertation, I focus on the following aspects of CO_2 storage.

Chapter 2: CO_2 Dissolution Trapping Rates in Heterogeneous Porous Media. An analytical model is used to provide estimates of the quantity of CO_2 dissolved and free-phase CO_2 propagation rates in heterogeneous layered reservoirs. The model assumes horizontal strata within the reservoir with CO_2 flow confined to the high permeability layers and ignores the buoyancy of the supercritical CO_2. It is assumed that there is no flow of CO_2 between layers, but there is diffusive exchange of CO_2 across the static, water-filled low permeability layers. The modelling provides a minimum estimate for CO_2 dissolution against which the effect of additional processes or field observations may be assessed.

Chapter 3: Leakage Dynamics of Fault Zones with Application to CO_2 Storage. An analytical model is developed to describe the dynamics of leakage through a fault zone that cross cuts multiple aquifers and seals, which is tested against a set of laboratory experiments using miscible fluids. To model flow in faults cross-cutting multiple aquifers, current analytical models for a buoyant plume in a semi-infinite porous media and a leaking gravity current are combined with a new model for fault leakage which accounts for increased pressure gradients within the fault due to an increase in Darcy velocity directly above the fault.

The results of the modelling are illustrated by application to a naturally occurring CO_2-charged aquifer system at Green River, Utah, using an extension of the model to calculate the fluid distribution across multiple vertically stacked aquifers, cross-cut by a fault.

Chapter 4: The Otway Project. A research scale CO_2 sequestration project in Australia called the Otway Project is described in detail. Time-lapse seismic surveys of a small CO_2 injection are interpreted to map a seismic anomaly associated with the CO_2 plume. Seismic waveform modelling of CO_2 thickness in the injection interval is combined with geological models of the reservoir obtained from well log data. Estimates of CO_2 saturation from pulsed neutron log data is used to constrain the thickness of the CO_2 plume.

Chapter 5: Vertically-integrated Flow Simulations of the Otway Stage 2C Injection. A vertically-integrated gravity current model including residual trapping of CO_2 is developed and benchmarked. The caprock topography from the baseline seismic survey, and fluid and injection parameters from the literature are used to simulated the Otway Stage 2C injection. Reservoir properties are inverted for by matching flow model results to CO_2 plume thickness estimates from Glubokovskikh *et al.* (2020). The effects of large-scale structural heterogeneity associated with a bounding fault zone are considered. Simulations are performed to investigate the role of residual trapping on the time to plume stabilisation. The effects of permeability variations in the injection interval and errors in reservoir geometry on the results of the numerical simulations is discussed.

Chapter 6: Conclusions and Further Work. I summarise the main conclusions from the work in this dissertation, and point towards avenues in which the work might be fruitfully extended.

Chapter 2

CO_2 Dissolution in Heterogeneous Porous Media

2.1 Introduction

The dissolution of injected CO_2 into the ambient brine within a saline aquifer is a key mechanism for increasing the security of long-term storage. At typical storage reservoir conditions, CO_2 is in the supercritical phase and is buoyant with respect to the surrounding reservoir fluid, and therefore presents a risk of migration to the surface. As CO_2 dissolves into water the density of the water increases (Teng & Yamasaki, 1998), eliminating the buoyancy of free-phase CO_2 and reducing the risk of leakage. Quantifying total dissolution rates post injection is therefore important for assessing the contribution of CO_2 dissolution to the long-term security of stored CO_2.

The rate of CO_2 dissolution in formation waters is controlled by the diffusive transport of dissolved CO_2 away from the CO_2-water contact and the area of the contact. Because

diffusive fluxes into a static system decrease as the square-root of time and the CO_2 diffusion coefficient is small ($\sim 2 \times 10^{-9}$ m^2s^{-1} (Cadogan *et al.*, 2014)), CO_2-enriched boundary layers in water in contact with free-phase CO_2 will grow to ∼10 cm thick in 1 year or ∼4 m in 100 years (Lindeberg & Wessel-Berg, 1997). The relative movement of water and CO_2 will therefore exert an important control on CO_2 dissolution rates. During injection of CO_2, the lower viscosity of the CO_2 will result in fingering (Saffman & Taylor, 1958) which will be strongly enhanced by reservoir heterogeneities. It is the resulting complexities in the geometry of the CO_2-water interface and flow of CO_2 that makes CO_2 dissolution difficult to quantify.

There are few constraints on CO_2 dissolution during CO_2 injection. Measurements of $CO_2/^3He$ ratios show that some natural CO_2 accumulations have lost more than 90% of their original CO_2 by dissolution over hundreds of thousands to millions of years (Gilfillan *et al.*, 2009). At Green River, Utah, where natural CO_2 has been migrating up a fault system for several hundred thousand years, Bickle & Kampman (2013) estimated that less than 1% of the CO_2 escaped to the surface, the rest being dissolved in permeable horizons intersected by the fault system. Most modelling of CO_2 dissolution has concentrated on the impact of convective circulation of the brine beneath CO_2 accumulations driven by the density increase as brine saturates with CO_2 (e.g. Ennis-King & Paterson, 2005; Neufeld *et al.*, 2010). However, the marked anisotropy of permeabilities in most reservoirs substantially reduces the convective circulation (Green & Ennis-King, 2014). Reservoir simulations using numerical models typically use grid sizes of more than 10 m which are unable to model flow heterogeneities on ∼1 m or less length scales over which diffusion characteristically dominates. There are limited constraints on dissolution rates from measurements on small-scale injection experiments. In the Frio experiment, Texas, Freifeld *et al.* (2005) noted that the arrival times of the tracer krypton lagged behind the arrival of the tracers sulfur hexafluoride and perfluorocarbon and attributed this to the higher solubility of krypton in brine. Likewise, Lu *et al.* (2012) observed a similar lag between sulfur hexafluoride and krypton tracers in the Cranfield, Mississippi CO_2 injection experiment. However, attempts to quantify such observations have had limited success (e.g. LaForce *et al.*, 2014). In a CO_2 injection phase at the Salt Creek, Wyoming enhanced oil recovery site, Bickle *et al.* (2017) observed that dissolution of CO_2 in formation brines drove significant reactions with silicate minerals, but

again the difficulty in modelling the complex flows in a heterogeneous reservoir have so far precluded quantitative estimates.

The CO_2-brine interactions which determine CO_2 dissolution will be controlled by the reservoir heterogeneities on all scales and these are difficult to model properly, both because it is not possible to determine the reservoir structure at the sub-metre scales which matter for the diffusive processes, and because numerical models of CO_2 and brine flows in reservoirs are not currently capable of running at such resolutions. In this chapter, I consider dissolution during CO_2 injection into a simple representation of a layered reservoir, and quantify the increased dissolution rates due to an increase in interfacial area between the CO_2 and the reservoir fluid. This provides a base case, given that the additional complexities are likely to substantially increase dissolution rates. The model is then evaluated using parameters appropriate to large-scale CO_2 injection such as reservoir bedding thickness, porosity, saturation and injection flux.

I model a horizontally layered reservoir comprising alternating higher and lower permeability layers. Free-phase, low viscosity CO_2 flow will preferentially be confined to the higher permeability layers. This channelisation is enhanced by capillary entry pressures which impede CO_2 entering the lower permeability layers (c.f. Sathaye *et al.*, 2014). The model assumes a simplified geometry or horizontal strata within the reservoir with CO_2 flow confined to the high permeability layers and ignores buoyancy of the supercritical CO_2. It is assumed further that there is no flow of CO_2 between layers, but there is diffusive exchange of CO_2 across the static, water-filled, low permeability layers. The modelling provides a minimum estimate for CO_2 dissolution, against which the effect of additional processes or field observations may be assessed. Mixing of CO_2 and water along formation boundaries, fingering of low viscosity CO_2 into formation waters and the consequent dissolution of CO_2 ahead of the CO_2 finger, and the much more complex permeability structures in most sedimentary rocks would all be expected to enhance dissolution rates, most probably by an order-of-magnitude or more. It will likely only be possible to estimate the impact of these processes by experiments in field settings.

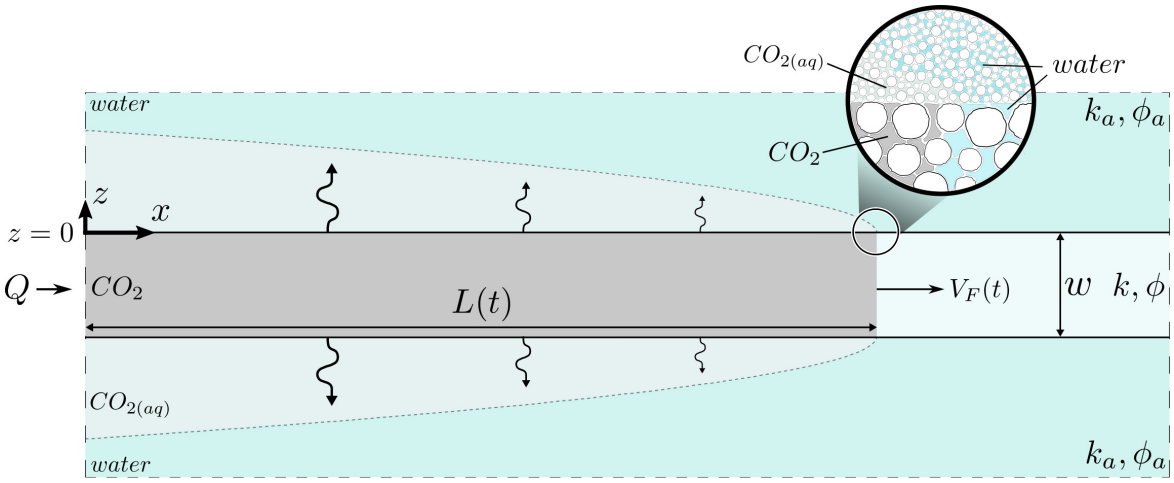

Figure 2.1: Schematic diagram of a two dimensional finger of free-phase CO_2 propagating along a high permeability porous layer that is initially saturated with water surrounded by a low permeability porous aquifer also saturated with water.

2.2 CO_2 Flow in a Single High Permeability Layer

2.2.1 Single Layer Model

I first consider CO_2 propagating along a single, high permeability layer of width w, porosity ϕ and permeability k in a low permeability, water saturated aquifer of porosity ϕ_a and permeability k_a (Figure 2.1). CO_2 is injected into the high permeability layer at constant volumetric rate Q. For simplicity, I assume that a finite capillary entry pressure confines the flow of free-phase CO_2 to the high permeability layer. The CO_2 finger has a total length $L(t)$ and a volume flux at the front of the finger $V_F(t)$. The length of the CO_2 finger is much greater than its width so diffusive dissolution across the CO_2-water interface at the finger front is neglected and the interface is modelled as planar for simplicity.

The diffusive CO_2 profile away from the CO_2-water interface (in the z direction) for a given value of x is given by the solution for diffusion into a semi-infinite layer (Carslaw & Jaeger, 1959, p. 59),

$$c = \begin{cases} c_0 \operatorname{erfc}\left[\dfrac{z}{2\sqrt{D(t - t_0(x))}}\right], & t > t_0, \\ 0, & 0 \leq t \leq t_0, \end{cases} \tag{2.1}$$

where erfc is the complimentary error function, c_0 is the maximum solubility of CO_2 in water as a dimensionless mass fraction, t is the time since injection commenced and $t_0(x)$ is the

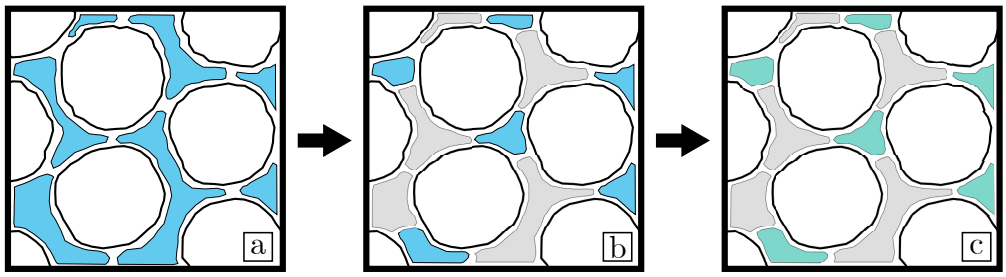

Figure 2.2: (a) Pore spaces in the high permeability layer are initially filled with water (blue). (b) CO_2 (grey) partially displaces the water. (c) CO_2 dissolves into the residual water leaving CO_2-saturated water (green).

time at which the front passes position $x = L(t_0)$. The effective diffusion coefficient of CO_2 in water is given by

$$D = D_m \frac{\phi_a}{\tau}, \tag{2.2}$$

where D_m is the molecular diffusion coefficient of CO_2 in water and ϕ_a and τ are the porosity and tortuosity of the low permeability layer (Pismen, 1974). The CO_2 concentration gradient in the water away from the CO_2 finger is therefore

$$\frac{\partial c}{\partial z} = -\frac{c_0}{\sqrt{\pi D(t - t_0)}} \exp\left[\frac{-z^2}{4D(t - t_0)}\right]. \tag{2.3}$$

The diffusive flux of CO_2 at each point along the high permeability layer is equal to $-D\frac{\partial c}{\partial z}\Big|_{z=0}$, hence the total vertical diffusive flux of CO_2 out of the high permeability layer at time t is,

$$F_{total}(t) \;=\; -2\phi_a \int_0^{L(t)} D\frac{\partial c}{\partial z}\Big|_{z=0} dx \;=\; 2\phi_a \int_0^{L(t)} c_0 \sqrt{\frac{D}{\pi(t - t_0(x))}}\, dx, \tag{2.4}$$

with ϕ_a introduced as CO_2 only diffuses into water within the pores and the factor 2 accounting for diffusion on both sides of the high permeability layer. As a non-wetting phase, CO_2 only partially displaces water in the high permeability layer. This reduces the fraction of the porosity occupied by CO_2 (given by the non-wetting saturation s_{nw}), and also means that some CO_2 dissolves into the water occupying the remaining pore space. This process is illustrated in Figure 2.2.

The velocity of the CO_2 front at $x = L(t)$ is a function of the input flux and diffusive losses given by lateral diffusion from the finger and complete saturation of the residual water within

the CO_2 finger,

$$V_F(t) = vw\phi s_{nw} = v_0 w\phi s_{nw} - 2\phi_a \rho_r \int_0^{L(t)} c_0 \sqrt{\frac{D}{\pi(t - t_0(x))}}\, dx - vw\phi c_0 \rho_r (1 - s_{nw}). \quad (2.5)$$

Here v is the interstitial velocity of CO_2 at the front and v_0 is the CO_2 interstitial velocity at $x = 0$ where $v_0 = Q/w\phi s_{nw}$. As the density of free-phase CO_2 (ρ_{CO_2}) is less than the density of CO_2 saturated brine ($\rho_{H_2O_{sat-CO_2}}$), the mass fraction of CO_2 required to saturate the brine will take up more volume in the free-phase, hence a density ratio $\rho_r = \rho_{H_2O_{sat-CO_2}}/\rho_{CO_2}$ is introduced to account for this volume change. By introducing the non-dimensional variables

$$\tilde{v} = \frac{v}{v_0}, \quad \tilde{c} = \frac{c}{c_0}, \quad \tilde{x} = \frac{c_0^2 \rho_r^2 \phi_a^2 D}{v_0 w^2 \phi^2 s_{nw}^2} x, \quad \tilde{t} = \frac{c_0^2 \rho_r^2 \phi_a^2 D}{w^2 \phi^2 s_{nw}^2} t, \quad (2.6)$$

(2.5) may be rewritten in the generic form

$$(1 + \alpha)\tilde{v} = 1 - 2 \int_0^{\tilde{L}(\tilde{t})} \sqrt{\frac{1}{\pi(\tilde{t} - \tilde{t_0}(\tilde{x}))}}\, d\tilde{x}, \quad (2.7)$$

where $\alpha = c_0 \rho_r (1 - s_{nw})/s_{nw}$ is a measure of how much CO_2 dissolves into residual water within the CO_2 finger. (2.7) gives the dimensionless front velocity as a function of dimensionless time. For notational convenience, the '$\sim$' is dropped from all subsequent quantities. (2.7) is solved numerically using a sequential iteration approach. The CO_2 concentration gradient at the interface is calculated every timestep allowing the total diffusive flux to be deducted from the input flux giving the CO_2 velocity, v, as a function of time. The new front velocity allows the position of the CO_2 front, $L(t)$, to be calculated for the next timestep.

Note that the single finger model derived in this section can also be used to describe CO_2 movement and dissolution rates in other reservoir settings where large permeability variations may exist, for example a high permeability fracture propagating through a low permeability host rock. In this case, the model could be used to calculate how dissolution changes the front velocity of the CO_2 as it moves through the fracture and therefore changes the breakthrough time of CO_2 leaking through the host rock, as demonstrated by Snippe *et al.* (2021).

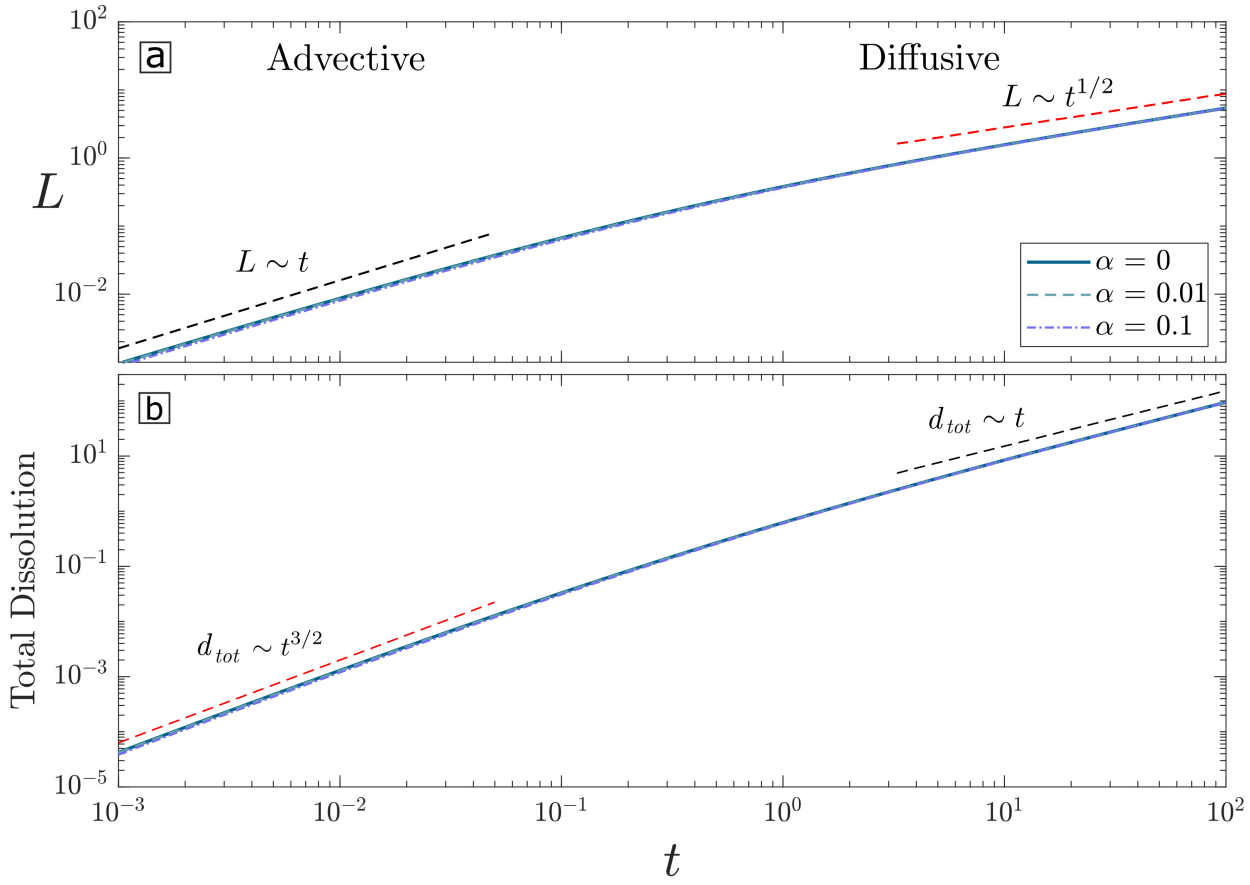

Figure 2.3: (a) Length of the CO_2 finger L as a function of time t. At early times, the length evolves as $L \sim t$ (black dashed line), and at late times it evolves as $L \sim t^{1/2}$ (red dashed line). (b) The total lateral dissolution of CO_2 from the high permeability finger into the surrounding water is plotted as a function of time. At early times, the total dissolution scales like $t^{3/2}$. At late times, the total dissolution tends towards scaling like t. Both graphs are plotted for $\alpha = 0$, 0.01, 0.1.

2.2.2 Results

The model for propagation of a CO_2 finger along a single, high permeability layer described in Section 2.2.1 is solved to obtain the length of the CO_2 finger as a function of time, thereby giving the rate at which free-phase CO_2 propagates through the reservoir, and also the quantity of CO_2 dissolved over time.

The length of the CO_2 finger (illustrated as a function of time in Figure 2.3a) is governed by the input flux and the total dissolution over the length of the finger. At early times ($t \ll 1$), the dissolution area to input flux ratio of the CO_2 finger is small, and so the amount of dissolution is negligible meaning that the growth of the CO_2 finger is dominated by the input flux and evolves as $L \sim t$. This is labelled as a period of advective growth in Figure

2.3. During this period, the diffusive CO_2 profile away from the CO_2-water interface (in the z direction) scales like $F \sim t^{-1/2}$, and since the total length of the finger is growing like $L \sim t$, the total diffusive flux F_{tot} across the length of the finger scales like

$$F_{tot}(t) \sim \int_0^{L(t)} F\, dx \sim t^{1/2}. \tag{2.8}$$

The total lateral dissolution d_{tot} into the low permeability layers is the sum of the total flux over time (figure 2.3b), and hence the scaling at early times is

$$d_{tot}(t) \sim \int_0^{t} F_{tot}\, dt \sim t^{3/2}. \tag{2.9}$$

At late times ($t \gg 1$), due to the increased length of the CO_2 finger, there is a greater area available for dissolution and so diffusive loss dominates, meaning the length of the finger tends towards the scaling $L \sim t^{1/2}$. The diffusive flux F at a point x on the finger continues to scale like $F \sim t^{-1/2}$, but as the growth of the finger tends towards the length scaling like $L \sim t^{1/2}$, the total diffusive flux tends to a constant, $F_{tot} \sim const.$ This means the total lateral dissolution into the low permeability layers scales like $d_{tot} \sim t$ at late times (Figure 2.3b). The transition between these two regimes happens when $L \sim t \sim 1$. Another way to show the quantity of CO_2 dissolved over time is by calculating the total CO_2 dissolved as a fraction of the total volume of free-phase CO_2 injected into the system (Figure 2.4a). The total dissolved CO_2 is defined as the total CO_2 injected into the system that has either diffused into the water within the low permeability layers or saturated the residual water within the CO_2 finger. This fraction increases with time as the increase in the surface area increases the ratio of diffusive loss to input flux and tends to 1 as $t \to \infty$. The total dissolution flux at a given time as a fraction of the total input flux also shows a similar trend (2.4b).

Figures 2.3 and 2.4 have been plotted for three values of α. When $\alpha = 0$, there is no residual water within the high permeability layer and CO_2 dissolves only by lateral diffusion into the water in the low permeability layers. At low values of α, the fraction of CO_2 dissolved in the residual water within the high permeability layer is small compared with lateral loss to the surrounding water, especially at later times. For a typical reservoir where $s_{nw} = 0.8$ (Krevor

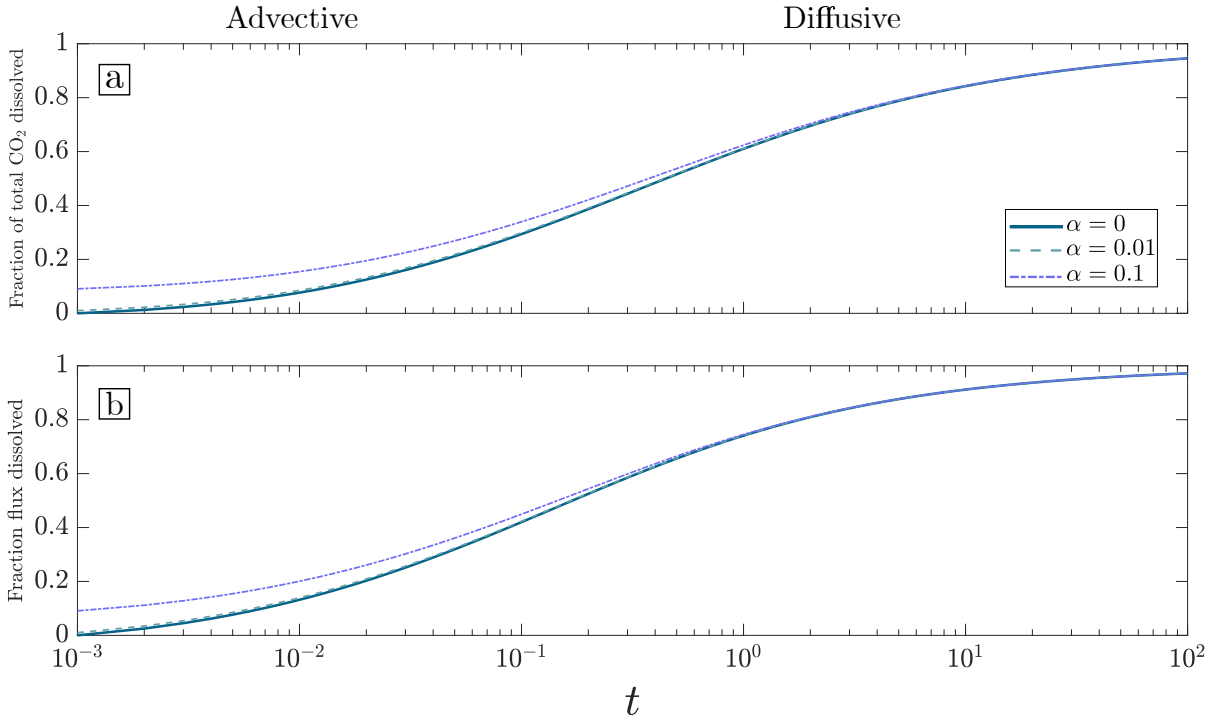

Figure 2.4: (a) Fraction of total injected CO_2 that has dissolved as a function of time. The fraction of the CO_2 dissolved consists of CO_2 that has diffused into the surrounding water as well as the CO_2 that has saturated the residual water within the CO_2 finger. (b) Dissolution flux at a given time as a fraction of the total input flux. Both graphs are plotted for $\alpha = 0$, 0.01, 0.1.

et al., 2015), $\rho_r = 1.5$ and $c_0 = 5.5$ $wt\%$ (Dubacq *et al.*, 2013), $\alpha = 0.02$ which suggests that the dominant diffusive process would be lateral CO_2 dissolution.

2.3 CO_2 Flow Along Periodic High Permeability Layers

2.3.1 Multilayered Model

The saline aquifers suitable for geological storage are characteristically sandstones bedded on 10^{-2} to 1 metre scales with permeabilities that vary by an order of magnitude or greater. Injection of CO_2 will primarily occupy the high permeability layers and the diffusive fringes about the CO_2-filled layers will overlap. I illustrate this behaviour with a periodically layered reservoir with high permeability layers of width w, porosity ϕ and permeability k interbedded with low permeability layers of width $2h$, porosity ϕ_a and permeability k_a. CO_2 flows into

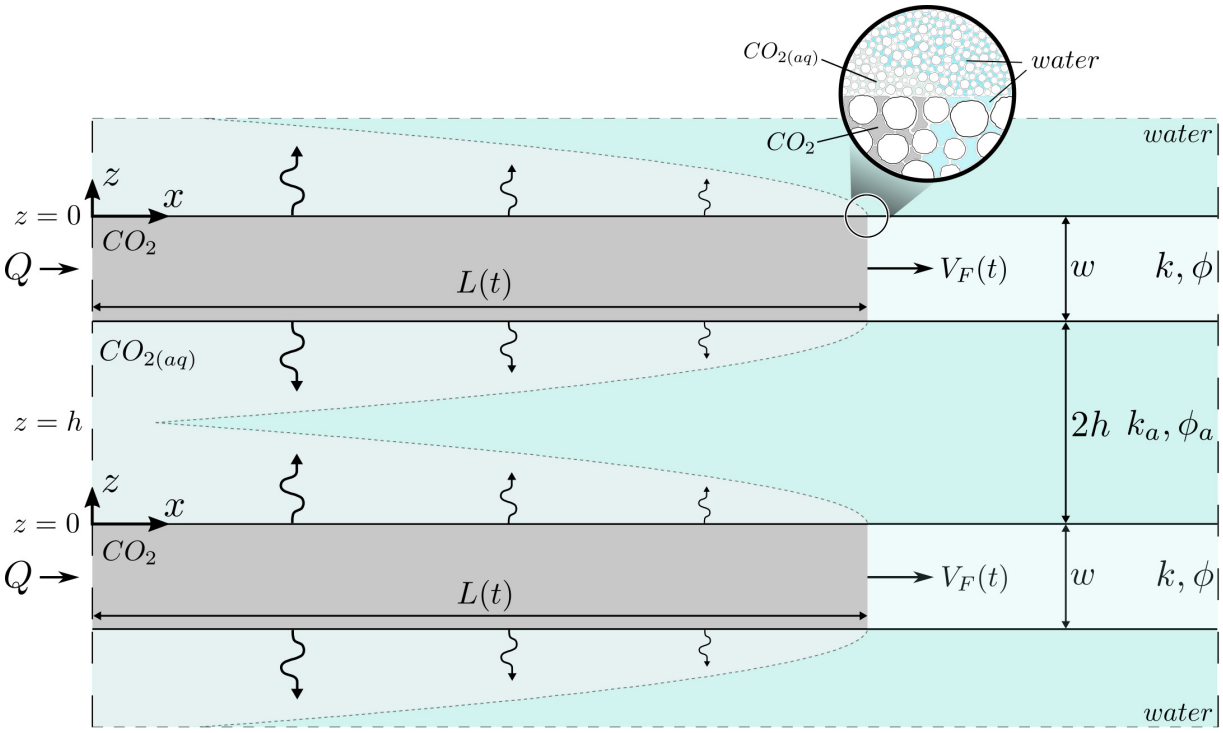

Figure 2.5: Schematic diagram of periodically repeating high permeability porous layers of width w, separated by low permeability porous layers of width, $2h$. The reservoir is initially saturated with water. CO_2 is injected into the high permeability layers. $z = 0$ at the high/low permeability interface and $z =$ h at the midpoint between the high permeability layers.

each of the high permeability layers at volumetric rate Q. It is assumed that a finite capillary entry pressure confines advective flow of free-phase CO_2 to the high permeability layers (see Figure 2.5). The diffusive profile between layers is given by the solution for diffusion into a layer bounded by two parallel planes (Carslaw & Jaeger, 1959, p. 100),

$$c = c_0 - \frac{4c_0}{\pi}\sum_{n=0}^{\infty}\frac{(-1)^n}{2n+1}\exp\left[\frac{-D(2n+1)^2\pi^2(t-t_0)}{4h^2}\right]\cos\left[\frac{(2n+1)\pi(1-\frac{z}{h})}{2}\right]. \tag{2.10}$$

This gives a vertical CO_2 concentration gradient in the water

$$\frac{\partial c}{\partial z} = -\frac{2c_0}{h}\sum_{n=0}^{\infty}(-1)^n\exp\left[\frac{-D(2n+1)^2\pi^2(t-t_0)}{4h^2}\right]\sin\left[\frac{(2n+1)\pi(1-\frac{z}{h})}{2}\right], \tag{2.11}$$

which evaluated at the interface between the free-phase CO_2 and water is

$$\frac{\partial c}{\partial z}\Big|_{z=0} = -\frac{2c_0}{h}\sum_{n=0}^{\infty}\exp\left[\frac{-D(2n+1)^2\pi^2(t-t_0)}{4h^2}\right]. \tag{2.12}$$

The velocity of the CO_2 front at $x = L$ is a function of the input flux, lateral diffusive loss and saturation of the residual water,

$$V_F(t) = vw\phi s_{nw} =$$
$$v_0 w\phi s_{nw} - \frac{4\phi_a c_0 \rho_r D}{h} \int_0^{L(t)} \sum_{n=0}^{\infty} \exp\left[\frac{-D(2n+1)^2\pi^2(t - t_0(x))}{4h^2}\right] dx \; - \; vw\phi c_0 \rho_r (1 - s_{nw}), \tag{2.13}$$

with ϕ_a introduced as CO_2 only diffuses into water within the pores and $\rho_r = \rho_{H_2O_{sat-CO_2}}/\rho_{CO_2}$ accouting for the volume change from free-phase to dissolved CO_2. Introducing the non-dimensional variables

$$\tilde{v} = \frac{v}{v_0}, \quad \tilde{c} = \frac{c}{c_0}, \quad \tilde{x} = \frac{D}{v_0 h^2} x, \quad \tilde{t} = \frac{D}{h^2} t, \quad \tilde{z} = \frac{z}{h}, \tag{2.14}$$

(2.13) can be rewritten as

$$(1 + \alpha)\tilde{v} = 1 - 4\beta \int_0^{\tilde{L}(\tilde{t})} \sum_{n=0}^{\infty} \exp\left[\frac{-(2n+1)^2\pi^2(\tilde{t} - \tilde{t_0}(\tilde{x}))}{4}\right] d\tilde{x} \; , \tag{2.15}$$

where $\alpha = c_0\rho_r(1 - s_{nw})/s_{nw}$ and $\beta = \frac{h\phi_a c_0 \rho_r}{w\phi s_{nw}}$. For notational convenience, the '$\sim$' is dropped from all subsequent quantities. A similar iterative solution to the single finger case is used to solve (2.15) to give the CO_2 front position and velocity, and total dissolution of CO_2 as a function of time for the multi-layered model.

2.3.2 Results

The length of the CO_2 fingers, and hence the rate at which the free-phase CO_2 propagates into the reservoir, evolve in three different stages (Figure 2.6a). At early times ($t \ll 1$), as with the single finger case, the dissolution area to input flux ratio of the CO_2 finger is small, and so the amount of dissolution is negligible meaning the growth of the CO_2 fingers is dominated by the input flux and they evolve as $L \sim t$. Since the diffusive flux away from the CO_2-water interface scales like $F \sim t^{-1/2}$ and the length of the finger grows like $L \sim t$, the total diffusive flux scales like $F_{tot} \sim t^{1/2}$ and hence the total dissolution of CO_2 over

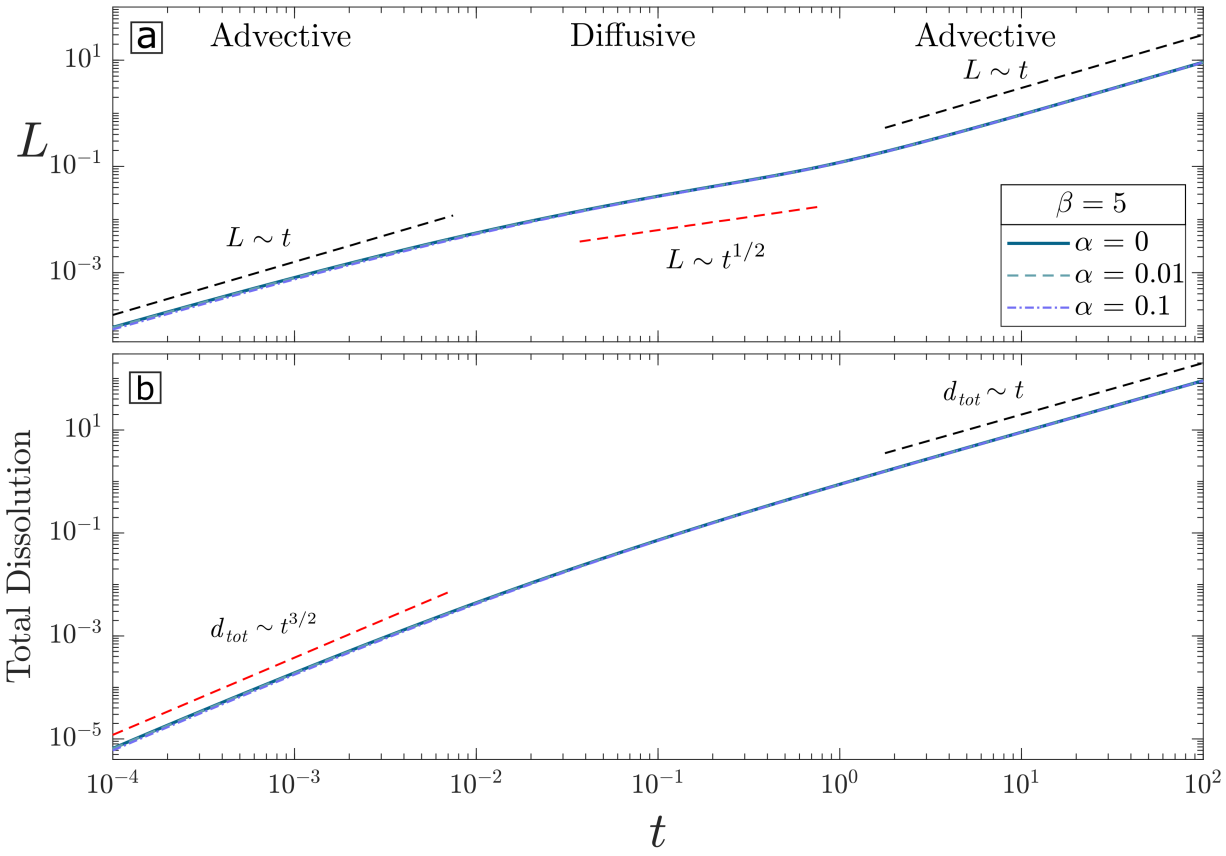

Figure 2.6: (a) Length of the CO_2 fingers L as a function of time t. Also plotted is the line $L \sim t$ (black dashed line), and the line $L \sim t^{1/2}$ (red dashed line). The length of the fingers increase as a linear function of t at both early and late times but with $L \sim t^{1/2}$ at intermediate times. (b) The total lateral dissolution from the CO_2 finger is plotted as a function of time. At early times, the total dissolution scales with $t^{3/2}$. At late times, the total dissolution evolves proportional to time, as the diffusive flux becomes constant. Both graphs are plotted for $\beta = 5$ and $\alpha = 0$, 0.01, 0.1.

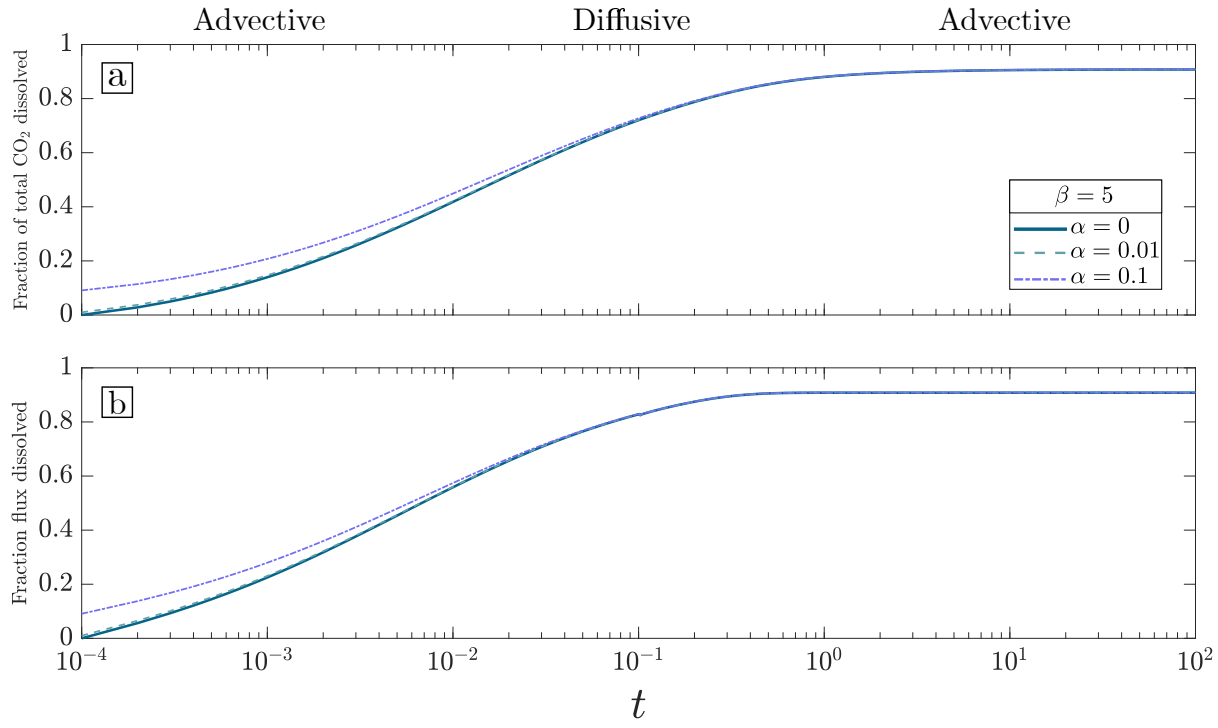

Figure 2.7: (a) Fraction of total injected CO_2 that has dissolved as a function of time. (b) Dissolution flux at a given time as a fraction of the total input flux. Both graphs are plotted for $\beta = 5$ and $\alpha = 0$, 0.01, 0.1.

time scales like $d_{tot} \sim t^{3/2}$ in this early advection dominated regime. At intermediate times, there is a transition to a diffusion dominated regime where an increase in the CO_2 finger length and hence CO_2-water contact area drives increasing dissolution. In this regime, the fingers evolve like $L \sim t^{1/2}$. However, unlike the single finger case, there is another transition from the intermediate diffusion dominated regime to a late-time advection dominated regime where the CO_2 fingers evolve like $L \sim t$. This is due to CO_2 saturation of water in the low permeability layers which dampens diffusion over the more proximal parts of the CO_2 layers. The system reaches a steady state with a constant length zone at the front of the CO_2 finger in which dissolution of CO_2 is significant. The total diffusive flux out of the CO_2 fingers goes to a constant, and the velocity at the front of the finger reaches a constant value which is lower than the initial velocity. As the lateral diffusive flux is constant and the fingers evolve $L \sim t$, the total lateral dissolution into the low permeability layers scales as $d_{tot} \sim t$ at late times (Figure 2.6b).

The total CO_2 dissolved as a fraction of the total volume of CO_2 injected into the system shows an initial increase in the first advective and diffusive regimes, before tending towards a

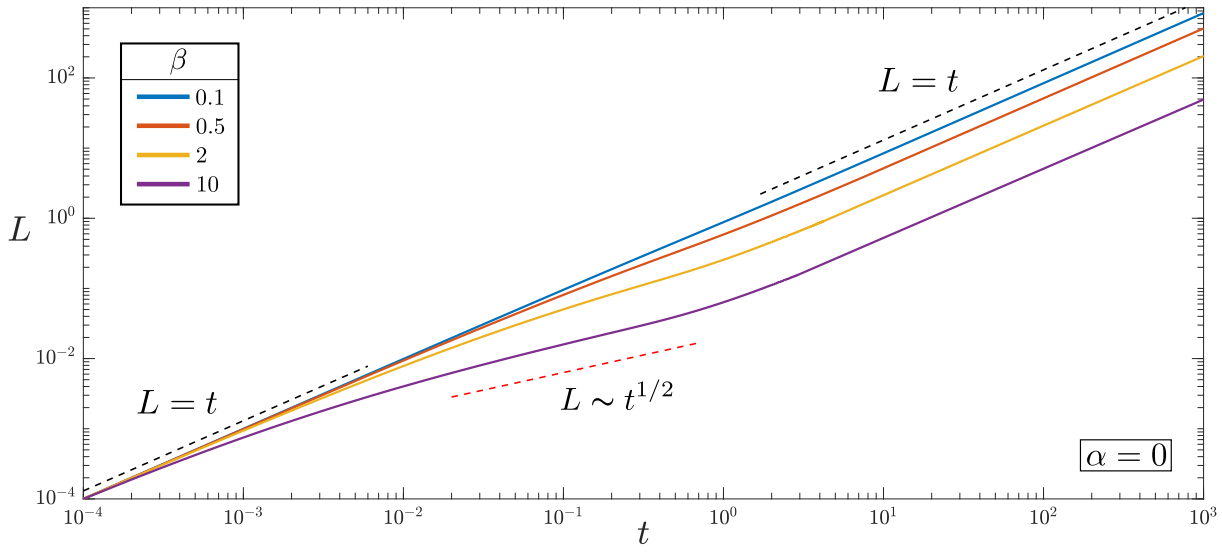

Figure 2.8: The length of the CO_2 fingers plotted as a function of time for four different values of β. Also plotted is the line $L \sim t$ (black dashed line), and the line $L \sim t^{1/2}$ (red dashed line). Larger values of β evolve with $L \sim t^{1/2}$ for longer before transitioning back to evolving with $L \sim t$.

constant value which corresponds with the late time advective regime (Figure 2.7a). At this point, the total diffusive flux out of the finger is constant, which can be seen when plotting the total dissolution flux at a given time as a fraction of the total input flux (Figure 2.7b).

Figures 2.6 and 2.7 were plotted for a single value of $\beta = 5$. The value of β ($= h\phi_a c_0 \rho_r / w\phi s_{nw}$) determines the relative significance of the three regimes, where β is a ratio between the volume available for CO_2 to dissolve into the low permeability layers ($h\phi_a c_0 \rho_r$) and the volume of CO_2 in the high permeability layers ($w\phi s_{nw}$). The effect of changing β on the length of the CO_2 fingers is shown in Figure 2.8, for $\alpha = 0$. Larger values of β correspond to systems which allow more CO_2 diffusion, leading to a more pronounced diffusive regime. This is illustrated by the purple line in Figure 2.8 corresponding to $\beta = 10$, which clearly evolves as $L \sim t^{1/2}$ at intermediate times. For small values of β, the water between the CO_2 fingers saturates quickly meaning that further CO_2 dissolution is suppressed, and results in a less significant diffusive regime, as shown by the blue line in Figure 2.8 for $\beta = 0.1$.

Importantly, β also determines the maximum fraction of CO_2 dissolved at long times, reflecting the ratio of the volume of water available for saturation with CO_2 and the volume of CO_2 in the high permeability layers. The total fraction of injected CO_2 that has dissolved is plotted as a function of time for changing β (Figure 2.9a), for $\alpha = 0$. Larger values of β

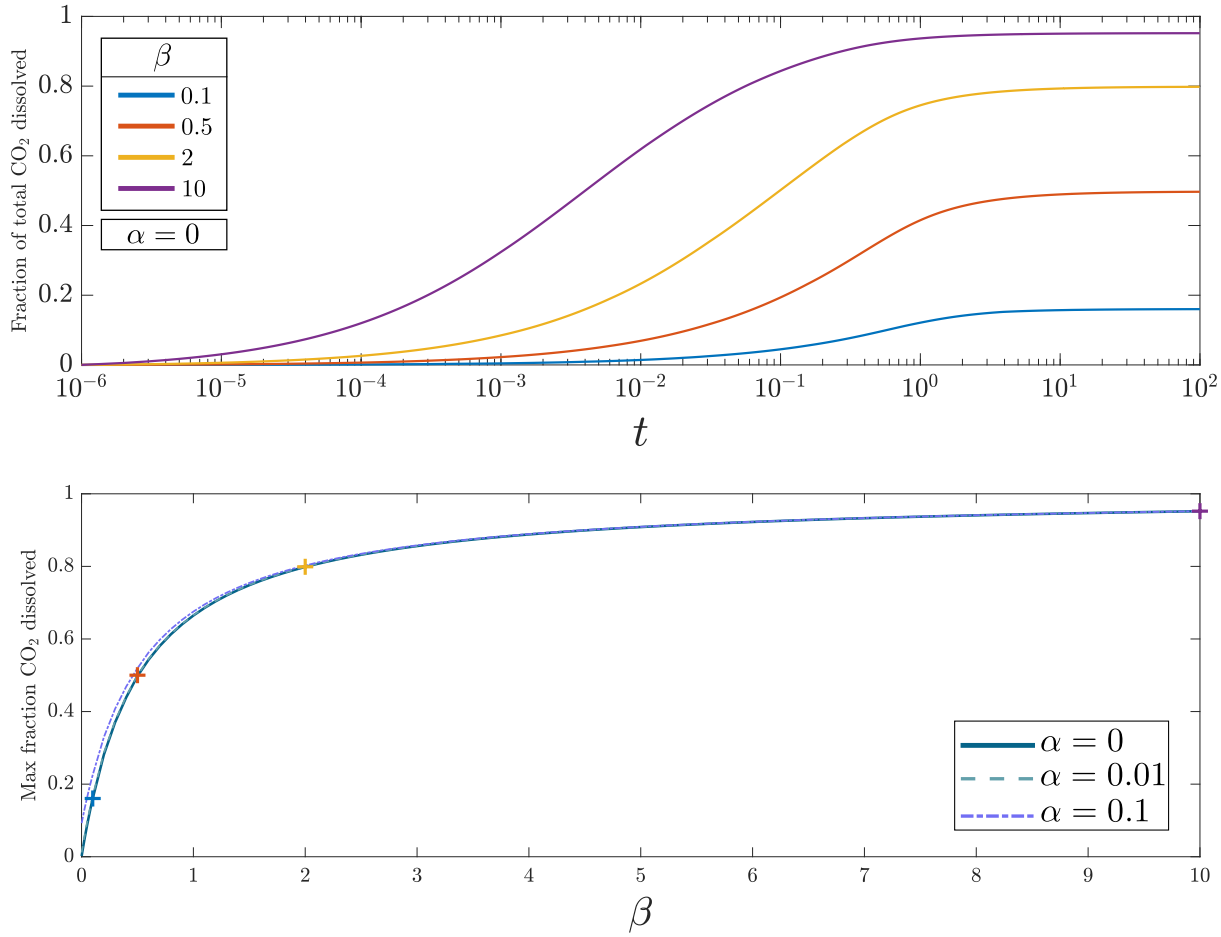

Figure 2.9: (a) Fraction of total injected CO_2 that has dissolved as a function of time is plotted for $\beta = 0.1$, 0.5, 2 and 10, with $\alpha = 0$. (b) The maximum fraction of injected CO_2 dissolved at steady state is plotted as a function of β for $\alpha = 0$, 0.01, 0.1. The coloured crosses correspond to the values of β and the late time maximum fractions obtained from (a).

correspond with a higher maximum fraction of injected CO_2 dissolving into the surrounding water at late times. The dependence of β on this late time maximum dissolved fraction is plotted in Figure 2.9b. There is a sharp increase in the maximum CO_2 dissolved up to $\beta \approx 2$, after which point the maximum dissolution fraction is less sensitive to increasing β. It is important to note that although larger values of β correspond with higher maximum dissolution fluxes as a fraction of the injection flux, if β is large due to the high permeability layers being further apart (i.e. large h), it will take longer for the system to reach this late time regime compared to a system with high permeability layers that are close together as the time scaling is proportional to h^2 (see (2.14)).

2.4 Discussion

I will now apply the model for CO_2 flow along periodic high permeability layers described in Section 2.3.1 to a real world example of a carbon storage reservoir, and then discuss the assumptions made in the model, and the extent to which the results from the model can be applied.

2.4.1 Application to CO_2 Reservoir

Evaluating the model using parameters appropriate to field settings establishes a practical sense of the permeability structures, lengths and timescales for which significant dissolution of CO_2 will occur. The Salt Creek Oil Field in Wyoming has been the site of CO_2 injection for enhanced oil recovery since 2004. In 2010, there was a monitored injection of CO_2 into a 20 m interval of the second Wall Creek sandstone unit. This is a highly heterogeneous deltaic sequence made up of mudstones, siltstones and sandstones in coarsening up sequences (Lee *et al.*, 2005).

Bickle *et al.* (2017) estimated the permeability profile of the injection interval using porosity measurements calculated from gamma ray density logs. Order-of-magnitude permeability variations were found on ~ 0.5 m length scales. However, the resolution of the permeability distribution was limited by the resolution of the gamma ray density logs, which was ~ 0.35 m, and it is probable that large variations in permeability on smaller length scales exist.

The periodically repeating layered model is evaluated using parameters from the CO_2 injection into the second Wall Creek sandstone unit. The parameters used in the calculation are $D_m = 2 \times 10^{-9}$ m^{2}s^{-1} (Cadogan *et al.*, 2014), $\phi_a = 0.12$, $\tau = 5$, CO_2 input velocity $v_0 = 4 \times 10^{-5}$ ms^{-1}, porosity $\phi = 0.2$ (Bickle *et al.*, 2017), fraction of the porosity occupied by CO_2 $s_{nw} = 0.8$ (Krevor *et al.*, 2012), maximum saturation concentration $c_0 = 5.5$ wt% calculated at 15 Mpa, 50°C and a salinity of 0.05 mol NaCl/kg(H_2O) (Dubacq *et al.*, 2013), densities $\rho_{H_2O_{sat-CO_2}} = 1025$ kg m^{-3} and $\rho_{CO_2} = 700$ kg m^{-3}, calculated at the same reservoir conditions (Garcia, 2001), and a high permeability layer spacing to width ratio $h/w = 1.5$ (Bickle *et al.*, 2017). This gives an effective diffusivity $D = 2 \times 10^{-11}$ m^{2}s^{-1} and a density

ratio $\rho_r = 1.5$. Using these values gives $\alpha = 0.02$ and $\beta = 0.1$.

Three different widths for the high permeability layer have been plotted. These are $w = 0.5$ m, as calculated by Bickle *et al.* (2017), as well as $w = 0.1$ m and $w = 0.05$ m, accounting for the limited resolution of the permeability distribution. On injection, it is important to know how far the CO_2 propagates into the reservoir. Figure 2.10a shows the length of the CO_2 fingers from the injection point as a function of time, which is a measure of propagation distance. A separate curve is plotted for each value of the high permeability layers w, with the ratio between high permeability layer spacing to layer width held constant. The length of the finger if no diffusive loss occurs is also plotted (black dashed line). For smaller values of w, with h/w fixed, the distance the CO_2 has propagated into the reservoir at a given time will be less, with a more pronounced discrepancy at later times. When $w = 0.05$ m, the CO_2 travels around 15% less far than if no dissolution had occurred. Where the bedded layers are thicker, $w = 0.5$ m, the propagation distance into the reservoir is only reduced by around 5%.

It is also important to know how much of the injected CO_2 dissolves into the surrounding water. Figure 2.10b shows the fraction of the total injected CO_2 that has dissolved into the surrounding water as a function of time. The high permeability layers of width 0.1 m and 0.05 m show total dissolution of around 9% and 14% of the total injection volume respectively within the first two years of injection. Less CO_2 dissolves as a fraction of the total injected if the bedded layers are thicker. The three curves plotted are all scaled from the same curve calculated for $\alpha = 0.02$ and $\beta = 0.1$. For reservoirs with thinner and more finely spaced bedding (blue curve), the total dissolution approaches the maximum fraction for that value of β after around three years. However, as the layer spacing gets wider, it takes longer to reach the maximum level of dissolution.

2.4.2 Assumptions in the Model

The first factor to consider is the extent to which the free-phase CO_2 will remain confined to the high permeability layers, thereby allowing a large CO_2-water interface to develop which enhances dissolution. The saturation distribution of CO_2 within a heterogeneous reservoir

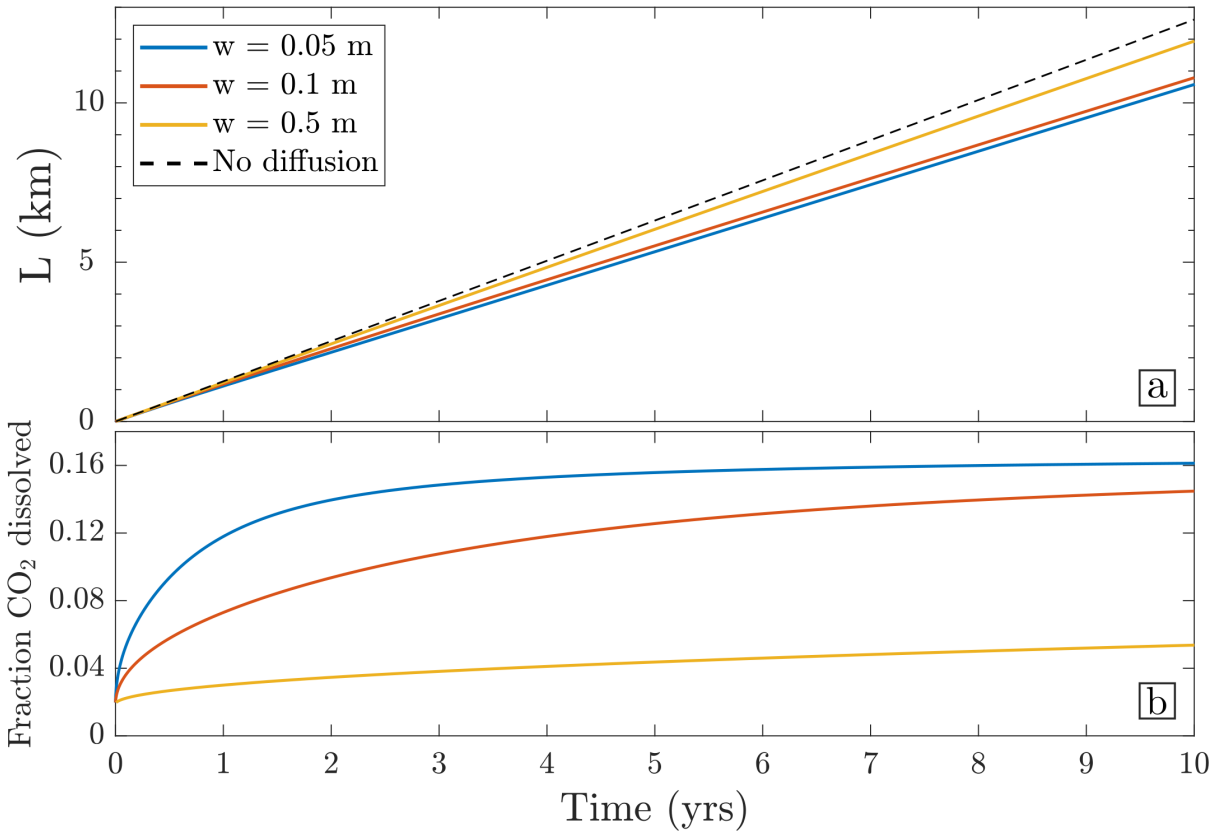

Figure 2.10: CO_2 propagation and total dissolution calculated for parameters from the Salt Creek field, Wyoming. (a) Length of the CO_2 finger as a function of time for three high permeability channel widths (solid lines) and the length of the finger if no diffusive loss of CO_2 occurs (black dashed line). (b) The fraction of CO_2 dissolved as a function of time for three high permeability channel widths, $w = 0.05$, 0.1, 0.5 m.

is often characterised by the non-dimensional capillary number,

$$N_c = \frac{h}{L}\frac{\Delta p}{\Delta p_e} \tag{2.16}$$

which is given as the ratio between the horizontal flow-driving pressure gradients $\Delta p/L$ and the typical vertical gradient in pore entry pressure $\Delta p_e/h$ (Benham *et al.*, 2021a; Jackson *et al.*, 2018; Virnovsky *et al.*, 2004). The pore entry pressure Δp_e is the minimum pressure required for the non-wetting phase (in this case CO_2) to enter the pore spaces of a given layer. It is dependent on the size and geometry of the pores, which can vary by orders of magnitude between different rock types. A commonly used scaling for pore entry pressure is $p_e \sim (\phi/k)^{1/2}$ (Leverett, 1941). At small values of N_c, also known as the capillary limit, the heterogeneity-driven capillary forces dominate the flow of fluid phases, with CO_2 confined to the high permeability layers. At large N_c, also known as the viscous limit, the background flow dominates such that capillary forces due to heterogeneities can be ignored. The capillary number can therefore inform for which injection and reservoir scenarios the injected CO_2 will be confined to the high permeability layers, as assumed by the model described in this chapter. The capillary entry pressure can be estimated using (Benham *et al.*, 2021b; Leverett, 1941),

$$p_e = p_0 \left(\frac{\phi}{k/k_0}\right)^{1/2}, \tag{2.17}$$

where p_0 is a characteristic pore entry pressure and k_0 is the average permeability of the reservoir. Using values from the Sleipner field of $p_0 = 1.3$ kPa and $k_0 = 1$ D (Williams & Chadwick, 2017), I obtain a difference in capillary entry pressure between high and low permeability layers of 13.8 kPa, using $\phi = 0.2$, $k_{high} = 2$ D, $\phi_a = 0.12$ and $k_{low} = 0.1$ mD. A typical change in pressure due to CO_2 injection into a heterogeneous formation is 180 kPa (Ennis-King *et al.*, 2017b). Using these values to evaluate the capillary number N_c, for a reservoir with permeability variations on a $\sim$0.5 m scale, the system will be in the capillary limit at distances greater than $\mathcal{O}(10$ m) from the injection location, meaning that beyond this distance the CO_2 should be confined to the high permeability layers, as assumed in the model. This is in agreement with distances from the injection well required for capillary equilibrium calculated by Jackson & Krevor (2020) for a range of injection rates.

The model assumes that CO_2 only dissolves into the water by molecular diffusion and no dispersion of CO_2 occurs. Mechanical dispersion causes a fluid to spread out over time as it takes different flow paths when moving through a complex porous matrix. Dispersion will act to increase mixing between the CO_2 and water and so enhance dissolution. For simplicity, this study only includes molecular diffusion and so presents a lower bound for dissolution rates which could be significantly enhanced by pore-scale dispersive mixing.

The model also assumes a planar interface between the injected CO_2 and ambient water within the high permeability layer. In a porous medium, when a low viscosity fluid such as CO_2 is injected into an ambient fluid with higher viscosity such as water, instabilities form at the interface between the fluids. These instabilities extend out as fingers into the ambient fluid (Saffman & Taylor, 1958). It is important to determine whether the length of the viscous fingers are significant relative to the total length of the CO_2 finger in the high permeability layer. Nijjer *et al.* (2018) found that at late times the viscous fingers coalesce to form a dispersive fringe which tends to a constant length. Scaling their results using parameters from Salt Creek, I find at 3.5 days, the dispersive fringe makes up 25% of the total length of the injected CO_2 finger whereas after 30 days it makes up 4% of the total length. Thereby, the length scale of the viscous fingers becomes small compared to the length of the CO_2 finger with time. Although Nijjer *et al.* (2018) focused on the shutdown of miscible viscous fingers, simulations of immiscible viscous fingering by Kampitsis *et al.* (2021) observed the same late time regime. These fingering effects would likewise act to increase the mixing and hence dissolution of CO_2 in ambient water.

Alternative geometries such as cross-bedding, graded bedding and finer scale isotropic heterogeneity potentially increase the surface area of the CO_2-water contact within high permeability layers leading to increased levels of dissolution. However, as the reservoir heterogeneity becomes more diverse, it becomes harder to predict the exact flow path of the active CO_2 phase and the fraction of the rock accessible by the active CO_2 phase may reduce.

The model ignores buoyancy effects between the injected CO_2 and the ambient water. Supercritical CO_2 has roughly two thirds the density of water at conditions of a typical subsurface CO_2 injection. When a more buoyant fluid is injected into a confined layer saturated with a less buoyant fluid, the injected fluid travels faster along the top of the layer than the

bottom (Pegler *et al.*, 2014a). This leads to a very different profile shape to the planar contact assumed in this model. The result is that the water within the high permeability layers would not be fully displaced by CO_2, and hence the CO_2 would travel further for a given input flux. This would also increase the contact area between the CO_2 and water, enhancing dissolution rates. This effect is largely captured in the current model by results for thinner high permeability layers. Buoyancy effects would become important when the buoyancy forces become large compared to the viscous background forces associated with the injection pressures. This would be the case for thicker high permeability layers, as well as at distances further from the injection well.

Finally, it is important to note that the current metric for total dissolution is as a fraction of the total injected fluid into an infinitely long reservoir. In real CO_2 storage sites, it is important that the injected CO_2 remains within a lease area, and hence the reservoir cannot be treated as infinite. It is important to maximise the space within the lease area that can be used to store CO_2, as well as the rate of secondary trapping mechanisms such as dissolution that act to stabilise the injected CO_2 over long time periods. For the model described in this chapter, the fraction of the storage reservoir that the free-phase injected CO_2 can enter is governed by the fraction of high to low permeability layers. However, the total mass dissolved when the fluid front reaches a certain distance from the source is ultimately determined by the length scale of the heterogeneities. Lots of small scale high and low permeability layers increases the surface area available for diffusion and hence increases dissolution rates. There is also a lower limit to length scale of the heterogeneities, below which background pressures due to injection will overcome the variations in capillary entry pressure and the CO_2 will perforate all the layers. This length scale varies with the injection pressure, and the distance from the injection zone, with CO_2 more confined to the high permeability layers further from the injection well due to lower background pressures.

2.5 Conclusion

Injecting CO_2 into saline reservoirs with interbedded high and low permeability layers substantially enhances dissolution rates. As the fluid travels farther into the reservoir, the

increase in surface area between the CO_2 and surrounding water causes increased diffusive loss. The velocity at which CO_2 travels in the reservoir is dominated by the advective input flux at early times and transitions to an intermediate diffusion dominated regime as diffusive loss increases. At late times, the water in the low permeability layers reaches CO_2 saturation, dampening diffusion and resulting in a return to an advection dominated regime. The significance of these regimes is governed by the ratio between the volume of water available for CO_2 dissolution in the low permeability layers and the volume of CO_2 within the high permeability layers. This ratio also governs the maximum fraction of injected CO_2 dissolved at late times. For reservoirs with characteristic bedding thicknesses of $\sim$0.1 m, the modelling implies that a significant fraction of the CO_2 will dissolve in water within a few years of injection. The tendency of low viscosity supercritical CO_2 to finger and the much more complex flow paths in real reservoirs will likely increase CO_2 dissolution rates above the minimum estimates from this model. This study shows that dissolution rates can be very significant when CO_2 flows through naturally heterogeneous formations, and crucially more than that driven by convective dissolution.

The chapter is adapted from Gilmore, K. A., Neufeld, J. A., and Bickle, M. J., (2020), CO_2 dissolution trapping rates in heterogeneous porous media, *Geophysical Research Letters*, Vol. 47(12), e2020GL087001

Chapter 3

Leakage Dynamics of Fault Zones with Application to CO_2 storage

3.1 Introduction

In typical CO_2 injection scenarios, the buoyant CO_2 rises until it reaches a structural seal, such as a low permeability rock layer made up of shale, anhydrite or salt, which prevents the fluid from migrating beyond the storage reservoir. For geological carbon storage to be successful, it is vital that the CO_2 remains securely trapped in the subsurface over long timescales (Metz *et al.*, 2005). Defects within the seal may allow stored CO_2 to leak into overlying aquifers and eventually to the surface. Therefore, it is important to understand how these defects may contribute to the migration of CO_2. Likewise, if groundwater contaminating non-aqueous phase liquids (NAPL) such as chlorinated organic solvents (Bear & Cheng, 2010; Taylor *et al.*, 2001) are released in the subsurface, defects in the reservoir seal may impact the dispersal of these contaminants.

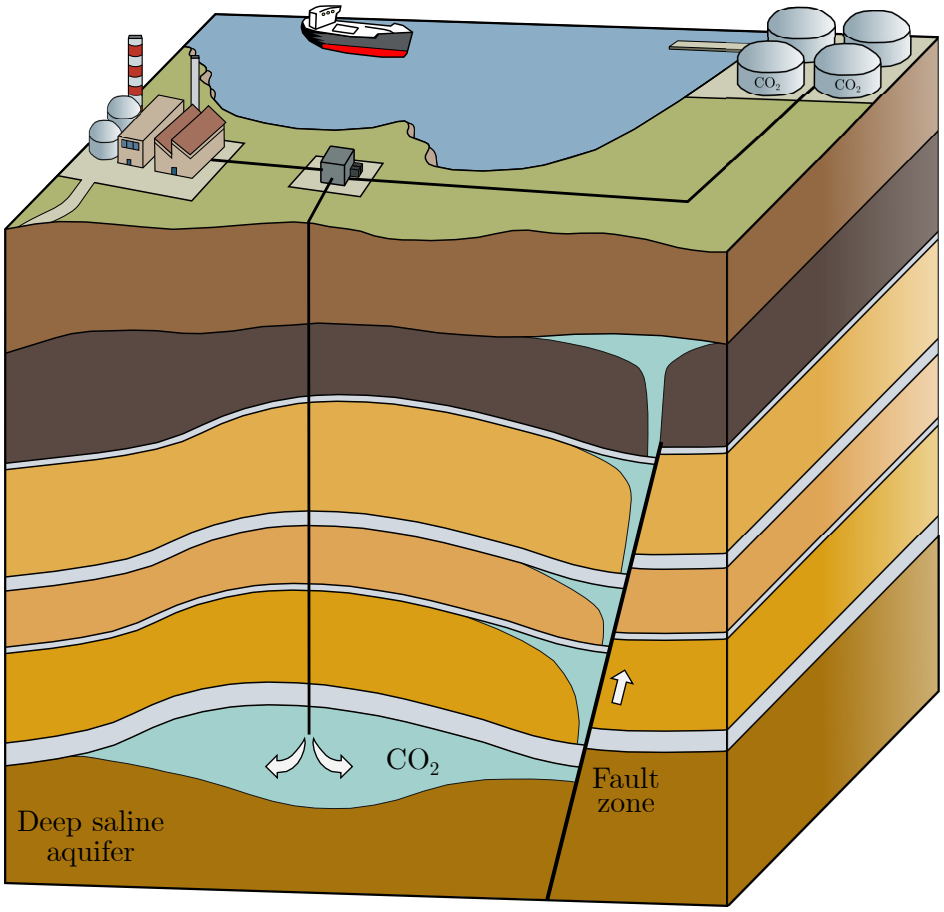

Figure 3.1: Illustrative figure showing the potential for fault zones to act as leakage pathways for trapped fluids.

Faults, which are localised zones of brittle deformation, are a common feature in geological reservoirs, and may act as leakage pathways for trapped fluids (Figure 3.1). There is a large body of work on the structure and fluid flow properties of fault zones (Caine *et al.*, 1996; Faulkner *et al.*, 2010; Nicol *et al.*, 2017). A simple model for the structure of a fault zone is a fault core, generally consisting of very fine grained crushed rock (gouge) and larger fragments of broken up host rock, surrounded by a heavily fractured damage zone (Wibberley *et al.*, 2008) (Figure 3.2). The fault core and surrounding damage zone have very different hydraulic properties. Laboratory measurements on samples of fault core show that the permeability can be reduced by two to three orders of magnitude compared to the unfaulted host rock (Zhang & Tullis, 1998; Shipton *et al.*, 2002, 2005). In contrast, the presence of fracture networks in the fault damage zone can increase the permeability of the host rock by two to three orders of magnitude (Simpson *et al.*, 2001; Oda *et al.*, 2002; Mitchell & Faulkner, 2008).

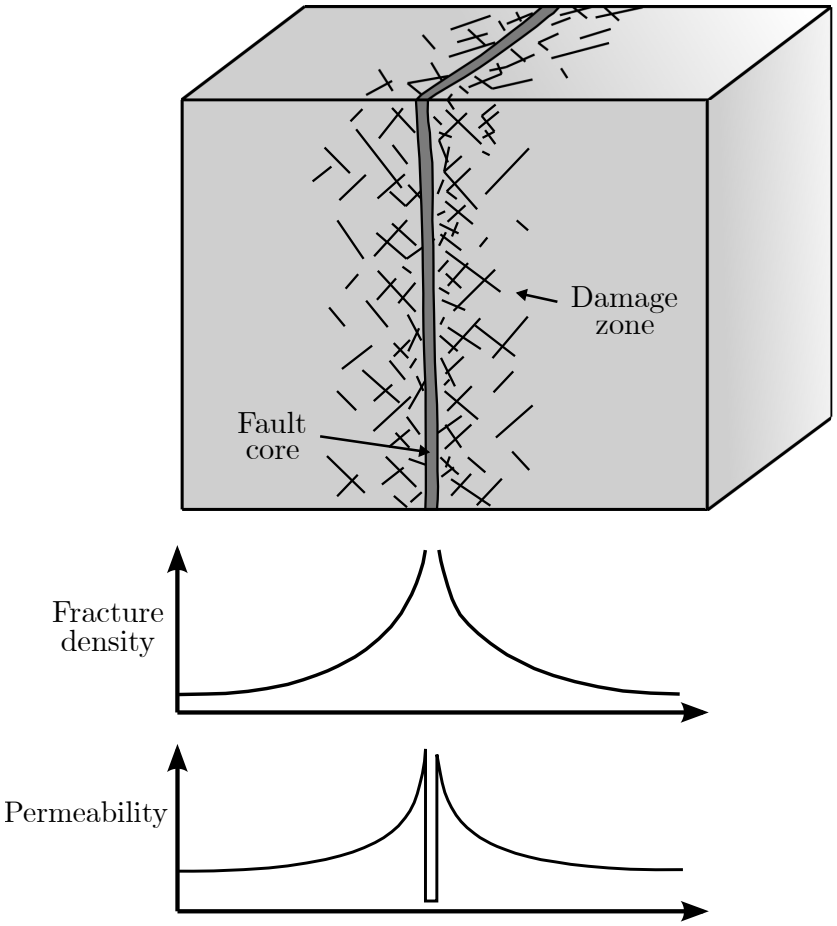

Figure 3.2: Structure of a typical fault zone consisting of a low permeability fault core surrounded by a heavily fractured, high permeability damage zone. Figure adapted from Faulkner *et al.* (2010).

The resultant model for fluid flow in fault zones is a barrier-conduit system, where the fault core acts as a barrier to across-fault flow and the fracture damage zone channels flow parallel to the fault plane (Caine *et al.*, 1996; Balsamo *et al.*, 2010). Studies have applied this model to explore vertical exchange flows through faults between multiple aquifers (Woods *et al.*, 2015) and upward migration of CO_2 into overlying permeable formations (Chang *et al.*, 2008; Kang *et al.*, 2014).

Faults are relatively small features in basin-scale models, so can be computationally challenging and expensive to model accurately by standard multi-scale numerical flow simulations (Class *et al.*, 2009; Nordbotten *et al.*, 2009). One option is to develop analytical models that describe fault behaviour, which are then integrated into larger-scale models (Kang *et al.*, 2014; Nordbotten & Celia, 2011). These models are limited to some extent by the assumptions needed to solve the mathematical system of equations, but solutions can be obtained

in seconds as opposed to hours/days, and developing these models also provides insight into the dominant physical processes in the system.

A number of studies have focused on analytical solutions for buoyancy-driven flows or on gravity currents in porous media with leakage from the current. This includes gravity currents in unconfined porous media leaking steadily through a permeable boundary (Acton *et al.*, 2001; Pritchard *et al.*, 2001; Pritchard & Hogg, 2002), or leaking through discrete fractures, where the leakage flux is driven by the hydrostatic pressure of the underlying less dense fluid (Pritchard, 2007) or with the added effect of the buoyancy of fluid in the fault (Neufeld *et al.*, 2009). Previous studies have also considered leakage in confined aquifers (Avci, 1994; Nordbotten *et al.*, 2004, 2005) where leakage is driven by an increased pressure due to injection or where a background pressure gradient between multiple aquifers contributes to driving leakage through fractures (Pegler *et al.*, 2014b). In all of these studies, the leakage flux is driven by the Darcy velocity in the leaking boundary or fracture, which is a product of the mobility of the injected fluid in the layer or fracture and the pressure gradient across it.

The movement of fluids through porous rocks and small scale fractures can be modelled by considering miscible porous media flows, where the flow is governed by Darcy's law. Miscible flows in porous media can be characterised by the Péclet number, $Pe = d_0 U\tau/D_d$, which describes the relative importance of advection to diffusion in fluid transport. Here d_0 is the mean grain diameter, U is the characteristic velocity of the flow, τ is the tortuosity of the porous media and D_d is the molecular diffusion coefficient. A composite transport coefficient D can model the diffusive and dispersive contributions to the spreading of concentration within the fluid, where

$$D = d_0 U\left(1 + \frac{1}{Pe}\right). \tag{3.1}$$

(Houseworth, 1984; Delgado, 2007). In diffusion dominated flows, where $Pe \ll 1$, the transport coefficient $D \simeq D_d/\tau$ is approximately constant whereas in advection dominated flows, where $Pe \gg 1$, $D \simeq d_0 U$ is dependent on the flow speed.

As a buoyant fluid is injected into a reservoir or escapes through a fracture into an adjacent aquifer, it initially forms a buoyant plume. The behaviour of a buoyant plume in a porous

medium was first studied by Wooding (1963), who mathematically modelled the dynamics of a rectilinear plume by treating the incompressible flow using Darcy's law and an advection-diffusion equation for conservation of concentration. He derived a similarity solution that predicts the amount of entrainment from the ambient and therefore describes the increasing volume flux of the plume with height. Sahu & Flynn (2015) derived a new similarity solution for Darcy plumes with large Péclet numbers to obtain expressions for the plume volume flux and mean reduced gravity as functions of vertical distance from the source.

In this chapter, I develop an analytical model to describe the dynamics of leakage through a fault zone cutting multiple aquifers and seals, which I test against a new set of laboratory experiments. To model flow in faults cross-cutting multiple aquifers, I combine current analytical models for a buoyant plume in a semi-infinite porous media (Sahu & Flynn, 2015) and a leaking gravity current (Pritchard, 2007; Neufeld *et al.*, 2009) with a new model for fault leakage which accounts for increased pressure gradients within the fault due to an increase in Darcy velocity directly above the fault. Previous studies providing analytical solutions to fault leakage problems have used numerical solvers to verify their models (Kang *et al.*, 2014). Here, I test the results with a novel set of porous media tank experiments which show a good fit to the model. The results of the modelling are illustrated by application to a naturally occurring CO_2-charged aquifer system at Green River, Utah, using an extension of the model to calculate the fluid distribution across multiple vertically stacked aquifers, cross-cut by a fault.

In Section 3.2, I formulate a theoretical model for the half-space plume in which the plume volume flux and mean reduced gravity are used as inputs in a model for a leaking gravity current and where leakage through the fault is driven by the hydrostatic pressure within the underlying gravity current and the buoyancy of the fluid in the fault. In Section 3.3, I show numerical results for the gravity current shape and leakage rates. Observations from experiments show that an increase in Darcy velocity within the secondary plume above the fault leads to enhanced pressure gradients within the fault. In Section 3.4, an expression for the pressure above the fault is coupled with the leakage model presented in Section 3.2, resulting in a new model for leakage through the fault. The model is matched against results from a set of analogue porous media tank experiment in Section 3.5 and then in Section

3.6, I demonstrate the application of the model in CO_2 storage, by applying an extension of the model to predict CO_2 leakage across multiple aquifers. In Section 3.7, I consider the validity of my model and discuss potential limitations and extensions, including the explicit inclusion of multiphase flow relationships in the plume, gravity current and fault leakage models. Finally, I present the conclusions from this chapter in Section 3.8.

3.2 Theoretical model

In this section, I present a model for calculating the leakage flux from an aquifer intersected by a fault. To achieve this, I couple a model for a buoyant plume in a semi-infinite porous medium with a model for a two-dimensional gravity current spreading under an impermeable base containing a fault of finite gap-width and thickness, and known permeability and porosity.

3.2.1 Buoyant plume in a semi-infinite porous aquifer

Here I derive a solution for the steady flow of a two-dimensional buoyant plume in a semi-infinite porous medium with unit thickness in the third dimension. A constant input flux q_0 of fluid with density ρ_0 is injected into a porous medium with permeability k and porosity ϕ saturated with a denser ambient fluid of density ρ_a. Both fluids are assumed to be miscible, with equal viscosities such that there are no capillary effects during the flow. The implications of this assumption for application to CO_2-water systems is discussed in Section 3.7. The injected fluid mixes with the ambient fluid and forms a plume with a volume flux $Q(z)$ and density $\rho(x, z)$ at a given height z (Figure 3.3a). I follow the analysis of Sahu & Flynn (2015) who considered an unconfined plume in a porous medium for Darcy flow with $Pe \gg 1$, in contrast to Wooding (1963). The analysis differs by considering a half-space model, with an impermeable vertical boundary contacting the injection location. Assuming steady, incompressible Boussinesq flow (shown in previous studies to be a useful approximation in CO_2-water systems (Amooie *et al.*, 2018; Soltanian *et al.*, 2016)), the governing equations based on mass continuity, momentum continuity, solute transport and a linear equation of

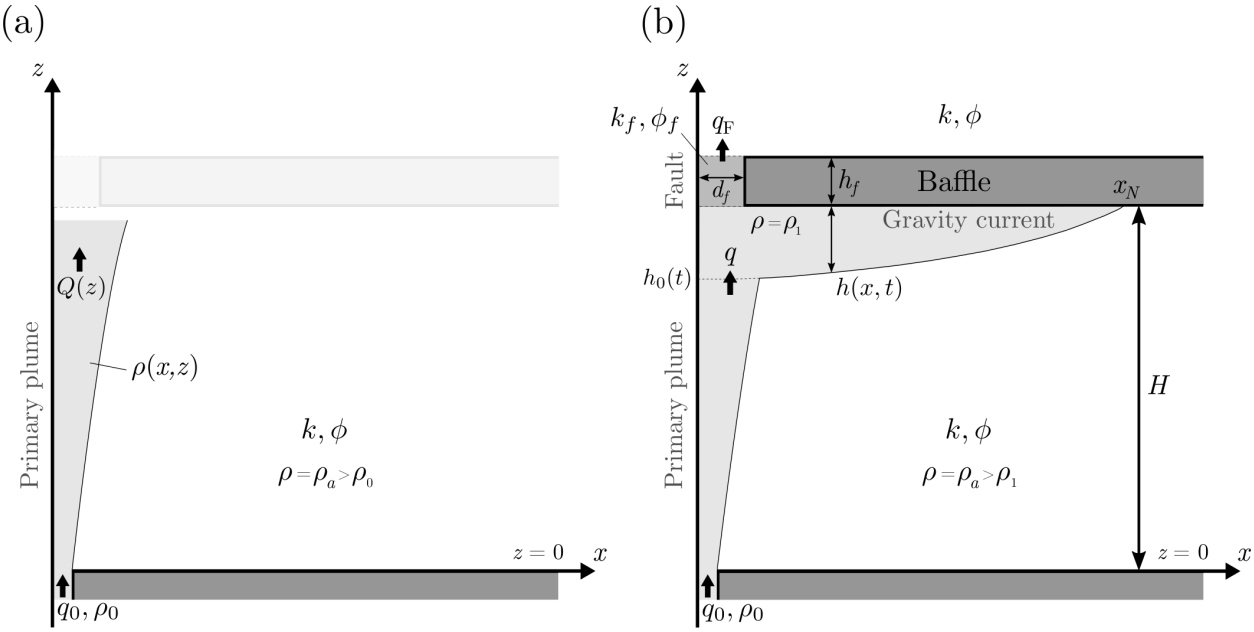

Figure 3.3: (a) Fluid with density ρ_0 is injected with a constant input flux q_0 into a porous medium with permeability k and porosity ϕ, saturated with an ambient fluid of density ρ_a. The fluid forms a plume with a volume flux $Q(z)$ and density $\rho(x, z)$ at a given height z. (b) After the buoyant plume reaches the top of the aquifer, it provides a constant input flux q of fluid with density ρ_1 into a gravity current which spreads into a porous medium of permeability k and porosity ϕ saturated with an ambient fluid of density ρ_a. The thickness of the current is given by $h(x, t)$. The current spreads under an impermeable baffle containing a fault of gap-width d_f, thickness h_f, permeability k_f and porosity ϕ_f between $x = 0$ and $x = d_f$. Injected fluid leaks through the fault with flux q_F.

state are

$$\frac{\partial u}{\partial x} + \frac{\partial w}{\partial z} = 0, \tag{3.2}$$

$$\frac{1}{\rho_a}\frac{\partial P}{\partial x} + \frac{\nu}{k}u = 0, \tag{3.3}$$

$$\frac{1}{\rho_a}\frac{\partial P}{\partial z} + \frac{\nu}{k}w = -\frac{g\rho}{\rho_a}, \tag{3.4}$$

$$\frac{1}{\phi}\left(w\frac{\partial C}{\partial z} + u\frac{\partial C}{\partial x}\right) = \frac{\partial}{\partial x}\left(D_T\frac{\partial C}{\partial x}\right) + \frac{\partial}{\partial z}\left(D_L\frac{\partial C}{\partial z}\right), \tag{3.5}$$

$$\rho = \rho_a(1 - \beta C), \tag{3.6}$$

where u and w are the fluid velocities in the x and z directions respectively, P is the fluid pressure, ν is the kinematic viscosity, g is the acceleration due to gravity, C is the solute concentration, β is the solutal expansion coefficient and D_L and D_T are the longitudinal and transverse dispersion coefficients respectively. Since the plume is long and thin, one can

neglect vertical variations in the horizontal velocity $\left(\frac{\partial w}{\partial x} \gg \frac{\partial u}{\partial z}\right)$ and longitudinal dispersion. Hence, the combined momentum equations and the solute transport equation become,

$$\frac{\nu}{k}\frac{\partial w}{\partial x} = -\frac{g}{\rho_a}\frac{\partial \rho}{\partial x}, \tag{3.7}$$

$$u\frac{\partial C}{\partial x} + w\frac{\partial C}{\partial z} = \phi\frac{\partial}{\partial x}\left(D_T\frac{\partial C}{\partial x}\right). \tag{3.8}$$

A streamfunction ψ is introduced such that $w = \frac{\partial \psi}{\partial x}$ and $u = -\frac{\partial \psi}{\partial z}$. For $Pe \gg 1$, the transverse dispersion coefficient may be approximated as

$$D_T \simeq \alpha w, \tag{3.9}$$

where α is the transverse dispersivity (Delgado, 2007). On using (3.6) and (3.9), (3.7) and (3.8) become

$$\frac{\partial^2 \psi}{\partial x^2} = \frac{g\beta k}{\nu}\frac{\partial C}{\partial x}, \tag{3.10}$$

$$\frac{\partial \psi}{\partial x}\frac{\partial C}{\partial z} - \frac{\partial \psi}{\partial z}\frac{\partial C}{\partial x} = \phi\alpha\left(\frac{\partial^2 \psi}{\partial x^2}\frac{\partial C}{\partial x} + \frac{\partial \psi}{\partial x}\frac{\partial^2 C}{\partial x^2}\right). \tag{3.11}$$

For a steady plume, the buoyancy flux, or equivalently the solute mass flux, remains constant with height, as the horizontally entraining ambient fluid only increases the volume of the plume but does not alter the solute mass. The buoyancy flux of the plume per unit thickness is conserved with height and is

$$F_0 = \int_0^\infty w g' \, dx, \tag{3.12}$$

where $g' = g(\rho_a - \rho)/\rho_a \equiv g\beta C$ is the reduced gravity. A scaling analysis of (3.10), (3.11) and (3.12) suggests that

$$\frac{\psi}{x^2} \sim \frac{g\beta k}{\nu}\frac{C}{x}, \tag{3.13a}$$

$$\frac{\psi C}{xz} \sim \phi\alpha\frac{\psi C}{x^3}, \tag{3.13b}$$

$$F_0 \sim w g' x \sim \psi g \beta C. \tag{3.13c}$$

Equation 3.13b motivates definition of a self-similar horizontal length scale of the plume

$$\eta = \frac{x}{\sqrt{\phi\alpha z}} \qquad (z > 0), \tag{3.14}$$

noting that $z = 0$ is the point of injection and therefore entrainment of the ambient fluid and the corresponding plume equations are applicable only for $z > 0$. It is also worth noting that the plume is defined as the region of the flow field where the concentration $C > 0$, or equivalently $g' > 0$. Now, on considering (3.13a), (3.13c) and (3.14) together, I can define the stream function and concentration of the plume in the forms of similarity functions $\mathscr{F}(\eta)$ and $\mathscr{G}(\eta)$ as

$$\psi = \left[\left(\frac{F_0 k}{\nu}\right)^2 \phi\alpha z\right]^{1/4} \mathscr{F}(\eta), \tag{3.15}$$

and

$$C = \frac{1}{g\beta}\left[\left(\frac{F_0\nu}{k}\right)^2 \frac{1}{\phi\alpha z}\right]^{1/4} \mathscr{G}(\eta), \tag{3.16}$$

respectively. These expressions for ψ and C are related by (3.10) such that $\mathscr{F}'(\eta) = \mathscr{G}(\eta)$. Similarly solute concentration, (3.11) implies that

$$\mathscr{F}'''\mathscr{F}' + \mathscr{F}''\mathscr{F}'' + \frac{1}{4}\mathscr{F}''\mathscr{F} + \frac{1}{4}\mathscr{F}'\mathscr{F}' = (\mathscr{F}''\mathscr{F}')' + \frac{1}{4}(\mathscr{F}'\mathscr{F})' = 0. \tag{3.17}$$

I solve (3.17) subject to the conditions that the solute concentration cannot be negative, and tends to the background concentration in the far field, $C(x, z) = 0$ and $\mathscr{F}'(\eta) = 0$ as $x, \eta \to \infty$, whereas inside the plume $C(x, z) > 0$ and $\mathscr{F}'(\eta) > 0$. The transverse velocity against the fault is zero, such that the value of the streamfunction $\psi(0, z) = 0$ so $\mathscr{F}(0) = 0$. With these conditions, it can be shown that

$$\mathscr{F}(\eta) = \begin{cases} c\sin\dfrac{\eta}{2}, & \eta < \pi, \\ c, & \eta > \pi, \end{cases} \quad \text{and} \quad \mathscr{G}(\eta) = \mathscr{F}'(\eta) = \begin{cases} \dfrac{c}{2}\cos\dfrac{\eta}{2}, & \eta < \pi, \\ 0, & \eta > \pi, \end{cases} \tag{3.18}$$

where $c = \sqrt{8/\pi}$ is a constant of integration which is obtained by applying the solutions for w $\left(= \frac{\partial\psi}{\partial x}\right)$ and g' $(= g\beta C)$ to (3.12). Therefore, the expression for the volume flux per unit

thickness of the plume is

$$Q = \int_0^\infty w \, dx = \left[\left(\frac{8F_0 k}{\nu \pi} \right)^2 \phi \alpha z \right]^{1/4}. \tag{3.19}$$

This result is a factor of $\sqrt{2}$ smaller than the volume flux of the unconfined plume given by Sahu & Flynn (2015). Using (3.19), the average reduced gravity across the plume can be calculated as a function of height,

$$\bar{g'} = \frac{F_0}{Q} = \left[\left(\frac{\pi F_0 \nu}{8k} \right)^2 \frac{1}{\phi \alpha z} \right]^{1/4}. \tag{3.20}$$

The equations here are for an ideal plume formed purely by a buoyancy flux, where the volume flux $Q \to 0$ as $z \to 0$. For a non-ideal plume with a finite volume flux these assumptions do not hold. I can correct for this by extrapolating the flow to negative values of z and defining a point $z = -z_0$ where the plume flux $Q(-z_0) = 0$. The virtual source location z_0 is given by

$$z_0 = \frac{1}{\phi \alpha} \left(\frac{\pi \nu}{8 F_0 k} \right)^2 q_0^4, \tag{3.21}$$

where q_0 is the volume flux into the system, and the buoyancy flux $F_0 = q_0 g_0'$ where g_0' is the reduced gravity of the injected fluid. Given these corrections for source conditions, expressions for the plume volume flux per unit thickness and mean reduced gravity are

$$Q = \left[\left(\frac{8 q_0 g_0' k}{\nu \pi} \right)^2 \phi \alpha (z + z_0) \right]^{1/4}, \tag{3.22}$$

and

$$\bar{g'} = \left[\left(\frac{\pi q_0 g_0' \nu}{8k} \right)^2 \frac{1}{\phi \alpha (z + z_0)} \right]^{1/4}. \tag{3.23}$$

3.2.2 Gravity current with leaking fault at the origin

Here I consider the behaviour of a two-dimensional density-driven flow of a fluid in a porous medium of permeability k and porosity ϕ saturated with an ambient fluid of higher density ρ_a and bounded on one side by a impermeable vertical boundary (Figure 3.3b). The injected

fluid spreads below an impermeable horizontal baffle containing a fault of gap-width d_f, thickness h_f, permeability k_f and porosity ϕ_f which abuts the boundary. At the horizontal baffle, a gravity current forms due to fluid input from a rising plume. The fluid density ρ_1 and input rate q into the gravity current are calculated using the expressions for the plume volume flux and mean reduced gravity derived in (3.22) and (3.23). The values of q and $\bar{g'}$ are evaluated at a vertical distance H from the initial injection point, which corresponds with the level of the base of the impermeable baffle. I assume that the depth of the ambient fluid is large compared to the thickness of the current ($H \gg h$). This means I can neglect the effects of flow in the ambient and assume the values of q and $\bar{g'}$ remain constant with time.

Using (3.22) and (3.23), I obtain expressions for the input flux into the current and reduced gravity of the current,

$$q = \left[\left(\frac{8q_0 g_0' k}{\nu\pi}\right)^2 \phi\alpha H(1+\theta)\right]^{1/4} \quad \text{and} \quad g' = \left[\left(\frac{\pi q_0 g_0' \nu}{8k}\right)^2 \frac{1}{\phi\alpha H(1+\theta)}\right]^{1/4}, \tag{3.24}$$

where the dimensionless parameter

$$\theta = \frac{z_0}{H} = \frac{1}{\phi\alpha H}\left(\frac{\pi\nu q_0}{8g_0' k}\right)^2. \tag{3.25}$$

At the impermeable baffle, the injected fluid forms a gravity current, with some fluid leaking through the fault. I assume that the current is long and thin, and the velocity is predominantly parallel to the baffle so that the pressure in the current is hydrostatic. The fault is modelled using the barrier-conduit system described in Section 3.1, with the fault damage zone within the baffle modelled using an average permeability k_f and width d_f. Neufeld *et al.* (2009) formulated a model for drainage through a fissure of given permeability and width, which incorporates both flow driven by hydrostatic pressure as well as the buoyancy of the fluid in the fault itself,

$$w_f(t) = \frac{k_f}{\mu}\frac{\Delta\rho g(h_0(t)+h_f)}{h_f} = \frac{k_f g' h_0(t)}{\nu h_f}\left[1+\frac{h_f}{h_0(t)}\right]. \tag{3.26}$$

Here k_f is the permeability of the fault, h_f is the length of the fault, μ is the dynamic viscosity

and ν is the kinematic viscosity of the leaking fluid, h_0 is the thickness of the current at $x = 0$ ($h_0 = h(0,t)$), and g' is the reduced gravity of the current. Note that despite the width of the fault, $d_f > 0$, I assume that its effect on the gravity current is localised to the point $x = 0$, and the leakage is driven by the thickness there. A sharp interface between the injected and ambient fluids is described by a thickness $h(x,t)$ below the baffle at $z = H$. Dispersion will occur predominantly at the edges of the gravity current as it propagates into the reservoir and is expected to alter the shape of the current, the implications of which are discussed during comparison with the experimental results in Section 3.5.3. However, where the plume feeds the current directly below the fault, dispersion will be less pronounced. Hence, I neglect dispersion in the gravity current as it does not significantly affect leakage through the fault. The flow in the gravity current is driven by gradients in the hydrostatic pressure, and the evolution of the height is determined by the divergence of the fluid flux,

$$\phi \frac{\partial h}{\partial t} = \frac{kg'}{\nu} \frac{\partial}{\partial x} \left(h \frac{\partial h}{\partial x} \right). \tag{3.27}$$

The current forms when the plume impacts the impermeable baffle, and has initial condition

$$h(x,0) = 0. \tag{3.28}$$

Subsequently the gravity current is fed by the plume and has boundary conditions,

$$\left[\frac{kg'}{\nu} h \frac{\partial h}{\partial x} \right]_{x=0} = -(q - q_F), \quad \left[\frac{kg'}{\nu} h \frac{\partial h}{\partial x} \right]_{x=x_N} = 0, \quad h(x_N, t) = 0, \tag{3.29a,b,c}$$

which describe the input flux at the origin (equal to the plume input flux q, minus the fault leakage flux q_F), a no flux condition through the nose of the current and zero thickness at the nose of the current respectively. The current satisfies global conservation of mass, given by

$$\phi \int_0^{x_N} h \, dx = qt - \frac{d_f \phi_f k_f g'}{\nu h_f} \int_0^t h_0 \left(1 + \frac{h_f}{h_0} \right) \, dt, \tag{3.30}$$

where the final term comes from (3.26) and is equal to the total volume of fluid that has leaked through the fault. Note that time $t = 0$ in (3.30) is the instant the plume first reaches the impermeable baffle at $z = H$.

Non-dimensionalisation

Based on (3.24), (3.27) and (3.30) I define the following dimensionless variables,

$$\tilde{x} = \frac{g' k_f^2 d_f^2 \phi_f^2}{kq\nu h_f^2} x = \frac{\pi k_f^2 d_f^2 \phi_f^2}{8k^2 h_f^2 \phi^{1/2} \alpha^{1/2} H^{1/2} (1+\theta)^{1/2}} x, \tag{3.31a}$$

$$\tilde{h} = \frac{g' k_f d_f \phi_f}{q\nu h_f} h = \frac{\pi k_f d_f \phi_f}{8k h_f \phi^{1/2} \alpha^{1/2} H^{1/2} (1+\theta)^{1/2}} h, \tag{3.31b}$$

$$\tilde{t} = \frac{g'^2 k_f^3 d_f^3 \phi_f^3}{k\phi q\nu^2 h_f^3} t = \frac{\pi^{3/2} k_f^3 d_f^3 \phi_f^3 q_0^{1/2} g_0'^{1/2}}{8^{3/2} k^{5/2} h_f^3 \nu^{1/2} \phi^{7/4} \alpha^{3/4} H^{3/4} (1+\theta)^{3/4}} t. \tag{3.31c}$$

By substituting (3.31a-c), (3.27-3.30) become

$$\frac{\partial \tilde{h}}{\partial \tilde{t}} = \frac{\partial}{\partial \tilde{x}} \left(\tilde{h} \frac{\partial \tilde{h}}{\partial \tilde{x}} \right), \tag{3.32}$$

$$\tilde{h}(\tilde{x}, 0) = 0 \quad \text{and} \quad \tilde{h}(\tilde{x_N}, \tilde{t}) = 0, \tag{3.33}$$

$$\int_0^{\tilde{x}_N} \tilde{h} \, d\tilde{x} = \tilde{t} - \int_0^{\tilde{t}} \tilde{h}_0 \left(1 + \frac{h_f}{\tilde{h}_0} \frac{k_f d_f \phi_f g'}{q\nu h_f} \right) \, d\tilde{t}. \tag{3.34}$$

I introduce the dimensionless parameter

$$\lambda = \frac{g' k_f d_f \phi_f}{q\nu} = \frac{\pi k_f d_f \phi_f}{8k\phi^{1/2} \alpha^{1/2} H^{1/2} (1+\theta)^{1/2}}, \tag{3.35}$$

which characterises the strength of leakage through the fault due to the buoyancy of fluid in the fault so that (3.34) now has the form

$$\int_0^{\tilde{x}_N} \tilde{h} \, d\tilde{x} = (1-\lambda)\tilde{t} - \int_0^{\tilde{t}} \tilde{h}_0 \, d\tilde{t}. \tag{3.36}$$

Here, $\lambda = 0$ describes the case where the leakage through the fault is only driven by the hydrostatic pressure within the underlying gravity current and not by the buoyancy of fluid in the fault.

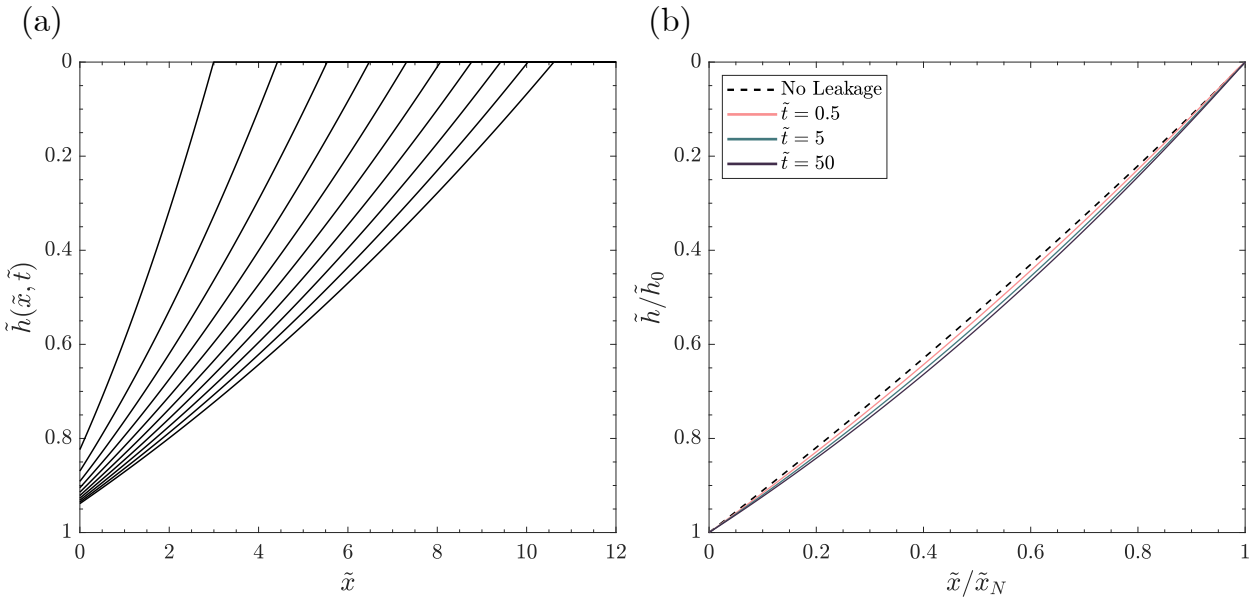

Figure 3.4: (a) Thickness profiles of the gravity current from $\tilde{t} = 5$ to $\tilde{t} = 50$ at intervals of 5 for the $\lambda = 0$ case. (b) Normalised thickness profiles for $\lambda = 0$ showing the change in shape of the current over time and deviation away from the self-similar zero leakage solution.

3.3 Numerical solutions

I solve for the full time-dependent behaviour of the gravity current numerically using a finite difference scheme. The thickness profile of the current is initially $\tilde{h}(\tilde{x}, 0) = 0$, and the subsequent evolution is described by (3.32)-(3.36). The thickness at $\tilde{x} = 0$ is obtained by solving (3.36) at each time step, using the thickness profile obtained from solving (3.32) and calculating the new leaked volume of fluid using $\tilde{h}_0$ from the previous time step. Results obtained are shown in Figures 3.4-3.6.

Figure 3.4a gives the solution for the gravity current shape as a function of time. The thickness profiles of the current are plotted from $\tilde{t} = 0$ to $\tilde{t} = 50$ at intervals of 5 with $\lambda = 0$, which describes the case where leakage through the fault is only driven by the hydrostatic pressure within the current below the fault. Figure 3.4b shows three height profiles at $\tilde{t} = 0.5$, $\tilde{t} = 5$ and $\tilde{t} = 50$ (solid lines), where the extent and height of the profiles have been normalised by the maximum extent $\tilde{x}_N$ and the thickness of the current at $\tilde{x} = 0$, $\tilde{h}_0$. The self-similar solution for the propagation of a gravity current through a porous medium with a constant input flux and with zero leakage (Huppert & Woods, 1995) is also plotted (dashed line). The solutions for the leaking gravity current deviate from the zero leakage

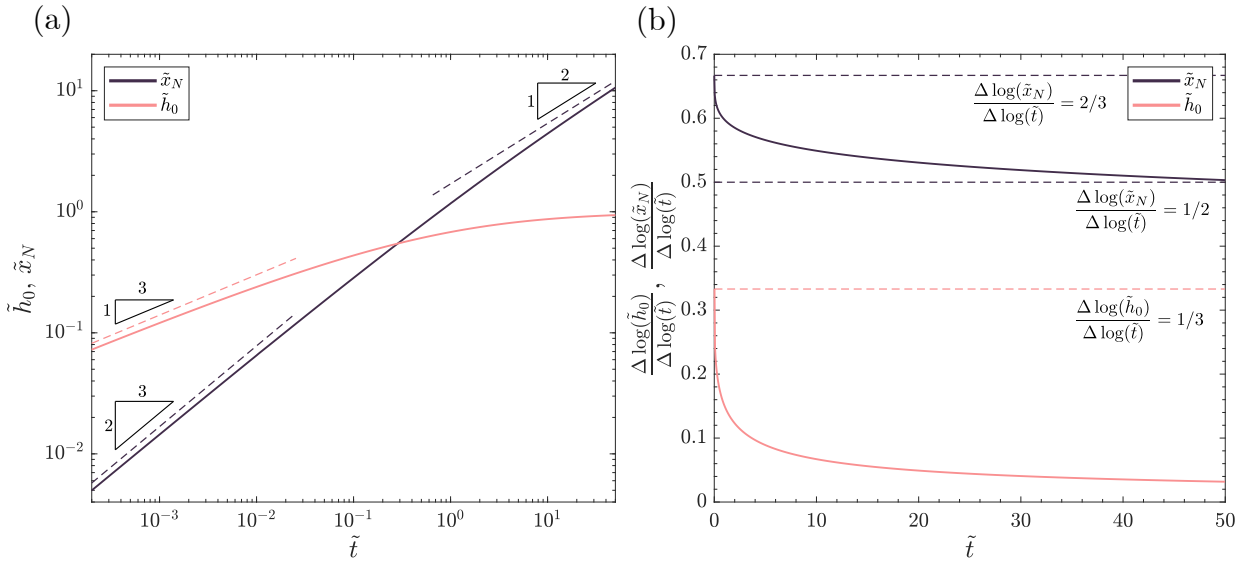

Figure 3.5: (a) Leaking gravity current horizontal extent and vertical extent at $\tilde{x} = 0$ plotted as a function of $\tilde{t}$ for the $\lambda = 0$ case (solid lines). Dashed lines show the power law behaviour of a gravity current with no leakage. (b) Gradient of the logarithmic horizontal and vertical extent evolution plotted as a function of time (solid lines). The horizontal and vertical extent deviate away from the 2/3 and 1/3 power law relationships of a gravity current with no leakage (dashed lines).

case over time, demonstrating a non self-similar behaviour of the leaking current.

In Figure 3.5a, the evolution of the horizontal and vertical extent of the leaking gravity current is plotted for $\lambda = 0$ (solid lines). At early times, the horizontal extent evolves following a $\tilde{t}^{2/3}$ power law relationship and the vertical extent of the current evolves following a $\tilde{t}^{1/3}$ power law relationship which agrees with the solutions for a gravity current with no leakage (Huppert & Woods, 1995). At late times, the evolution of the horizontal and vertical extent evolution deviate from these power law relationships. The vertical extent of the current tends to a constant value, resulting in a constant rate of leakage from the current. Late time asymptotic behaviour of (3.29) and (3.30) indicates that the thickness at the origin h_0 asymptotes to a constant as the gravity current nose tends towards infinity. It is possible to show (by considering a small perturbation to this equilibrium point) that the nose position approaches infinity like $x_N \sim (qt)^{1/2}$ in this late time regime (see Appendix A). This late time behaviour can be seen if the gradients of the log-log graph for the vertical and horizontal extent of the current are plotted as a function of time (Figure 3.5b).

The total injected volume of fluid into the system increases linearly with time and partitions between the gravity current and any leaked volume through the fault. A quantitative un-

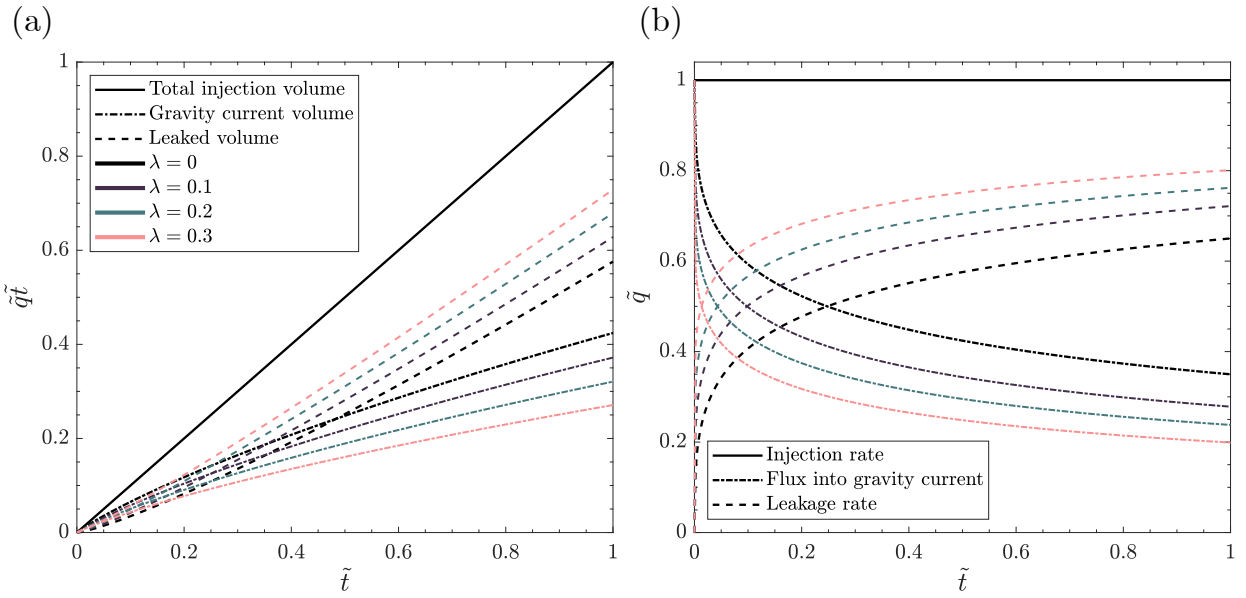

Figure 3.6: (a) Total injection volume, gravity current volume and total leaked volume plotted as a function of time for $\lambda = 0$, 0.1, 0.2 and 0.3. (b) Injection rate, rate of fluid input into the gravity current and the rate of leakage through the fault as a function of time.

derstanding of this partitioning is a key metric for the storage security of injected fluids in the subsurface. The total injection volume, gravity current volume and total leaked volume, represented by the terms $\tilde{t}$, $\int_0^{\tilde{x}_N} \tilde{h}\, d\tilde{x}$ and $\int_0^{\tilde{t}} (\tilde{h}_0 + \lambda)\, d\tilde{t}$ in (3.36), are calculated as a function of time and plotted in Figure 3.6a for different values of λ.

Initially, the volume of fluid going into the gravity current is greater than the volume of the fluid leaking through the fault. However, as the height of the current below the fault increases, a larger hydrostatic pressure drives more fluid through the fault and the volume of fluid leaking becomes larger than the volume of fluid going into the gravity current. This transition can be seen when the fluxes of fluid going into the gravity current and leaking through the fault are plotted as a function of time (Figure 3.6b). The value of λ signifies the buoyancy of fluid in the fault. As λ increases, the buoyancy flux through the fault increases, and so the leakage flux is a larger proportion of the total flux into the system.

3.4 A simple model for the pressure above the baffle

The theoretical model described in Section 3.2 accounts for leakage due to the hydrostatic pressure in the underlying gravity current and the buoyancy of the fluid in the fault. In

several of the laboratory experiments (presented in Section 3.5), a thinning of the secondary plume that forms above the baffle close to the fault is observed (Figure 3.7c). The thinning may be caused by an acceleration of the secondary plume, leading to differential negative pressures near the fault which increase the total pressure gradient across the fault. Transport of concentration in the secondary plume is similar to that described in Section 3.2.1, but the length scale over which this dispersion plays an important role is much larger than the length scale for the thinning of the plume (fig 3.13b), hence these effects are not included. In this section a model for the pressure above the baffle is derived by considering an asymptotic expansion in terms of a small deviation to the plume inlet velocity. The perturbation theory in Section 3.4.1 was derived by Dr. Graham Benham from the Department of Earth Sciences, University of Cambridge as part of a paper published in *Journal of Fluid Mechanics*, but I have included it here for completeness.

3.4.1 Thinning plume model

The scenario considered is illustrated in Figure 3.7a. Note the redefined position of $z = 0$. The secondary plume $z \geq 0$ is fed by a vertical inlet velocity w_f which is slightly smaller than the buoyancy velocity $w_b = k\Delta\rho g/\mu$, such that $w_f = w_b(1-\epsilon)$ for some small parameter $\epsilon \ll 1$. As a result, the width of the plume, which is denoted $d(z)$, must reduce from an initial value d_f to a far-field value $d_b = w_f d_f / w_b$. Note that it is possible for ϵ to be negative, in which case the width of the secondary plume would increase. Flow into the secondary plume is modelled using Darcy's law and mass conservation,

$$\mathbf{u} = -\frac{k}{\mu}\nabla\left(p + \rho_1 g z\right), \quad \nabla \cdot \mathbf{u} = 0, \tag{3.37a, b}$$

along with boundary conditions corresponding to constant inflow across the fault, impermeability at the vertical left-hand wall and far-field velocity conditions

$$w = w_b(1-\epsilon), \quad \text{at} \quad z = 0, \tag{3.38}$$

$$u = 0, \quad \text{at} \quad x = 0, \tag{3.39}$$

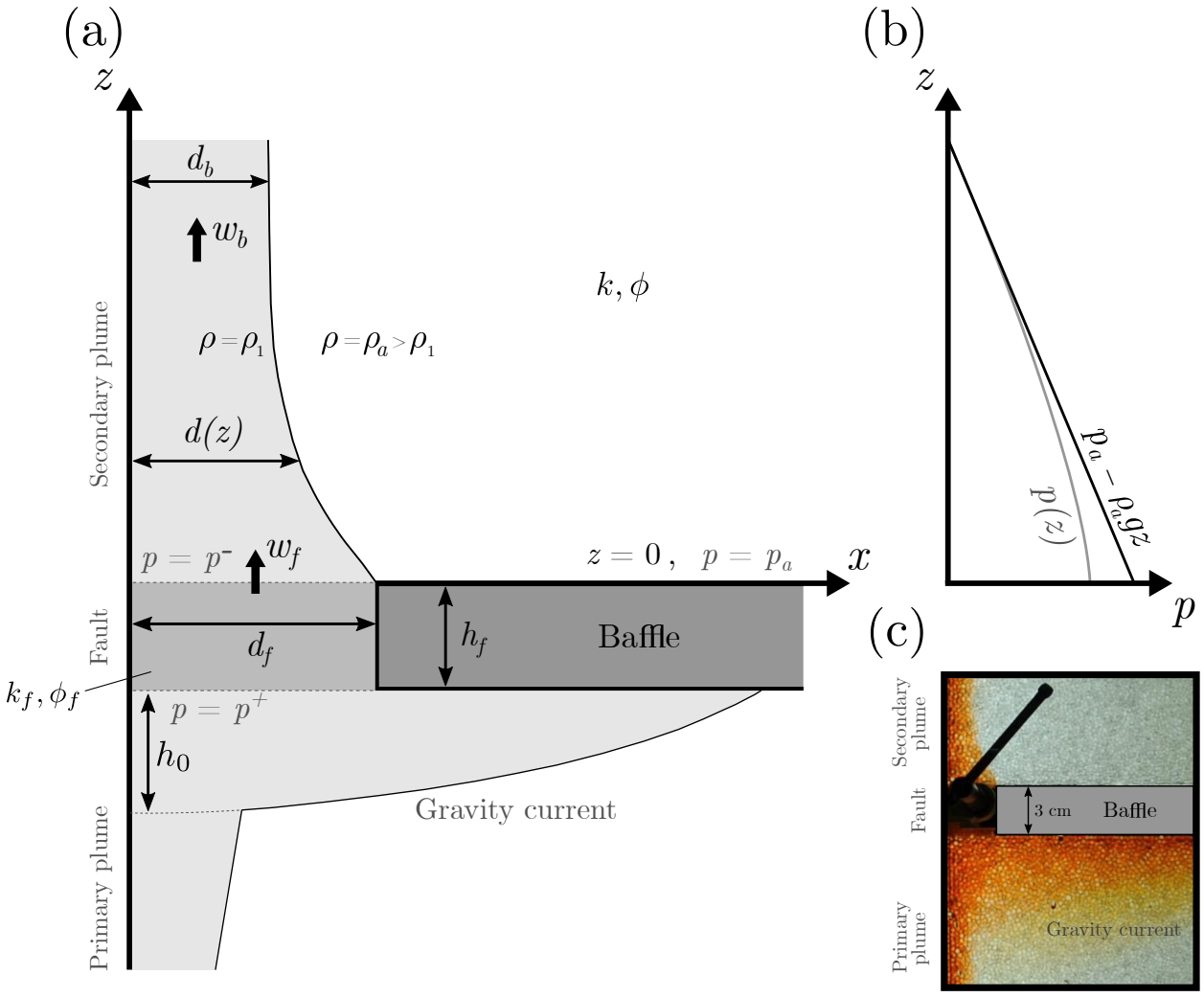

Figure 3.7: (a) Schematic diagram illustrating the different parameters of the problem. The secondary plume $z \geq 0$ is fed by a pressure-driven flow w_f through the fault, but must accelerate to match the natural buoyancy velocity w_b downstream. Hence, the plume width $d(z)$ thins out from initial width d_f to ultimate width d_b, resulting in a differential negative pressure p^- near its source. Note the redefined position of $z = 0$. (b) Figurative plot of the vertical pressure profile above the fault. (c) Close up of a laboratory experiment showing thinning of the secondary plume above the baffle (Note orientation of experimental image has been rotated by 180°, see Section 3.5).

$$w \to w_b, \quad \text{at} \quad z \to \infty, \tag{3.40}$$

respectively, where u and w are the fluid velocities in the x and z directions. At the edge of the steady plume, a kinematic boundary condition is imposed and the pressure is set equal to the ambient hydrostatic,

$$u = w\frac{\mathrm{d}d}{\mathrm{d}z}, \quad \text{and} \quad p = p_a - \rho_a g z, \quad \text{at} \quad x = d(z). \tag{3.41a, b}$$

The pressure at the edge of the plume is hydrostatic (3.41), since it must match with the pressure in the adjacent static ambient fluid. Consider an asymptotic solution of the form

$$u = \epsilon\hat{u}(x,z) + \ldots, \tag{3.42}$$

$$w = w_b + \epsilon\hat{w}(x,z) + \ldots, \tag{3.43}$$

$$p = p_a - \rho_a g z + \epsilon\hat{p}(x,z) + \ldots, \tag{3.44}$$

$$d = d_f + \epsilon\hat{d}(z) + \ldots \tag{3.45}$$

for $\epsilon \ll 1$. Clearly in the limit $\epsilon \to 0$ the leading order terms in (3.42)-(3.45) satisfy (3.37)-(3.41), as expected. At first order in ϵ, the pressure must satisfy the linear system

$$\nabla^2\hat{p} = 0, \tag{3.46}$$

$$\frac{\partial\hat{p}}{\partial z} = \Delta\rho g, \qquad \text{at} \quad z = 0, \tag{3.47}$$

$$\frac{\partial\hat{p}}{\partial x} = 0, \qquad \text{at} \quad x = 0, \tag{3.48}$$

$$\frac{\partial\hat{p}}{\partial z} \to 0, \qquad \text{at} \quad z \to \infty, \tag{3.49}$$

$$\hat{p} = 0, \qquad \text{at} \quad x = d_f, \tag{3.50}$$

$$\frac{\partial\hat{p}}{\partial x} = -\Delta\rho g\frac{\mathrm{d}\hat{d}}{\mathrm{d}z}, \qquad \text{at} \quad x = d_f. \tag{3.51}$$

Conservation of mass (combining (3.37a, b)), dictates that the pressure must satisfy Laplace's equation. Since Laplace's equation is linear, this applies to leading order pressure as well as the first order pressure correction, resulting in (3.46). Likewise, the boundary conditions (3.38)-(3.40) and the hydrostatic condition in (3.41b) are all linear equations. Hence, they

must apply to leading and first order pressure terms alike. The leading order pressure solution (first part of (3.44)) satisfies all of these trivially. However, inserting the first order pressure solution (second part of (3.44)) into (3.38)-(3.40) and (3.41b) results in (3.47)-(3.50), respectively. The only nonlinear equation is (3.41a), also known as the kinematic condition. In this case, one must expand out the variables, keeping only first order terms, which gives (3.51). Conveniently, (3.46)-(3.50) can be solved independently of (3.51), indicating that the plume shape and the pressure are decoupled to leading order. Then, after the solution for $\hat{p}$ is known, (3.51) can be integrated with boundary condition $\hat{d}(0) = 0$ to get the plume shape. The pressure solution is calculated by separation of variables, giving

$$\hat{p} = -\frac{8\Delta\rho g d_f}{\pi^2} \sum_{n=0}^{\infty} \frac{(-1)^n}{(2n+1)^2} \cos\left[(2n+1)\frac{\pi x}{2d_f}\right] e^{-(2n+1)\pi z/2d_f}. \tag{3.52}$$

Hence, the pressure (including both leading and first order terms) at $x = z = 0$, denoted p^-, is given by

$$p^- = p_a - \Delta\rho g d_f \left[\frac{8G}{\pi^2}\left(1 - \frac{w_f}{w_b}\right)\right], \tag{3.53}$$

where $G = \sum_{n=0}^{\infty}(-1)^n/(2n+1)^2 \approx 0.9160$ is Catalan's constant. The plume shape is calculated by evaluating (3.51) and (3.52), which converge to the differential equation

$$\frac{\mathrm{d}\hat{d}}{\mathrm{d}z} = -\frac{4}{\pi}\tanh^{-1}\left[e^{-\pi z/2d_f}\right]. \tag{3.54}$$

Equation 3.54 is solved numerically with boundary condition $\hat{d}(0) = 0$ and the solution plotted in Figure 3.8a. Clearly, $\hat{d} \to -d_f$ as $z \to \infty$, such that the the total plume shape $d_f + \epsilon\hat{d}$ asymptotes to the far field plume width $d_b = d_f w_f / w_b$, as required.

Note that both the pressure p^- and the inlet velocity w_f are unknown in (3.53). Hence, to close the system a second equation relating these two quantities is required. This is given by considering the flow through the fault $-h_f < z \leq 0$. In particular, as illustrated in Figure 3.7, the flow through the fault is driven by a difference in pressure $p^+ - p^-$, where p^+ is set by the thickness of the gravity current,

$$p^+ = p_a + \Delta\rho g h_0 + \rho_a g h_f. \tag{3.55}$$

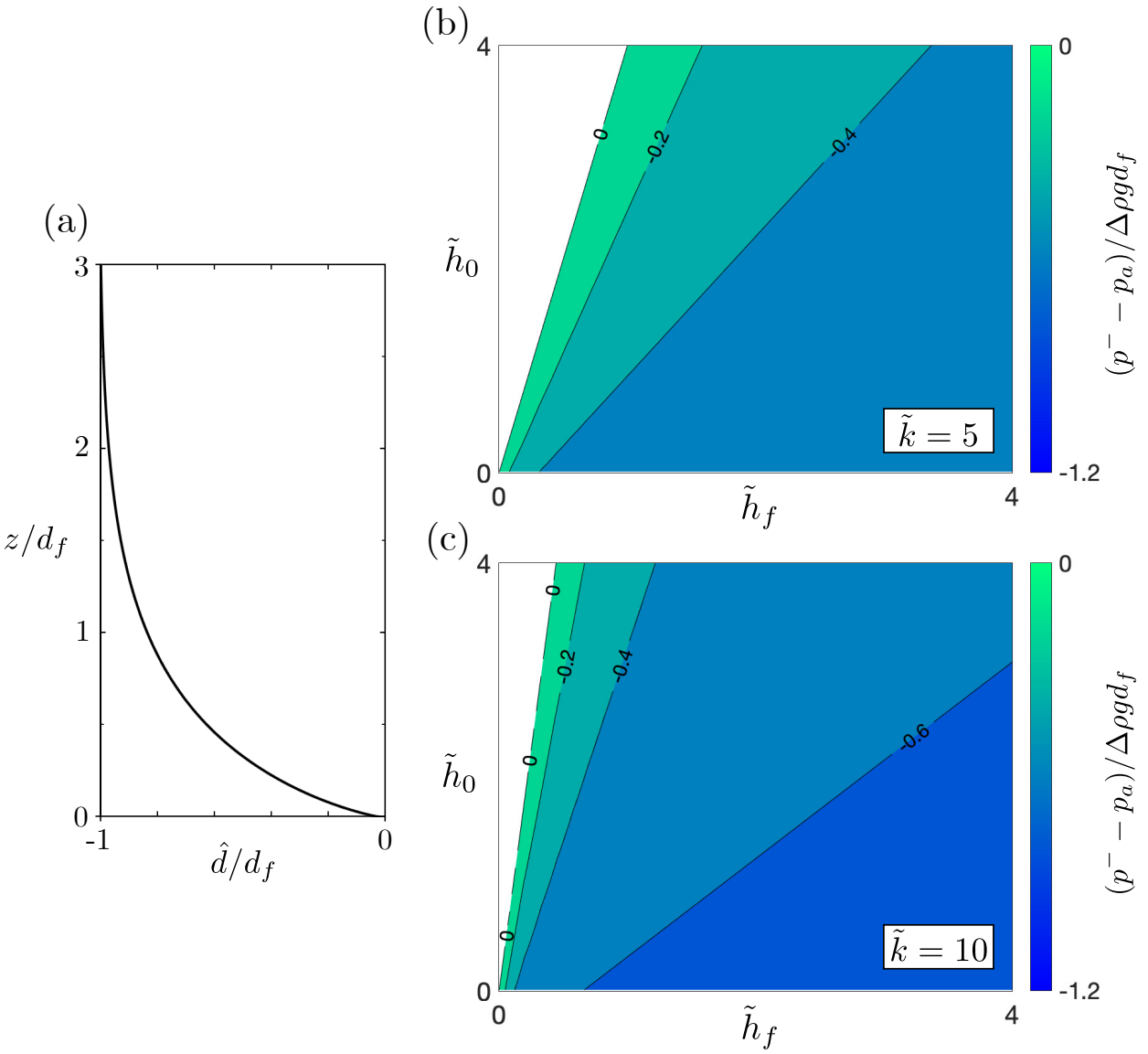

Figure 3.8: (a) Perturbation of the width of the secondary plume (3.54). (b, c) Contour plots of the pressure above the baffle p^- (3.53), normalised to give a dimensionless value $(p^- - p_a)/\Delta\rho g d_f$, for the different parameters of the problem $\tilde{h}_0 = h_0/d_f$, $\tilde{h}_f = h_f/d_f$ and $\tilde{k} = k/k_f$. Regions of the contour plots resulting in a widening plume $w_f/w_b > 1$ and positive values of p^- are omitted.

Hence, by approximating Darcy's law across the fault, a second relationship is obtained,

$$w_f = -\frac{k_f}{\mu}\left[\frac{p^- - p^+}{h_f} - \rho_1 g\right]. \tag{3.56}$$

Rearranging (3.53) and (3.56) gives the dimensionless equations for w_f/w_b and p^-,

$$\frac{w_f}{w_b} = \frac{1 + (\tilde{h}_f + \tilde{h}_0)\pi^2/8G}{1 + \tilde{k}\tilde{h}_f\pi^2/8G}, \tag{3.57}$$

$$p^- = p_a - \Delta\rho g d_f\left[\frac{\tilde{h}_f(\tilde{k}-1) - \tilde{h}_0}{1 + \tilde{k}\tilde{h}_f\pi^2/8G}\right], \tag{3.58}$$

where $\tilde{h}_0 = h_0/d_f$, $\tilde{h}_f = h_f/d_f$ and $\tilde{k} = k/k_f$ are known parameters. From (3.57) and (3.58) it is clear that negative values of $p^- - p_a$ correspond with $w_f/w_b < 1$, and positive values of $p^- - p_a$ correspond with $w_f/w_b > 1$.

The pressure p^- (written in dimensionless form $(p^- - p_a)/\Delta\rho g d_f$) is illustrated in Figures 3.8b and 3.8c using contour plots. Largest negative pressures are observed for small values of the gravity current thickness $\tilde{h}_0$, or large values of $\tilde{h}_f$ and $\tilde{k}$ (corresponding to small velocity ratios w_f/w_b). Note, however, that the asymptotic solution is not expected to be valid for $w_f/w_b \ll 1$. In such situations a full numerical simulation is required to determine p^-. Nevertheless, for the parameter range of the current study ($w_f/w_b \in [0.5, 1.2]$), (3.58) is expected to remain a good approximation.

3.5 Laboratory study

I conducted a series of laboratory experiments to test two aspects of the theoretical predictions. First, the spatial distribution of the gravity current was measured as a function of time. Second, the partitioning of fluxes between the gravity current and the fault was measured by calibrating the image intensity and dye concentration. As it was easier to model experimentally, I considered a system in which the injected fluid is more dense with respect to the ambient. Given the Boussinesq approximation, this system behaves symmetrically to a less dense fluid rising in an aquifer saturated with a denser fluid. The experimental images

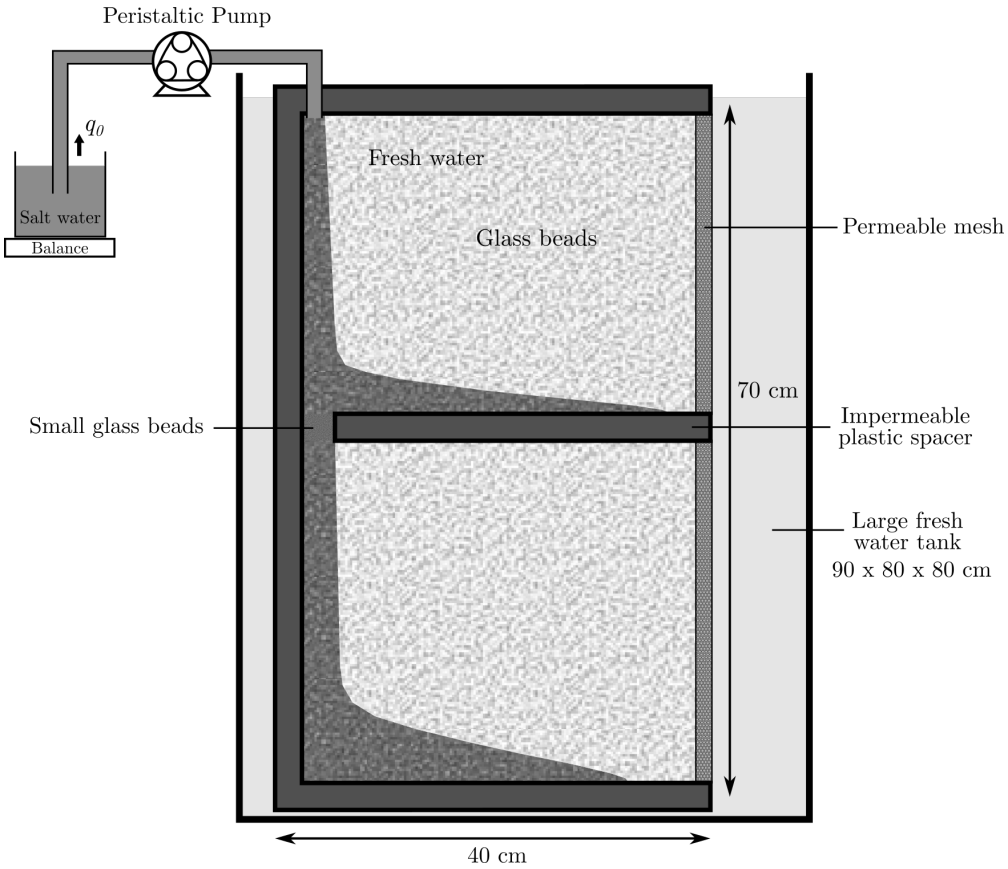

Figure 3.9: Schematic of the experimental setup.

presented are rotated by 180° for ready comparison between the analytical and experimental results.

3.5.1 Experimental Setup

The experiments were performed within a perspex cell of length 40 cm, height 70 cm and internal thickness 1 cm (Figure 3.9). The cell was filled with glass ballotini which formed a porous layer. The glass ballotini filling the majority of the cell had diameter $b_0 = 3.1 \pm 0.2$ mm except for the region adjacent to a central plastic spacer that lies across the cell where the ballotini diameter $b_f = 1.0 \pm 0.1$ mm. The porosity of 3 mm glass ballotini in a cell of width 1 cm was measured by Sahu & Neufeld (2020) and found to be $\phi = 0.41 \pm 0.01$, which is slightly higher than the value of $\phi = 0.37$ for randomly close-packed beads as the width of the cell is comparable to the bead size. The permeability of the larger porous medium

Exp.	Symbol	d_f (cm)	h_f (cm)	H (cm)	q_0 (cm^3 s^{-1})	ρ_0 (g cm^{-3})	λ
A1	△	1.2	1.0	30.0	0.240	1.030	0.12
A2	◊	1.2	1.0	30.0	0.129	1.030	0.16
A3	×	1.2	1.0	30.0	0.040	1.070	0.19
B1	○	1.9	1.5	40.0	0.239	1.030	0.18
B2	△	1.9	1.5	40.0	0.139	1.030	0.23
B3	◊	1.9	1.5	40.0	0.115	1.070	0.26
B4	×	1.9	1.5	40.0	0.039	1.070	0.27
C1	○	2.5	2.0	40.0	0.245	1.030	0.24
C2	△	2.5	2.0	40.0	0.141	1.030	0.30
C3	◊	2.5	2.0	40.0	0.112	1.070	0.34
C4	×	2.5	2.0	40.0	0.040	1.070	0.35
D1	○	3.0	3.0	29.9	0.242	1.030	0.31
D2	△	3.0	3.0	29.9	0.182	1.030	0.36
D3	◊	3.0	3.0	29.9	0.102	1.030	0.43
D4	×	3.0	3.0	29.9	0.041	1.070	0.49

Table 3.1: Parameter values used in the experiments with associated value of λ from (3.35). Typical uncertainties in these measurements are $d_f \pm 0.05$ cm, $h_f \pm 0.05$ cm, $H \pm 0.1$ cm, $q_0 \pm 0.001$ cm^3 s^{-1} and $\rho_0 \pm 0.005$ g cm^{-3}.

filling the majority of the cell was estimated using the Kozeny-Carman relation

$$k = \frac{b_0^2}{180}\frac{\phi^3}{(1-\phi)^2} \approx 1.06 \pm 0.15 \times 10^{-8} \text{ m}^2. \tag{3.59}$$

The Kozeny-Carman relationship breaks down when applied to a small volume of beads, hence the permeability of the region with smaller ballotini was treated as an unknown parameter and fitted for (see Section 3.5.3). The entire cell submerged in a large water tank with dimensions $90 \times 80 \times 80$ cm filled with fresh water of density $\rho_a = 0.998$ g cm^{-3}. The cell was closed on three sides, with one side open but lined with a permeable mesh so that this unconfined side created a hydrostatic pressure boundary condition at the right hand side of the cell. A total of 15 experiments were conducted, using four different fault geometries (A-D), as summarised in Table 3.1.

During the experimental run, a peristaltic pump was used to inject aqueous solutions of

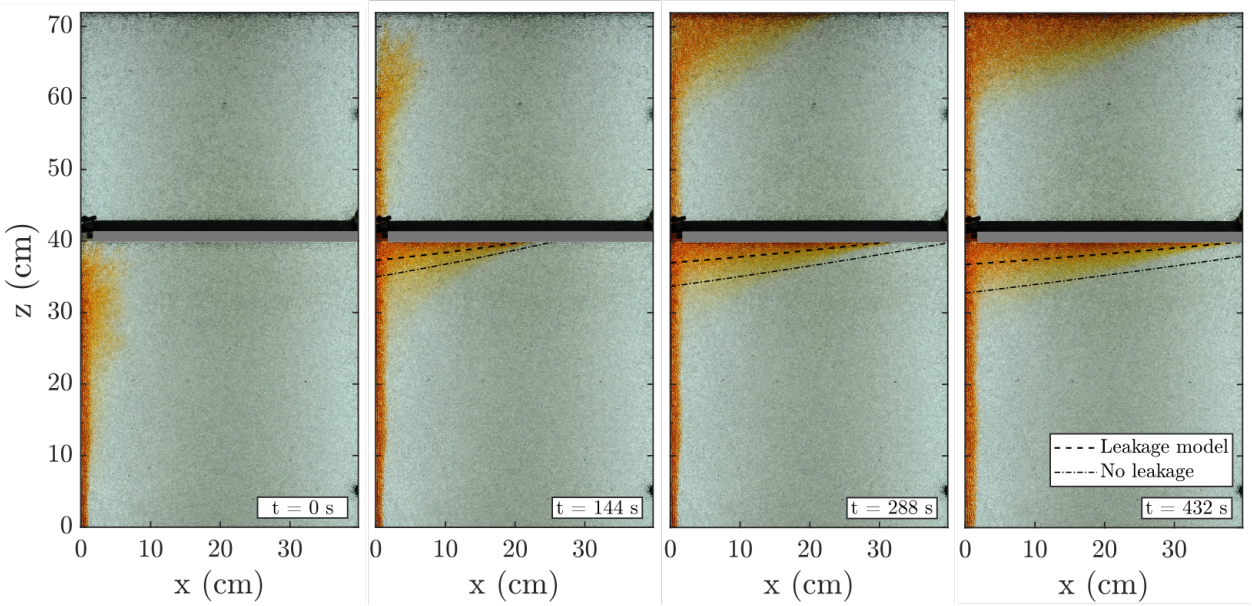

Figure 3.10: Images showing the evolution of experiment B2. The theoretical predictions for the position of the interface $h(x,t)$ are shown for the thinning plume model presented in Section 3.4 and the zero leakage model (Huppert & Woods, 1995). Images are rotated 180° to allow comparison with theoretical results (see Section 3.5).

sodium chloride (brine) dyed with red food colouring into the cell at a constant rate q_0 which ranged from 0.039 - 0.245 cm^3s^{-1}, and was calculated by measuring the mass of the brine container over the course of the experiment. The injected brine solutions had an initial dye concentration of $c_0 = 3.00 \pm 0.05$ g/L and an initial density $\rho_0 = 1.030$ g cm^{-3} or 1.070 g cm^{-3}, assuming a water temperature of 20°C (Green & Southard, 2019). The kinematic viscosity of the water was 0.01 cm^2 s^{-1} and the transverse dispersivity of the glass ballotini was assumed to be $\alpha = 0.005$ cm (Delgado, 2007). The experimental parameters were selected so experiments spanned a range of λ values. I used a Nikon D5000 DSLR camera with a resolution of 4288×2848 pixels to capture images over the course of the experiment with a time gap which ranged from 4-10 s. The cell was backlit using a LED light panel with a perspex diffuser to ensure uniform illumination.

3.5.2 Post-processing scheme

A set of photographs for experiment B2 is shown in Figure 3.10, rotated by 180° for ready comparison between the analytical and experimental results. The theoretical predictions for the position of the gravity current interface $h(x,t)$ in the bottom portion of the cell is plotted

for the thinning plume model, along with the interface for the zero leakage model (Huppert & Woods, 1995). The time $t = 0$ is defined as the point where the plume first makes contact with the bottom of the central spacer. The horizontal extent of the gravity current was measured as a function of time by picking the furthest front of the current above a threshold value. The error range of the measurements was set by calculating the extent for a range of threshold values. The results were verified by manually checking the front location from photographs and showed excellent agreement. The height of the current was more difficult to interpret due to dispersion from the plume making the top of the current uncertain.

To measure the flux of fluid leaking through the fault, the concentration of the injected fluid throughout the cell must be determined, and so a series of calibration experiments were performed to determine the functional relationship between the image intensity and dye concentration. In each calibration experiment, the cell was uniformly saturated with a red dye solution with concentration C_d. The light intensity for the calibration image was calculated by subtracting the light intensity from a reference image containing no dye. A total of 20 different concentrations between 0 g/L and 3.00 ± 0.05 g/L were used to construct calibration curves for the green and blue colour channels (Figure 3.11), where each colour channels refers to the respective RGB value of pixels in the image. The dye calibration is more sensitive to different colour channels at different dye concentrations, so a hybrid calibration curve was used which weighted contributions from the green and blue curves. The functional forms of the calibration curves for the green and blue channels are

$$C_G = aI_G^4 + bI_G^3 + cI_G^2 + dI_G, \tag{3.60}$$

and

$$C_B = \begin{cases} aI_B, & I \leq 106, \\ (b + cI_B)^{-1/d}, & I > 106. \end{cases} \tag{3.61}$$

where I_G and I_B are differences in the green or blue image intensity between the reference and calibration images and a, b, c and d are fitting coefficients.

The calibration curve for the blue channel is sensitive to small changes in dye concentration for concentrations up to ~ 0.9 g/L, but insensitive at higher concentrations due to image saturation. In comparison, the green channel is less sensitive at low concentrations but

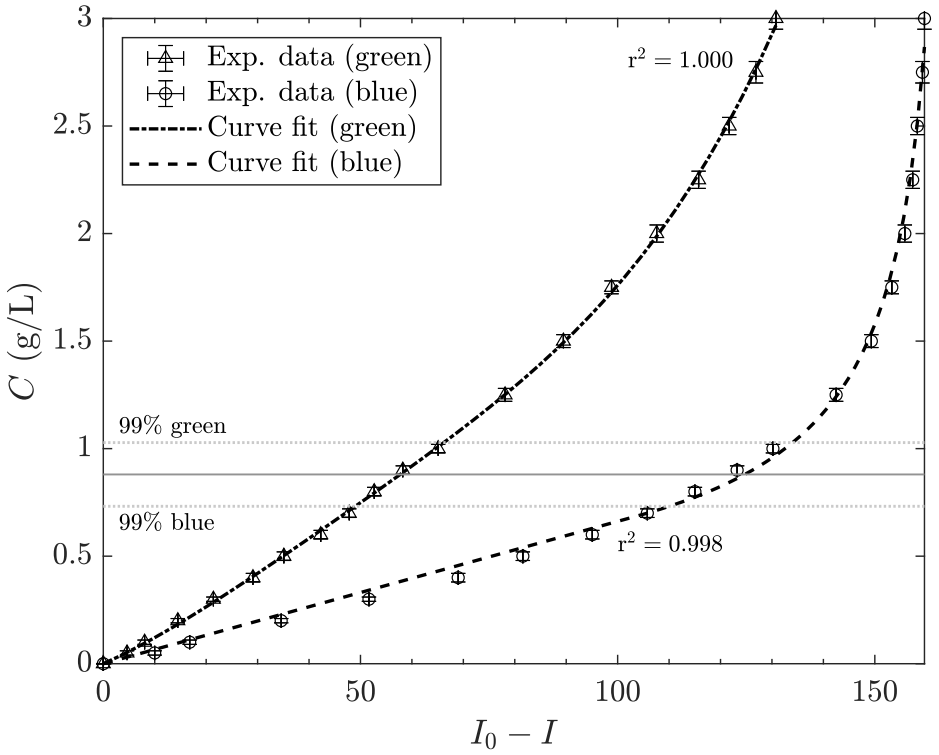

Figure 3.11: Calibration curves of image intensity against dye concentration for the green and blue colour channels (black dashed lines). Also plotted is the effective concentration where both calibration curves have equal weighting (grey solid line) and the 99% intervals above and below which the green and blue curves dominate the effective concentration (grey dashed lines).

has greater sensitivity at dye concentrations above 0.9 g/L. The best calibration results are obtained when using a weighted average of the two curves to convert image intensity to dye concentration. The effective concentration is determined by the function

$$C_{eff} = C_B + \left(\frac{C_G - C_B}{2}\right)\left[1 + \tanh\left(\frac{C_{avg} - \tau}{\delta}\right)\right], \tag{3.62}$$

where C_B and C_G are the concentrations calculated from the blue and green calibration curves, $C_{avg} = \frac{C_B + C_G}{2}$, τ is the concentration at which C_{eff} is a result of equal contributions from C_B and C_G (grey solid line, Figure 3.11) and δ sets the width of the region both curves contribute significantly towards C_{eff} (grey dashed lines, Figure 3.11). The calibration curves in Figure 3.11 were calculated using an average light intensity across the full calibration images. Calibration curves were plotted for subregions of the cell to check for the potential effect of small variations in light intensity. However, it was found that effects of spatial

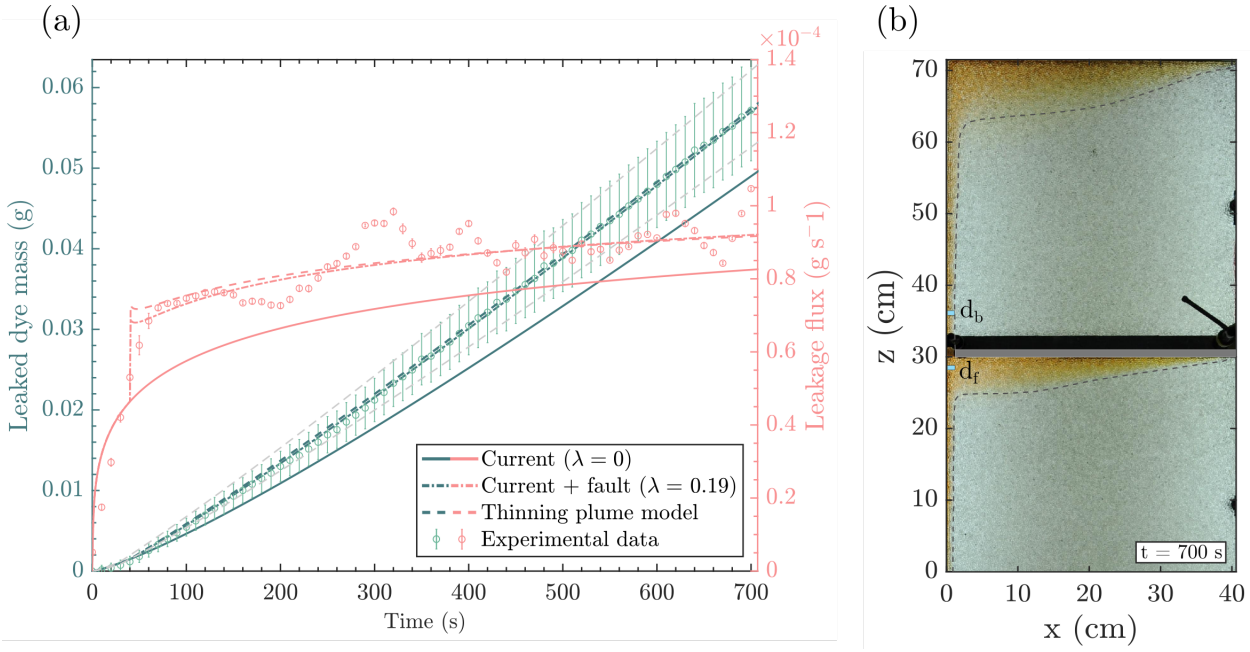

Figure 3.12: (a) Total leaked dye mass (green circles) and leakage flux (pink circles) plotted as a function of time for experiment A3 along with results for three leakage models (green and pink lines). Grey dashed lines display thinning plume model solutions for an uncertainty range for input $k_f \pm 20\%$. (b) Picture of the experiment at time $t = 700$ s with width of fault d_f and width of secondary plume d_b indicated.

variation were minimal.

The mass of dye across the cell is calculated by summing the average concentration within 0.5×0.5 cm^2 sized bins, with the leaked mass equal to the total mass below the top of the baffle. The total error in measurement is the sum of two errors. First, the leaked dye mass shows a linear behaviour at late times. A root-mean-square deviation from a regression line was calculated, with the deviations likely caused by small variations in light intensity between each photo, for example due to trapped air bubbles. Second, the total measured mass of dye across the cell was compared to the known input dye mass for each experiment. The measured mass increases linearly as a function of time but the post-processing recovers 83-97% of the input dye mass across experiments. The partial measurement of the input dye is likely due to sensitivity of the calibration curve to smaller concentrations. For each experiment, the measured dye mass is scaled to the known input dye mass and the difference is defined as the error in measurement.

3.5.3 Experimental results and comparison with theory

Figure 3.12a shows the total leaked dye mass (green circles) and leakage flux (pink circles) as a function of time for experiment A3. The leaked flux is calculated by taking the gradient of a quadratic polynomial fitted over a seven element moving window. The errors bars represent a 95% confidence interval for the regression coefficients.

The experimental results are compared to theoretical results from three different models presented in Sections 3.2 and 3.4. The first model only considers the contribution from the hydrostatic pressure within the underlying current ($\lambda = 0$). The second model considers contributions from the underlying current and the buoyancy of fluid in the fault ($\lambda \neq 0$), and the third model includes both of these effects but also considers the contribution of flow-enhancing pressure deviations directly above the fault (thinning plume model). There is very little difference between the solutions for the second and third model, suggesting that the effects of pressure deviations above the baffle due to thinning of the secondary plume are minimal. This agrees with experimental observations (Figure 3.12b), which show that the width of the secondary plume is the same as the width of the fault ($d_b/d_f \approx 1$).

Due to the difficulty in estimating the fault permeability k_f, this was calculated by minimising the misfit between the experimental data and the thinning plume model using a least-squares regression for one of the experiments. Experiment A3 (Figure 3.12) was selected to fit the fault permeability due to the agreement between the thinning plume model and the $\lambda \neq 0$ model. A value of $k_f = k_0/3.9 \approx 2.7 \pm 0.3 \times 10^{-9}$ m^2 was obtained and this value was used to calculate the theoretical results across the other experiments. It is possible that there is some variation in the fault permeability across different experiments, but this should be small as the faults are a similar size and were all packed using the same method. The sensitivity of the thinning plume model to changes in fault permeability is shown by the grey dashed lines in Figure 3.12a, in which the model solutions are displayed for $k_f \pm 20\%$.

Figure 3.13a shows the total leaked dye mass (green circles) and leakage flux (pink circles) as a function of time for experiment D4, along with theoretical results for the three models. There is a clear difference between the model which allows for a thinning plume above the baffle and the model only considering contributions from the underlying current and

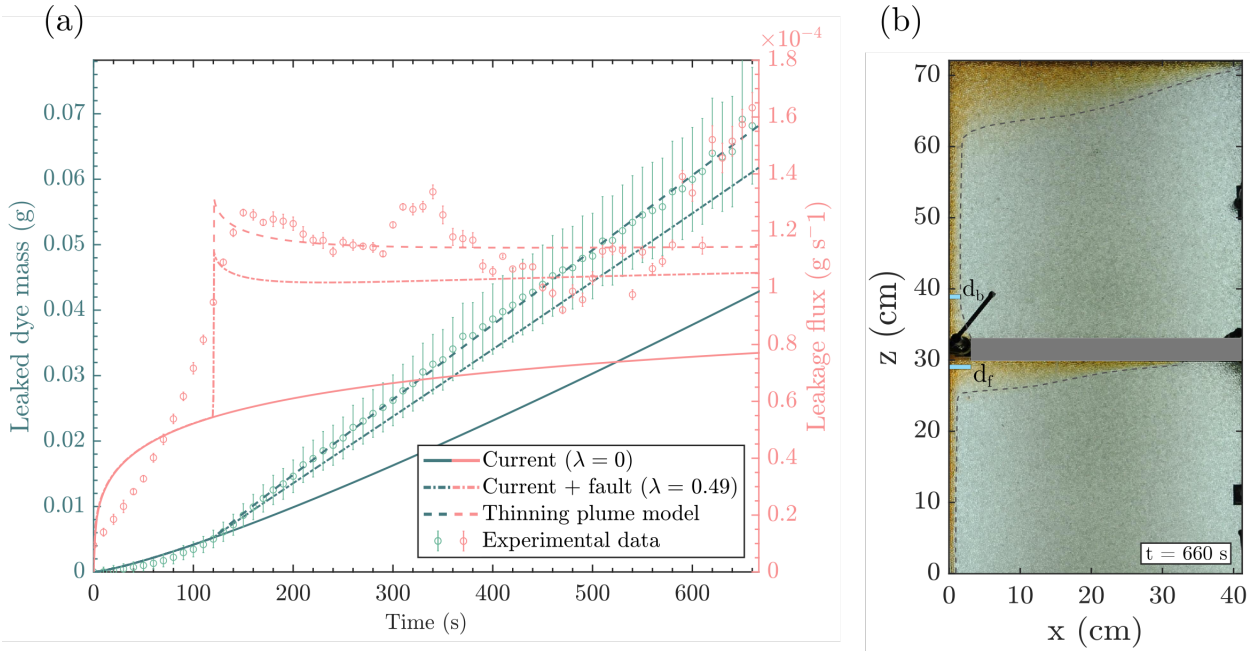

Figure 3.13: (a) Total leaked dye mass (green circles) and leakage flux (pink circles) plotted as a function of time for experiment D4 along with results for three leakage models (green and pink lines). (b) Picture of the experiment at time $t = 660$ s with width of fault d_f and width of secondary plume d_b indicated.

buoyancy in the fault, suggesting that acceleration and thinning of the secondary plume is leading to enhanced pressure gradients within the fault. Experimental observations are in agreement (Figure 3.13b), where significant thinning of the secondary plume can be seen above the fault ($d_b/d_f < 1$).

Note that the model considering buoyancy in the fault assumes that the fault is initially full of the injected fluid. Furthermore, the thinning plume model assumes that a secondary plume has reached a quasi-steady state profile above the fault. In reality, at early times the fault remains filled with the ambient fluid so the only driving force is the hydrostatic pressure in the underlying current. To account for this, a breakthrough time is introduced, defined as the time it takes for the injected fluid to fill the fault and breakthrough into the upper reservoir. The breakthrough time is obtained from experimental observation by calculating the average concentration just above the fault as a function of time (Figure 3.14).

The concentration is initially low before breakthrough, then rises sharply before levelling off at a constant value. The grey shaded area in Figure 3.14 shows the potential range in breakthrough time. The lower limit is when injected fluid first starts to enter the lower

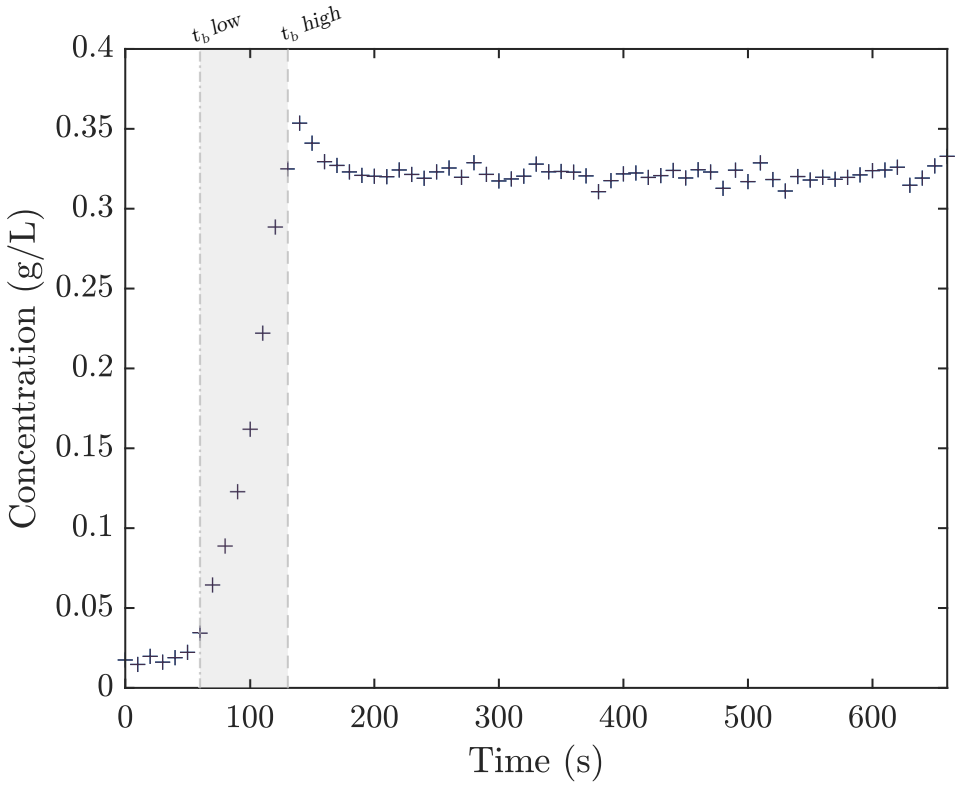

Figure 3.14: Average concentration directly above the fault plotted as a function of time for experiment D4. Dashed lines show the upper and lower bounds for the breakthrough time t_b, defined as the time it takes for the injected fluid to fill the fault and breakthrough into the upper reservoir.

reservoir. The upper limit is when the fault is full of injected fluid and so the concentration just above the fault becomes constant. Across all the experiments, the average difference between the upper and lower limit is ~ 50 s. The upper limit breakthrough time is chosen when running the numerical models as this is the point where the fault is filled with fluid of a concentration similar to the gravity current and the plume above the fault has reached a steady concentration.

Prior to the breakthrough time, all three models only consider the contribution from the underlying current. After the breakthrough time, the other driving forces are taken into account. The sensitivity of the plume thinning model to the range of breakthrough times is shown in Figure 3.15. Here, the leaked dye mass and leakage flux are plotted as a function of time for experiment D4, and compared against results from the model with leakage only driven by hydrostatic pressure in the underlying current and the thinning plume model. The thinning plume model has been calculated using the upper and lower bound breakthrough

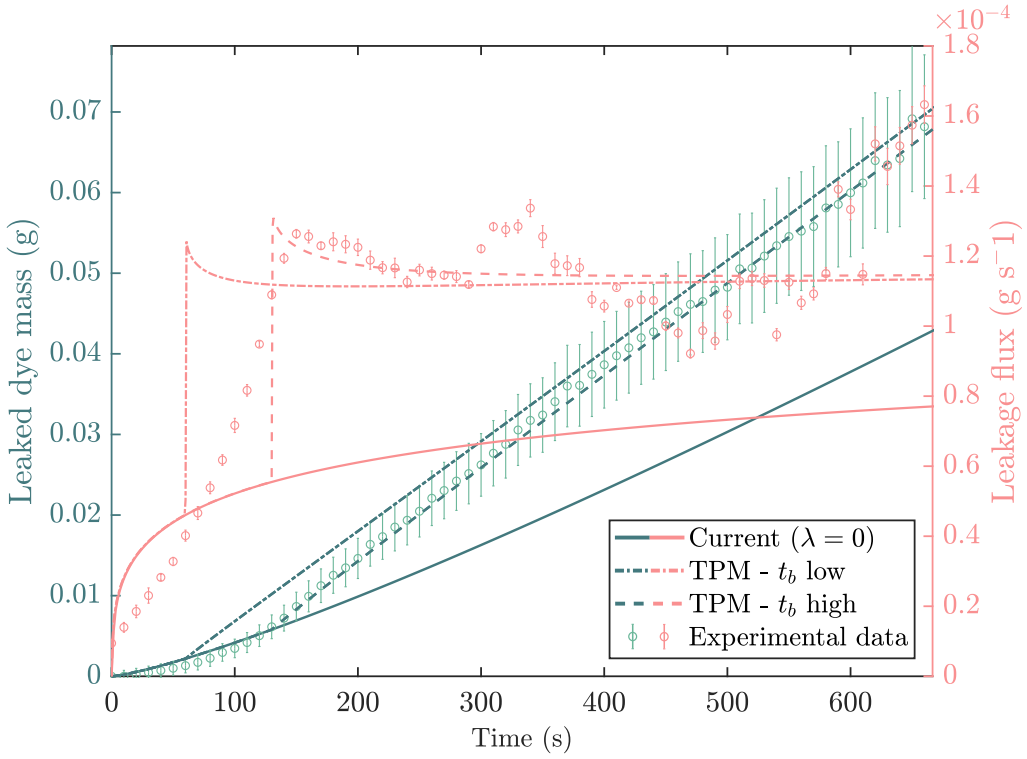

Figure 3.15: Sensitivity of the plume thinning model to the breakthrough time. Total leaked dye mass (green circles) and leakage flux (pink circles) plotted as a function of time for experiment D4 along with results for leakage driven by hydrostatic pressure within the underlying current (unbroken line), and thinning plume model (dashed and dash-dotted) for upper and lower bound breakthrough time t_b.

times ($t_b - high$ and $t_b - low$), obtained from Figure 3.14. The models converge to a similar solution, within the range of experimental error.

This modification to the theory results in a discontinuous leakage flux profile (pink dashes, Figures 3.12a, 3.13a), where the leakage flux increases rapidly at the breakthrough time. These predictions broadly agree with the behaviour seen in the experimental data, where initial leakage rates are slow as the fault fills with the injected fluid before increasing rapidly to a higher and constant rate. The thinning plume model shows good agreement with the experimental data in both total leaked dye mass and leakage flux.

Figure 3.16 shows the total leaked dye mass as a function of time across all experiments, with symbols listed in Table 3.1. The solutions for the thinning plume model are plotted for each experiment and show good agreement across all experimental setups A-D.

The horizontal extent of the underlying gravity current along with solutions from the thinning

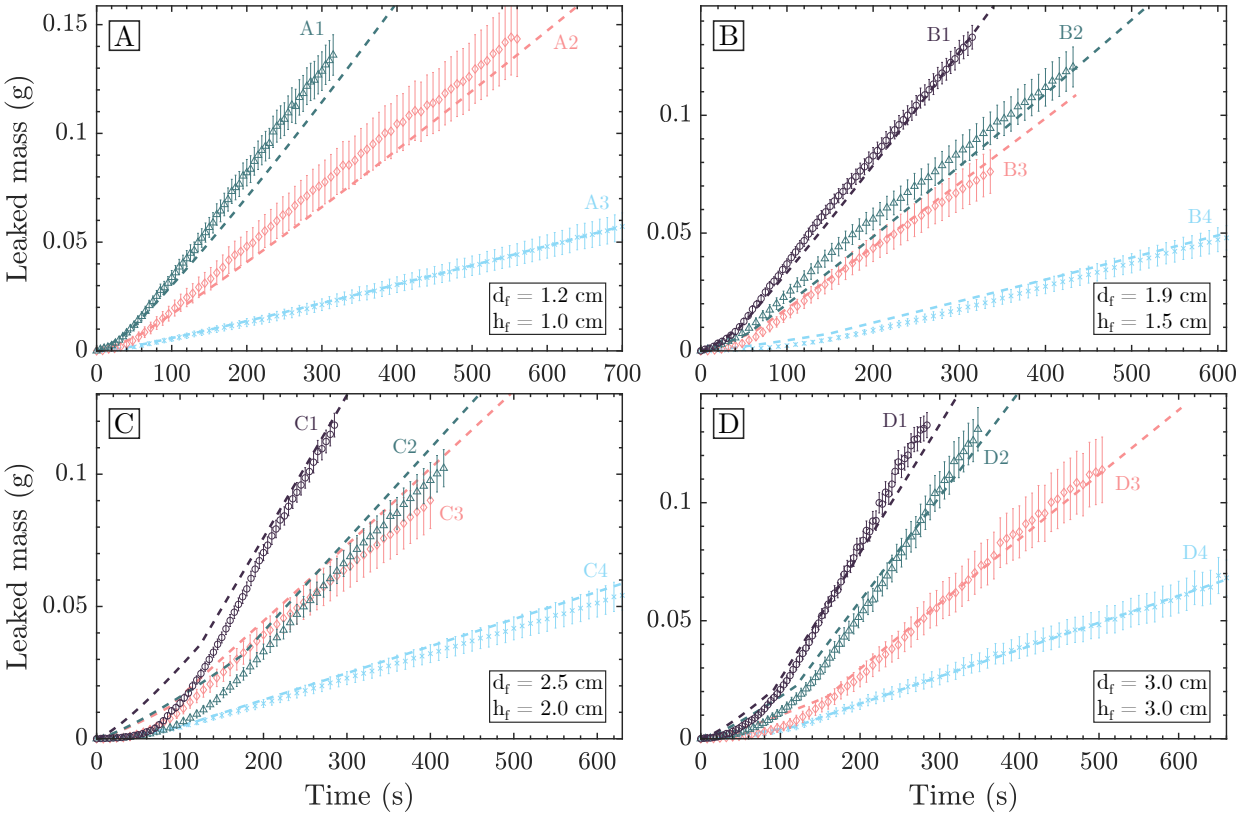

Figure 3.16: Total leaked dye mass through the fault plotted as a function of time for the experimental setups A-D, with symbols listed in Table 3.1. Theoretical predictions of the leakage mass for each experiment calculated from the thinning plume model plotted as dashed lines.

plume model is plotted in Figure 3.17 for experimental setups A-D. In general the theoretical model shows good agreement with the experimental data, although it tends to overpredict the horizontal extent of the current. A possible explanation is that the gravity current entrains ambient fluid as it moves into the reservoir which is not captured in the model. This decreases the reduced gravity of the current, and hence reduces the distance it travels. This effect would also cause the thickness of the current to increase, and this can be seen in Figure 3.10, where the experimental current has a greater thickness than the thinning plume model predicts, but appears more dispersed towards its outer edge.

3.6 Application to a CO_2 storage reservoir

In reservoirs with multiple faulted aquifers and seals, a fraction of the injected fluid will flow into the aquifers at each level and a diminishing amount will continue to leak through the

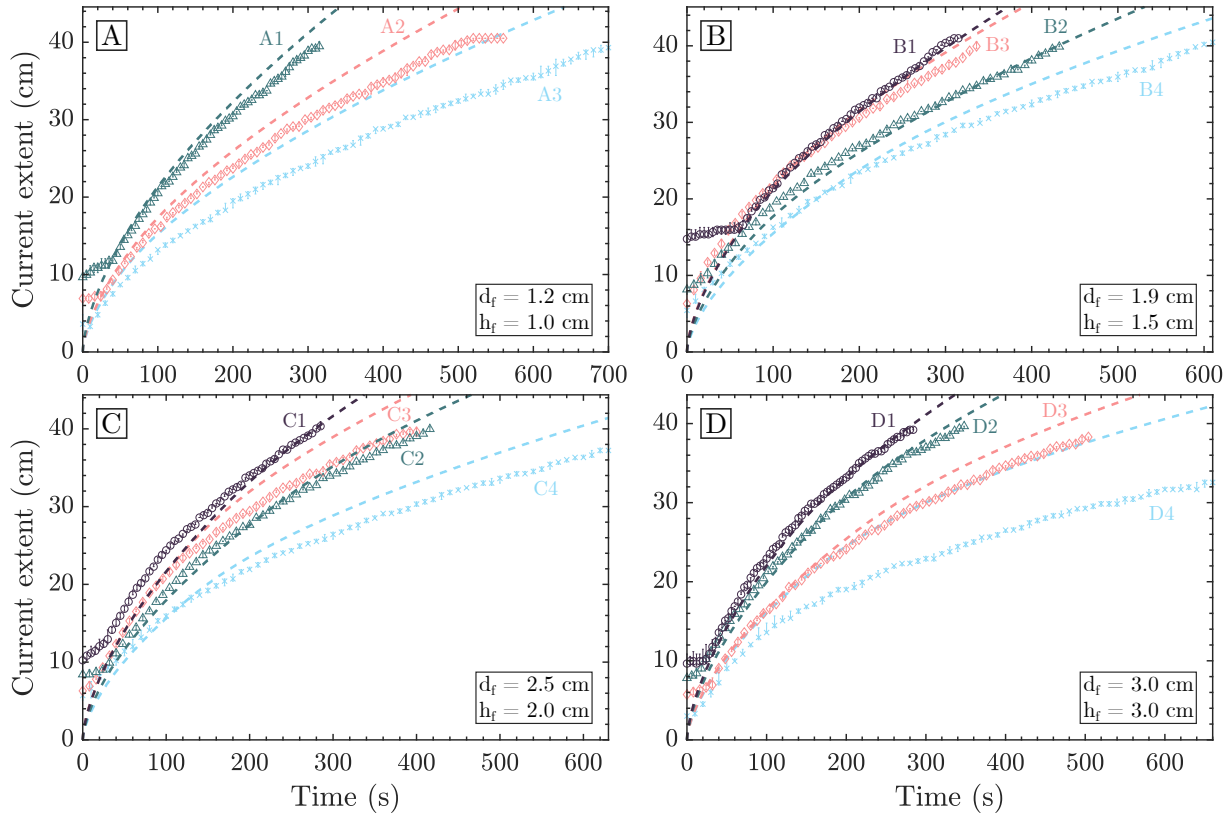

Figure 3.17: Evolution of horizontal extent of the gravity current x_N plotted for the experimental setups A-D, with symbols listed in Table 3.1. Theoretical predictions for the extent growth plotted as black dashed lines.

fault. When applied to geological CO_2 sequestration, this has important implications for providing an initial estimate of the security of a potential field scale storage site, especially where numerical reservoir simulations are unable to include the details of faults. The critical properties of the faults such as their damage zone widths and permeabilities may be estimated from scaling relationships, analogue surface outcrops or drill cores if available.

To address the case of a fault cutting through multiple layers, I now extend the model developed in Section 3.2 and Section 3.4 and briefly discuss the results. Three aquifers and seals are stacked vertically with a fault cutting through the layers (Figure 3.18a). The same physical parameters are used for each layer, and are modelled on a natural CO_2-charged aquifer at Green River, Utah, where CO_2 has been escaping along fault zones for several hundred thousand years (Bickle & Kampman, 2013). The aquifer properties used in the model are thickness $H = 122$ m, permeability $k = 1.4 \times 10^{-15}$ m^2 and porosity $\phi = 0.15$. The seals have thickness $h_f = 50$ m and are cut by a fault of width $d_f = 9$ m (measured

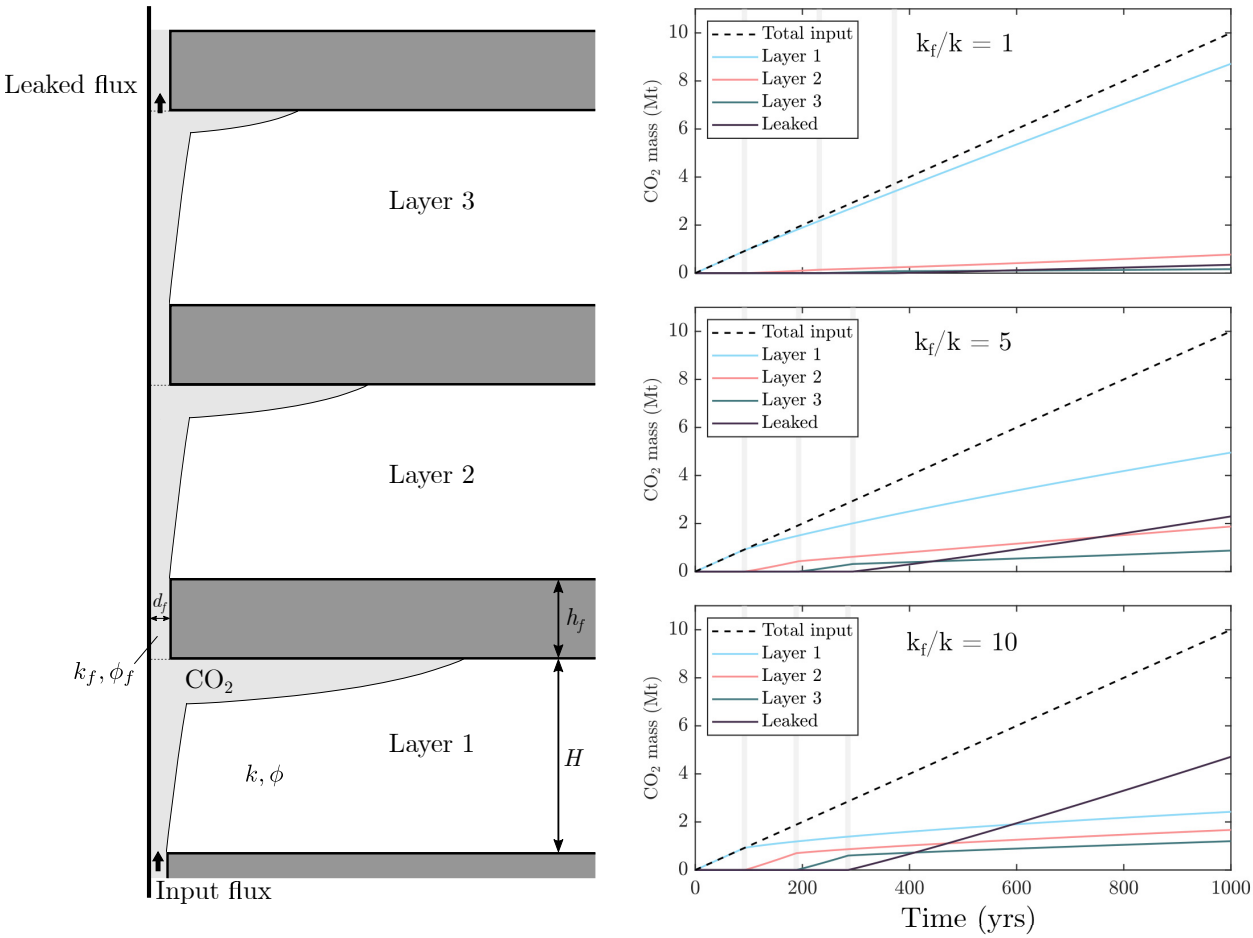

Figure 3.18: (a) Schematic showing injection of CO_2 into a system with multiple stacked aquifers and seals with a fault cutting through the layers. (b) The total CO_2 mass in each layer as well as the total leaked CO_2 (leakage from layer 3) plotted as a function of time for three different values of the fault permeability. The breakthrough time into each layer is marked with a grey vertical line.

from drill core) with porosity $\phi_f = 0.07$ (Kampman *et al.*, 2014). The system is initially saturated with water of density $\rho_a = 1000$ kg m^{-3}. Less dense CO_2 is injected at a constant rate of 0.1 Mt yr^{-1} at the bottom of Layer 1, and assumed to have constant density $\rho = 790$ kg m^{-3} and dynamic viscosity $\mu = 6.9 \times 10^{-5}$ Pa s, calculated at typical storage reservoir conditions of 15 MPa and 40°C (Dubacq *et al.*, 2013). The mass flux of injected CO_2 is converted into a two-dimensional input flux assuming an along-fault system length of 1 km. These parameters give an initial value of $\lambda = 0.26$.

The total CO_2 mass in each layer as well as the total leaked CO_2 (defined as the leakage from Layer 3) is plotted as a function of time for three different values of the fault permeability (Figure 3.18b). Note that the experiments performed in Section 3.5 had $k_f/k < 1$ whereas

the scenarios shown here have $k_f/k \geq 1$. When the fault permeability is comparable to or less than the reservoir permeability, the majority of the CO_2 remains trapped within layer 1 over a roughly 1000 year time scale. However, when the fault permeability is larger than the reservoir permeability, a significant fraction of the injected CO_2 leaks all the way through the system. For example, in the two cases where $k_f/k = 5$ and $k_f/k = 10$, layers 2 and 3 do not accumulate significant amounts of CO_2. However, even with $k_f/k = 10 \sim 55\%$ of the CO_2 remains trapped after 1000 years. Note that this is the simple case where all layers have equal permeabilities. In a more realistic system where the permeability varies across layers, it is likely that larger accumulations of CO_2 would be seen in more permeable aquifers, regardless of their position. This system represents the worst case scenario for CO_2 storage as trapping mechanisms such as capillary trapping and dissolution trapping are neglected. In reality, as the CO_2 rises and spreads out into different aquifers these other mechanisms would contribute towards long-term storage of the CO_2.

The model has a limit, when the flux into the aquifer is small, in which all the flux into the aquifer leaks up the fault. This critical flux below which this phenomenon occurs is equal to the flux driven by buoyancy through the fracture zone. For a reservoir with multiple aquifers and seals, the leakage flux through the top layer will eventually reach this limit, as the amount leaked decreases at each subsequent aquifer.

3.7 Discussion

I have presented a new analytical model that describes the dynamics of leakage through a fault zone given properties relating to fault, aquifer and fluids. This new model has been tested against results from analogue porous media tank experiments, from which I obtain good fits with the experimental data. This model has then been applied to predict the CO_2 distribution and leakage rates from a naturally-occurring CO_2 reservoir. I find that when the permeability of the fault is comparable to the reservoir, the majority (>96%) of the CO_2 remains trapped after 1000 years. However, it is important to highlight the limitations of the current model and discuss to what extent it can be applied directly in its present form, and in which ways it might be fruitfully enhanced as part of a future study.

The gravity current model uses a sharp-interface approximation (Huppert & Woods, 1995; Hesse *et al.*, 2007), originally developed for miscible flows in porous media. This is valid for settings such as saline intrusions, but extra multiphase effects need to be considered when applied to immiscible settings such as CO_2-water systems (Golding *et al.*, 2011). When CO_2 is injected into water-saturated reservoirs, capillary forces play a key role in determining the saturation distribution and flow properties through the relative permeability and capillary pressure relationships (Nordbotten & Celia, 2011). When the fault and reservoir have relatively uniform permeability, I expect the behaviour of the system to scale in a similar manner to the miscible case, with the effective permeability instead replaced by the product of intrinsic and relative permeability. However, geologically heterogeneous reservoirs may have significant gradients in capillary pressure, which tend to rearrange the CO_2 saturation into high permeability regions, thereby accelerating plume migration (Benham *et al.*, 2021b; Jackson *et al.*, 2018). An extension of the present model to fault zones with significant capillary heterogeneity therefore remains an outstanding and important question in predicting the flux through such systems.

Another potential refinement to the model is that the fault zone will have a capillary entry pressure that needs to be overcome before leakage can occur and so the underlying current may have to build up to a large thickness before breakthrough can occur. It is also possible that the CO_2 will be constrained to more localised flow paths with lower entry pressures which, depending on the entry pressure and permeability of the fault and intervening reservoirs, may affect the vertical migration of CO_2. These may be simply accommodated by the addition of a critical height the gravity current must overcome to achieve breakthrough in the fault (Sayag & Neufeld, 2016; Woods & Farcas, 2009).

The present gravity current model also assumes that the aquifer is unconfined ($h \ll H$). This means that there is negligible flow of the ambient fluid and so fluid propagation is independent of the viscosity ratio between the fluids (Huppert & Woods, 1995; Vella & Huppert, 2006). Pegler *et al.* (2014a) showed that background pressure-driven flow due to confinement starts to play a role when ratio of the current depth and aquifer depth (h/H) is comparable to the viscosity ratio of the injected and ambient fluid. In the case of CO_2 and water, the viscosity ratio $\mu_{CO_2}/\mu_w \simeq 0.1$, hence the assumption that the size of the reservoir

is much larger than the thickness of the current is valid for currents up to ∼10% of the height of the aquifer, as is the case at many CO_2 storage sites. As the experiments performed in this chapter were between fluids of near equal viscosity, the thickness of the currents across all experiments are well within the limit for the unconfined approximation. For cases in which $h_{CO_2} \simeq 0.1H$, Pegler *et al.* (2014b) found that confinement causes greater leakage at earlier times due to the introduction of background pressure, but at later times, as the CO_2 fills the entire depth of the aquifer, the maximum hydrostatic head below the fracture is limited and hence the leakage rate is also limited. Incorporating the effects of confinement on the gravity current would be an interesting additional extension of the present work.

There are other important fluid dynamical processes which stabilise the storage of CO_2, including for example the dissolution of CO_2 into the brine. Dissolution depends on the relative flows of CO_2 and brine over the small (e.g. centimetre) length scales related to CO_2 diffusion, presenting significant modelling challenges. However, the mixing of CO_2 and brine within the rising plumes and fault zone is likely to enhance dissolution of the CO_2 (c.f. Kampman *et al.*, 2014).

Constraining the hydraulic properties of fault zones in the field remains a much studied area with many different factors affecting the flow of fluids, such as the host rock composition (Wibberley & Shimamoto, 2003), fracture density (Mitchell & Faulkner, 2012) and fracture connectivity (Sævik & Nixon, 2017) and their contribution towards the overall permeability. The model presented in this chapter constrains the sensitivity of CO_2 leakage rates to bulk fault properties such as permeability, width and thickness. By observing the resultant plume behaviour around complex fault zones, this simplified model could be used to provide an estimate of these bulk properties. When applied in a suitable geological context, the model presented here can be used to characterise the flow dynamics of fault zones.

3.8 Summary and conclusions

I have presented an analytical model that describes the dynamics of leakage through a fault zone, motivated by the potential risk to storage security of anthropogenic CO_2. It comprises a two-dimensional gravity current in a porous medium, fed by a buoyant plume and spreading

under a horizontal impermeable baffle. The medium is bounded by an impermeable vertical boundary and the horizontal baffle contains a fault through which the current is leaking. This system constitutes a reduced order model of a faulted caprock, whereby an impermeable fault core is surrounded by a high permeability fracture zone (Wibberley *et al.*, 2008) through which leakage occurs.

I have thoroughly tested this model of flow and fault leakage using analogue laboratory experiments in which the evolution of the plume, gravity current and leakage could be continuously measured. During these experiments, I observed thinning of the secondary plume above the fault due to an increase in Darcy velocity, leading to increased pressure gradients across the fault. A new model for leakage through the fault was derived, including this effect. In contrast to previous analytical fault models which use numerical solvers to verify their models (Kang *et al.*, 2014), I matched results using a series of analogous porous media tank experiments, which supported the dependence of the fault width, fault height, input flux and input density on leakage rates as derived by the model. Crucially, this analysis showed how these parameters control the ratio of fluid flux into the aquifer compared to fluid leaking through the fault, which is significant for storage efficiency.

I demonstrated the utility of the model for assessment of storage security of anthropogenic CO_2 by application to a naturally occurring CO_2-charged aquifer at Green River, Utah, using an extension of the model to calculate the fluid distribution and leakage rates across multiple vertically stacked aquifers, cross-cut by a fault. This showed the dependence of leakage rates on the fault/aquifer permeability contrast, with significant leakage occurring when the fault permeability is larger than the reservoir permeability. A detailed discussion of the limitations of the model in application to CO_2-water systems was provided in Section 3.7.

It is important to note that while other trapping mechanisms such as dissolution trapping, residual trapping and mineral trapping are important in CO_2 storage, they occur on longer timescales and so structural trapping remains the principal mechanism for storage of CO_2. Understanding to what extent faults within caprocks can act as potential leakage pathways is crucial for ensuring safe storage of CO_2.

The chapter is adapted from Gilmore, K. A., Sahu, C. K., Benham, G. P., Neufeld, J.

A., and Bickle, M. J., (2022), Leakage dynamics of fault zones: experimental and analytical study with application to CO_2 storage, *Journal of Fluid Mechanics*, Vol. 931, A31, doi.org/10.1017/jfm.2021.970

Chapter 4

The Otway Project

4.1 Introduction

The Otway Project is a pilot scale CO_2 sequestration project, located in the onshore Otway Basin in Victoria, Australia (Figure 4.1). The project demonstrates multiple stages of the carbon capture and storage (CCS) workflow, namely CO_2 extraction from a natural reservoir, processing and compression of the CO_2 into a supercritical state and injection of CO_2 into a sub-surface storage reservoir where it can be remotely monitored (Cook, 2014). There have been various phases of the Otway Project which have investigated different methods of storage (see Table 4.1).

Stage 1 took place between March 2008 and August 2009, with the aim of demonstrating safe capture, transport and storage of CO_2 at the Otway site (Jenkins *et al.*, 2012). 65,445 tonnes of CO_2-rich gas, composed of 75% CO_2, 21% CH_4 and 4% heavier hydrocarbons, was extracted from the nearby Buttress gas field and injected into the Waarre sandstone reservoir, an old gas field depleted by Santos between 2002-2003 (Boreham *et al.*, 2011). Stage 2 of the

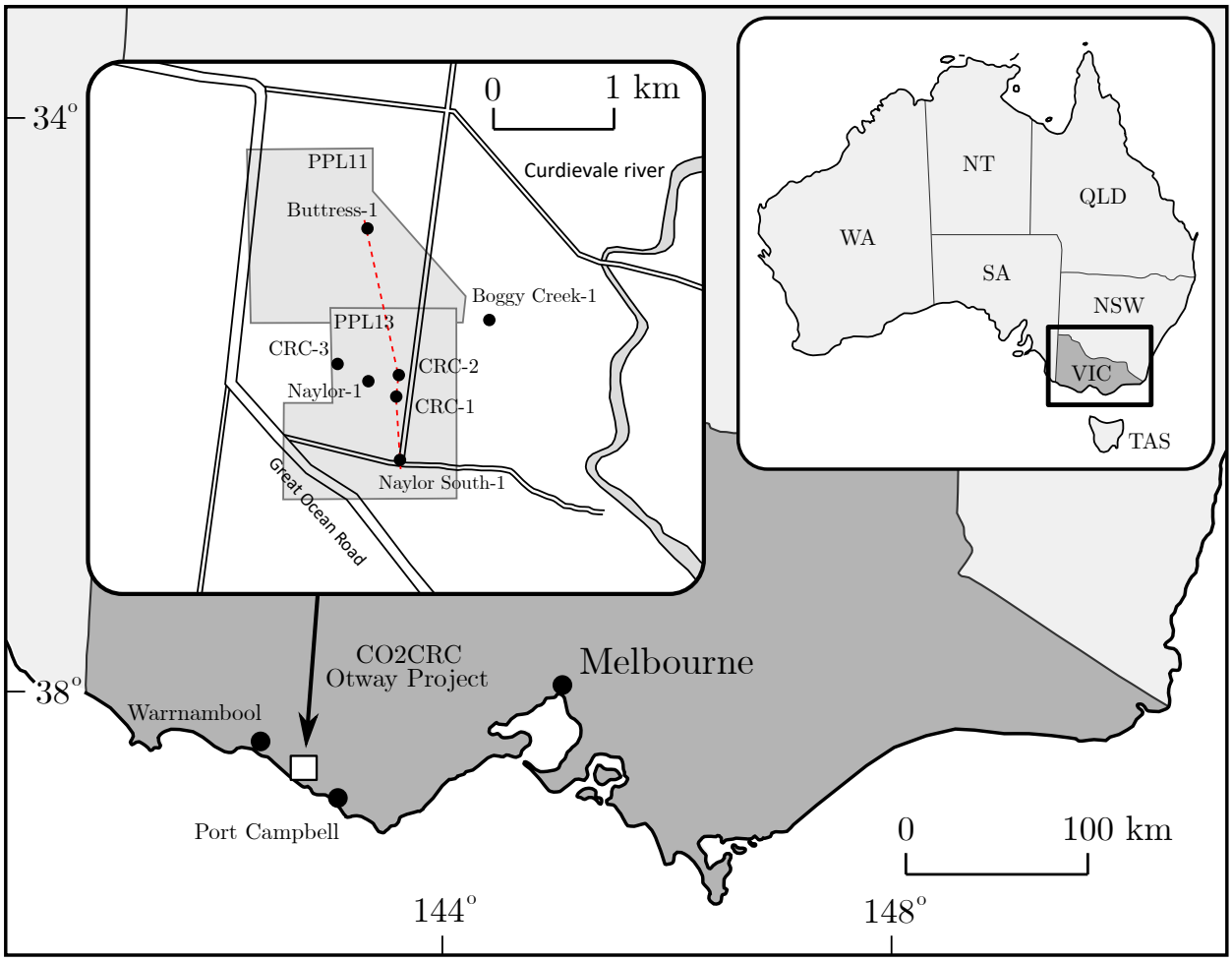

Figure 4.1: Location map of the CO2CRC Otway Project showing positions of the major wells. Red line gives the position of the cross-section in Figure 4.2. Figure adapted from Boreham *et al.* (2011).

project was divided into four phases: Stage 2A which finished in Februrary 2010, Stage 2B which took place between June and September 2011, Stage 2B extension in 2014 and Stage 2C which took place between 2014-2018. The primary aim of Stage 2A was to characterise the Paaratte Formation, the storage formation for Stage 2. A new injection well, CRC-2, was drilled and cased, and stratigraphic logs, core samples and wireline data were acquired. The aim of Stage 2B was to quantify the residual and solubility trapping of CO_2 in a saline formation in the absence of a structural seal (Paterson *et al.*, 2013). 150 tonnes of pure CO_2 was injected followed by 454 tonnes of water to drive the CO_2 to residual saturation. A series of tests including a pulsed neutron log (RST), noble gas tracer partitioning (LaForce *et al.*, 2014), reactive ester tracer partitioning (Myers *et al.*, 2015), dissolution testing (Haese *et al.*, 2013), and thermal logging (Zhang *et al.*, 2011) were conducted to measure the residual saturation of the reservoir. The Stage 2B extension consisted of an injection of water spiked with methanol, Kr and Xe, followed by an injection of 110 t of CO_2 which was driven to residual saturation by a further injection of CO_2-saturated water, with the aim of measuring the residual saturation of the reservoir (Ennis-King *et al.*, 2017a; Serno *et al.*, 2016). Stage 2C, which is the focus of this chapter, involved the injection of 15,000 tonnes of CO_2-rich gas into a saline aquifer accompanied by time-lapse seismic monitoring (Watson *et al.*, 2018). Stage 3 took place between March 2020 and May 2021, with a total injection volume and target formation identical to Stage 2C, but the injection well, CRC-3, situated ∼600 m down dip from CRC-2 (Jenkins *et al.*, 2018). The seismic monitoring program focused on development of an automated continuous downhole monitoring system using five wells instrumented with fibre-optic sensing cables and nine permanently deployed surface orbital vibrators (SOVs). Continuous time-lapse vertical seismic profile (VSP) were acquired giving plume evolution in near-real-time (Pevzner *et al.*, 2021).

The rest of this chapter focuses on Stage 2C of the Otway Project. I review the geology of the storage reservoir and the acquisition and processing of the seismic reflection data. The geometry of the reservoir and the amplitude anomaly associated with the CO_2 plume are interpreted from the seismic data. Amplitude difference measurements, seismic waveform modelling and CO_2 saturation logs are used to constrain the thickness of the CO_2 plume. Measured CO_2 plume distributions are required for comparison against numerical simulations performed in Chapter 5.

The Otway Project	
Stage 1	Injection of 65,445 t of CO_2-rich gas into the Waarre Formation at the CRC-1 well and related monitoring (complete)
Stage 2A	Drilling of new injection well CRC-2 into the Paaratte Formation and site characterisation (complete)
Stage 2B	Injection of 140 t of pure CO_2 into the Waarre Formation and determination of residual saturation (complete)
Stage 2B Ext.	Injection of 110 t of pure CO_2 and geochemical tracers to estimate residual CO_2 saturation (complete)
Stage 2C	Injection of 15,000 t of CO_2-rich gas into the Paaratte formation with related seismic monitoring (complete)
Stage 3	15,000 t of CO_2-rich gas into the Paaratte formation with continuous seismic monitoring (complete)

Table 4.1: Various phases of the Otway Project (Cook, 2014; Pevzner *et al.*, 2021)

4.2 Reservoir Geology and Conditions

4.2.1 Geological History

The location of the Stage 2C injection was the Paaratte Formation, located in the eastern side of the Port Campbell Embayment within the Otway basin (Dance *et al.*, 2012). The area is associated with the eastern Gondwanan and Tasman breakup along the Australian Southern Margin (Woollands & Wong, 2001). The Paaratte Formation lies in the Cretaceous Sherbrook Group and is Campanian to Maastrichtian in age (Partridge, 2001). It was deposited during a stage of rifting in the Otway Basin, with the extension resulting in NW-SE trending normal faults, downthrown to the south (Krassay *et al.*, 2004) which form a series of large fault bounded half grabens (Hill & Durrand, 1993).

4.2.2 The Paaratte Formation

The Paaratte Formation is subdivided into three units by correlating palynology to global eustatic cycles (Partridge, 2011). These are Unit A, Unit B and Unit C with Unit A stratigraphically lowest in the formation (Figure 4.2). Unit A was selected as the injection location for Stage 2C as the other two units are juxtaposed against the Timboon Sandstone aquifer

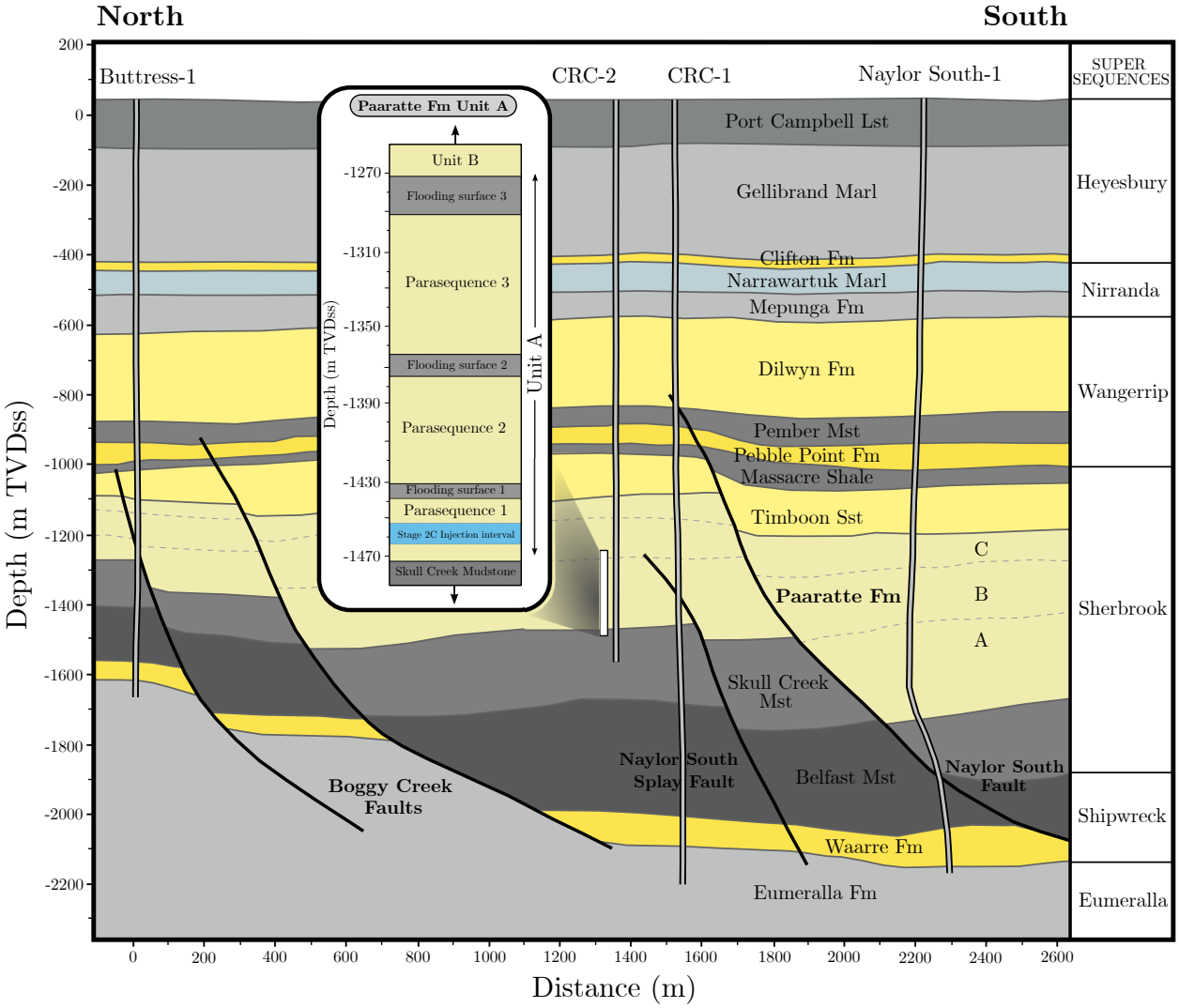

Figure 4.2: Geological cross-section through the Otway site from north to south showing stratigraphic units and major faults (see red-dashed line on Figure 4.1 for location of cross-section). Inset shows the stratigraphy for Unit A of the Paaratte Formation at a greater resolution, including the injection interval for the Stage 2C injection. Figure adapted from Dance *et al.* (2012) and Glubokovskikh *et al.* (2016).

by the nearby Naylor South fault, which may present a contamination risk (Watson *et al.*, 2012). Within Unit A there are several higher order parasequences that define reservoirs and seals (see Figure 4.2 inset). The parasquences are correlated across the Paaratte Formation using a combination of well cores and logs, seismic horizons and neutron/density and micro-resistivity measurements from down-well probes (Dance *et al.*, 2012). The parasequences are known as PS1, PS2 and PS3, with PS1 stratigraphically lowest in the unit, and the target for the Stage 2C injection.

PS1 and PS2 comprise deltaic sediments occurring as clay rich distal mouth bars grading

to more sand rich proximal mouth bars and distributary channels. The distal mouth bars are a mixed lithology with some poor reservoir rocks. In contrast, the proximal mouthbars and distributary channels are high quality sandstones with large porosity (∼25-30%) and permeability (1-2 Darcy) (Dance *et al.*, 2019). The surfaces between parasequences, known as flooding surfaces, are defined by extensive mudstone seals deposited in a shallow marine delta front setting. Delta front facies have low average porosity (<15%) and permeability (<10 mD) and high capillary entry pressures with the potential to act as a seal for a CO_2 plume several tens of metres thick (Daniel, 2012). PS3 has similar deltaic deposits towards the base, but more estuarine deposits (channels and heterolithic sands) towards the top. The top of PS3, also the top of Unit A, is coincident with a major flooding surface comprising a moderately mudstone layer of 20-25 m thickness (Dance *et al.*, 2012). Overprinting the system are numerous calcite and dolomite cemented layers or nodules, formed by post-depositional precipitation from meteoric fluids at depth (Dutton *et al.*, 2000). They have very low porosity and permeability and are clearly identifiable in core samples. Their lateral extent remains an uncertainty, but similar facies within the extensively mapped Frontier Formation of central Wyoming, USA, which reflects a paleo-environmental system most applicable to the Paaratte Formation, suggests that the cemented horizons are likely to be discrete stringers on the order 40-200 m and hence more likely to act as baffles (Dance *et al.*, 2019; Dutton *et al.*, 2002; Willis *et al.*, 1999).

Well data

There are a number of wells in the study area from which various forms of data have been collected. CRC-1, CRC-2, Naylor-1 and Boggy Creek-1 form a natural grouping of wells because they sit within the same NW-SE orientated fault block. Naylor South-1 lies is located on the down thrown side of the main Naylor South fault and shows significant thickening of the Paaratte Formation. Buttress-1 is located in an up-thrown fault block to the north and shows thinning of the formation (Watson *et al.*, 2012). For the Stage 2C injection, CRC-2 is the injection well and CRC-1, which lies ∼170 m to the south, is used to directly monitor the CO_2 plume. The other wells are further afield and not involved in the Stage 2C injection.

Core and well log data were obtained for the CRC-1 and CRC-2 wells. For CRC-2, a total 176.1 m of core was recovered encountering a range of lithologies including shales from the seal intervals and heterogeneous claystones, siltstones, sandstones and gravels (Dance, 2010; Lawrence *et al.*, 2012). Immediately after drilling, wire-line logs were run in CRC-2 to determine clay volume fraction, porosity, permeability, detailed lithology, structural dip, cumulative thickness, minimum and maximum horizontal stress directions and fracture identification (Lawrence *et al.*, 2013). Pressure testing was also conducted using a modular formation dynamics test (MDT) tool to obtain a complete vertical pressure-depth profile along the CRC-2 well section (Bunch *et al.*, 2012; Dance *et al.*, 2012). No conventional well logging tool can be used to directly measure permeability. However, nuclear magnetic resonance (NMR) logging data in conjunction with permeability models can be used to predict permeability. A commonly used model is the Timur-Coates model (Coates *et al.*, 1999), which has the form,

$$k = \left(\frac{\phi}{C}\right)^m \left(\frac{1 - S_{wi}}{S_{wi}}\right)^n, \tag{4.1}$$

where S_{wi} is the irreducible water saturation and C, m and n are model parameters which can be derived statistically from lab NMR experiments on core samples. The permeability profile obtained correlates well with the wire-line log results and permeameter measurements of core slab faces and core plugs (Dance *et al.*, 2012).

Gamma ray, clay volume fraction, porosity and permeability logs of CRC-2 have been plotted over a depth interval centered around the injection location (Figure 4.3). In general, the Skull Creek Mudstone and FS1 (the mudstone seal marking the top of PS1), have a lower porosity and permeability and a higher clay volume fractions than PS1 and PS2. The cemented layers which overprint the system are characterised by very low porosities and permeabilites.

4.2.3 Regional faulting

There are several NW-SE trending normal faults associated with late Cretaceous extension that bound the injection zone. The major faults cut through the entire Paaratte Formation and tend to die out before the top of the Sherbrook group (Dance *et al.*, 2019). The Naylor South fault is a major fault to the south of the injection zone with a throw of up to 190

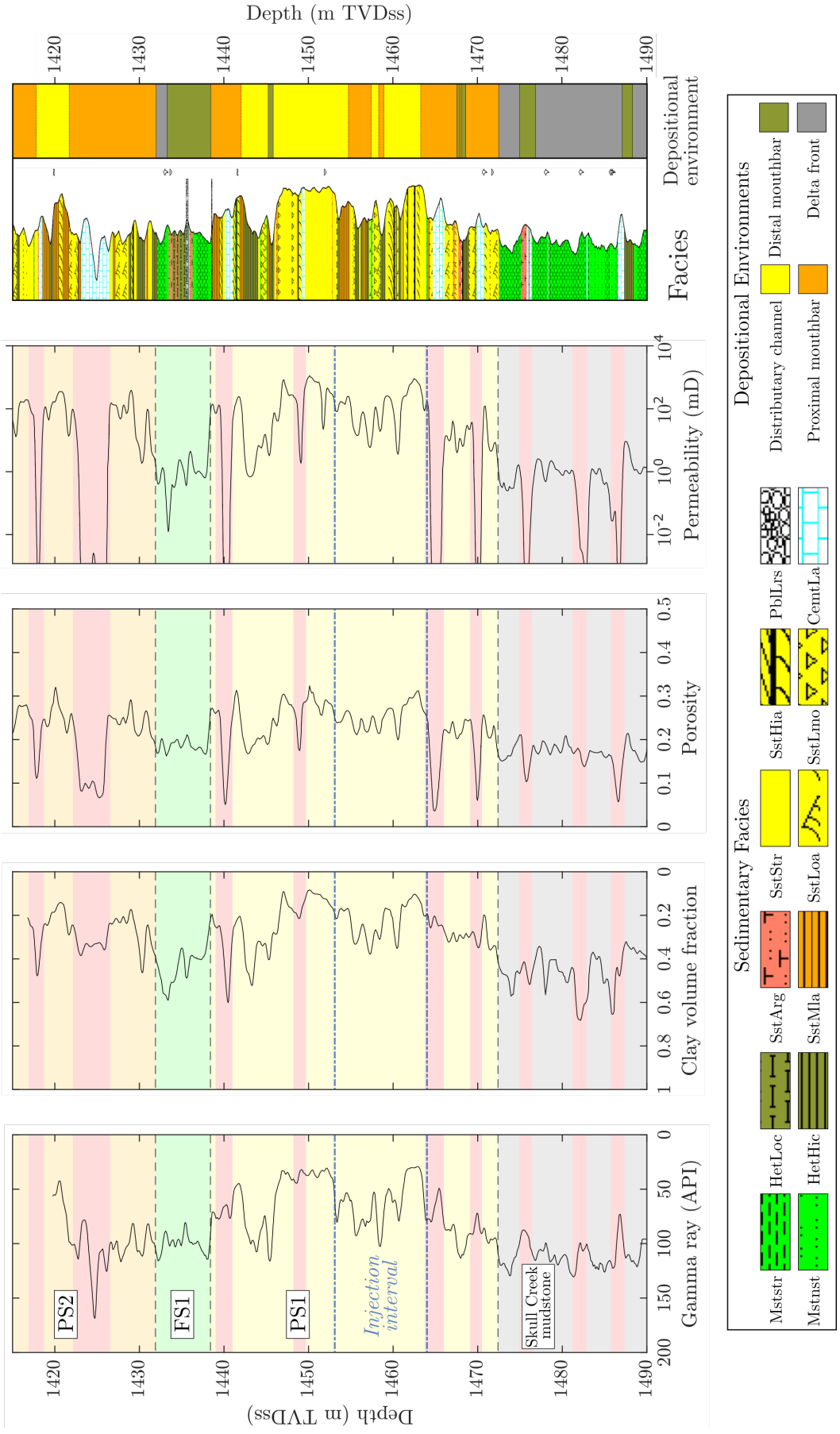

Figure 4.3: Gamma ray, clay volume fraction, porosity, permeability and facies logs for the CRC-2 well. The Skull Creek Mudstone and FS1 (the mudstone seal at the top of PS1), are characterised by higher clay volume fractions and have lower porosity and permeability. Dolomitic stringers overprinting the system (shaded red) have very low porosity and permeability. Facies and depositional environment schematics adapted from Lawrence *et al.* (2012).

m. The vertical extent of the fault and the fault throw increases from west to east. The Naylor South splay fault, several hundred metres north of the main Naylor South fault, exists parallel to the main fault and is approximately 1500 m long with a maximum offset at the Paaratte level of 15-30 m. It is of particular interest for the Stage 2C injection due to its proximity to the injection region and its potential to effect plume migration. The splay fault appears to die out before the top of the Paaratte Formation, which implies that any flow up the fault plane would result in CO_2 entering an upper layer of the formation and still remain contained (Tenthorey *et al.*, 2014). However, it is still important to assess to what extent the fault may act as a barrier or conduit to flow.

Tenthorey *et al.* (2014) investigated likelihood of fault reactivation due to CO_2 injection as well as the across-fault and fault-parallel flow potential of the Naylor South splay fault. Due to the small injection pressures associated with injection (Ennis-King *et al.*, 2017b), fault reactivation is very unlikely. The shale gouge ratio algorithm, which estimates the proportion of shale or clay that might be entrained in the fault zone, was used to quantify the across-fault flow potential of the splay fault and it was found that the fault should be sealing and restrict lateral movement of CO_2. Fault-parallel permeabilities are harder to assess, with many factors such as rock type, fracture size/density and local stress fields affecting the flow potential up the fault. Tenthorey *et al.* (2014) used empirical relationships of permeability anisotropy to convert estimates of across-fault permeability into an estimate for vertical permeability (Antonellini & Aydin, 1994; Arch & Maltman, 1990; Faulkner & Rutter, 1998; Zhang *et al.*, 2001). These studies find that in general vertical permeability is 1-2 orders of magnitude greater than across-fault permeabilities due to preferential orientation of clay minerals and deformation band effects. Dynamic simulations of high fault permeability scenarios were performed and it was found that CO_2 migrates 10s of metres vertically after 100 years which is still more than 350 m below the top of the Paaratte Formation.

4.2.4 Hydrodynamic properties of the reservoir

The Paaratte Formation is an extensive, regionally confined aquifer with flow paths that are not well characterised. (Dance *et al.*, 2012) speculates that flow rates within the formation are not sufficient to impact the Stage 2C test, based on regional flow paths from the overlying

Upper Cretaceous aquifer (Bush, 2009). The best estimates for the salinity of the Paaratte Formation in the injection region are from 1000-2000 mg/L total dissolved solids (TDS) (Dance *et al.*, 2012). A modular formation dynamics test (MDT) tool was run in CRC-1 and CRC-2 to measure the formation temperature and recorded a maximum temperature gradient of 0.02°C m^{-1}, which gives a temperature of 62.4±0.5°C in the injection interval. The MDT tool also gives formation pressure measurements with depth, with a pressure of 14.5±0.1 MPa in the injection interval (Dance *et al.*, 2012; Pevzner *et al.*, 2017).

4.3 Previous Geophysical Interpretation of the Paaratte Formation

Several horizons within the Paaratte Formation have been interpreted using a variety of different datasets. Initial interpretation used regional 3D surveys extending over a total area of 83.5 km^2, which have a 24 fold resolution (number of receivers that record a given data point) to a depth of 4 seconds with a bin size of 20 m. Supplementing the regional survey is a reprocessed 2000 survey, repeated CO2CRC baseline and monitoring surveys acquired in 2008, 2009 and 2010 and 3D vertical seismic profile (VSP) data which provides greater detail directly over the study area (Dance *et al.*, 2012) (see Figure 4.8b,d).

A series of studies have also interpreted data from the Stage 2C baseline and time-lapse seismic reflection and VSP surveys. For the seismic reflection dataset processed using the fast-track pre-stack time migration workflow, clear reflections are seen at ∼1200 ms TWTT or ∼1450 m TVDss in the seismic difference cubes (difference between a given time-lapse seismic cube and the baseline seismic cube). Root-mean-square (RMS) amplitudes computed within a 24-ms time window corresponding to the injection interval show a clear anomaly localised around the injection well CRC-2, with amplitudes that are much stronger (6-8 times) than away from this location (Pevzner *et al.*, 2017, 2020).

A seismic inversion workflow which assimilated borehole measurements and geological models was used to convert the pre-stack time migration time-lapse seismic difference to relative change in acoustic impedance (Glubokovskikh *et al.*, 2016, 2018, 2020), which is an analogue for rock stiffness. Post-injection analysis of this dataset by Dance *et al.* (2019) showed that the impedance anomaly associated with the CO_2 plume preferentially extends along the main

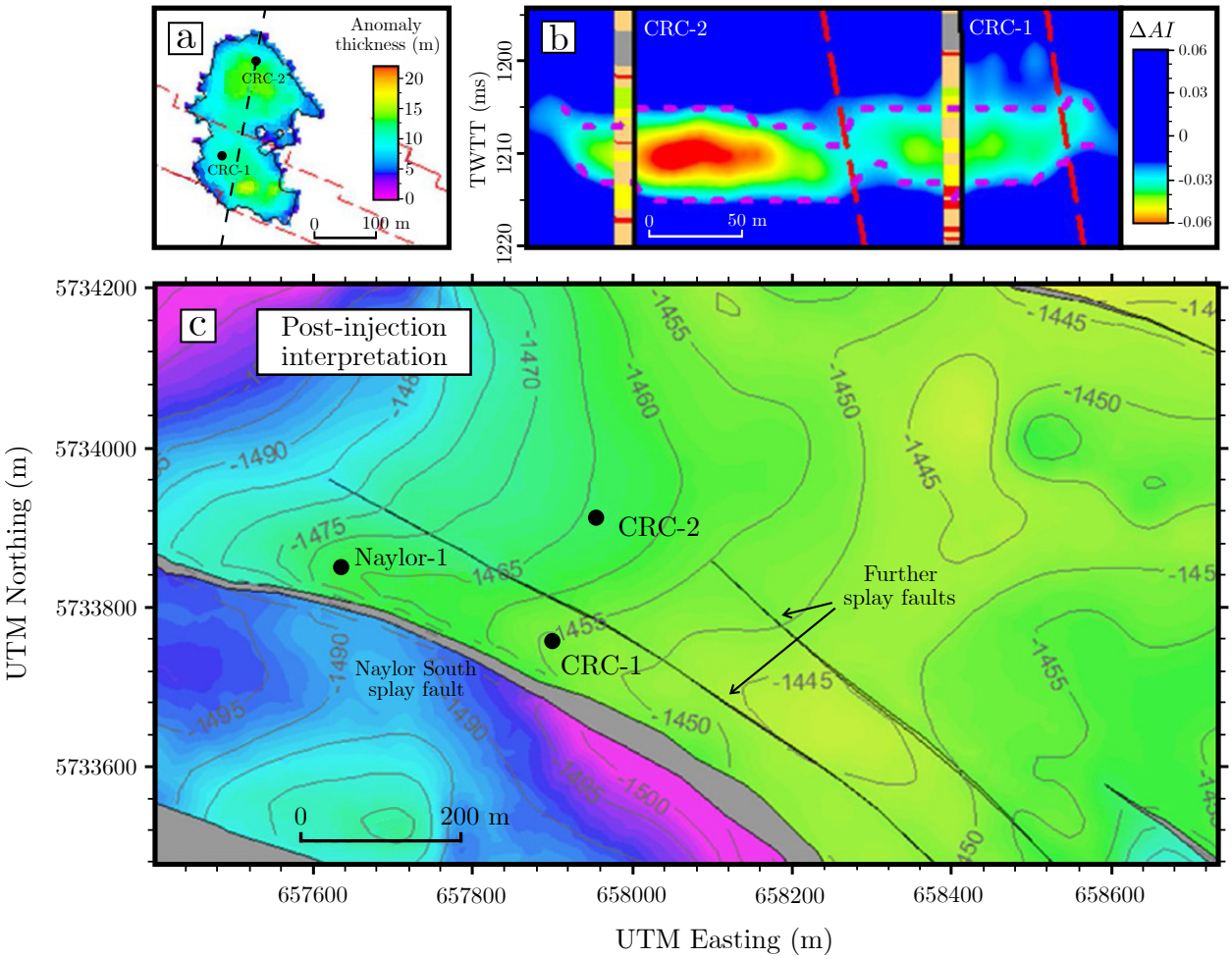

Figure 4.4: (a) Thickness of acoustic impedance ΔAI anomaly post injection of 5kt CO_2 (TL seismic 1). (b) Cross section of acoustic impedance anomaly showing bifurcation, interpreted as due to additional splay faults (red dashed lines). (c) Updated topography map of the injection interval in PS1 with new splay faults. Figures adapted from (Dance *et al.*, 2019).

splay fault which indicates a high permeability zone either caused by a high permeability fracture zone or a high permeability facies parallel to the fault. There is also a bifurcation of the anomaly within the reservoir which Dance *et al.* (2019) interpreted as an additional small minor fault running parallel with the the main splay fault and bisecting the CRC-1 and CRC-2 wells (Figure 4.4a,b). An updated topography map of the top of the Stage 2C injection interval in PS1 as interpreted by (Dance *et al.*, 2019) is shown in Figure 4.4c.

Initial interpretation of the post-stack time migration Stage 2C seismic reflection dataset by (Popik *et al.*, 2020), shows similar plume distributions in the seismic difference cubes, and similar RMS amplitude anomalies around the injection interval as with the pre-stack time migration data. The vertical seismic profile (VSP) difference data also shows a comparable

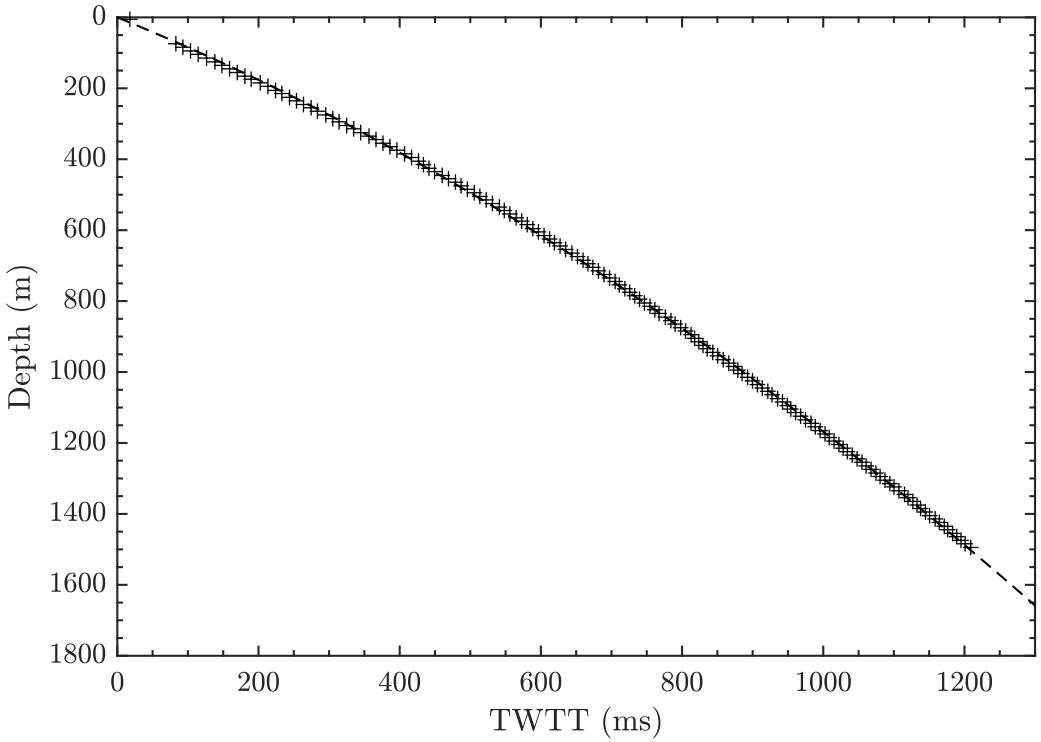

Figure 4.5: Time to depth conversion using VSP data from CRC-1 and CRC-2. Figure adapted from Dance *et al.* (2012).

TL signal and RMS maps around the plume, although it has lower coverage and lower fold than the surface seismic data (AlNasser *et al.*, 2017; Pevzner *et al.*, 2020).

The VSP data available in the Naylor-1, CRC-1, CRC-2 and Boggy Creek-1 wells allows time to depth domain conversion via well to seismic ties. Given the wells are vertical, a velocity model was created by Dance *et al.* (2012) assuming a linear velocity function in each layer. The model was built layer by layer (known as a layer cake model), with well corrections performed after each layer. The resultant two-way travel time (TWTT) to depth relationship for the CRC-1 and CRC-2 wells is shown in Figure 4.5. The TWTT-depth relationships for the Boggy Creek-1 and Naylor-1 wells show very similar results, which suggests that there is not significant lateral velocity variations across the fault block (Dance *et al.*, 2012).

4.4 Time-lapse seismic reflection surveys

A total of 15,006 tonnes of CO_2-rich gas was injected into CRC-2 at an average rate of 120 tonnes a day over the period from 2nd December 2015 to the 4th April 2016 (Figure 5.7). The gas was injected into PS1, Unit A of the Paaratte Formation, over a perforated interval between 1453.1 m and 1464 m TVDss (metres below mean sea level). The injected fluid is a supercritical CO_2-rich gas mixture extracted from the nearby Buttress reservoir with fluid composition 78.7% CO_2, 18.9% CH_4, 1.38% N_2 and 1.04% C_5+ by molar percentage (Watson *et al.*, 2018).

A baseline seismic survey and five subsequent time-lapse surveys were undertaken in the Stage 2C test. The baseline survey took place in March 2015, with injection commencing in December 2015. Two of the time-lapse surveys were undertaken during injection, after 5,000 tonnes and 10,000 tonnes of CO_2 had been injected respectively and the third survey was undertaken at the end of injection, after 15,000 tonnes had been injected. Two surveys more were undertaken one year and two years after the end of injection. The purpose of the time-lapse surveys was to monitor the movement and stabilisation of the CO_2 plume. The acquisition and processing workflows of the seismic data was kept as uniform between surveys as possible to allow for direct comparison between them.

4.4.1 Receiver array

A total of 908 5-Hz seismic sensors were divided between eleven receiver lines ∼100 m apart, with the sensors spacer at 15 m intervals along each line (Pevzner *et al.*, 2015). The geophones were buried at 4 m depth in the ground to reduce ambient noise and variability in geophone coupling with the ground (Shulakova *et al.*, 2015).

4.4.2 Acquisition

For the seismic source, two Inova 26,000 lb vibroseis units were used, operating in flip-flop mode to increase efficiency. The vibroseis units were moved around obtaining a total of 3003

source points grouped into 27 lines. Sources were spaced at 15 m intervals along the line and lines were spaced 50-100 m apart. A single 24 second 6-150 Hz sweep with 0.5 second cosine tapers and 5 second listening time was used on every shot point (Pevzner *et al.*, 2017).

4.4.3 Processing

Two methods have been used to process the seismic dataset, differing in their seismic migration process. The first approach produces plume images quickly, using a post-stack time migration (Pevzner *et al.*, 2017) whereas the second approach is more time-consuming but results in a more detailed characterisation of the plume's lateral and vertical extent and increases image quality around fault zones through use of a pre-stack time migration (Popik *et al.*, 2020). The second approach was used to process the seismic data analysed in this chapter and is detailed here.

Identical processing workflows were used across all vintages to allow direct comparison between seismic surveys, with the aim to suppress surface waves, shorten the source wavelet, stack the data in a common midpoint domain and apply post-stack denoising. The main addition to the this approach was the inclusion of a pre-stack Kirchhoff time migration (Popik *et al.*, 2020). Seismic migration is carried out to move the reflective surface back to its actual position and angle. In pre-stack time migration, the migration is applied before the stacking process, which provides better results especially when imaging complex structures such as fault zones (Popik *et al.*, 2018). The velocity model obtained from the baseline survey was used to pre-stack migrate all time-lapse surveys. Small time shifts may exist between seismic volumes due to subtle changes in the shallow sub-surface, for example due to changes in ground water level. To account for this, all time-lapse vintages were shifted to match the baseline vintage using a post-migration time-shift, based on cross-correlation in a 400-1170 ms window above the plume position. Time-shifts were between -0.5 ms and 0.5 ms. Further details of the processing workflow are given in Table 4.2.

Processing stages	Procedures
Data Input and geomotry assignment	SEG-D data input; Correlation with sweep signal; Geometry assignment; Binning;
Velocity analysis and statics	Velocity analysis; Elevation statics
Noise attenuation	Time-frequency domain noise attenuation; Ground roll removal
Deconvolution	Surface-consistent spiking deconvolution
Residual static corrections	Surface-consistent MaxPower autostatics
Migration	Pre-stack Kirchhoff Time Migration
Post-migration processing	FK-filtering; Stacking; FK-filtering; FXY-deconvolution

Table 4.2: Seismic processing workflow (Popik *et al.*, 2020).

4.5 Interpretation of Pre-injection Survey

Seismic reflections surveys measure the reflectivity between layers in the sub-surface as a function of two-way travel time (TWTT). TWTT is the time it takes for a seismic wave to travel from the source to the receiver, via a reflection at a sub-surface boundary. To convert from TWTT to depth requires the velocity structure of the sub-surface to be known, which can be determined from seismic processing velocities, sonic logs from well data or checkshot and VSP surveys (Francis, 2018). The latter was used to create a velocity model for the Otway site (Figure 4.5).

If a seismic wave crosses a boundary at a normal incidence, the reflectivity R at the boundary is a function of the change in impedance,

$$R = \frac{I_2 - I_1}{I_2 + I_1} = \frac{\rho_2 v_2 - \rho_1 v_1}{\rho_2 v_2 + \rho_1 v_1}, \tag{4.2}$$

where I_i is the impedance of the upper ($i = 1$) or lower ($i = 2$) layer, which is a product of the overall density ρ_i and seismic velocity v_i of the layers. The larger the impedance contrast at a boundary, the greater the amplitude of the reflected wavelet and hence the brighter the reflection on the seismic reflection survey. A reduction in impedance across a boundary (e.g. at the upper boundary of a CO_2-saturated layer), results in a negative polarity reflection which is coloured blue on the seismic reflection images. An increase in impedance across a boundary (e.g. at the lower boundary of a CO_2-saturated layer), results in a positive

polarity which is coloured red in the seismic reflection images. Reflection amplitudes are extracted from the seismic reflection surveys using Schlumberger's seismic interpretation software Petrel, which tracks the depth and lateral extent of the peak amplitude of the reflected wavelets.

Seismic reflection surveys highlight boundaries between contrasting layers within the subsurface, hence provide a good estimate of the geological structure and geometry of the reservoir. This is important as the geometry of low permeability horizons such as the mudstone seals will play an important role in governing the migration of CO_2 throughout the reservoir. In this section, I present a geological interpretation of the baseline survey and the topographic structure of horizons proximal to the Stage 2C injection.

4.5.1 Geological Interpretation

Four different cross-sections of the baseline pre-injection seismic survey are shown in Figure 4.7, along with their geological interpretations. The location of each of the seismic lines is shown in Figure 4.6.

Figure 4.7 shows the three main units within the Paaratte Formation (Units A, B and C), with Unit A further subdivided into the three parasequences, PS1, PS2 and PS3, which are separated by mudstone seals, FS1, FS2 and FS3. Further geological formations above and below the Paaratte Formation are also shown. In general, the units are shallowly dipping towards the Northwest, and there is a topographic high ∼400 m east of the CRC-2 injection well. The seismic reflection images show many regularly spaced high amplitude reflections, especially within the Paaratte Formation, which suggests a high level of heterogeneity within the formation. Some of these layers are not continuous, either due to termination at faults or thinning out, and cannot be traced across the area.

The Naylor South fault and Naylor South splay fault can be clearly seen, with ∼100 m and ∼40 m of average offset seen respectively. The Naylor South fault cuts through the entire Paaratte Formation and dies out around the base of the Dilwyn Formation. The splay fault dies out towards the top of Unit A in the Paaratte Formation. Units appear to be thicker on the downthrown side of the main fault. Towards the edges of the seismic lines,

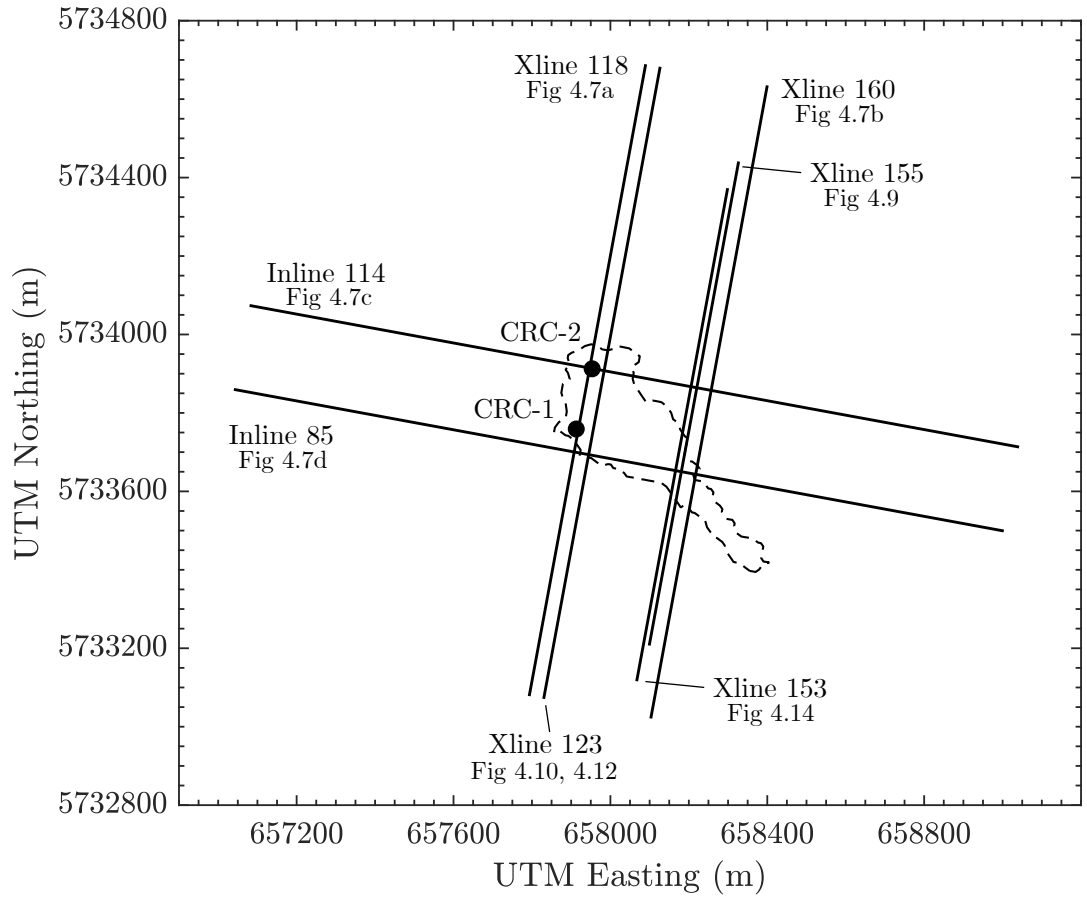

Figure 4.6: Location of seismic lines. Dashed line = extent of plume from TL5 survey.

horizons appear to curve upwards rapidly. This is a seismic processing artifact known as overmigration (Zhu *et al.*, 1998) which is caused by inaccurate velocity estimates due to the reduced seismic data coverage in these areas.

The mudstone layer FS1 at the top of PS1 appears to be of a similar thickness to PS1, even though the CRC-2 well log data (Figure 4.3) suggests that FS1 is ∼8 m thick whereas PS1 is ∼30 m thick. This highlights a resolution issue with the seismic reflection images. The frequency of the seismic waves determine the minimum vertical thickness of a layer that can be resolved in the seismic data. In general, it is possible to detect a layer down to 1/32 wavelength, where the wavelength $\lambda = v/f$, where v is the seismic velocity and f is the frequency of the seismic wave. However, for layers of thickness less than 1/4 wavelength, interference between the reflections at the top and bottom of the layer mean that the thickness of the layer cannot be resolved from seismic reflection images. In these cases, the distance between the top and bottom reflections will remain at a $\lambda/4$, even though the layer thickness is less. Evaluating $\lambda/4$ for the Paaratte Formation using $v = 3195\,\mathrm{m\,s^{-1}}$ and $f = 40\,\mathrm{Hz}$, gives a vertical resolution of 20 m, which is approximately half the thickness of PS1, hence could explain why FS1 appears a similar thickness to PS1.

Synthetic waveform modelling presented in Section 4.7.4 suggests that some of the seismic reflections may be picking out the cemented layers within the Paaratte Formation, rather than the mudstone seals. There is evidence to suggest that some of the sealing layers appear to pinch out in the seismic images (e.g. FS1 in Figure 4.7a). However, most of these cemented layers are on the order ∼1 m thick, which is below the seismic detection threshold, and are not laterally extensive, in contrast to the seismic reflections picked out (e.g. FS1) which have lateral extents on the order of kms (Figure 4.8a, FS1 horizon).

Figure 4.7: Baseline seismic reflection survey (overleaf) (a)-(d) show different seismic lines across the Otway site, the locations of which are shown in Figure 4.6. Top: seismic reflection images, red/blue reflections correspond to positive/negative amplitudes respectively. Bottom: Interpreted images, showing major faults, formations and wells. DF (orange) = Dilwyn Formation; PM (green) = Pember Mudstone; PPF (yellow) = Pebble Point Formation; MS (green) = Massacre Shale; TS (Orange) = Timboon Sandstone; PF (yellow) = Paaratte Formation; SKM (green) = Skull Creek Mudstone.

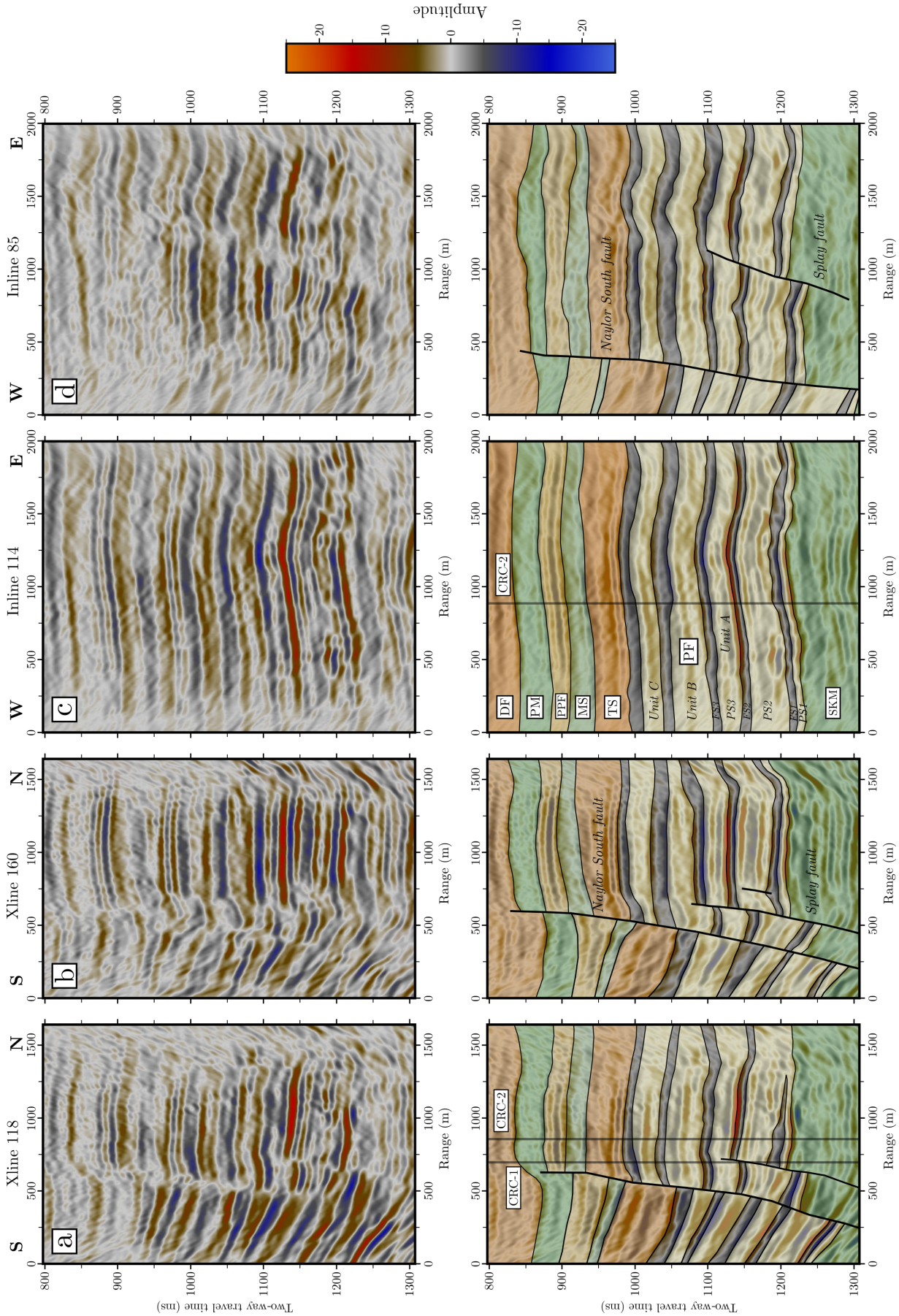
Amplitude
20
10
0
-10
-20
a
b
c
d
S
N
W
E
Xline 118
Xline 160
Inline 114
Inline 85
Two-way travel time (ms)
Range (m)
CRC-1
CRC-2
Naylor South fault
Splay fault
DF
PM
PPF
MS
TS
Unit C
PF
Unit B
Unit A
PS3
PS2
PS1
SKM

4.5.2 Horizon Geometry

The Stage 2C injection takes place into parasequence 1 (PS1), Unit A of the Paaratte Formation. The top of PS1 is defined by an extensive mudstone seal, under which the injected CO_2 is expected to spread. The negative (blue) reflection at 1200 ms two-way travel time (TWTT) is interpreted as the boundary between the bottom of the mudstone and the top of PS1. The maximum amplitude of this reflection was picked across the baseline seismic survey to give the lateral extent of the horizon in TWTT. The TWTT to depth relationship in Figure 4.5 was then used to convert from travel time to depth, and a correction of 50.4 m applied to convert from metres depth (MD) to metres below mean sea level (m TVDss) (Lawrence *et al.*, 2012).

The resultant horizon is plotted in Figure 4.8a. The Naylor South fault and splay fault are clearly visible with both showing increasing throw from west to east. The splay fault transitions into a fold to the west of the area. For comparison, the topography of the top of the PS1 sand as interpreted by Dance *et al.* (2012) is shown in Figure 4.8b. Both horizons dip towards the northwest in the northwest section of the area. To the east of the wells, the 2015 survey plateaus out, with a small topographic high ∼400 m east of CRC-2, whereas the 2012 interpretation continues rising to the southeast. Note that the splay fault is visible but the main Naylor South fault has not been interpreted in this survey.

The top of the Skull Creek Mudstone (also the base of the Paaratte Formation), was interpreted as the positive (red) reflection at ∼1215 ms TWTT. This horizon was also picked across the baseline survey and converted to depth below mean sea level (Figure 4.8c). The same horizon as interpreted by Dance *et al.* (2012) is plotted for comparison (Figure 4.8d). In general, the Skull Creek mudstone reflection is found ∼20 m below the top of PS1 reflection in the 2015 survey, whereas the distance between the horizons in the 2012 interpretation is ∼35 m. The topographic differences between the two Skull Creek horizons reflect the differences seen in the PS1 horizons.

The difference in depth between the top of the PS1 sand in the 2012 interpretation and the 2015 baseline survey is shown in Figure 4.9a, with darker regions corresponding to shallower depths in the 2012 interpretation. Around the injection location, the two broadly agree,

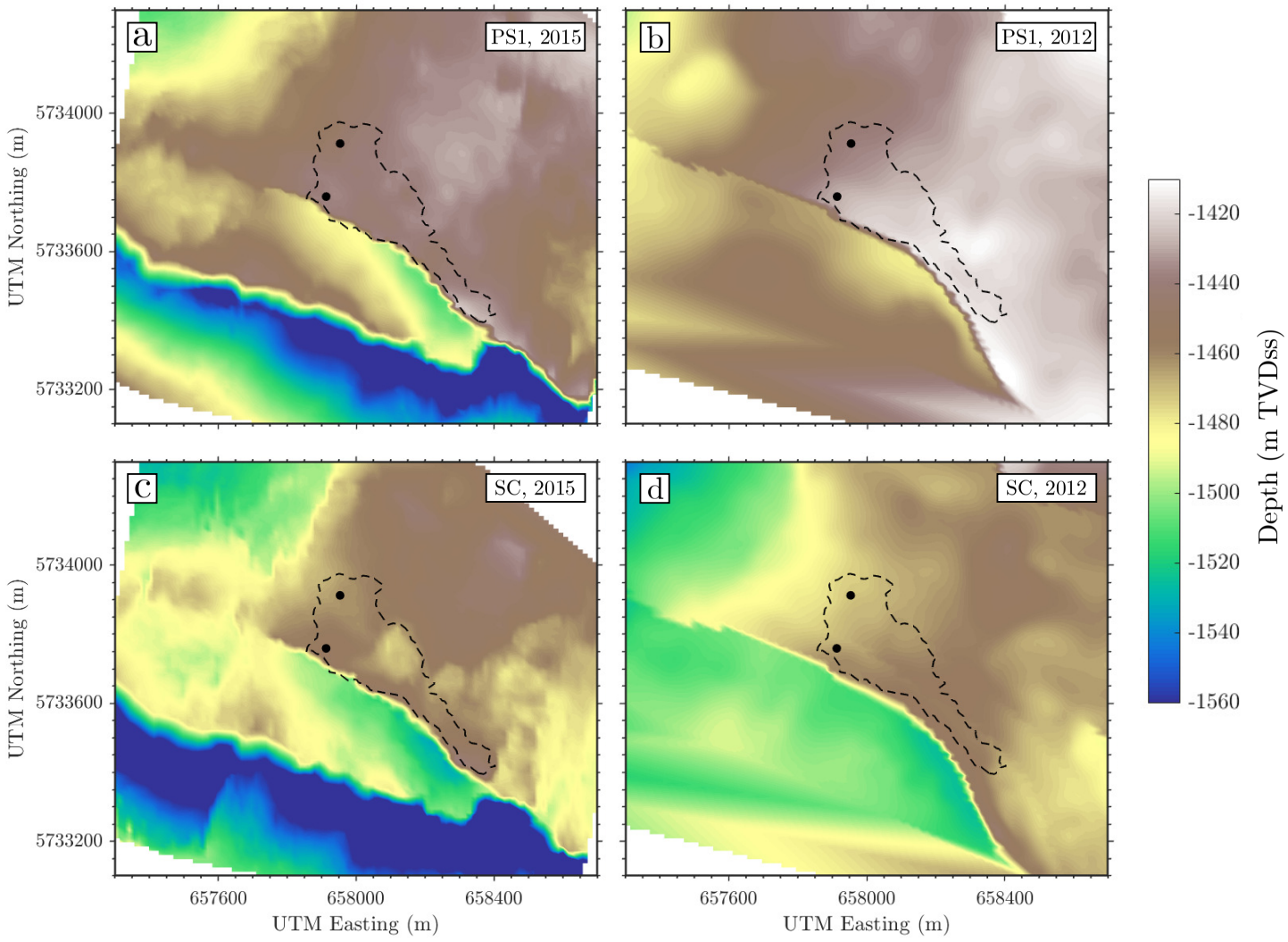

Figure 4.8: Depth to top of PS1 and top of Skull Creek Mudstone in metres below sea level. (a) and (c) show the top of the PS1 and Skull Creek Mudstone horizons respectively as interpreted from the 2015 baseline survey. (b) and (d) show the same horizons as interpreted by Dance *et al.* (2012) from a set of surveys conducted from 2000-2010 (see Section 4.3). Dashed line = extent of plume from TL5 survey. Black circles = CRC-2 injection well (top) and CRC-1 monitoring well (bottom).

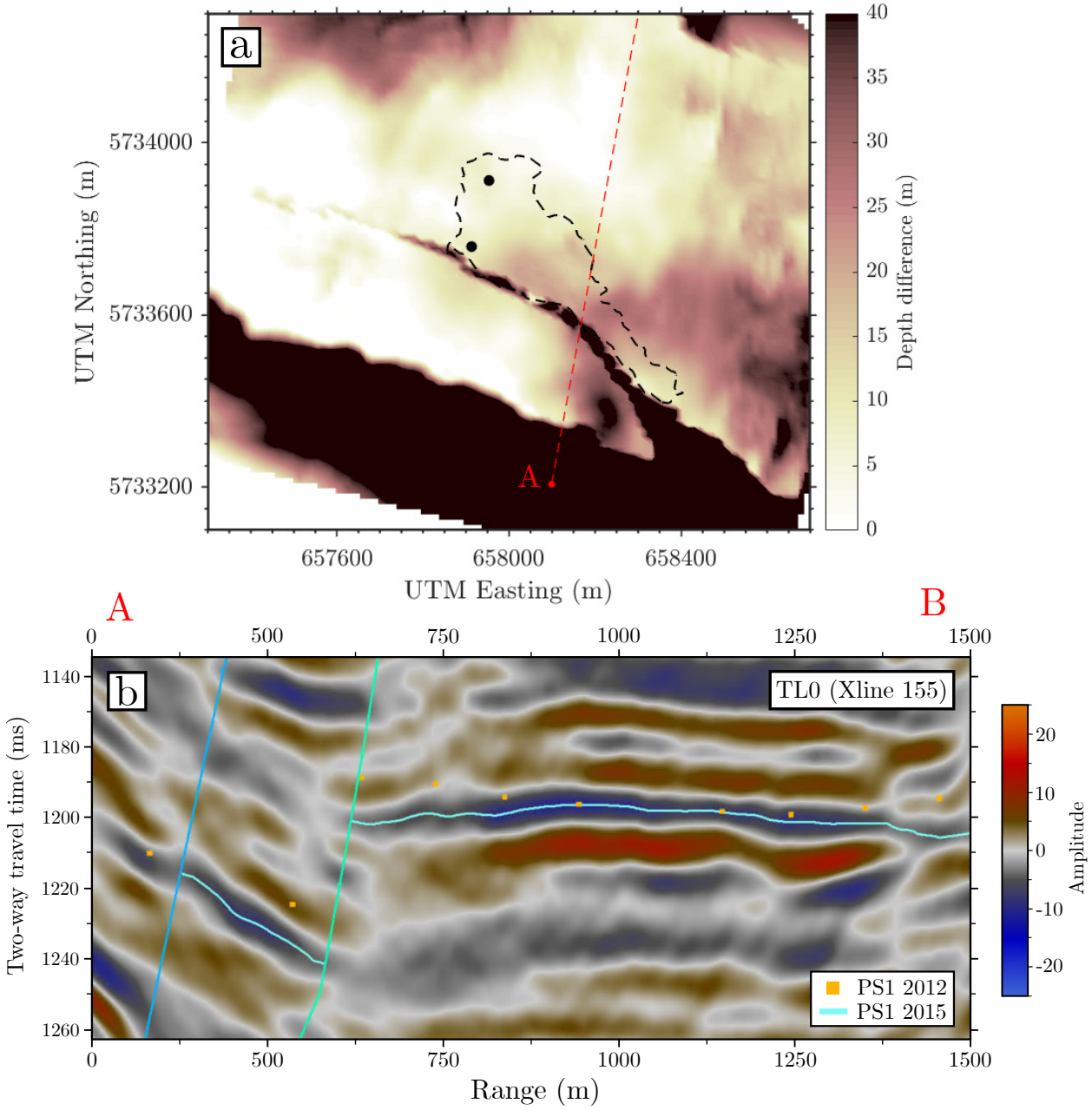

Figure 4.9: (a) Top of PS1 depth discrepancy between 2012 and 2015 interpretations where shallower depths in the 2012 interpretation correspond with darker regions. (b) Cross section of the 2015 baseline survey showing discrepancy of the 2012 interpretation (yellow squares) around the fault zone.

however there is some discrepancy towards the edges of the survey and around the fault. Horizons were picked by hand so there is a $\sim \pm 1$ ms error in two-way travel time, which corresponds to a ± 2 m depth error. However, some discrepancies between the surveys are larger than this. The discrepancy at the edges of the survey are likely due to over-migration during seismic processing. Figure 4.9b shows the discrepancy of the 2012 interpretation around the fault zone when it is overlaid on the 2015 survey. Seismic imaging of fault zones is challenging and conventional seismic reflection methods do not work well due to complex geometries and large variations in the velocity structure. Other possible reasons for differences between the two surveys are variations in the acquisition and processing workflows, updated velocity models used in the time-to-depth conversion and different survey resolutions. As the 2015 baseline survey has a greater resolution over the target area, and a higher signal-to-noise ratio due to the use of a buried receiver array, it is used in the analysis conducted in the remainder of this chapter.

4.6 Interpretation of post-injection surveys

The seismic lines for all time-lapse surveys are shown in Figure 4.10. There is an increase in brightness for the negative (blue) and positive (red) amplitudes reflections above and below the injection zone (marked by the green circle), associated with the top of the PS1 formation and the bottom of the PS1 formation (coincident with the top of the Skull Creek Mudstone) respectively. There is also a negative amplitude region below the injection zone at $\sim$1250 ms two-way travel time (TWTT) that brightens in the time-lapse surveys.

Studies determining the CO_2 distribution at the Sleipner field using time-lapse seismic reflection surveys used sharp reductions in amplitude within a horizon to determine the edge of the CO_2 plume (Bickle *et al.*, 2007; Boait, 2012). However, the significant heterogeneity in the Paaratte Formation means that there are greater amplitude variations across horizons, and so high amplitude regions are not exclusively due to the presence of CO_2. This is illustrated in Figure 4.11, where the negative amplitude reflection at top of PS1 is plotted in plan view for the baseline and TL3 seismic surveys (Figure 4.11a,b). The amplitude distribution for this horizon across both of these surveys is plotted in Figure 4.11c. There is an increase

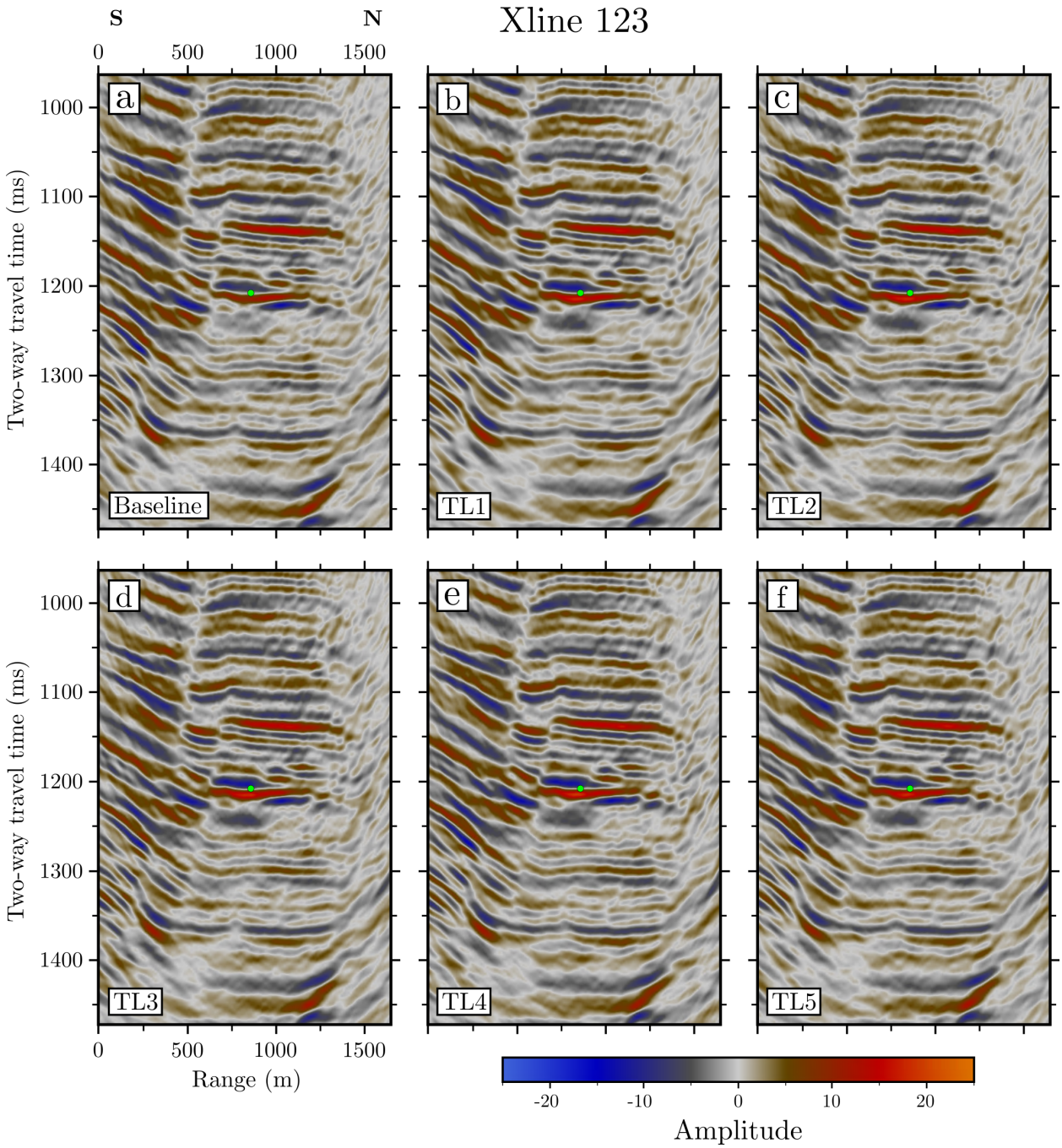

Figure 4.10: Seismic line (cross-line 123) for all time-lapse surveys, with injection interval marked by green circle.

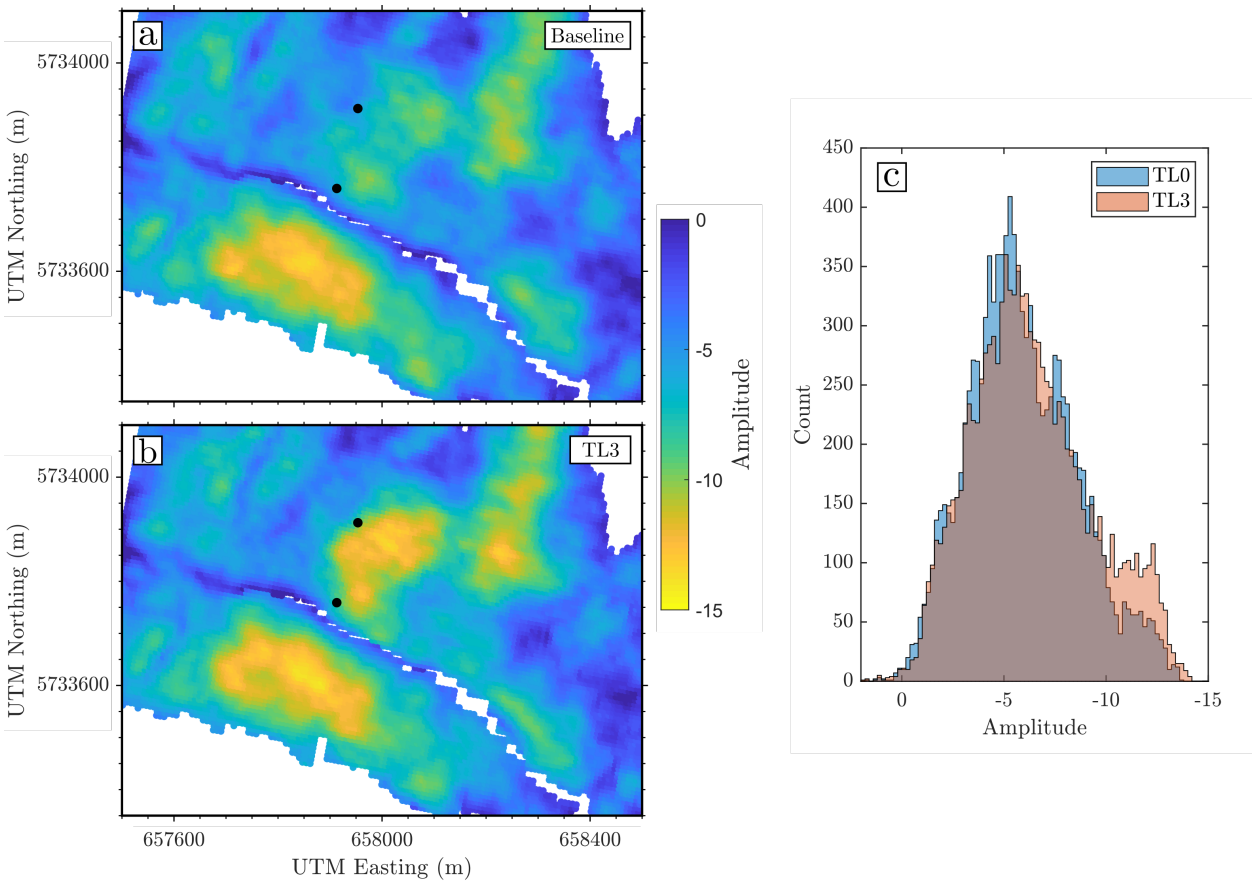

Figure 4.11: Amplitude of the negative (blue) reflection at 1200 ms TWTT corresponding with the top of PS1 plotted for (a) baseline and (b) TL3 seismic surveys. Black circles = location of CRC-2 injection well (top) and CRC-1 monitoring well (bottom). (c) Histogram showing the amplitude distribution for that horizon across the baseline (blue) and TL3 (red) surveys. Histogram is coloured brown where blue and red bars are both present. There is an increase in high amplitude reflections in the TL3 survey but there still significant high amplitude reflections in the baseline survey.

in high amplitude regions from TL0 to TL3 due to the injected CO_2, especially in close proximity to the injection well. However, in the baseline survey there are still significant regions displaying high amplitudes due to reservoir heterogeneity, hence it is difficult to tell whether high amplitudes in the time-lapse surveys are due to CO_2 or reservoir heterogeneity.

Seismic difference volumes can be used to more easily pick out the changes in sub-surface reflections due to the presence of CO_2. Here, the baseline seismic volume is subtracted from a time-lapse seismic volume, leaving a volume which contains the amplitude differences between the two, which is a result of both amplitude changes and shifts in travel-time. The increase in reflectivity of the horizons at the top and bottom of PS1 can be clearly seen in the time-lapse seismic difference volumes (Figure 4.12b-f). If all seismic surveys

were acquired and processed under identical conditions, the only reflections in the seismic difference volumes would be due to changes in the sub-surface, in this case due to CO_2. However, noise in the seismic data results in additional amplitude anomalies in the seismic difference volumes, can be seen in Figures 4.12b-f.

Also clearly visible is the negative seismic anomaly below the injection site at ∼1250 ms. Pevzner *et al.* (2020) suggests the reduction in seismic velocity in the CO_2-invaded area results in pushdown in the time-lapse surveys, which results in the negative anomaly below the injection zone. However, analysis of the two-way travel time of horizons below the injection zone suggests that minimal pushdown occurs. Instead, seismic waveform modelling around the injection zone suggests that the negative anomaly is caused by constructive interference of the seismic wavelets, and is discussed further in Section 4.7.4.

The extent of the negative amplitude anomaly (top of PS1) and positive amplitude anomaly (top of Skull Creek Mudstone) in the seismic difference volumes is interpreted by picking the peak amplitude of the reflections. The peak amplitude of both reflections is plotted spatially in Figure 4.13, where only amplitudes above a threshold value of 2 are included. Also plotted are the contours for the outline of the reflection if the threshold is set at 1.6 (dashed blue line) and 2.4 (solid red line).

Figures 4.13a-e show the time-lapse evolution of the negative amplitude anomaly and Figures 4.13f-j show the time-lapse evolution of the positive amplitude anomaly. In general, both reflections display a similar behaviour over time, with an increase in the size of the anomaly from TL1-TL4, and preferential spreading towards to the southeast. Both also display a low amplitude region, ∼100 m east of CRC-1. Amplitudes are highest close to the injection well, but the positive amplitude anomaly shows higher amplitude changes and also a greater spatial distribution.

Within the seismic difference volumes there are other reflections associated with noise. These can either be due to variations in amplitude between the surveys, or small travel-time shifts of the horizons meaning that reflections shift out of phase resulting in a difference in the seismic difference volume. Where amplitude anomalies associated with CO_2 and amplitude anomalies due to noise are in close proximity, it can make interpretation of the seismic difference plots difficult. Figure 4.14 shows a close-up of the TL4 seismic difference volume

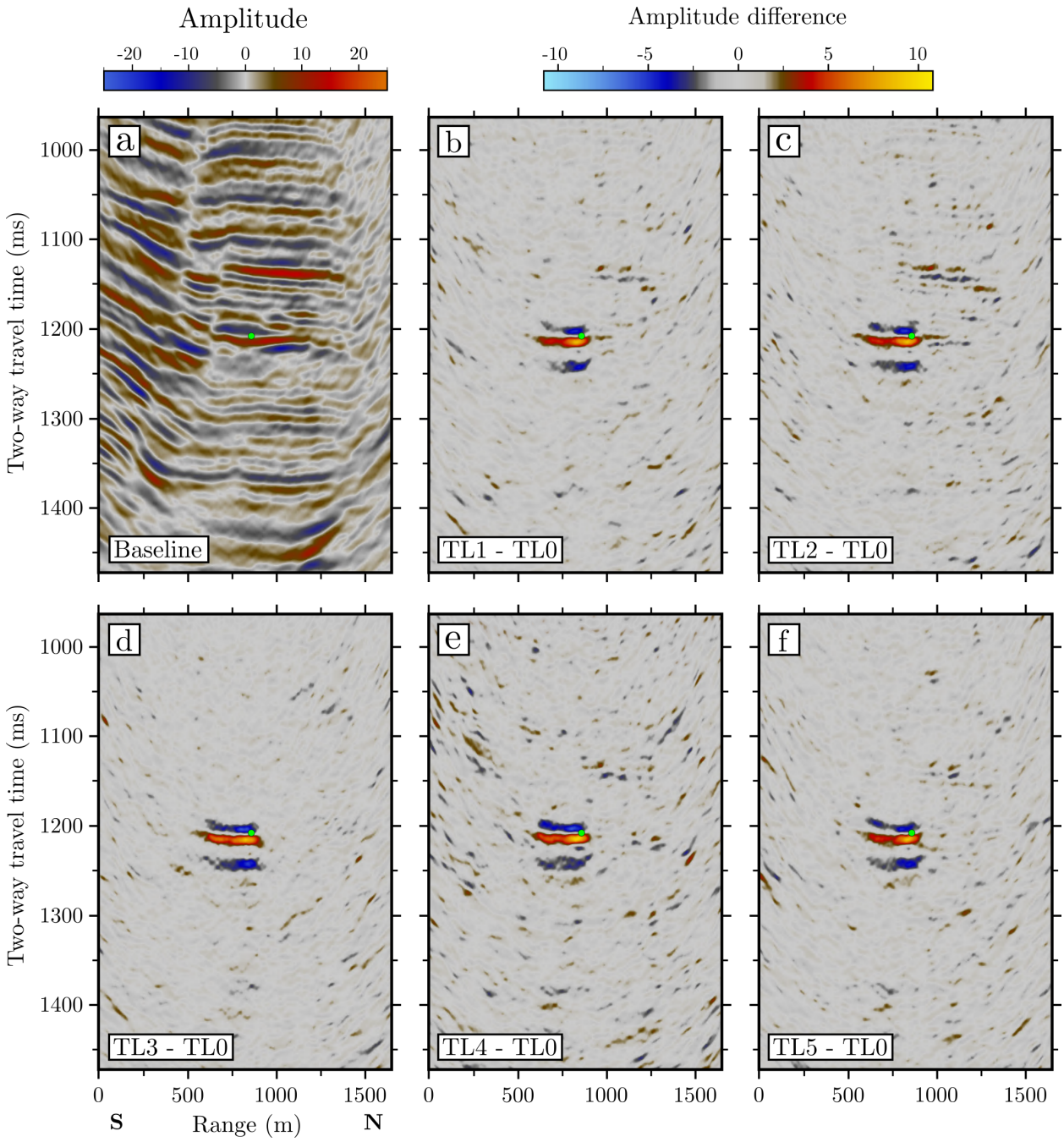

Figure 4.12: (a) Baseline seismic line (cross-line 123). (b)-(f) Seismic difference volumes for each of the time-lapse seismic surveys (cross-line 123) calculated by subtracting the baseline seismic volume from each of the time-lapse seismic volumes. Note the different amplitude scale for the seismic difference volumes. Green circle = injection interval.

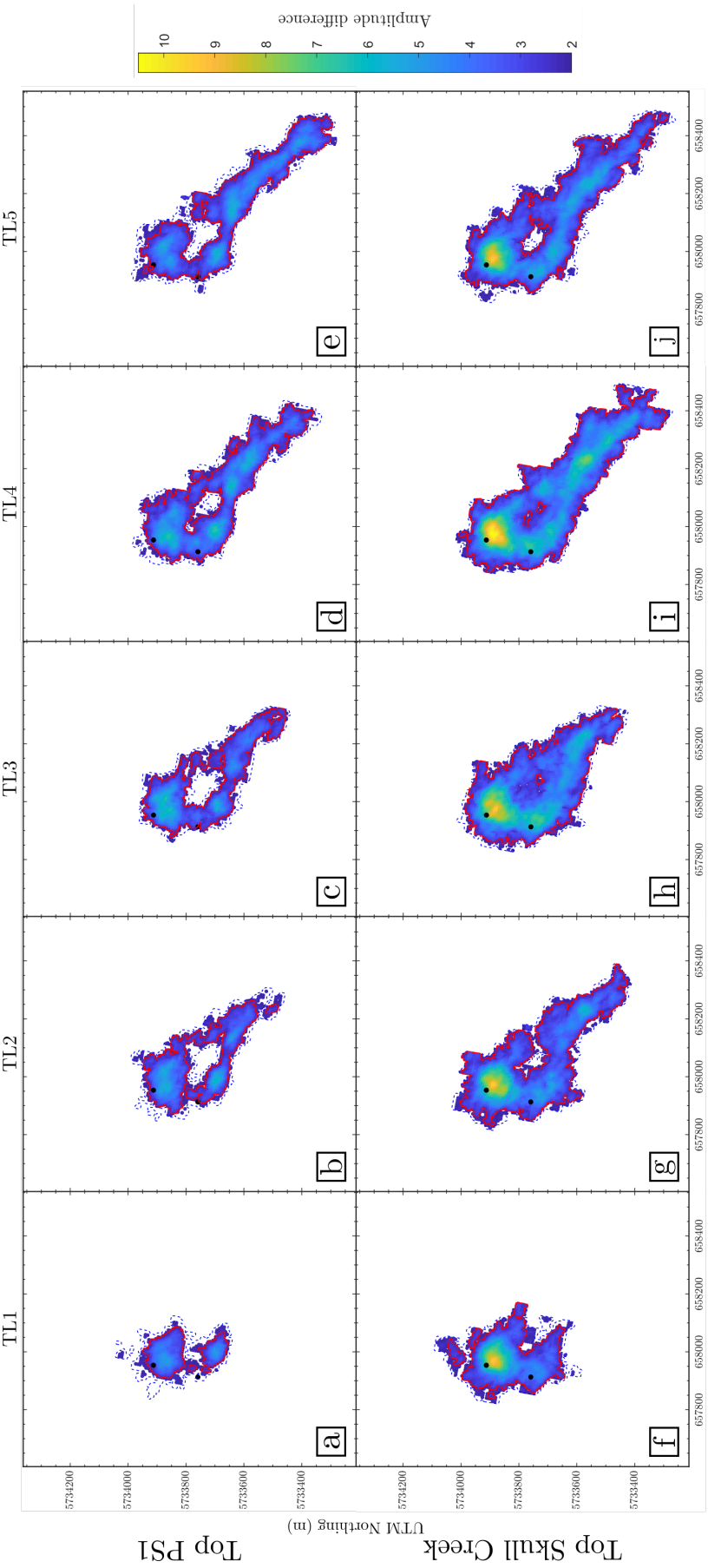

Figure 4.13: Amplitude of horizons in seismic difference volumes. (a)-(e) show the amplitude distribution of the negative (blue) reflection at 1200 ms in the seismic difference volume. (f)-(j) show the amplitude distribution of the positive (red) reflection at 1225 ms in the seismic difference volume. Only amplitudes above a minimum threshold value of 2 are plotted. Also plotted are the contours for the outline of the plume if the threshold is 1.6 (dashed blue line) and 2.4 (solid red line). Black circles = location of CRC-2 injection well (top) and CRC-1 monitoring well (bottom).

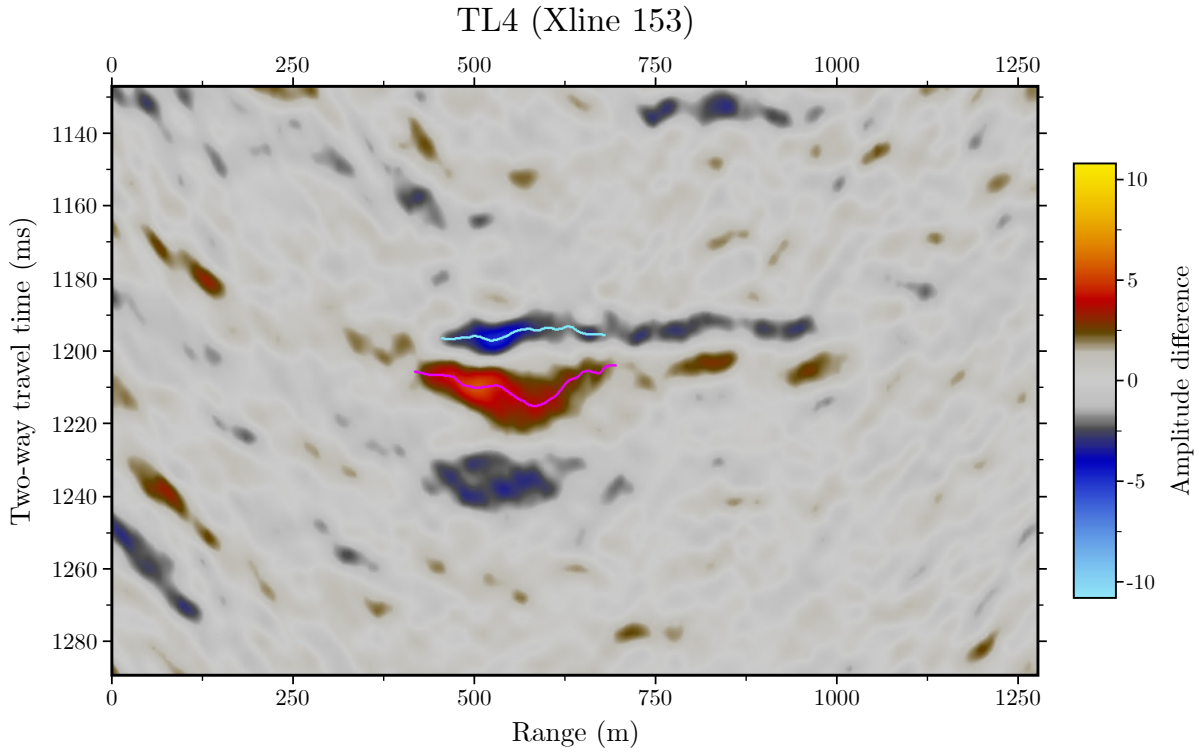

Figure 4.14: Close-up of the TL4 seismic difference volume, with blue and red lines showing the manually picked extent of the plume. Amplitude anomalies surrounding the plume are due to noise between the seismic surveys. Blue reflection below the injection zone is caused by constructive interference of seismic wavelets (see Section 4.7.4)

with interpretations for the top and bottom horizons associated with the CO_2 plume (blue and red lines). Just to the right of the plume are amplitude anomalies due to noise which make it difficult to interpret where the edge of the plume is.

Another method can be used to obtain changes in amplitude between the baseline and time-lapse seismic surveys. Here, the position of the peak amplitude for a reflection is picked in the baseline survey and each of the time-lapse surveys across the full horizon. The baseline amplitudes are then subtracted from the time-lapse amplitudes to obtain the amplitude difference across the horizon. This also eliminates the effect of travel-time shifts, as the peak amplitude is picked regardless of TWTT, which means that changes in reflectivity are due to amplitude differences between the layers.

Figure 4.15 shows the amplitude difference between the baseline and time-lapse surveys for the negative amplitude reflection at the top of PS1 (Figure 4.15a-e) and the positive amplitude reflection at the top of the Skull Creek Mudstone (Figure 4.15f-j). Amplitude differences above a threshold value of 2 are plotted, with contours for the outline of the

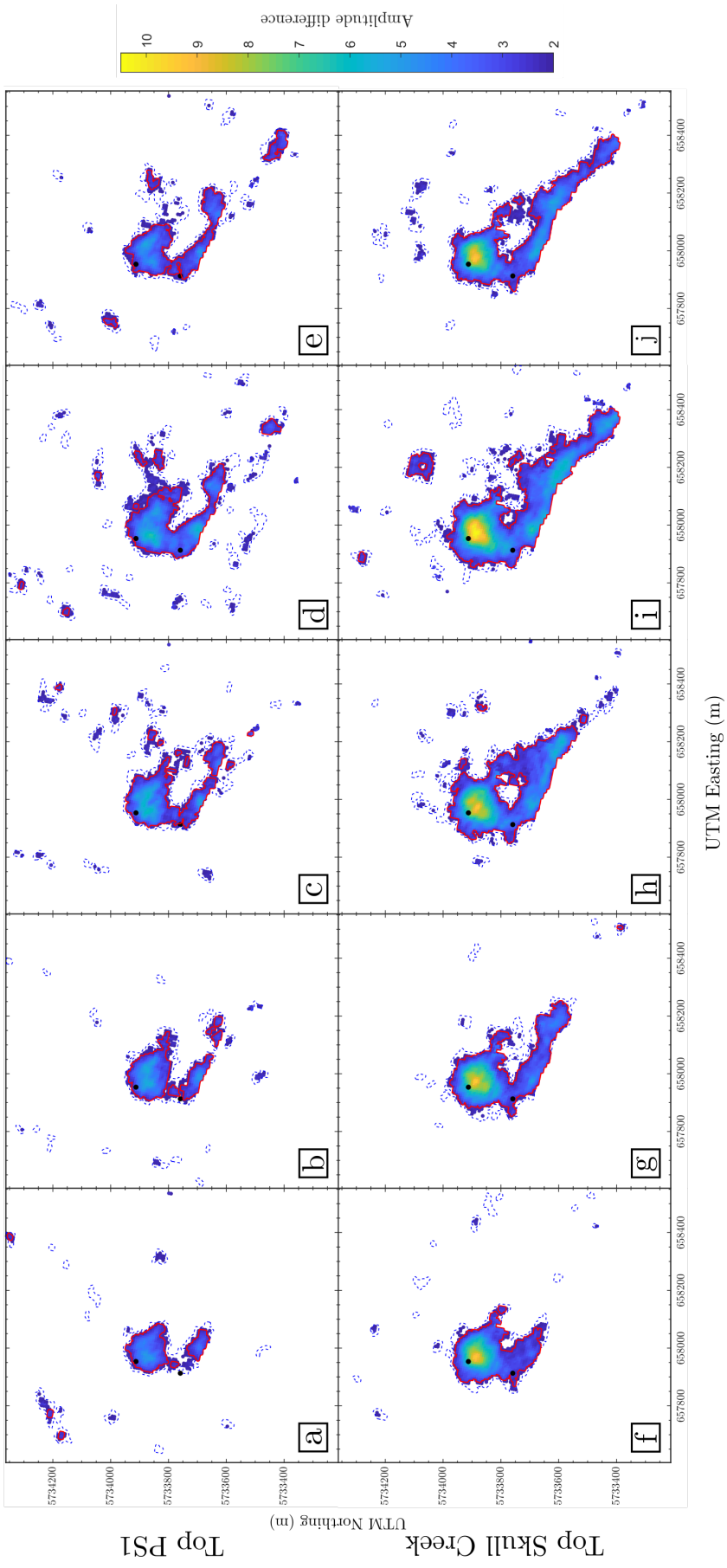

Figure 4.15: Amplitude difference of horizons between baseline and time-lapse surveys. (a)-(e) show the difference in amplitude of the negative (blue) reflection at 1200 ms between the baseline and time-lapse seismic surveys. (f)-(j) show the difference in amplitude of the positive (red) reflection at 1225 ms between the baseline and time-lapse seismic surveys. Only differences in amplitude above a minimum threshold value of 2 are plotted. Also plotted are the contours for the outline of the plume if the threshold is 1.6 (dashed blue line) and 2.4 (solid red line). Black circles = location of CRC-2 injection well (top) and CRC-1 monitoring well (bottom).

plume if the threshold is 1.6 (dashed blue line) and 2.4 (solid red line) also shown. The behaviour of the amplitude anomalies is similar to the anomalies extracted from the seismic difference volumes, with preferential movement to the southeast and a low amplitude region ∼100 m east of CRC-1. The positive amplitude anomaly associated with the top of the Skull Creek Mudstone shows higher amplitude differences and a greater spatial distribution than the negative amplitude anomaly at the top of PS1. Some reflections around the main plume due to seismic noise are still visible, especially when the threshold is set to 1.6, but most of these reflections are not present when the threshold is 2.4.

4.6.1 Growth of the CO_2 layer

The areal extent of the CO_2 plume, as interpreted for the positive and negative amplitude anomalies using both methods (picking reflections in the seismic difference volumes and taking the difference between reflections in the baseline and time-lapse seismic surveys), is plotted in Figure 4.16. The points correspond to an amplitude threshold of 2, with the limits defined by the error bars corresponding to thresholds of 1.6 and 2.4. All methods robustly show an increase in plume area during injection, followed by a period of steady areal extent with possibly a decline at later times. This is consistent with CO_2 spreading under buoyancy, then stabilising under a topographic high with some capillary trapping and CO_2 dissolution at later times reducing the volume of the CO_2 plume. Where the methods differ is in the magnitude of the measured area. The lower reflection (Top Skull Creek) is more sensitive to impedance changes in the injection interval caused by the injected CO_2, and shows a higher maximum amplitude increase, as well as detectable amplitude changes towards the edges of the plume where the CO_2 thickness is smaller, which results in greater areal extents. This is consistent with the waveform modelling performed in Section 4.7.4, where significant amplitude changes are seen at lower CO_2 thicknesses for the lower reflection compared to the upper reflection (Figure 4.30). The difference seismic volumes show higher areal extents, especially around the fault zone. In the fault zone, small shifts in horizon travel times between the baseline and time-lapse surveys may be reflected as amplitude changes in the difference seismic volumes.

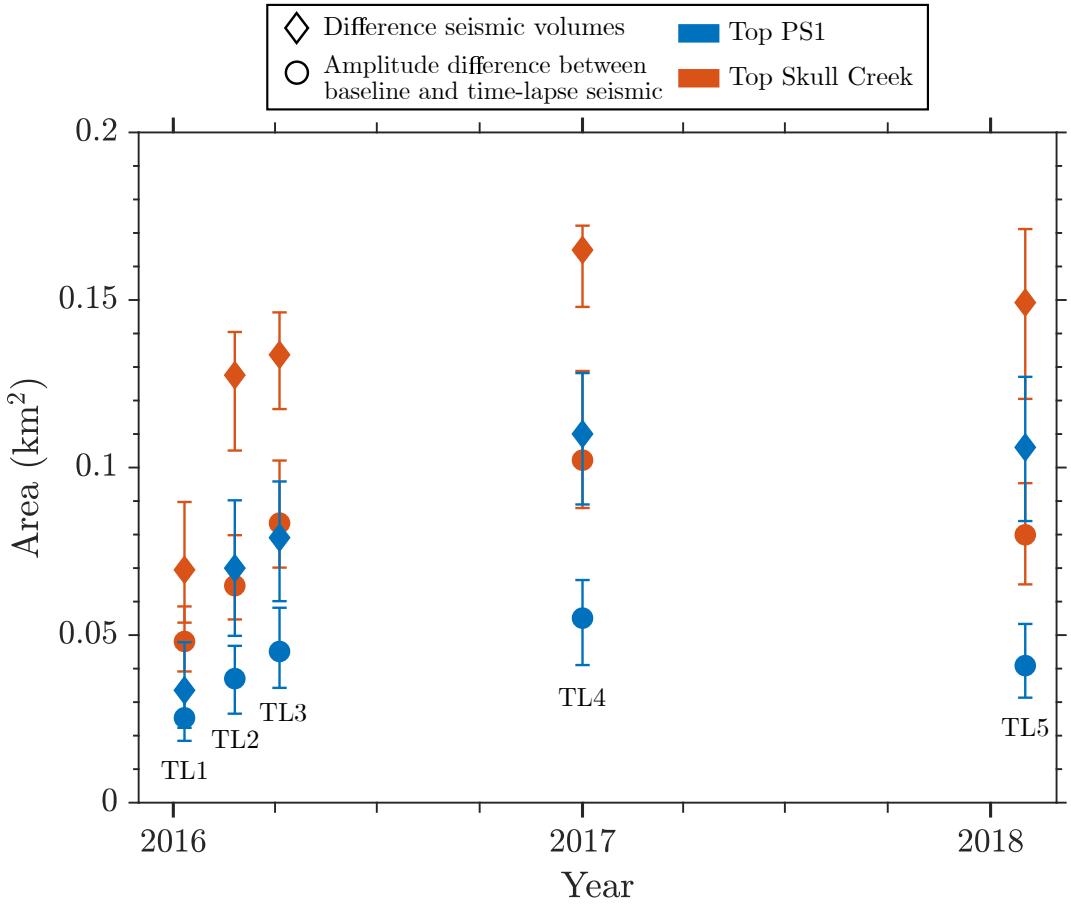

Figure 4.16: CO_2 plume areal extent plotted for each time-lapse seismic survey. Blue markers correspond to the areal extent as interpreted from the negative reflection at 1200 ms, red markers correspond to the positive reflection at 1225 ms. Circles = areal extent obtained from seismic difference volumes. Diamonds = areal extent obtained from horizon amplitude differences between baseline and time-lapse surveys. Areas calculated for an amplitude threshold of 2, and error bars reflect the areas calculated at amplitude thresholds of 1.6 and 2.4.

4.7 Seismic Response of CO_2 Saturated Rocks

4.7.1 Estimating the acoustic velocity of a CO_2-saturated sandstone

When interpreting seismic reflection surveys, the amplitude and polarity of measured signals are a result of the impedance contrasts between layers. These impedance contrasts are dependent on the velocity and density contrasts between layers. The acoustic velocity of a rock is affected by the properties of the rock frame and the properties of the interstitial fluid. Rock physics models such as the Gassmann's relations (Gassmann, 1951; Smith *et al.*, 2003) can be used to estimate the velocity of a CO_2-saturated sandstone.

The Gassmann Model

The velocities of body waves travelling through a homogenoeus, elastic, isotropic medium are given by

$$v_p = \left(\frac{K + \frac{4}{3}\mu}{\rho} \right)^{\frac{1}{2}}, \tag{4.3}$$

$$v_s = \left(\frac{\mu}{\rho} \right)^{\frac{1}{2}}, \tag{4.4}$$

where v_p and v_s are the P-wave and S-wave velocities, K is the effective bulk modulus of the rock, μ is the shear modulus and ρ is the density. This means that if the P-wave and S-wave velocities are known, the effective bulk and shear moduli of the medium can be estimated using the expressions

$$\mu = \rho v_s^2, \tag{4.5}$$

$$K = \rho(v_p^2 - \tfrac{4}{3}v_s^2). \tag{4.6}$$

When a rock undergoes compression, for example due to a seismic wave, a pore-pressure change is induced which resists compression, therefore increasing the stiffness of the rock. The Gassmann-Biot theory (Biot, 1956; Gassmann, 1951) predicts the resulting increase in effective bulk modulus K, of the saturated rock using the following equation

$$\frac{K}{K_{min} - K} = \frac{K_{dry}}{K_{min} - K_{dry}} + \frac{K_{fl}}{\phi(K_{min} - K_{fl})} \tag{4.7}$$

where K_{dry} is the effective bulk modulus of the dry rock, K_{min} is the bulk modulus of the mineral making up the rock, K_{fl} is the effective bulk modulus of the pore fluid and ϕ is the porosity. K_{dry} can be determined by laboratory measurements on rock samples. Note that the shear modulus of the rock is unchanged by pore fluid (i.e. $\mu = \mu_{dry}$).

The most common use of the Gassmann relations is to predict the change in effective bulk modulus when one fluid is substituted for another. In this case, I investigate the partial substitution of interstitial brine by CO_2 and treat the brine/CO_2 mixture as a single effective fluid, which is a common approach to modelling partial saturation. One can algebraically eliminate the dry rock modulus from (4.7) to obtain

$$\frac{K_{sat}}{K_{min} - K_{sat}} - \frac{K_{br}}{\phi(K_{min} - K_{br})} = \frac{K_{sat}(S_{CO_2})}{K_{min} - K_{sat}(S_{CO_2})} - \frac{K_{fl}(S_{CO_2})}{\phi[K_{min} - K_{fl}(S_{CO_2})]} \tag{4.8}$$

where K_{sat} is the bulk modulus of the brine saturated rock, S_{CO_2} is the CO_2-saturation of the rock, $K_{sat}(S_{CO_2})$ is the bulk modulus of the partially CO_2-saturated rock, K_{br} is the bulk modulus of the brine and $K_{fl}(S_{CO_2})$ is the effective bulk modulus of the CO_2 and brine fluid mixture that occupies the pore space.

It is well established that the Gassmann theory is valid only at sufficiently low frequencies ($<$ 100 Hz) so that the induced pore pressure can equilibrate throughout the pore space, allowing sufficient time for the pore fluid to flow and eliminate wave-induced pore-pressure gradients (Mavko *et al.*, 2020). If all of the fluid phases are mixed at the finest scale (i.e. saturation is uniform), the effective bulk modulus of the mixture of fluids is described well by the Reuss average,

$$K_{fl}(S_{CO_2}) = \left[\frac{S_{CO_2}}{K_{CO_2}} + \frac{(1 - S_{CO_2}}{K_{br}}\right]^{-1}. \tag{4.9}$$

An assumption of the Reuss average is that differences in wave-induced pore pressure have time to flow and equilibrate throughout the different phases. A characteristic relaxation time for diffusion of pore pressures across a critical length scale L_c is

$$\tau \approx \frac{L_c^2}{D}, \tag{4.10}$$

where $D = kK_{fl}/\eta$ where is the diffusivity, k is the permeability and K_{fl} and η are the bulk

modulus and viscosity of the most viscous fluid respectively. At a seismic frequency $f = 1/\tau$, the critical length scale where pore pressures will have time to equilibrate over is

$$L_c = \sqrt{\frac{kK_{fl}}{f\eta}}. \tag{4.11}$$

Where saturation is heterogeneous over length scales greater than L_c (i.e. saturation is patchy), each patch will have a different effective fluid bulk modulus described by the Reuss average, and hence the bulk modulus of the rock will vary spatially. An approximation to calculating this patchy-saturation bulk modulus can be found by computing the Voigt average of the fluid modulus

$$K_{fl}(S_{CO_2}) = S_{CO_2}K_{CO_2} + (1 - S_{CO_2})K_{br}. \tag{4.12}$$

Brie *et al.* (1995) suggest an empirical fluid mixing law, given by

$$K_{fl}(S_{CO_2}) = (K_{br} - K_{CO_2})(1 - S_{CO_2})^n + K_{CO_2}, \tag{4.13}$$

where n is an empirical constant, typically equal to about $n \approx 3$. While the Voigt and Reuss are bounds for the effective fluid, a more useful range is to assume the effective fluid modulus will fall roughly between the Reuss and Brie averages (Mavko *et al.*, 2020).

On determining the bulk modulus of the partially CO_2-saturated rock $K_{sat}(S_{CO_2})$, it's velocity can be calculated,

$$v_p(S_{CO_2}) = \left(\frac{K_{sat}(S_{CO_2}) + \frac{4}{3}\mu}{\rho(S_{CO_2})}\right)^{\frac{1}{2}}, \tag{4.14}$$

remembering that the shear modulus is unchanged by the pore fluid and the density of the partially saturated rock is given by

$$\rho(S_{CO_2}) = (1 - \phi)\rho_{min} + \phi S_{CO_2}\rho_{CO_2} + \phi(1 - S_{CO_2})\rho_{br}. \tag{4.15}$$

	PS2	FS1	PS1	Skull Creek
Density (kg m^{-3})	2294±62	2430±51	2290±72	2399±46
Porosity	0.25±0.03	0.19±0.02	0.25±0.04	0.19±0.03
P-wave velocity (m s^{-1})	3150±78	3283±67	3195±78	3269±87
S-wave velocity (m s^{-1})	1710±71	1740±54	1749±94	1737±97

Table 4.3: Average parameters obtained from the CRC-1 and CRC-2 well logs. Uncertainty range indicates one standard deviation from the mean.

4.7.2 Acoustic velocity of the Paaratte Formation

Average parameters of the PS1 formation in Unit A of the Paaratte Formation are used to calculate the seismic velocity $v_p(S_{CO_2})$ of the CO_2-saturated sandstone. Density, porosity, P-wave velocity and S-wave velocity measurements taken from well logs of the CRC-1 and CRC-2 wells are shown in Figure 4.17. The different geological units are highlighted, with boundaries between units indicated by horizontal dashed lines. The positions of the cemented calcite layers that overprint the formation are interpreted in red, characterised by very high density and seismic velocity, and low porosity. It should be noted that the appearance and position of these cemented layers appears consistent between the wells, suggesting that they are laterally continuous, at least over the distance between the wells (∼150 m).

The properties for each unit obtained from the well logs are shown in Table 4.3. The values are calculated by taking the average across the depth interval for that unit using data from both wells, and excluding the depths which contain the cemented layers (highlighted in red on Figure 4.17). The uncertainty range indicates one standard deviation from the mean.

The parameters in Table 4.4 are used to estimate the P-wave velocity of the PS1 sandstone as a function of CO_2 saturation $v_p(S_{CO_2})$ using the model described in Section 4.7.1. The P-wave velocity v_p, S-wave velocity v_s and porosity ϕ are average values for the PS1 formation obtained from the well logs. The CO_2/CH_4 mix bulk modulus K_{CO_2} and density ρ_{CO_2} are calculated at reservoir conditions (fluid pressure 14.5±0.1 MPa, temperature 62.4±0.5°C) using the GERG 2008 equation of state (Kunz & Wagner, 2012), and the bulk modulus K_{br} and density ρ_{br} of the brine (Dubacq *et al.*, 2013; Fine & Millero, 1973) are taken from the literature, with the uncertainty range reflecting the uncertainty in the reservoir conditions.

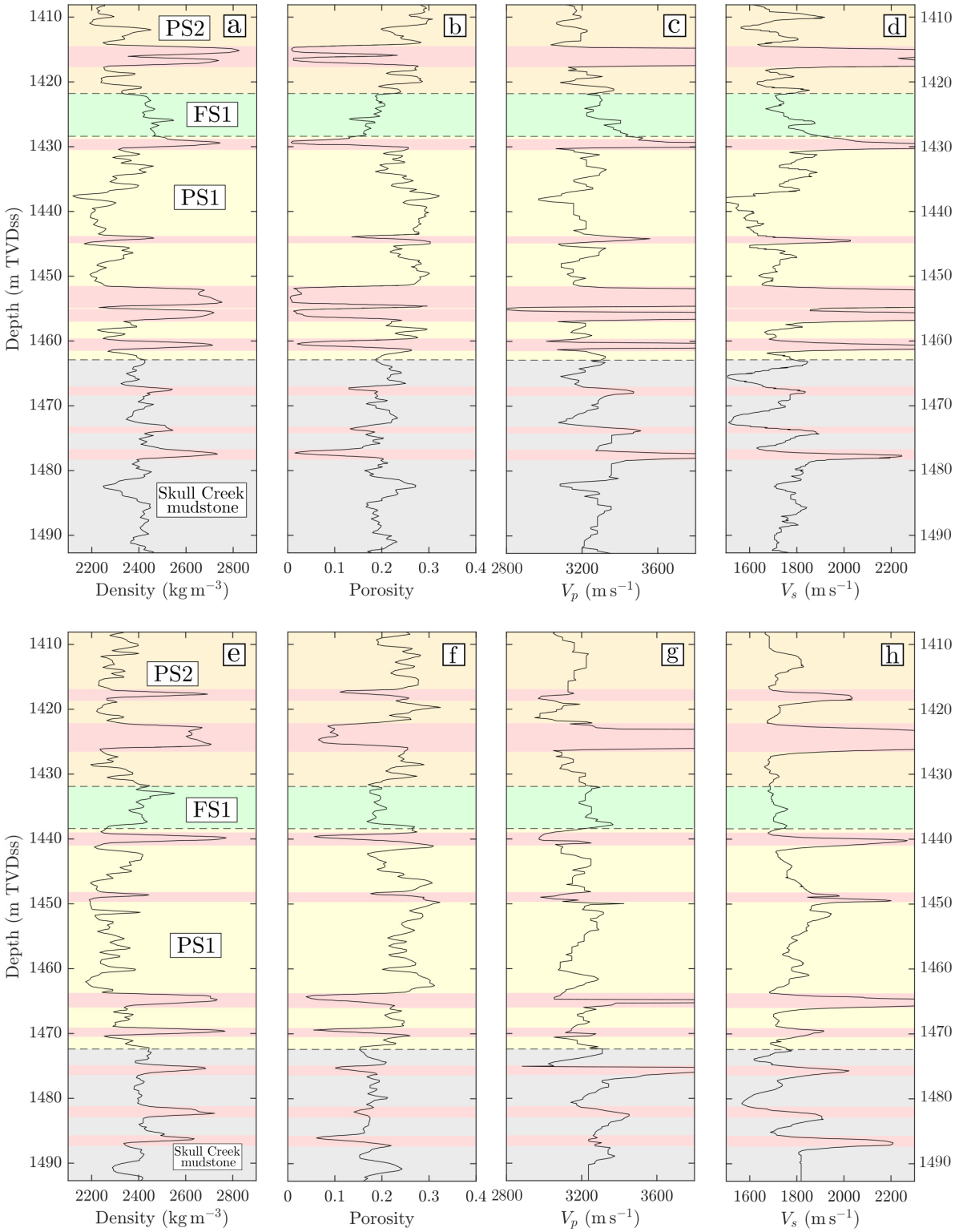

Figure 4.17: Density, porosity, P-wave and S-wave velocity logs for the CRC-1 well (a-d) and CRC-2 (e-h) well. Geological boundaries are marked by horizontal black dashed lines. Cemented calcite layers are shaded red. Well log data from Lawrence *et al.* (2012).

Parameter	Symbol	Value	Uncertainty	Units
P-wave velocity	v_p	3195	±78	m s^{-1}
S-wave velocity	s_p	1749	±94	m s^{-1}
Mineral bulk modulus	K_{min}	37	±0.1	GPa
Mineral density	ρ_{min}	2650	±25	kg m^{-3}
Porosity	ϕ	0.25	±0.04	
Brine bulk modulus	K_{br}	2.25	±0.05	GPa
Brine density	ρ_{br}	988	±2	kg m^{-3}
CO_2/CH_4 mix bulk modulus	K_{CO_2}	10.6	±0.2	MPa
CO_2/CH_4 mix density	ρ_{CO_2}	348	±10	kg m^{-3}

Table 4.4: Parameter values used to calculate $v_p(S_{CO_2})$.

The mineral bulk modulus K_{min} and mineral density ρ_{min} of quartz are used for the mineral making up the rock (Mavko *et al.*, 2020).

The velocity of the PS1 sandstone as a function of CO_2 saturation $v_p(S_{CO_2})$ is plotted in Figure 4.18. The effective bulk modulus of the fluid mixture $K_{fl}(S_{CO_2})$ is calculated using the Reuss, Voigt and Brie averages which are represented by the solid, dotted and dashed lines respectively. The use of (4.15) for calculating the density of the partially saturated rock can be checked by comparing the density of the brine saturated rock to the density measured in the well logs. When $S_{CO_2} = 0$, (4.15) becomes $\rho_{sat} = (1 - \phi)\rho_{min} + \phi\rho_{br} = 2235$ kg m^{-3}, which is within error of the average value calculated from the well logs. There is significant variation in seismic velocity across the three curves, particularly at lower CO_2 saturations, so it is important to determine which average best represents the PS1 formation.

To understand the sensitivity of $v_p(S_{CO_2})$ to the uncertainty in each parameter, $v_p(S_{CO_2})$ is plotted using the Reuss average for the effective bulk modulus, varying each parameter in turn (Figure 4.19). The black line shows the $v_p(S_{CO_2})$ for the partially CO_2-saturated using the values in Table 4.4. The blue and red lines show $v_p(S_{CO_2})$ calculated using the upper and lower bounds of the uncertainty range. The uncertainties associated with v_p, v_s and ϕ show the largest effect on the acoustic velocity.

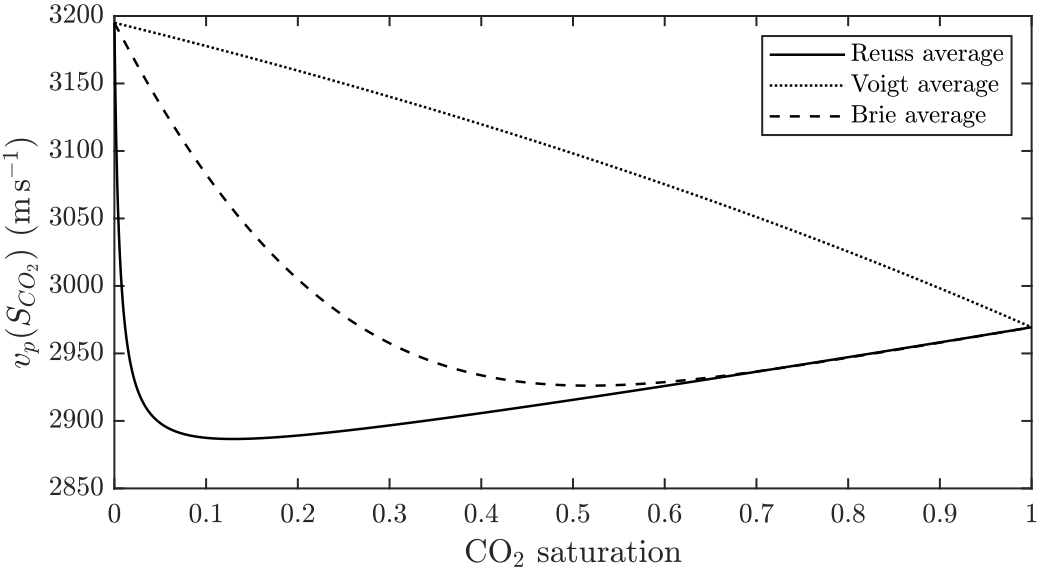

Figure 4.18: P-wave velocity of the PS1 sandstone as a function of CO_2 saturation $v_p(S_{CO_2})$ calculated using the Gassmann model. Different lines represent different models for the effective bulk modulus of the fluid mixture. Solid line = Reuss average, Dashed line = Brie average, Dotted line = Voigt average.

4.7.3 CO_2 saturation in the injection interval

In a heterogeneous rock such as the Paaratte Formation, permeability variations between layers can mean that the CO_2 saturation may vary across adjacent layers. These differences in saturation can be below the seismic resolution but may still affect the velocity-saturation relationship and hence the seismic response (Watson *et al.*, 2012). The two end-member saturation distributions are illustrated in Figure 4.18, described by the Reuss average and Voigt average, which correspond to fully mixed and fully unmixed CO_2 saturations respectively.

Caspari *et al.* (2015) performed a 1D synthetic sensitivity study to determine the role of CO_2 saturation heterogeneity length scales on the seismic velocity of the Paaratte Formation. Alternating layers of 100% CO_2/CH_4 saturated and 100% brine saturated porous media were generated at different length scales, and the change in P-wave velocity as a function of average saturation was calculated for a frequency of 45 Hz, taking wave-induced pressure diffusion into account (Figure 4.20). The velocity-saturation relationship deviates significantly away from the Reuss average for heterogeneities at length scales greater than 0.1 m, and approaches the Voigt average at a 10 m length scale. This corresponds well with the critical length scale given by (4.11) for the PS1 formation, $L_c \approx 0.1$ m, evaluated using the bulk modulus and

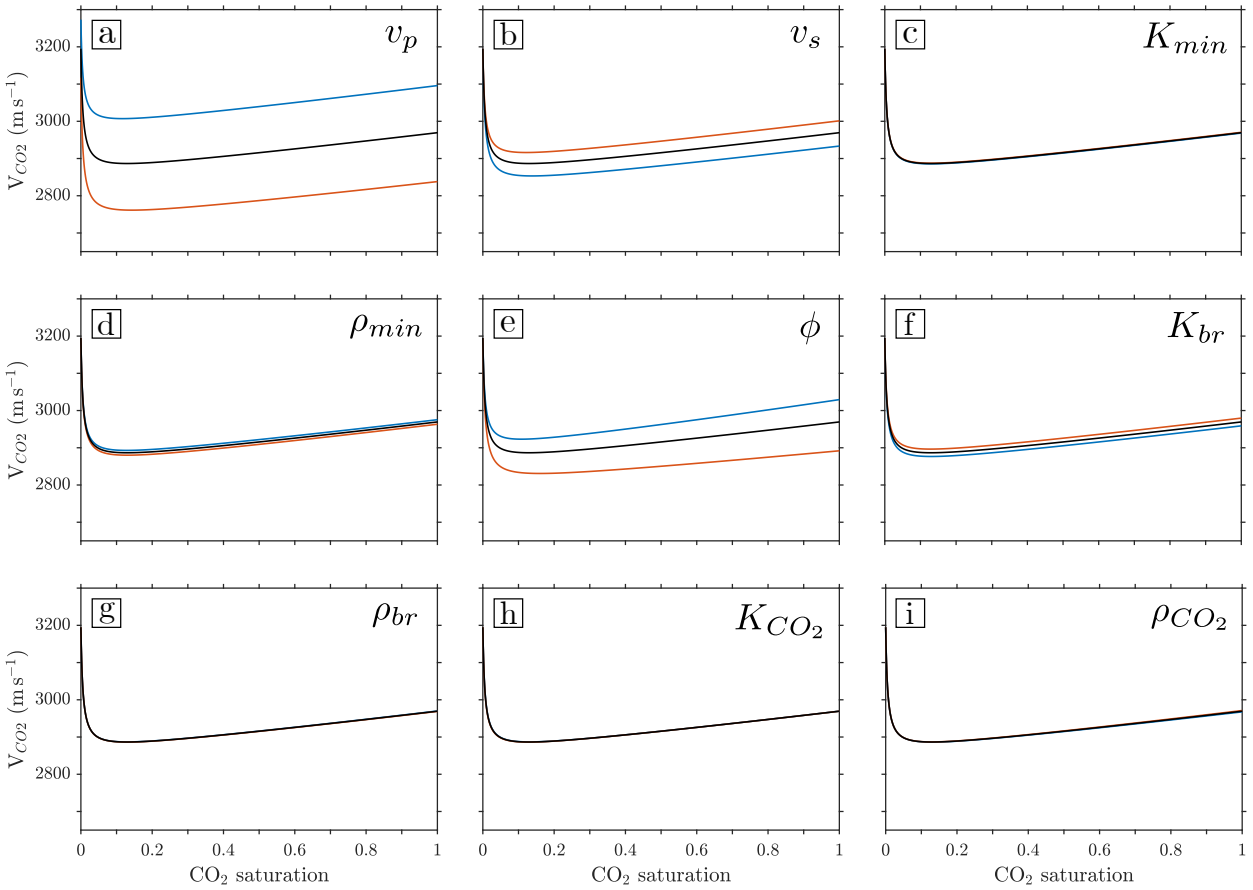

Figure 4.19: P-wave velocity of a partially CO_2-saturated sandstone with sensitivity to parameter uncertainties. (a) P-wave velocity. (b) S-wave velocity. (c) Mineral bulk modulus. (d) Mineral density. (e) Porosity. (f) Brine bulk modulus. (g) Brine density. (h) CO_2/CH_4 mix bulk modulus (i) CO_2/CH_4 mix density.

viscosity of brine at reservoir conditions, frequency 45 Hz and an average permeability of 82±7 mD for the PS1 formation, calculated by taking the geometric mean of the well log data in Figure 4.21a and Figure 4.21b.

However, this analysis focused on the end-member case where the layers were either saturated with 100% gas or 100% brine. As can be seen in Figure 4.18, at a uniform CO_2 saturation of 0.05 (Reuss average), the velocity of the rock is already greatly reduced. Hence, if Caspari *et al.* (2015) had modelled layers with 100% gas or 5% gas (95% brine), the velocity would lie close to the Reuss average, irrespective of the heterogeneity length scale. This means that if the CO_2 saturation across the injection interval is uniformly above ∼0.05, the Reuss average is the most suitable for estimating the velocity-saturation relationship.

This has also has important implications for the seismic response of residually trapped CO_2.

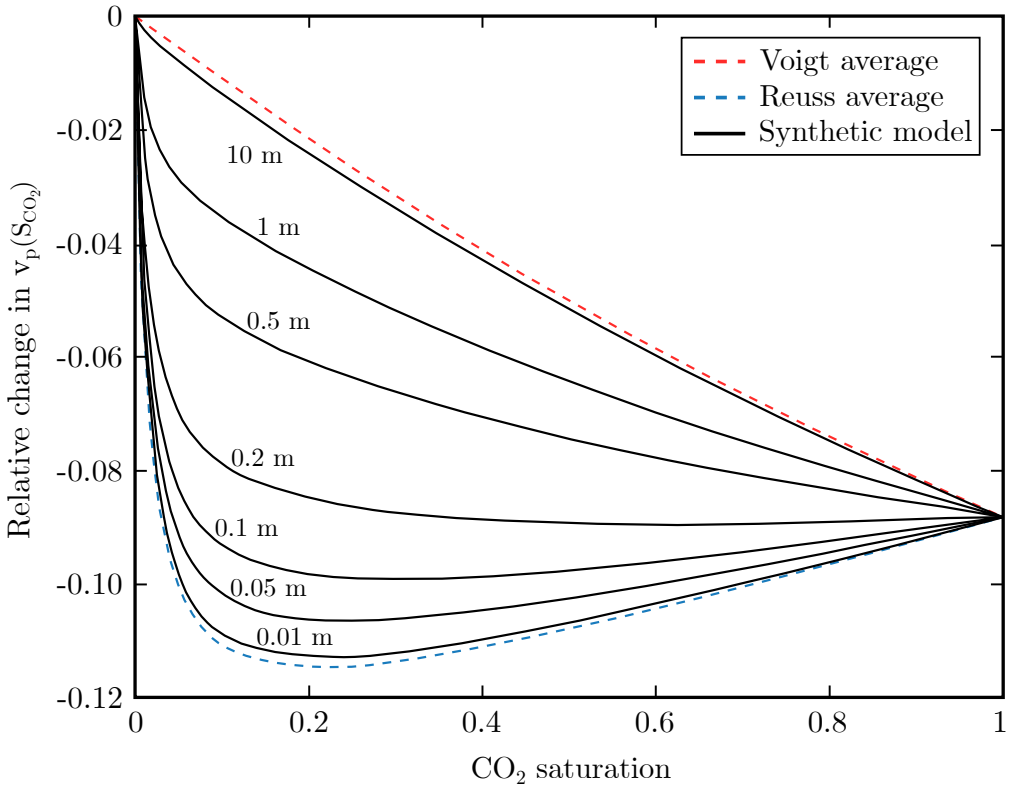

Figure 4.20: Sensitivity of seismic velocity to saturation heterogeneity. Figure adapted from Caspari *et al.* (2015).

During the Stage 2B phase of the Otway Project, the residual gas saturation in the PS2 unit of the Paaratte Formation was estimated to be between 0.18-0.22. At this saturation, the velocity of the rock will be reduced and hence cause a brightening of the reflection on the seismic survey. Therefore, the seismic anomaly associated with the injected CO_2 will indicate where both the active CO_2 plume and the residually trapped CO_2 are located.

Pulsed neutron log saturation measurements

The CO_2 saturation in the CRC-1 and CRC-2 wells was measured 1 month after CO_2 injection finished by pulsed neutron logging (Marsh *et al.*, 2018). A pulsed neutron tool emits high energy neutrons that interact with neutrons in the formation producing gamma rays which are detected by several detectors. There are two types of gamma rays produced at varying depths in the formation (Inanc *et al.*, 2009). These are inelastic gamma rays, formed by inelastic interactions between fast neutrons and nuclei in the environment close to the logging tool, and capture gamma rays, formed when neutrons are capture by the nuclei,

which can only happen when the neutrons have lost nearly all their energy and hence are formed further from the borehole. Ratios of the gamma ray count between the short space and long space detectors can be used to calculate the CO_2 saturation.

RIN13 is the ratio of the inelastic gamma ray count and has a 15-25 cm depth of investigation (Figure 4.21b). RATO13 is the ratio of the capture gamma ray count and has a 30-40 cm depth of investigation (Figure 4.21d). Other measurements from the pulsed neutron tool are the formation corrected sigma (SGFC), which is derived from the rate of captured neutrons in the formation and has a 30-40 cm depth of investigation (Figure 4.21e), and the RBOR, which measures the neutron decay rate at the short space detector, and is used to detect the presence of CO_2 in the annulus between the tubing and casing (Figure 4.21c). The vertical resolution is defined by the source detector spacing, here around $\sim$30 cm.

Gas saturation is computed using a pulsed neutron measurement (RIN13 or RATO13), and a corresponding Monte Carlo N-Particle (MCNP) model, which predicts pulsed neutron responses in particular borehole environments given inputs such as lithology, fluid properties and borehole specifications (Carter & Cashwell, 1975; Forster *et al.*, 1990).

Pulsed neutron log measurements for the CRC-2 injection well are shown in Figure 4.21b-e, along with the permeability structure of the formation (Figure 4.21a). The CO_2 saturation varies across the formation, with higher saturations generally corresponding to regions with high permeability. The highest saturation region is found at the top of the injection interval, where the CO_2 saturation is 1. The RIN13 log shows a high saturation region above the injection interval, but this is thought to be due to CO_2 within the tubing-to-casing annulus at depths of $\sim$1437-1453 m, which can be seen in the RBOR log. The RATO13 log also detects some CO_2 at these depths, but there is no indication of CO_2 in the SGFC log. The CO_2 saturation across the rest of the injection interval varies between in the 0.1-0.5 RIN13 log and 0.2-0.8 in the RATO13 log. This difference is due to re-invasion of water into the perforations after CO_2 injection has finished, which affects the RATO13 log less as it is more sensitive at further distances in the formation.

Differences in the resolution of the MCNP input data and pulsed neutron data can cause bed boundary effects and minor depth-matching variations that result in discrete spikes on

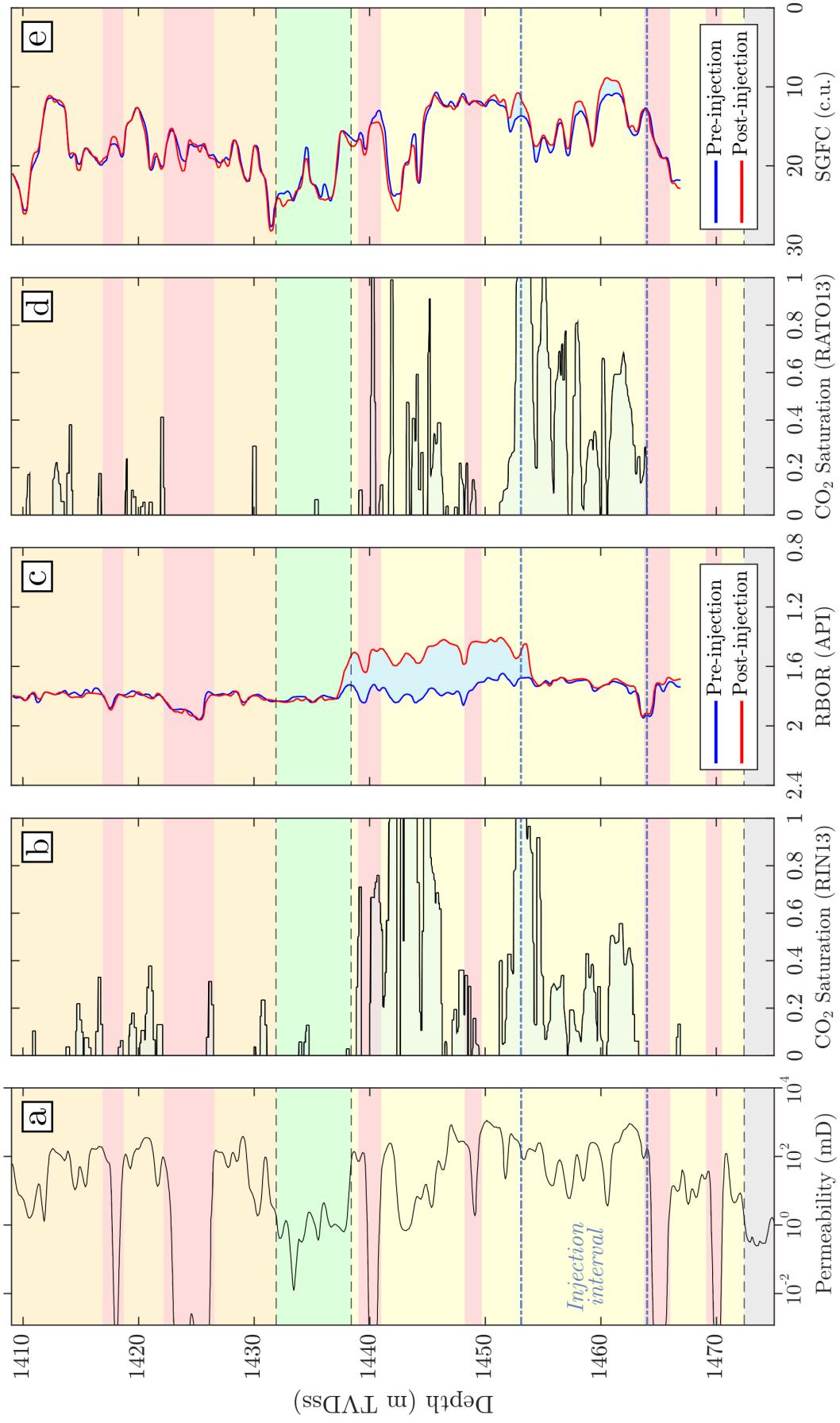

Figure 4.21: CO_2 saturation logs for well CRC-2. Data from Marsh *et al.* (2018).

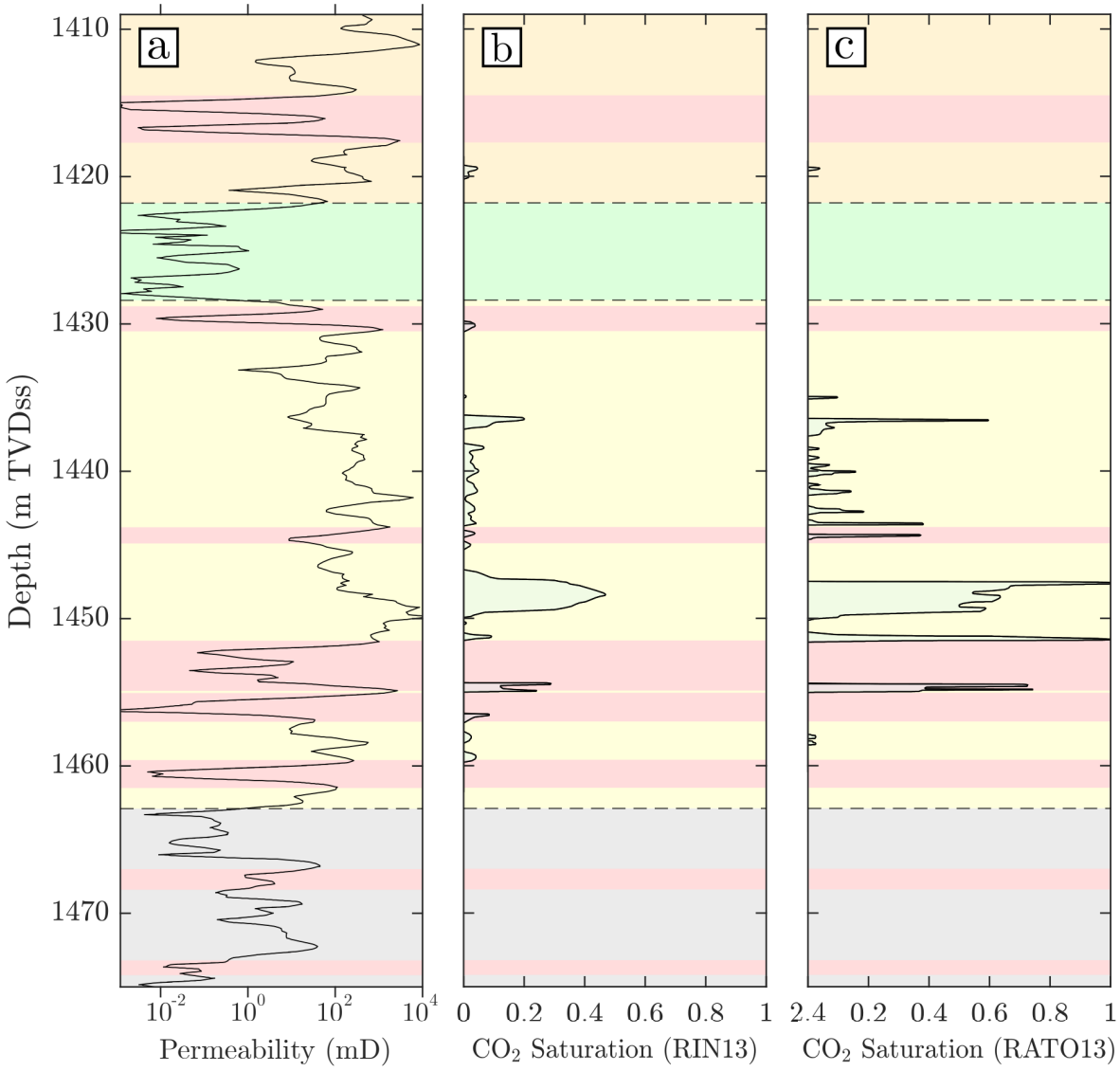

Figure 4.22: CO_2 saturation logs for CRC-1. Data from Marsh *et al.* (2018).

the gas saturation log at depths where no CO_2 is present (Marsh *et al.*, 2018). This explains the spikes in CO_2 saturation above the FS1 caprock seen in the RIN13 and RATO13 logs.

Saturation measurements for the CRC-1 observation well are shown in Figure 4.22, and good agreement is seen between the RIN13 and RATO13 logs. There is a ∼3 m interval from 1447-1450 m depth where the saturation varies from 0.4-0.6. Above this, there is a ∼10 m interval of low saturation (∼0.05-0.1) also seen in both logs.

4.7.4 Seismic Reflections of the Injected CO_2

Now that I have determined the velocity of the reservoir rock for varying CO_2 saturations, I can investigate how this is expected to affect the seismic response of the reflection survey. Following the analysis of (Arts *et al.*, 2004; Chadwick *et al.*, 2005; Cowton *et al.*, 2016), I consider the amplitude change of a seismic wavelet caused by changes in impedance of the Paaratte formation due to the presence of CO_2 and interference of seismic wavelets which is strongly dependent on the thickness of the CO_2. I model a zero-phase Ricker wavelet, $\psi(t)$, with normalised amplitude

$$\psi(t) = [1 - 2\pi f_p(t - t_1)^2] \exp[-\pi f_p(t - t_1)^2], \tag{4.16}$$

where t is time, t_1 is the time position of the peak of the wavelet and f_p is the peak frequency of the wavelet (Ryan, 1994), estimated at 40 Hz for the Stage 2C time-lapse seismic by (Glubokovskikh *et al.*, 2020), using the algorithm by Walden & White (1998) in a 940 to 1240 ms window. Where this wavelet meets a boundary, such as a change in rock type, the amplitude and polarity of the reflected wavelet is dependent on the change in impedance at the boundary. If two boundaries, such as the top and bottom of a CO_2 saturated layer, are in close proximity, the reflected wavelets from both boundaries will interfere, forming a composite wavelet with amplitude, arrival time and shape strongly dependent on the spacing of the boundaries. I model the expected composite wavelet along the length of a wedge-shaped low impedance layer that forms when reflected wavelets from the top and bottom of the layer interfere (Figure 4.23). The composite wavelet produced by interference has the form,

$$\chi(t) = A_1[\psi(t) + A_r\psi(t + \delta)], \tag{4.17}$$

where δ is the separation of the upper and lower boundaries in two-way travel time (TWTT), A_1 and A_2 are the amplitudes of the reflections from the upper and lower boundaries and $A_r = A_2/A_1$. A_1 and A_2 are dependent on the impedance contrast at the boundaries, which can be caused by contrasting lithologies or CO_2 saturation in the pore space.

There are two features of the seismic waveforms plotted in Figure 4.23 which can be used to estimate CO_2 thicknesses below the tuning thickness (Cowton *et al.*, 2016; Furre *et al.*,

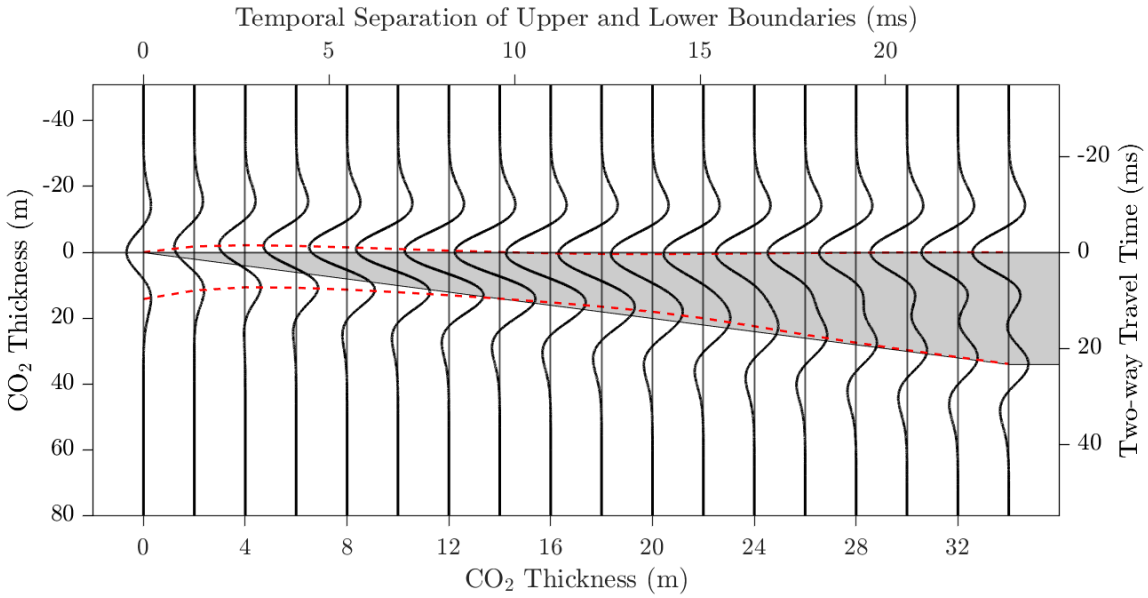

Figure 4.23: Seismic reflection modelling of a wedge of CO_2. Grey wedge represents a wedge of CO_2-saturated PS1 sandstone under a FS1 caprock with properties given in Table 4.3. Black wiggle at CO_2 thickness of 0 represents the seismic trace obtained by convolving the impedance contrast between FS1 and PS1 with a zero-phase Ricker wavelet. The subsequent wiggles are the composite wavelets formed from the interference between seismic traces formed at the top and bottom of the CO_2 wedge. Red dashed lines mark the maximum and minimum amplitude position of the seismic waveform.

2015; Ghaderi & Landrø, 2009). Firstly, as the thickness of the CO_2 layer gets larger, that maximum amplitude of the resultant wavelet gradually increases up to a peak value at a CO_2 layer thickness of 14.5 m. This thickness is known as the tuning thickness, and is commonly thought of as the minimum thickness that can be resolved seismically by measuring the distance between the top and bottom reflections. Secondly, for CO_2 layer thicknesses up to 15 m, there is a decrease in TWTT of the amplitude peak due to interference between the top and bottom reflections. Both these trends are illustrated in Figure 4.24, which shows the minimum amplitude of the negative amplitude reflection at the top of the CO_2 layer and the change in TWTT of the peak of the top reflection as a function of CO_2 thickness.

The colours in Figure 4.24 illustrate the effect of varying the average CO_2 saturation on the amplitude and time anomaly response. The velocity of the CO_2 layer has been estimated using the Reuss average for an average CO_2 saturation of $S_{CO_2} = 0.5$. The CO_2 saturation will change the seismic velocity, which will in turn affect the seismic response of the CO_2 layer. Higher CO_2 saturations result in slightly larger amplitude changes because of the

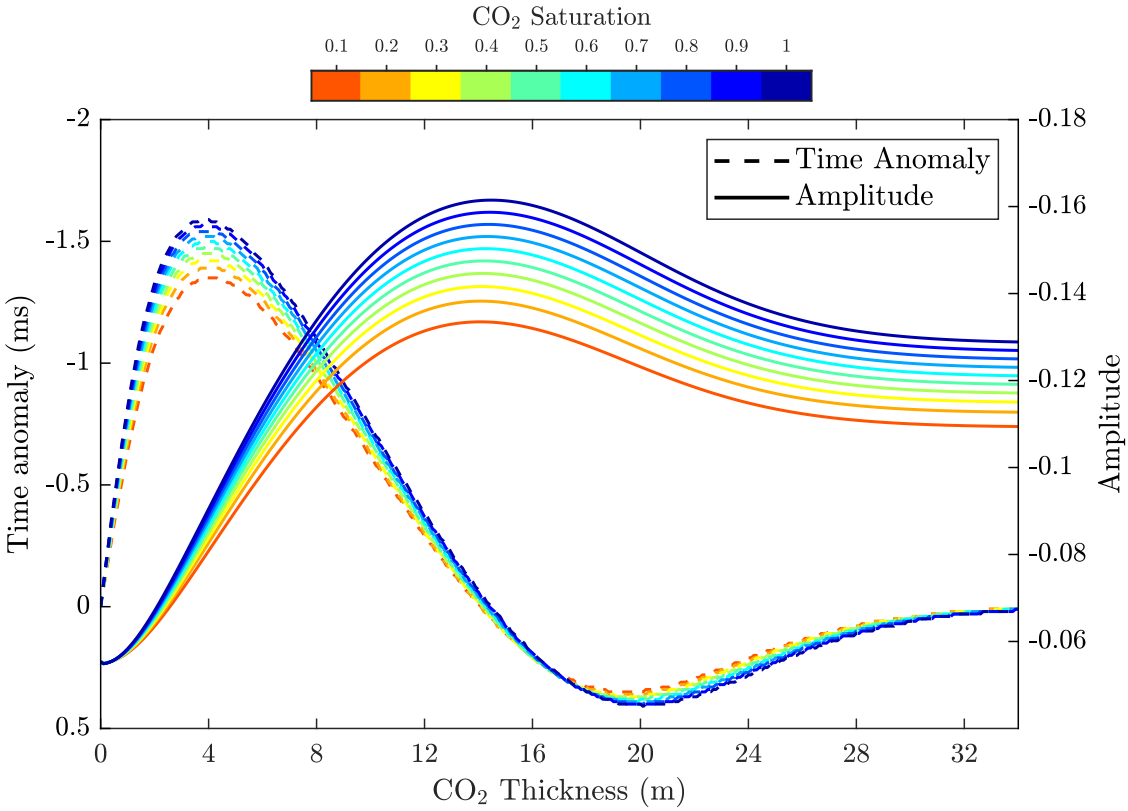

Figure 4.24: Dashed lines = Two-way travel time of the minimum amplitude position of the seismic waveforms shown in Figure 4.23 relative to the waveform formed when no CO_2 is present. Solid lines = Minimum amplitude of the composite waveform. The effect of changing the CO_2 saturation of the wedge is described by the colour of the lines.

increased impedance contrast due to the lower density of the CO_2 saturated rock.

4.7.5 Waveform modelling of synthetic reservoir models

The seismic waveform analysis described above assumes that the CO_2 layer ponds directly below a low permeability caprock and saturates the uppermost region of the reservoir rock. However, the saturation logs in Figures 4.21 and 4.22 suggest that the injected CO_2 remains largely confined to the injection interval, which is towards the middle of the PS1 formation. Therefore, to determine whether the TWTT and amplitude dependence on CO_2 thickness shown in Figure 4.24 still hold for the Stage 2C injection, I model the resultant seismic waveform from a synthetic reservoir consisting of units PS2, PS1, FS1 and Skull Creek Mudstone, using thicknesses and average properties obtained from well logs given in Table 4.3 (Figure 4.25a,b). I also model the synthetic case including a 10 m thick CO_2 saturated

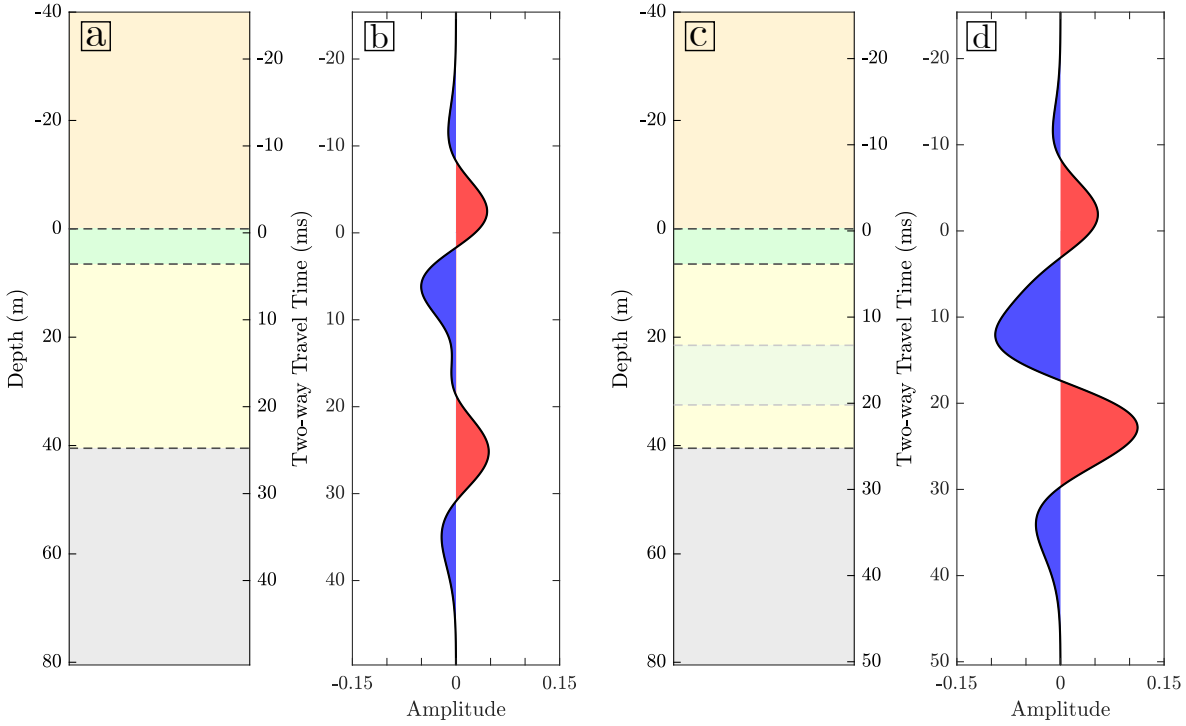

Figure 4.25: Synthetic seismic waveform for injection location. (a) and (c) Simplified geological model for the injection region without and with a 10 m interval of CO_2-saturated rock. Depths and geological units taken from the CRC-2 well log. Geological model units: Orange = PS2, Green = FS1, Yellow = PS1, Grey = Skull Creek Mudstone, Light blue = CO_2-saturated PS1. (b) and (d) Resultant composite wavelet formed by interference of the reflections from each impedance boundary.

layer with average saturation $S_{CO_2} = 0.5$ across the injection interval (Figure 4.25c,d).

The addition of a CO_2 layer results in a large increase in amplitude for the negative and positive peaks at 5 ms and 25 ms TWTT respectively. The peak of the negative reflection also displays noticeable push down, shifting down 7 ms. There is also a smaller increase in amplitude for negative and positive peaks at 35 ms and 0 ms TWTT. These synthetic waveforms can be compared to the observed seismic waveforms in the time-lapse surveys.

Figure 4.26 shows a close-up of the baseline and TL3 seismic surveys around the injection zone. In the baseline survey, there is a clear negative amplitude anomaly above and positive amplitude anomaly below the injection spot. The peaks of these anomalies are 10 - 15 ms apart, which is less than the 20 ms difference in TWTT between the same peaks in the baseline synthetic waveform (Figure 4.25b). Both of these reflections increase significantly

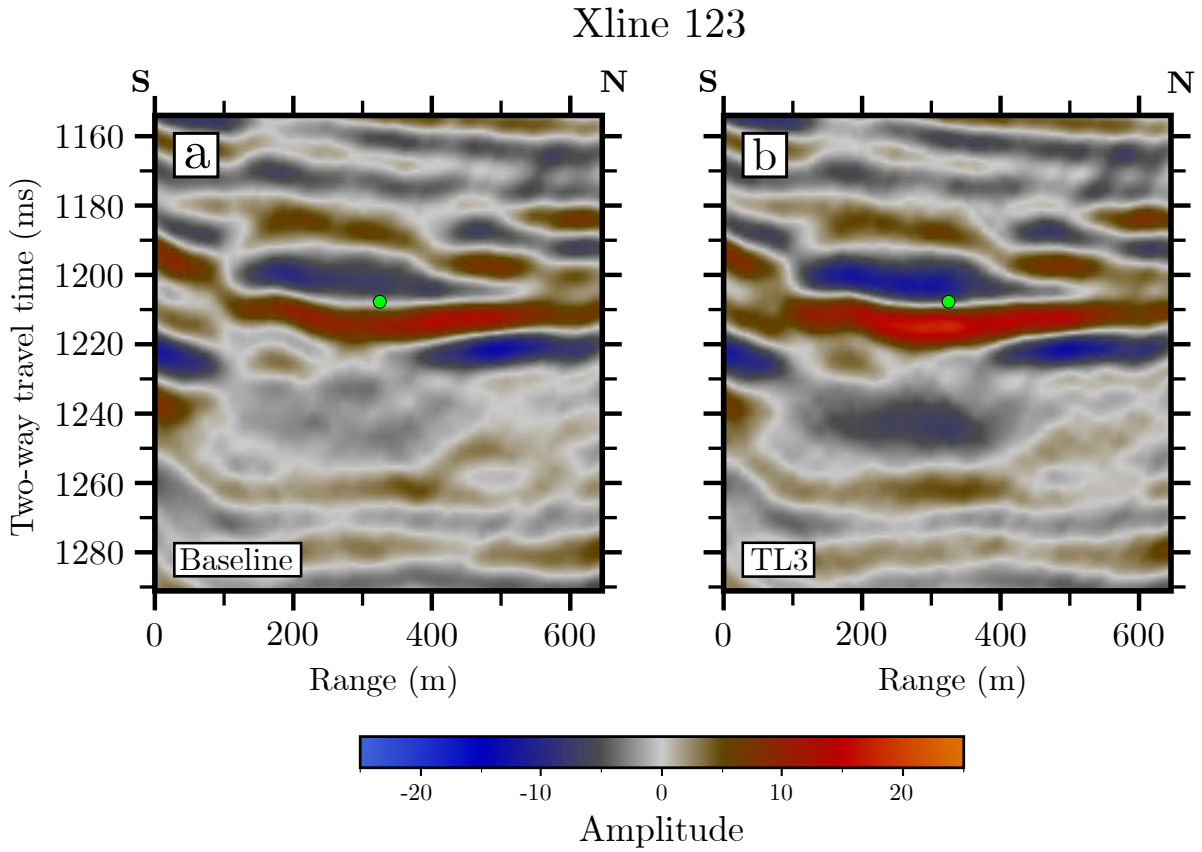

Figure 4.26: Close-up of baseline (a) and TL3 (b) seismic surveys for cross-line 123. Injection location marked by green circle.

in amplitude in the TL3 seismic survey, as a result of the CO_2 present. However, there is no noticeable shift in the travel time of the observed negative amplitude anomaly, in contrast to the synthetic case, suggesting that the simple reservoir model does not explain the observed seismic waveform.

Seismic response of the calcite baffles

The calcite baffles that overprint the geology and can be seen in the well log data are not included in the synthetic reservoir models presented above. It is possible that the thickness of the calcite baffles may be lower than the minimum detectable thickness, in which case they will not appear in the seismic waveform. To determine the minimum thickness of calcite baffle that may be detected, I model a calcite baffle of variable thickness with velocity $v = 3800\,\mathrm{m\,s^{-1}}$ and density $\rho = 2700\,\mathrm{kg\,m^{-3}}$, within a section of PS1 and plot the resultant synthetic waveform (Figure 4.27). Baffles thinner than $\sim$1 m are below the seismic resolution

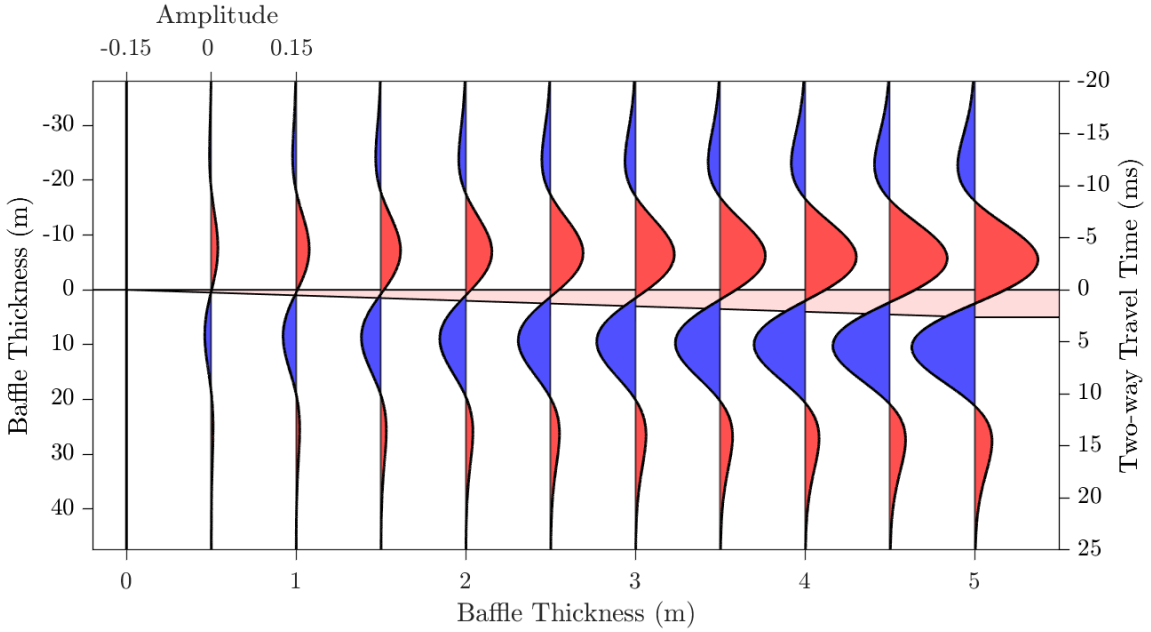

Figure 4.27: Seismic reflection modelling of calcite baffles. Red wedge = baffle with velocity $v = 3800\,\mathrm{m\,s^{-1}}$ and density $\rho = 2700\,\mathrm{kg\,m^{-3}}$ within a section of PS1 sandstone. Resultant waveforms are formed by interference of the reflections from the top and bottom of the baffle. The frequency of the source wavelet used is 40 Hz.

and will not affect the composite waveform for the formation. However, baffles thicker than this show significant amplitude anomalies, and should be included in synthetic waveform modelling as they will affect the resultant waveform.

Figure 4.28a shows the synthetic geological model for the CRC-2 well now including the calcite baffles. The peaks and troughs in the resultant seismic waveform (Figure 4.28b) seem to correspond with heights at which the baffles are located, rather than changes in geological units. On comparison between the synthetic waveforms and the observed waveforms (Figure 4.26), there is good agreement between the positions of amplitude peaks and troughs. The amplitudes of the negative and positive anomalies above and below the injection zone increase significantly with the addition of CO_2, as well as a noticeable increase of the lower negative amplitude anomaly, which is reflected in the seismic observations. There is also no noticeable push-down of the negative amplitude anomaly, which agrees with observation.

The synthetic waveform from the geological model containing the calcite baffles matches the seismic response of the time-lapse seismic surveys. This is important for interpretation of the seismic surveys, as it suggests that the seismic anomalies correspond to locations of the

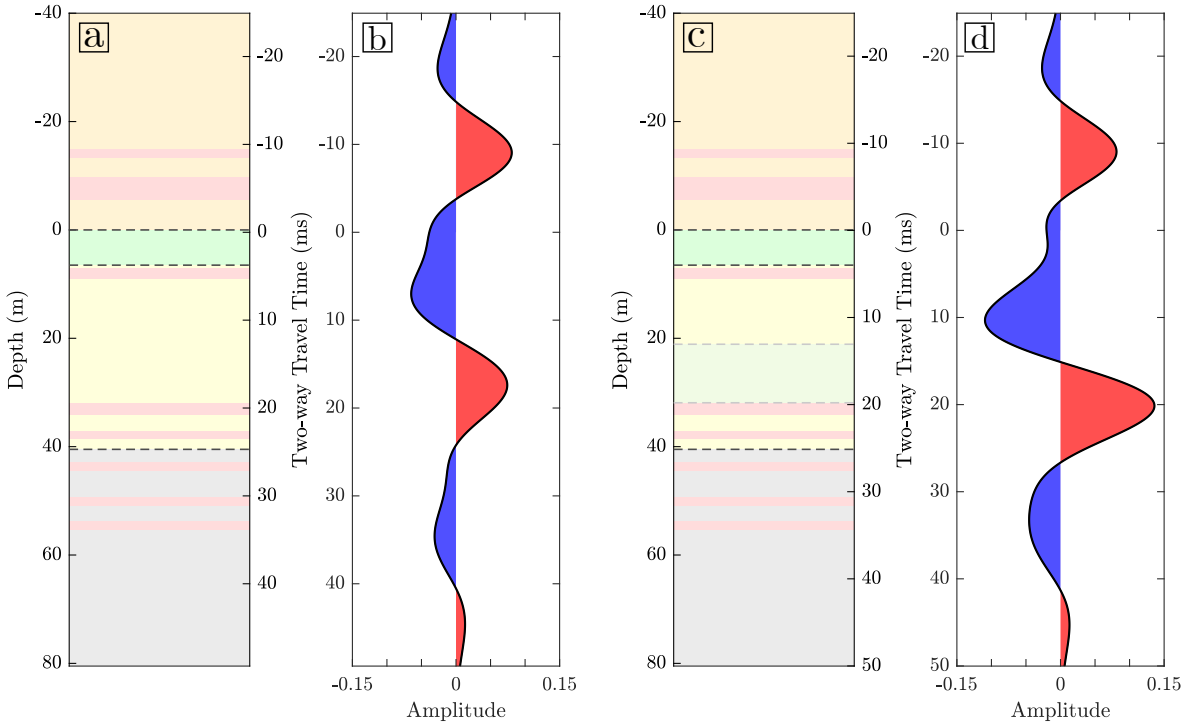

Figure 4.28: Synthetic seismic waveform for injection location including calcite baffles. (a) and (c) Simplified geological model for the injection region without and with a 10 m interval of CO_2-saturated rock. Depths and geological units taken from the CRC-2 well log. Geological model units: Orange = PS2, Green = FS1, Yellow = PS1, Grey = Skull Creek Mudstone, Red = Calcite baffles, Light blue = CO_2-saturated PS1. (b) and (d) Resultant composite wavelet formed by interference of the reflections from each impedance boundary.

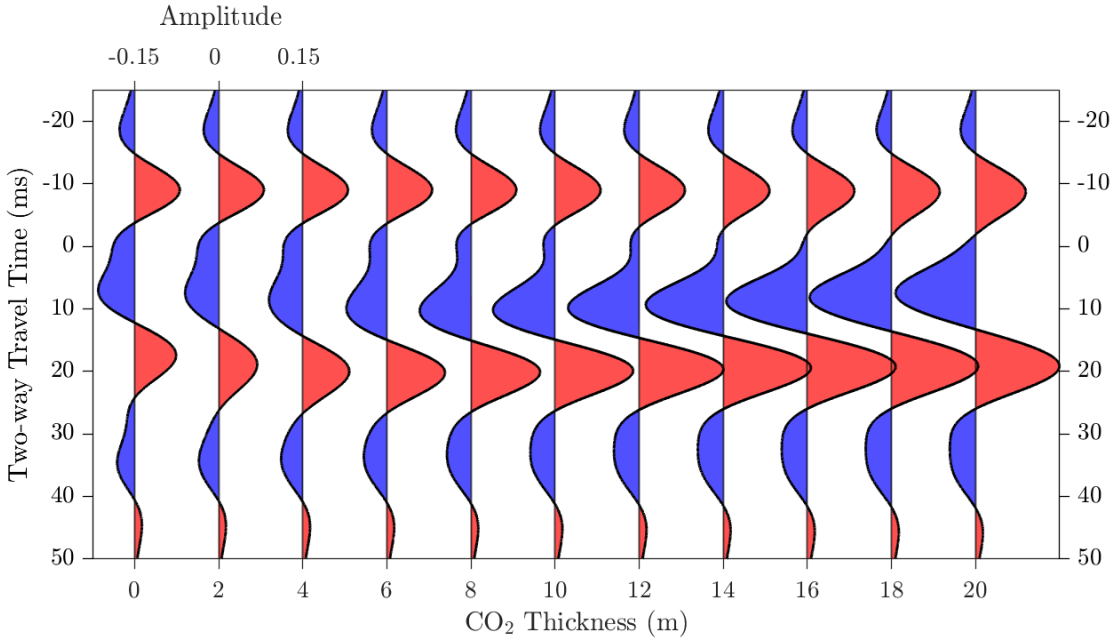

Figure 4.29: Seismic waveform modelling of the CRC-2 well with varying CO_2 thickness. Simplified geological model including calcite baffles (Figure 4.28c) including a layer of CO_2-saturated rock with thickness indicated on the x-axis. Resultant composite waveform formed by interference of the reflections from each impedance boundary is plotted.

calcite baffles, rather than larger scale changes in the geological units.

The effect of adding calcite baffles to the geological model on the amplitude and time anomaly of the seismic waveform is now investigated. The resultant waveforms when adding a layer of CO_2-saturated rock ($S_{CO_2} = 0.5$) of varying thickness (increasing from the bottom of the injection interval upwards) to the synthetic reservoir model is shown in Figure 4.29. The minimum and maximum amplitudes of the negative and positive anomalies associated with the top and bottom of the CO_2 layer respectively, are plotted as a function of CO_2 thickness, as well as the change in travel time anomaly with respect to the baseline survey (Figure 4.30). Both amplitude anomalies show the same general trend, with a small initial decrease in amplitude at small CO_2 thickness followed by a relatively linear increase in amplitude until a thickness of around 16 m where further increases in CO_2 thickness results in a reduction in amplitude. In contrast to the CO_2 wedge below a caprock presented in Figure 4.23, there is an increase in TWTT for CO_2 thicknesses up to ~8 m, after which the time anomaly decreases again.

When the time anomaly between the baseline and time-lapse seismic surveys is calculated

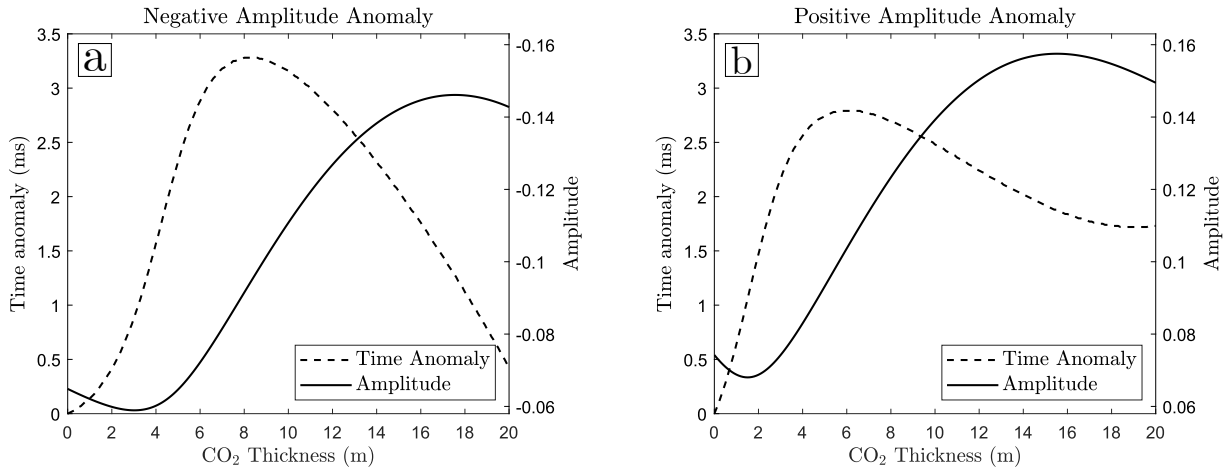

Figure 4.30: Two-way travel time and amplitude anomalies for varying CO_2 thickness at the CRC-2 well. Position and amplitude of the (a) trough and (b) peak in figure 4.29.

around the CO_2 plume, there is significant noise over a ± 2 ms range, especially in close proximity to the fault. This makes attributing any changes in TWTT which may be due to the presence of CO_2 difficult. There is also noise in the amplitude difference over a ± 1 range, but regions associated with the plume show amplitude differences up to 11, so are well above the noise threshold (e.g. see Figure 4.15). For this reason, I can not use travel time anomalies to constrain CO_2 thicknesses and am limited to changes in amplitude.

4.8 Finding the thickness of the CO_2 plume

4.8.1 Amplitude-thickness relationships

Time-lapse surveys TL1, TL2 and TL3 all take place during, or immediately following the injection phase, so the volume of CO_2 within the reservoir during these surveys is known. This information is used to estimate the thickness of the CO_2 layer in these surveys, assuming that the thickness of the plume scales like some monotonic function of the amplitude. To motivate the form of this function, I take the results of the synthetic study shown in Figure 4.30, and plot the thickness of the CO_2 layer as a function of the change in amplitude of the positive anomaly associated with the base of the CO_2 layer (Figure 4.31a). Above a CO_2 layer thickness of 3 m, the thickness scales relatively linearly with amplitude change up to a

thickness of ∼15 m.

The amplitude difference maps of the time-lapse plume shown in Figure 4.15f-h are used to constrain the amplitude-thickness relationship. This is done by converting amplitude to thickness using the polynomial function that returns the minimum least squares misfit between the known injected CO_2 mass and the calculated total mass across the plume using that function (Figure 4.31c). Since the CO_2 mass of the plume depends on the CO_2 saturation, a different minimum misfit polynomial function is found for each CO_2 saturation, assuming an average CO_2 saturation across the plume. Hence, when using conservation of mass to convert from amplitude to thickness, there is a trade-off between the average CO_2 saturation and the thickness of the plume. Therefore, unless the average CO_2 saturation distribution across the plume is known, amplitude measurements alone cannot be used to calculate the thickness of the CO_2 layer. In addition, using a conservation of mass statement to calculate the thickness of the CO_2 plume likely leads to an overestimate, as the areas of the plume which are below the limit of seismic detection are not counted within the total plume volume.

4.8.2 Thickness derived from acoustic impedance change obtained from seismic inversion

Changes in amplitude from a single horizon are unable to constrain the thickness of the CO_2 layer. It is also not possible to pick the top and bottom of the plume from a vertical slice of the difference seismic as interference in the waveform means that time-lapse amplitude anomalies are seen well above and below the CO_2 layer, as demonstrated by the synthetic waveforms in Figure 4.28. A seismic inversion workflow has been developed by Glubokovskikh *et al.* (2020), which uses knowledge of the source wavelet and the measured time-lapse response to invert for the three-dimensional impedance structure of the reservoir. Their approach was tested on the Otway 2C dataset and shown to be able to characterise a small CO_2 plume.

In their analysis, CO_2 is detected when the change in impedance from the baseline survey to time-lapse survey is above a pre-defined threshold value. The CO_2 thickness is calculated from the two-way travel time between the top and bottom of the impedance anomaly using a

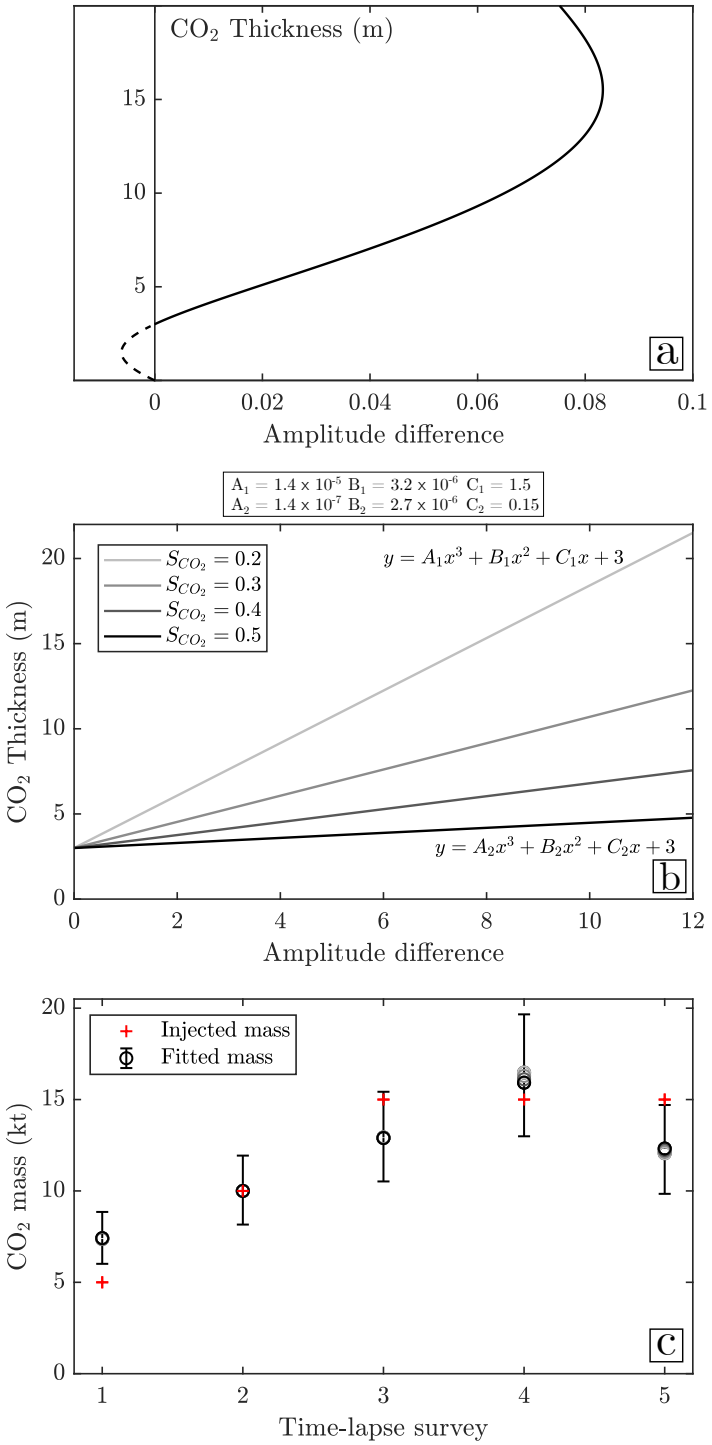

Figure 4.31: (a) Change in maximum amplitude of the positive anomaly associated with the base of the CO_2 layer plotted as a function of CO_2 thickness. (Adapted from Figure 4.30b). (b) Best fit amplitude difference-CO_2 thickness relationships obtained by minimising the misfit between known injected CO_2 mass and CO_2 mass in the seismic plumes in Figure 4.15f-j. Amplitude-thickness relationship is very sensitive to the average CO_2 saturation across the plume. (c) CO_2 mass obtained using the relationships in (b) compared against the known injected mass. Error bars reflect the uncertainty range in the parameters used to calculate the mass.

constant velocity of $v_p = 3200\,\mathrm{m\,s^{-1}}$. In reality, the velocity through the plume will vary by up to 10% depending on the CO_2 saturation, introducing error to the calculated thickness. The threshold impedance value chosen also introduces a trade-off between missing parts of the plume and miss-classification of noise as CO_2. During synthetic tests, plume thicknesses of 2-20 m were obtained. However, when inverting the Stage 2C seismic data, it was difficult to accurately estimate plume thicknesses below 8 m due to noise in the data, so it is likely that thin regions at the plume edge have gone undetected. Although no formal characterisation of errors in thickness estimates are given in the study, synthetic tests show that plume thickness is overestimated in the middle and is undetected at the edges, with thickness errors on the order of 20-30%. Although this method can determine the total thickness of the CO_2 plume, the CO_2 saturation throughout the plume is still unknown. The evolution of the injected CO_2 as mapped in the time-lapse seismic inversion is given in Figure 4.32. These are the CO_2 distributions used for comparison against numerical simulations performed in Chapter 5.

4.9 Summary

Stage 2C of the Otway Project involved an injection of 15,000 tonnes of CO_2-rich gas into the Paaratte formation at a depth of $\sim 1500\,\mathrm{m}$, accompanied by time-lapse seismic monitoring. A baseline seismic reflection survey was carried out prior to injection, three surveys conducted during injection and two conducted one and two years after the end of injection. Parasequence 1 (PS1), within Unit A of the Paaratte formation, was the location of the injection and comprises of deltaic sediments ranging from clay rich distal mouth bars grading to sand rich proximal mouth bars and distributary channels. The unit is relatively heterogeneous, with large variations in porosity and permeability caused by numerous calcite and dolomite cemented layers that overprint the system, formed by post-depositional precipitation from meteoric fluids at depth. These layers are around 1-2 m thick but their lateral extent is uncertain. The surfaces between parasequences are defined by extensive mudstone seals deposited in a shallow marine delta front setting. The injection interval is bounded to the south by the Naylor South splay fault, which runs parallel and eventually joins the

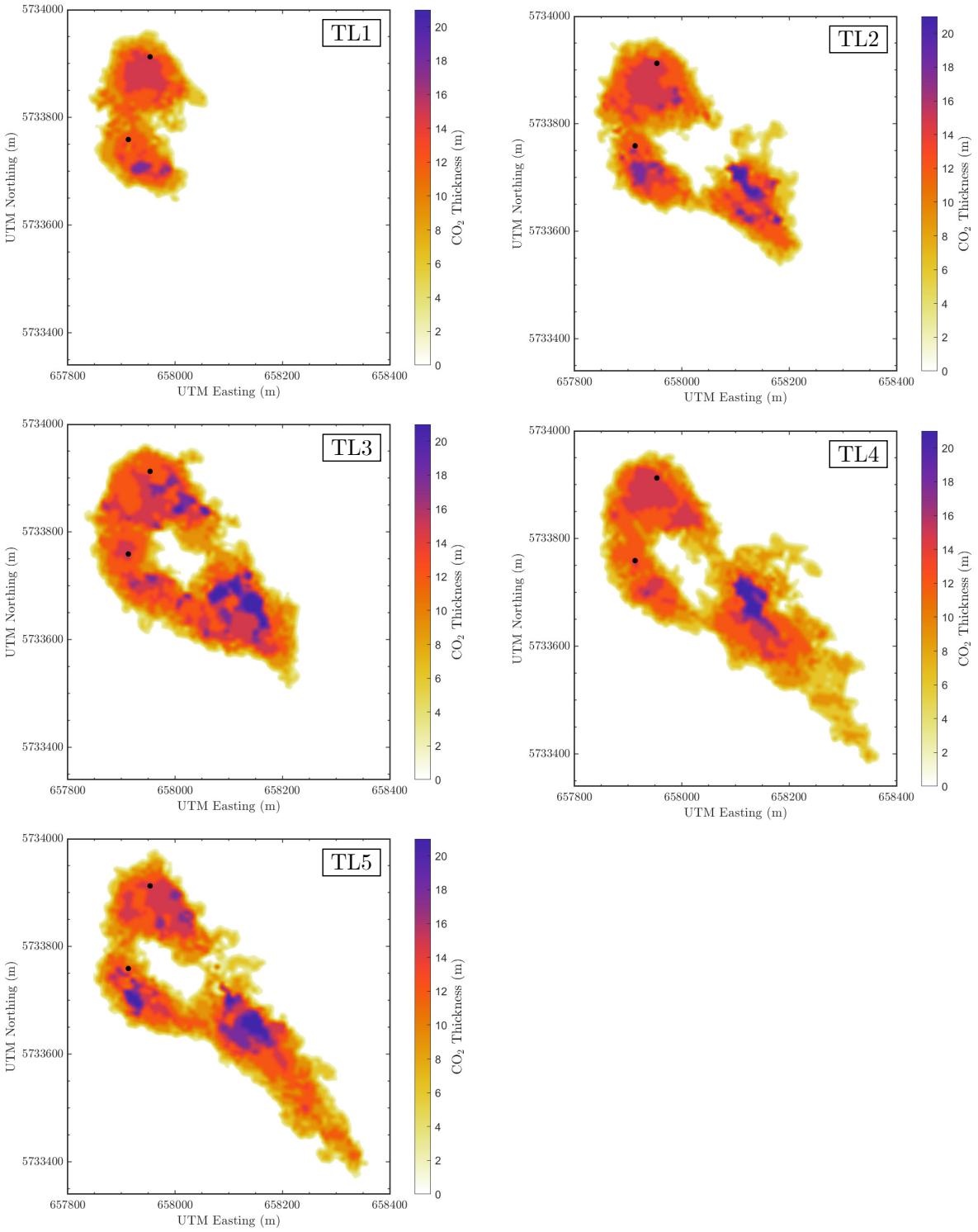

Figure 4.32: CO_2 plume thickness maps for the Otway Stage 2C injection. Thickness is computed from the two-way travel time thickness of the difference impedance above a threshold value using a constant velocity $v_p = 3200\,\mathrm{m\,s^{-1}}$. Data from Glubokovskikh *et al.* (2020).

larger Naylor South fault. The splay fault has a maximum offset of 15-30 m.

Comparison between the baseline seismic survey and subsequent post-injection surveys shows an increased amplitude positive and negative reflection around the injection zone. Analysis of seismic difference volumes reveals an amplitude anomaly associated with the CO_2 plume that spreads and extends along the fault zone towards the southeast, forming an elongate plume roughly 750 m in length. Highest amplitudes, and hence likely the thickest region of the plume, are seen around the injection region. The areal extent of the anomaly varies depending on the horizon analysed and the differencing method used, but all horizons display the same overall behaviour of an increase in plume area during injection followed by a period of steady areal extent with possible decline at later times.

Waveform modelling of a synthetic geological model of the target formation built from well log data suggests that high amplitude reflections correspond to calcite baffles, rather than changes in geological units. Modelling a CO_2 layer of variable thicknesses in the synthetic model shows that there is a roughly linear scaling between the amplitude difference and CO_2 thickness. The total volume of CO_2 injection into the reservoir can be used to constrain the exact amplitude-thickness scaling, provided the CO_2 saturation in the plume is also known. The CO_2 saturation at the CRC-2 injection well and CRC-1 observation well was measured by pulsed neutron logging one month after injection. An average CO_2 saturation of 0.5 with saturations up to 1 over a 10 m interval was measured at the injection well, and CO_2 saturations of 0.4-0.6 over a 3 m interval was measured at the observation well. The lack of further constrains on the CO_2 saturation in the plume mean that amplitude measurements alone cannot be used to estimate the thickness of the CO_2 plume, as there is a trade-off between CO_2 saturation and layer thickness. The CO_2 thickness measurements used for comparison against numerical simulations in Chapter 5 are obtained from a seismic inversion workflow developed by Glubokovskikh *et al.* (2020), which uses knowledge of the source wavelet and the measured time-lapse response to invert for the three-dimensional impedance structure of the reservoir.

The main objective of time-lapse seismic reflection surveys for CO_2 storage is to image the extent and growth of the plume through time. The technique is good at imaging the areal extent of a plume, with the caveat that areas of the plume where the thickness is below

the seismic detection threshold can go unseen. For small CO_2 volume injections, such as at the Otway site, this may be a significant fraction ($\sim$40%) of the total plume area, whereas the fraction of the plume below the detection limit at industrial scale storage sites would be less. Another limitation of seismic reflection surveys is that they are poor at resolving saturation heterogeneity within the plume, and differentiating between the active CO_2 phase and residually trapped CO_2. This could mean that areas of the plume could be filling in, (i.e. the saturation is increasing but the total thickness remaining constant), but this would go undetected in the seismic data. Nevertheless, if the user understands the extent of the information that can be gained from seismic reflections surveys, they remain a useful tool for monitoring the flow of CO_2 in the subsurface.

Chapter 5

Vertically-integrated flow simulations of the Otway Stage 2C Injection

5.1 Introduction

Numerical simulations of CO_2 flow prior to injection are an important means to test the suitability of storage sites as well as for identifying potential leakage pathways or other hazards prior to injection. Accurate numerical modelling of CO_2 flow in storage reservoirs is difficult, as it relies on having detailed knowledge of the geological structure and stratigraphy of the target reservoir, which may included large variations in properties such as porosity and permeability on length scales below the resolution of seismic imaging or well log measurements. In addition, secondary processes that occur following injection of CO_2 into a reservoir, such as dissolution and capillary trapping, take place across distances down to the pore scale (mm), and modelling this detail over the large length scales (km) and time scales of CO_2 injections is impractical. Opportunities to test the ability of these models to predict

plume migration and trapping in reservoir settings are also limited due to the relatively small number of monitored CO_2 injections both at the pilot and commercial scale, and due to the difficulties in accurately determining the exact extent, thickness and saturation distribution of the CO_2 plume post injection.

Previous flow modelling of the Otway Stage 2C injection (Glubokovskikh *et al.*, 2020; Watson *et al.*, 2012, 2018) was undertaken using the commercial flow simulation package Eclipse300, which solves Darcy's law for flow in porous media on a three-dimensional grid. Flow is driven by pressure gradients caused by injection of CO_2 into the reservoir and by buoyancy forces. Due to the large number of parameters, Darcy flow simulators can be computationally expensive meaning that grid sizes may be large compared to the bedding, on the order $50 \times 50 \times 20$ m. The geological models used in these Darcy flow simulations were created using a sequential indicator simulation (SIS) (Journel & Alabert, 1990). Here, the geological model is built from the well log facies data at well locations, but away from the wells it is randomly generated, guided by variograms and depositional environment analogues (Dance *et al.*, 2019). Figure 5.1a shows an outline of the CO_2 plume from the pre-injection numerical flow simulation from Watson *et al.* (2012) for the Stage 2C injection two years after injection (red), as well as the outline of the fifth time-lapse seismic plume (TL5) from Glubokovskikh *et al.* (2020) for comparison. There is significant spreading of the simulated plume towards the north-east, due to a local topographic high in the high permeability sandstone within the geological model used.

After injection, history matching of the Stage 2C time-lapse data was used to update the reservoir model to calculate key patterns in the monitoring data. This included the addition of two more smaller internal splay faults which run parallel to the main splay fault. These faults have a low across-fault permeability, which helps account for the bifurcation seen within the observed plume (Figure 4.5), and also have a high permeability fracture zone associated with them which increases fault-parallel flow towards the southeast. Better history matching was also achieved by including a structural or stratigraphic baffle to the north-east of CRC-2, and including relative permeability functions and end-point saturation data determined from experimental measurements on CRC-2 core samples (Watson *et al.*, 2018). The history matched numerical simulation using the new geological model is shown in Figure

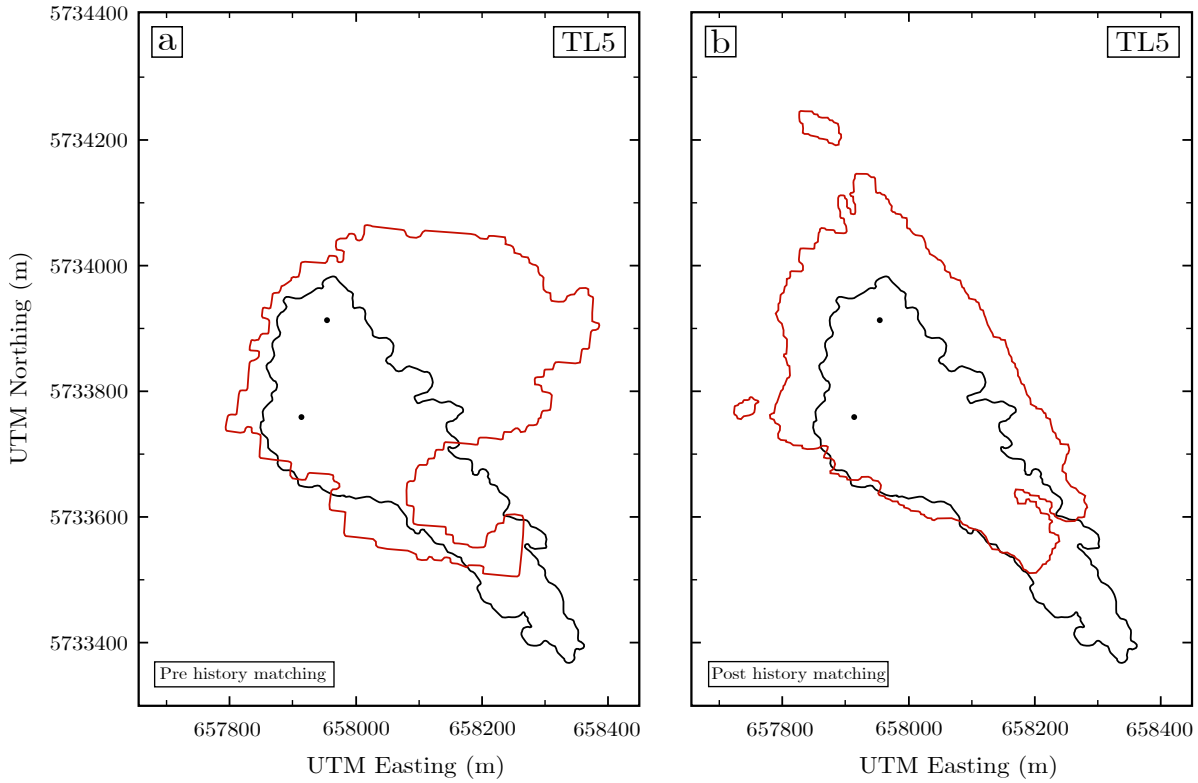

Figure 5.1: (a) Red line = Pre-injection numerical flow simulation from Watson *et al.* (2012), produced using Eclipse simulator with a 5% gas saturation cut-off. Black line = Outline of TL5 plume from Glubokovskikh *et al.* (2020). (b) Red line = History matched numerical flow simulation incorporating stratigraphic baffle to the north east of CRC-2 and relative permeability and end-point saturation data (Glubokovskikh *et al.*, 2020; Watson *et al.*, 2018). Black line same as (a).

5.1b and shows a more comparable shape to the measured plume.

The velocity of a fluid travelling through a porous media can be evaluated using Darcy's equation, which forms the basis for a suite of analytical models describing the flow of CO_2. Bear (1988) first derived a sharp-interface, vertical-equilibrium gravity current model accounting for the slope of the aquifer and confining horizons above and below the flow. Huppert & Woods (1995) found that for unconfined gravity currents on a slope, the flow of the injected fluid would initially be driven by diffusive gravitational slumping of the current, and at later times dominated by advection of the fluid up-slope. Analytical solutions for radial flow on a horizontal boundary were given for unconfined flows by Lyle *et al.* (2005) and the three-dimensional case for an unconfined gravity current on a slope was studied by Vella & Huppert (2006). In their analysis they suggest a timescale at which point the current transitions from spreading axisymmetrically to spreading predominantly downslope. Using

injection and fluid parameters representative of the Otway Stage 2C injection and PS1 storage formation, their analysis suggests the CO_2 movement would be dominated by advection after 1.4-4.9 years, which is well within the time scale captured by the time-lapse seismic surveys.

CO_2 injection into a vertically confined aquifer introduces new dynamics compared to unconfined flows. While flows in unconfined media are driven solely by the buoyancy of the CO_2, confined layers have background pressure gradients, for example due to the pressure difference between the injection point and the aquifer far field, which drive fluids horizontally, with the speed at which the CO_2 front progresses outward from the injection well controlled by the mobility ratio between the CO_2 and ambient water phase (Nordbotten *et al.*, 2005; Nordbotten & Celia, 2006). Pegler *et al.* (2014a) showed that the relative importance of injection-driven flow to buoyancy driven flow can be characterised by the dimensionless ratio $\tilde{G} \equiv MH/h$, where $M = \mu_{CO_2}/\mu_{H_2O}$ is the mobility ratio (ratio of the viscosities between the CO_2 and ambient water), H is the aquifer height and h is the height of the CO_2 current. For $\tilde{G} \gg 1$, the dynamics are dominated by gradients in the hydrostatic pressure due to variations in the slope of the interface. For $\tilde{G} \ll 1$, the dynamics are dominated by background pressure gradients often due to injection.

As a CO_2 current advects up-slope, CO_2 will be permanently trapped at the receding interface of the current by capillary forces in a process known as residual trapping (Krevor *et al.*, 2015). Empirical evidence suggests the residual saturation depends on the historical maximum CO_2 saturation before imbibition (Pentland *et al.*, 2010). Both linear and non-linear trapping models are used to describe the relationship between these values. The effect of residual trapping on the post-injection spreading and up-slope migration of a CO_2 current has been incorporated into sharp-interface models (Hesse *et al.*, 2006, 2008; Juanes *et al.*, 2010; MacMinn *et al.*, 2010). Here, a constant saturation of residually trapped CO_2 is left at the receding interface of the current as it propagates, as in Kochina *et al.* (1983), causing the total volume of the active current to reduce over time. Hesse *et al.* (2008); Juanes *et al.* (2010); MacMinn *et al.* (2010) find that diffusive spreading has a negligible effect on the long-term evolution of the plume, and the essential features of the plume shape and migration are dominated by advective effects, both from up-slope migration and background

flows, as well as capillary trapping. Two-phase models using a non-uniform CO_2 saturation have also incorporated the effects of residual trapping (Golding *et al.*, 2011, 2013, 2017). Here, the residual saturation varies across the CO_2 current according to the initial-residual saturation relationship used.

Vertical-equilibrium reservoir simulators utilise the large body of work on vertical-equilibrium Darcy flow models to simulate fluid flow over the long time and length scales of CO_2 storage projects (Liu *et al.*, 2010; Nilsen *et al.*, 2016). These simulators are much more computationally efficient than commercial three-dimensional flow simulators and can be used to model fluid flow in geological settings where analytical solutions cannot be found. Computational efficiency is significantly increased as the flow of CO_2 may be solved on a two-dimensional grid due to the vertically-integrated formulation. For example, when simulating CO_2 flow in Layer 9 at the Sleipner field, Bandilla *et al.* (2014) reports running times of 12 minutes on a single core for their vertical-equilibrium model, compared to several hours on 100 cores using the TOUGH2 Darcy flow simulator. Cowton *et al.* (2018) developed a vertically-integrated reservoir simulator based on the theory of topographically controlled, porous gravity currents. This was used to invert for the spatial distribution of reservoir permeability and find a geologically informed reservoir model that produced a good match between measured and modelled CO_2 spreading in Layer 9 at the Sleipner field.

In this chapter, I further develop the reservoir simulator from Cowton *et al.* (2018) to included residual trapping at the receding interface of the CO_2 current. First, I describe the simplifying assumptions associated with the model and quantitatively assess the extent to which these assumptions hold for the Otway Stage 2C injection. Next, numerical simulations are benchmarked against analytical solutions to test the accuracy of the model. The simulator is then used to model the flow of CO_2 during the Otway Stage 2C project using average properties of the reservoir from well log data and average saturation estimates from CO_2 plume volume measurements. When comparing the CO_2 distribution to time-lapse seismic measurements, the CO_2 in simulations is seen to propagate towards the north-east instead of predominantly following the direction of the splay fault towards the south-east. The flow model is inverted to find the simplest set of reservoir parameters that minimise the difference between the observed and modelled CO_2 distribution. Better agreement is seen

between the observed and modelled CO_2 distribution when including a high permeability fault damage zone around the Naylor South fault and associated splay fault which bound the storage reservoir. However, in flow simulations significant CO_2 still ponds under a small structural trap towards the north-east, which is not seen in the seismic surveys. Finally, I summarise the results of the flow simulations and present conclusions from this chapter.

5.2 Vertically-integrated flow model with residual trapping

The flow simulator described in this section models CO_2 flow through a saturated porous media as a buoyancy-driven gravity current, with the CO_2 spreading driven by diffusive slumping of the current and advection along topographic gradients. In the simulations, I presume that a constant saturation of residually trapped CO_2 is left at the receding interface of the current as it propagates, as in Kochina *et al.* (1983). The governing gravity current equations used in these studies models the vertically integrated flow within the current, meaning that it is assumed that any vertical variations in reservoir properties may be captured in a simple vertical average. This has proved to be a valid assumption at relatively homogeneous storage reservoirs such as Sleipner, but may be a greater limitation of the analysis at Otway, where the injection interval contains larger variations in porosity and permeability as can be seen from the well log data (Figure 4.3). The extent to which vertical variations in heterogeneities can be averaged and upscaled for use in numerical models is an outstanding question that recent studies have begun to address (Gershenzon *et al.*, 2015; Jackson & Krevor, 2020; Li & Benson, 2015).

It is important to consider whether the storage reservoir is vertically confined or unconfined. In unconfined aquifers, the thickness of the CO_2 flow is much smaller than the total thickness of the aquifer, and hence the flow of ambient water may be neglected. In a confined aquifer, the CO_2 plume is of comparable thickness to the permeable layer, and the flow of both the ambient and the CO_2 must be calculated, as driven for example by injection pressures. Pegler *et al.* (2014a) showed that confining dynamics may be neglected if the height h of the CO_2 current

$$h \ll \frac{\mu_c}{\mu_a} H, \tag{5.1}$$

where μ_c and μ_a are the dynamic viscosities of the CO_2 and ambient phases and H is the height of the aquifer. In the parasequence 1 (PS1) storage interval at Otway, it is difficult to know exactly what value to take as the height H of the confining aquifer. The total thickness of PS1 as measured in the CRC-2 injection well is 34 m. However, it is possible that increased pressures due to injection may be confined by the low permeability calcite baffle layers that overprint the Paaratte Formation. Two of these baffles straddling the injection interval are 22.8 m apart. In either case, assuming a viscosity ratio of $\mu_c/\mu_a \simeq 0.07$ suggests that where the plume is thinner than 2.4 m or 1.6 m, the CO_2 behaves like an unconfined current, and where it is thicker, confining forces will start to play a role. It is worth nothing that (5.1) applies to a uniform, two-dimensional reservoir and does not include the effects of topographic gradients within the caprock.

In a confined layer, the background pressure gradient due to injection or large scale ambient flow can govern the dynamics of the flow by driving fluids horizontally. Ambient flow paths in the Paaratte Formation are not well characterised, but regional flow paths from the overlying Upper Cretaceous aquifer suggest that flow rates within the PS1 formation are not sufficient to impact the Stage 2C test (Bush, 2009; Dance *et al.*, 2012). During the Otway Stage 2C injection, the pressure was monitored using multiple gauges both in the injection interval and in the PS2 formation above the FS1 caprock (Figure 5.2) (Ennis-King *et al.*, 2017b).

Pressure diffusion through a low permeability baffle at the top of PS1 explains the magnitude and decay of the pressure signal in the PS2 formation above the injection zone (Figure 5.2c) (Ennis-King *et al.*, 2017b). The pressure response was not measured in the CRC-1 observation well so there is no indication of pressure decay in the horizontal. In the next section, I show that elevated pressures are localised to a radius of $\sim$ 100 m around the injection well, due to the small size of the injection and a logarithmic pressure decay.

As can be seen in Figure 5.2b, the elevated injection pressures also die away quickly after injection ceases, meaning that viscous flow diminishes at later times. It is also the case that buoyancy driven flows constantly get thinner over time, hence they are always approaching the unconfined limit. The relative importance of viscous and buoyancy forces with increasing distance from the injection well is estimated in the following section.

Another consideration is the extent to which capillary forces will affect the flow of CO_2. Su-

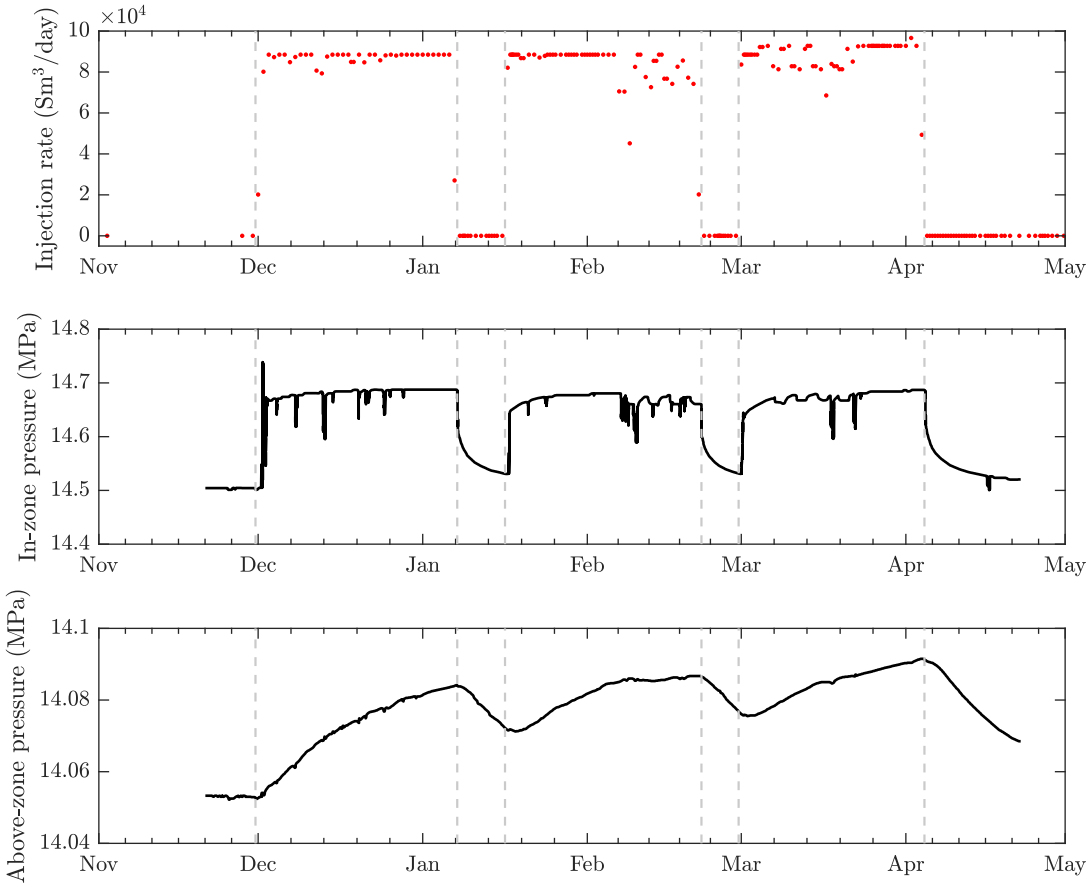

Figure 5.2: (a) Injection rate during the Stage 2C Otway injection. (b) Measured pressures in the PS1 injection interval. (c) Measured pressures above the injection interval. Grey vertical lines outline the three injection intervals. Pressure data from Ennis-King *et al.* (2017b).

percritical CO_2 and water are largely immiscible fluids and so surface tension effects between them mean that each phase will occupy a fraction of the pore space within a rock. This changes the behaviour of the CO_2-water system in two ways. Firstly, the pore space available for CO_2 to move through the rock is reduced by the remaining saturation of the water phase. Secondly, the effective permeability of the porous medium is dependent on the saturation of the phases present (Bennion & Bachu, 2005; Jackson *et al.*, 2018; Krevor *et al.*, 2012). Analytical studies incorporating capillary effects in homogeneous porous media (Golding *et al.*, 2011, 2013) find that capillary forces tend to thicken the current as increased capillary forces reduce the CO_2 saturation resulting in a reduced effective permeability of the rock. In homogeneous systems, the rate of migration of the plume is found to be largely insensitive to capillary effects. However, in heterogeneous layered porous media, when capillary forces are dominant the CO_2 saturation may be dynamically rearranged into high permeability regions, accelerating plume migration and enhancing multiphase effects such as relative permeability (Benham *et al.*, 2021b; Jackson & Krevor, 2020).

5.2.1 Flow controlling forces

For reasons outlined above, it is important to make a quantitative assessment of the relative contributions of the three forces, viscous, capillary and buoyancy, in controlling the flow of CO_2 within the Paaratte Formation at varying distances from the injection well. To obtain the relative strength of the viscous forces requires an estimate of the background pressure gradient due to injection. Assuming that the CO_2 has reached near steady-state flow at a constant average saturation S_{CO_2}, and neglecting the buoyancy of the fluid, the pressure P_r, at a distance r from the injection well can be found by extending the Dupuit-Theim theorem (Dupuit, 1863; Thiem, 1906) to multiple phases, as shown by Jackson & Krevor (2020). Here,

$$P_r = P_0 - \frac{\mu_{CO_2} Q}{2\pi K k_{rCO_2} H} \ln \frac{r}{R_0} \tag{5.2}$$

where P_0 is the equilibrium pressure at some outer boundary R_0, μ_{CO_2} is the dynamic viscosity of CO_2, Q is a constant injection flux, K is the upscaled absolute permeability of the aquifer, k_{rCO_2} is the upscaled relative permeability of the CO_2 and H is the height of

the confined aquifer.

(5.2) is evaluated using parameters from the Otway Stage 2C injection and PS1 storage formation (Figure 5.3a). The background pressure $P_0 = 14.5\,\text{MPa}$ at a distance of 500 m from the injection well, $\mu_{CO_2} = 3 \times 10^{-5}$ Pa s, $K = 82\,\text{mD}$ and $h = 34\,\text{m}$. The pressure is plotted for three values of the relative permeability of the CO_2 phase, $k_{rCO_2} = 0.1$, 0.2 and 0.3. $k_{rCO_2} = 0.2$ gives a pressure at the injection well that matches the measured pressure increase during injection (Figure 5.2b). This also corresponds with relative permeability measurements for a core sample of Paaratte Formation sandstone taken at higher interval at 1400 m depth for a CO_2 saturation of 0.5 (Krevor *et al.*, 2012).

The strength of the capillary forces can be evaluated by estimating the maximum change in capillary entry pressure ΔP_c in the storage interval, across a characteristic vertical length scale H_c (Benham *et al.*, 2021a; Jackson *et al.*, 2018). The maximum and minimum capillary entry pressures can be estimated using (Benham *et al.*, 2021b; Leverett, 1941)

$$p_c = p_e \left(\frac{\phi}{k/K} \right)^{1/2}, \tag{5.3}$$

where p_e is a characteristic pore entry pressure for the reservoir, ϕ is the porosity, k is the permeability of the layer and K is the upscaled absolute permeability of the aquifer. Using $\phi = 0.25$, $K = 82\,\text{mD}$, $k_{min} = 4\,\text{mD}$ and $k_{max} = 500\,\text{mD}$ from well log data, and $p_e = 2.1\,\text{kPa}$ calculated from a Paaratte sandstone core sample (Krevor *et al.*, 2012), gives a maximum change in capillary entry pressure $\Delta P_c = 4.3\,\text{kPa}$, over a characteristic vertical distance of 1 m.

Finally, the strength of the buoyancy forces can be estimated using the expression $\Delta\rho g$, where $\Delta\rho = \rho_w - \rho_{CO_2}$ is the density difference between the CO_2 and brine which gives rise to a buoyancy force, and g is gravitational acceleration. The relative strength of these three competing forces can be evaluated using three dimensionless numbers, the capillary number N_c, the gravity number N_g and the Bond number N_b. The capillary number is the ratio of the viscous pressure drop to the characteristic capillary pressure variation between layers (Virnovsky *et al.*, 2004)

$$N_c = \frac{H_c(P_r - P_0)}{R_0 \Delta P_c}. \tag{5.4}$$

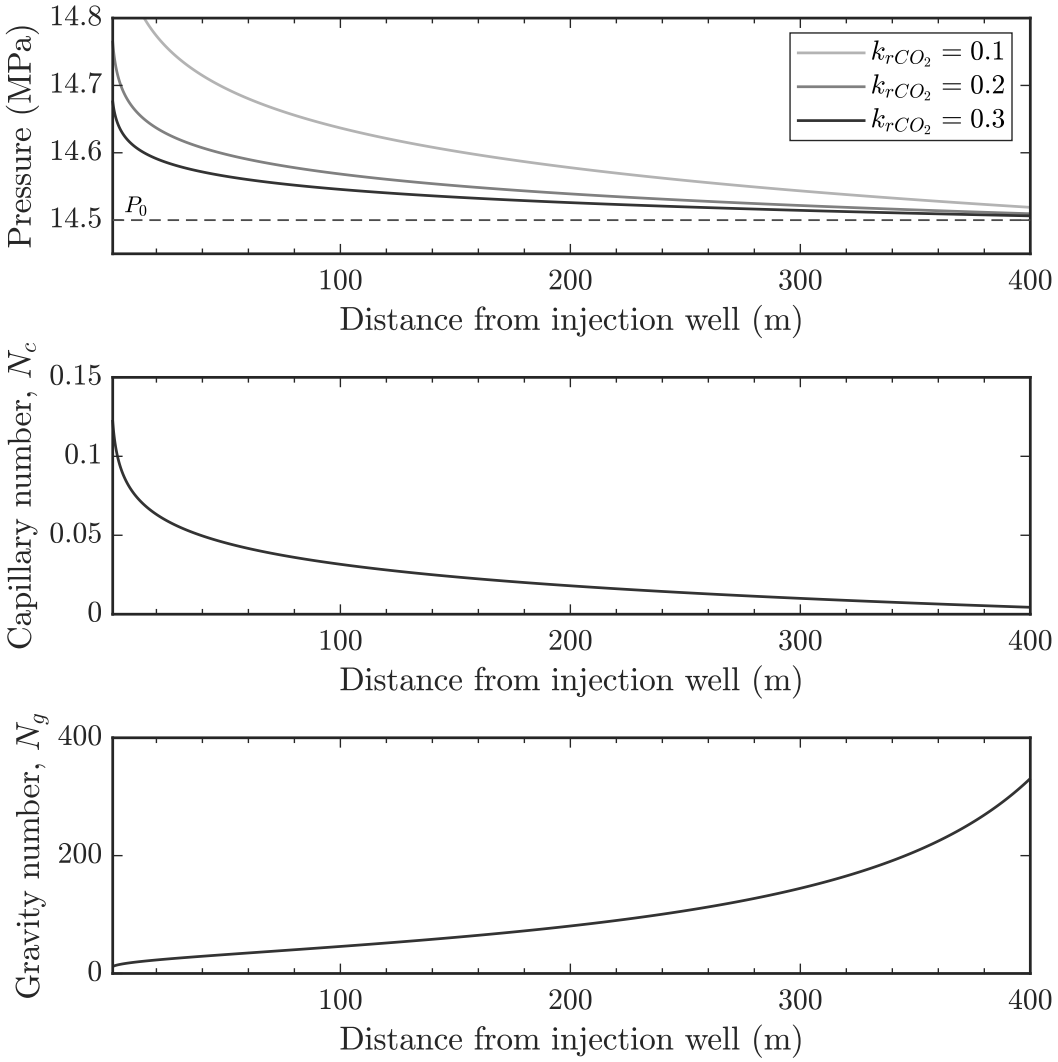

Figure 5.3: (a) Injection pressure for the Otway Stage 2C injection as a function of radial distance from the injection well. (b) Typical capillary number (ratio between viscous forces and capillary forces) and (c) gravity number (ratio between buoyancy forces and viscous forces) for the Otway Stage 2C injection.

For capillary numbers $N_c < 1$, the CO_2 saturation distribution is predominantly governed by gradients in capillary pressure between heterogeneous layers, while at large capillary numbers the flow is driven by the background pressure due to injection. The capillary number is plotted for the Stage 2C injection as a function of distance from the injection well in Figure 5.3b. The low capillary number suggests that capillary forces play a dominant role in rearranging the CO_2 saturation, even around the injection location. This agrees with the well log saturation measurements (Figure 4.21), which shows that high CO_2 saturations correspond with the higher permeability layers. The gravity number N_g and the Bond number N_b are the ratio of the buoyancy force with viscous and capillary forces respectively,

$$N_g = \frac{\Delta\rho g R_0}{P_r - P_0}, \qquad N_b = \frac{\Delta\rho g H_c}{\Delta P_c}. \tag{5.5}$$

Large gravity and Bond numbers correspond with situations where the buoyancy forces dominate the flow behaviour over the viscous or capillary forces. The gravity number is plotted for the Stage 2C injection as a function of distance from the injection well in Figure 5.3c. At a distance of 40 m from the injection well, the gravity number $N_g = 30$, which suggests that over most of the CO_2 plume extent at Otway the buoyancy forces will dominate the flow behaviour over viscous forces. The Bond number for the flow $N_b = 1.5$, meaning that both buoyancy and capillary forces are important in controlling the flow. (Benham *et al.*, 2021b) suggests that once the injection phase ends, the vertical length scale used to define the Bond number is governed by the gravity current thickness, which is small at the edges of the plume. Hence in these regions the Bond number is correspondingly small and capillary effects will govern the CO_2 flow.

The flow model described in this chapter makes the simplification that the aquifer is unconfined and neglects capillary forces. It is likely that viscous forces due to injection pressures will play a role in governing the flow behaviour at early times close to the injection well, but the gravity number suggests that buoyancy forces should dominate the flow further from the injection well. The Bond number suggests that capillary effects will contribute towards rearranging the saturation into high permeability layers, enhancing multiphase effects. For this reason, incorporating multiphase effects such as relative permeability into a vertically-integrated reservoir simulator, as well as introducing confinement and flow of the ambient

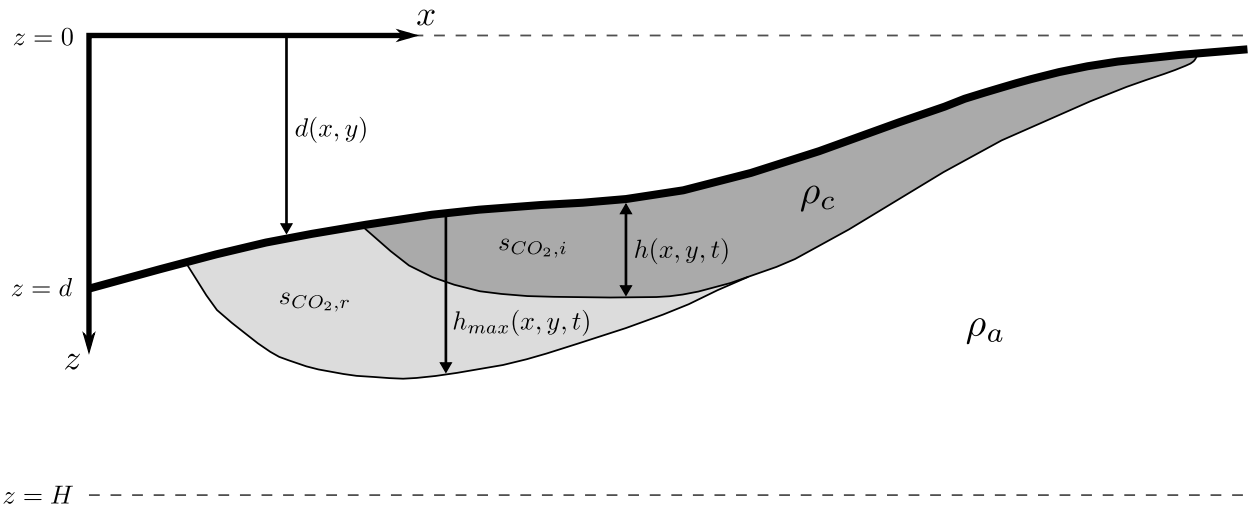

Figure 5.4: Schematic of a two-dimensional section through a three-dimensional gravity current moving under a caprock with topography $d(x, y)$. The active current with CO_2 saturation $S_{CO_2,i}$ and density ρ_c has height $h(x, y, t)$ and is coloured dark grey. The ambient fluid has density ρ_a. As the current moves up-slope it leaves behind a region of residually trapped CO_2 with saturation $S_{CO_2,r}$ and height $h_{max}(x, y, t) - h(x, y, t)$, where $h_{max}(x, y, t)$ is the maximum thickness of the active current has achieved at a particular point (x, y) up to the time of consideration.

phase are important areas for future research.

5.2.2 Flow model

This model describes the flow of a single-phase gravity current with a sharp interface and uniform saturation propagating below a slope in an unconfined aquifer. A constant fraction of the flow is residually trapped in the pore space at the receding interface of the current (Figure 5.4).

Fluid flow in porous media is governed by Darcy's law which relates driving forces due to background pressure gradients and buoyancy to viscous drag at the pore scale,

$$\phi\tilde{\mathbf{u}} = \mathbf{u} = -\frac{k}{\mu_c}(\nabla P + \rho g\hat{z}), \tag{5.6}$$

where ϕ is the porosity, $\tilde{\mathbf{u}}$ is the interstitial fluid velocity, $\mathbf{u} = (u, v, w)$ is the Darcy or transport velocity, k is the permeability, μ_c is the dynamic viscosity of the CO_2 phase, $\nabla P = (\frac{\partial P}{\partial x}, \frac{\partial P}{\partial y}, \frac{\partial P}{\partial z})$ is the pressure gradient, ρ is the CO_2 density, g is gravitational acceleration and $\hat{z}$ is a unit vector in the vertical.

Assuming that the matrix and CO_2 are both incompressible, a simplified statement of conservation of mass may be written in terms of the Darcy velocity $\mathbf{u}$ as

$$\nabla.\mathbf{u} = 0. \tag{5.7}$$

If the lateral extent of the gravity current is much larger than the vertical extent, as is the case for most CO_2 injections, the vertical velocity is negligible compared to the horizontal velocity, $w \ll (u, v)$, and hence the pressure in the current can be approximated as hydrostatic,

$$P = \begin{cases} P_H - \rho_a g[H - (d+h)] - \rho_c g[(d+h) - z], & d < z < d+h, \quad (5.8a) \\ P_H - \rho_a g(H - z), & d+h < z < H, \quad (5.8b) \end{cases}$$

where P_H is the pressure at a reference horizon below the gravity current at $z = H$, ρ_c and ρ_a are the densities of the ambient and injected phases where $\rho_c < \rho_a$, $h(x, y, t)$ is the height of the active gravity current and $d(x, y)$ is the topography of the impermeable caprock.

On applying Darcy's law to (5.8a), assuming that P_H remains constant, the horizontal velocity $\mathbf{u_H} = (u, v)$ is given by

$$\mathbf{u_H} = -\frac{k}{\mu_c}\nabla_H P = -u_b \nabla_H (d+h), \tag{5.9}$$

where ∇_H is the horizontal gradient operator and $u_b = k\Delta\rho g/\mu_c$ is the characteristic buoyancy velocity for the reservoir where $\Delta\rho = \rho_a - \rho_c$.

Residual trapping is introduced as a source/sink term R_c in the evolution equation of the plume, which accounts for the volume of CO_2 that is lost as residual saturation $s_{CO_2,r}$ in the wake of the plume (Hesse *et al.*, 2008). As in Kochina *et al.* (1983), the residual saturation $s_{CO_2,r}$ is assumed to be constant, such that

$$R_c = \begin{cases} \phi s_{CO_2,r} \frac{\partial h}{\partial t} & \text{for } \frac{\partial h}{\partial t} < 0, \\ 0 & \text{for } \frac{\partial h}{\partial t} \geqslant 0. \end{cases} \tag{5.10}$$

Empirical evidence suggests the residual saturation $s_{CO_2,r}$ depends on the historical maxi-

mum CO_2 saturation before imbibition (Pentland *et al.*, 2010). Both linear and non-linear trapping models are used to describe the relationship between these values. A commonly used non-linear model for the residual saturation is Land's trapping model (Land, 1968), which relates the initial saturation of CO_2 in the pore space $s_{CO_2,i}$ to the residual saturation according to the relationship,

$$s_{CO_2,r} = \frac{s_{CO_2,i}}{1 + C.s_{CO_2,i}} \tag{5.11}$$

where C is a dimensional constant known as the Land coefficient, which can be determined experimentally with data from the maximum initial and residual saturations,

$$C = \frac{1}{s_{CO_2,r_{max}}} - \frac{1}{s_{CO_2,i_{max}}}. \tag{5.12}$$

Land's model captures the behaviour that with decreasing initial saturation, the residual saturation also decreases, but notably the trapping fraction increases.

In the case of a vertically uniform permeability structure, horizontal flow within the current is uniform as a function of depth, and so the equation for the evolution of the gravity current interface can be obtained by integrating the conservation of mass, (5.7), in combination with (5.9) over the depth of the current to give,

$$\phi s_{CO_2,i}(1-\epsilon)\frac{\partial h}{\partial t} - \nabla_H.\left(\frac{k\Delta\rho g}{\mu_c}h\nabla_H d\right) = \nabla_H.\left(\frac{k\Delta\rho g}{\mu_c}h\nabla_H h\right), \tag{5.13}$$

where

$$\epsilon = \begin{cases} s_{CO_2,r}/s_{CO_2,i} & \text{for } \frac{\partial h}{\partial t} < 0, \\ 0 & \text{for } \frac{\partial h}{\partial t} \geqslant 0. \end{cases} \tag{5.14}$$

5.2.3 Benchmarking the numerical scheme

The evolution of the gravity current given by (5.13) is solved using a Crank-Nicholson finite difference scheme, centered in time and space (Press *et al.*, 2007). Tridiagonal elimination is implemented to solve subsequent time steps efficiently. A predictor-corrector scheme is used to evaluate the non-linear diffusive buoyancy (Press *et al.*, 2007). The model also includes an adaptive time step which can increase or decrease based on whether changing the time

step results in an error above or below a threshold value (Cowton *et al.*, 2018; Lister, 1992).

To improve the stability of the model in regions of numerical instability, such as sharp gradients in topography, the Il'in three-point differencing scheme is implemented (Il'in, 1969; Clauser & Kiesner, 1987). This scheme is able to handle sharp changes in parameters by ensuring that the 'upwind' cell is used to calculate advective fluxes into or out of each cell. In this case, the Peclet number, which is the ratio of advection to diffusion, determines the amount of 'upwinding' required to keep the model stable. At high positive or negative Peclet numbers, the advective term is strongly upwind or downwind, and at low Peclet numbers the scheme reverts to the space-centred Crank-Nicholson scheme (Cowton, 2017).

An alternating-direction-implicit (ADI) scheme is used to calculate the propagation of the current in three-dimensions (Peaceman & Rachford, 1955; Press *et al.*, 2007). Here, the numerical simulation is advanced by a half time step in the x-direction, and then by half a step in the y-direction, advancing the simulation by a full time step after one iteration.

The numerical scheme was benchmarked against analytical solutions for unconfined gravity currents in two- and three-dimensions presented by Huppert & Woods (1995) and Vella & Huppert (2006) by Cowton (2017). The numerical scheme, including residual trapping, is benchmarked against analytical solutions from Kochina *et al.* (1983) (Figure 5.5). Here, I model two-dimensional gravity-driven flow of a finite volume release of fluid for varying residual saturations s_r. Figure 5.5a and 5.5b show the active current extent X_n and current depth at the origin $H = h(0, t)$ as a function of time for $s_r = 0$ and $s_r = 0.5$. Where there is no residual trapping, the current extent and height evolve according to $X_n \sim t^{1/3}$ and $H \sim t^{-1/3}$, which agrees with the analytical solutions for the point release of a buoyant fluid on a horizontal boundary given by Huppert & Woods (1995). Although there are no equivalent analytical solutions for a gravity current with residual trapping, it has been shown that an asymptotic self-similar solution of the second kind exists, with the extent and height evolving as a power law at late times, which can be seen for the $s_r = 0.5$ solutions. The power law exponent β, where $X_n \sim t^{\beta}$ and $H \sim t^{\alpha}$ where $\alpha = 1 - 2\beta$, is plotted for varying values of s_r in Figure 5.5c, along with the numerical solution from (Kochina *et al.*, 1983), solved using a shooting method. Both solutions show consistent power law exponents, even at high residual saturations.

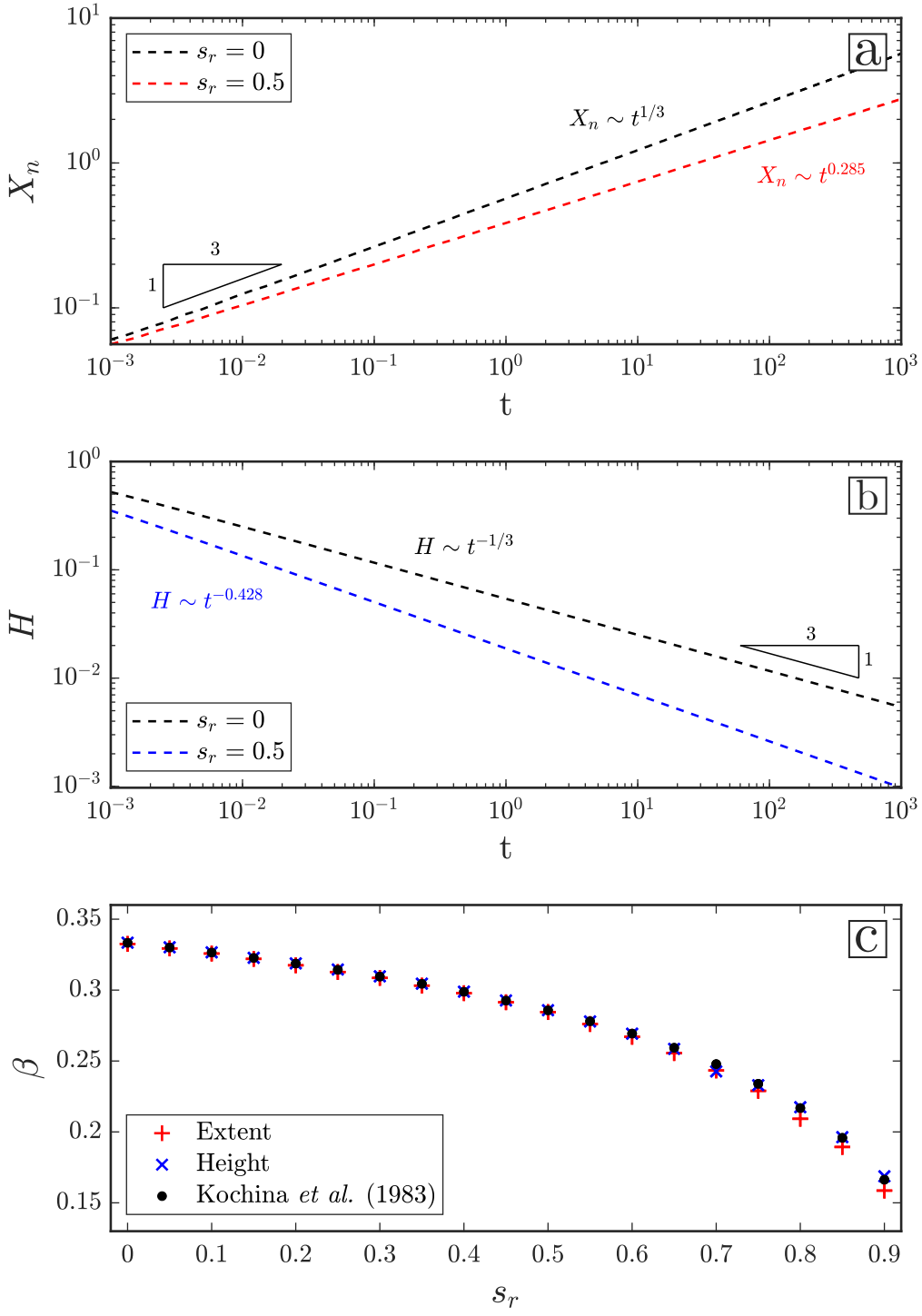

Figure 5.5: Extent (a) and height (b) of a 2D gravity current with and without residual trapping. (c) Power law exponent of the extent β and height ($\beta = (1 - \alpha)/2$ where α is the exponent of the height) plotted as a function of residual saturation s_r.

5.3 Forward modelling of the Otway Stage 2C injection

The flow simulator solves (5.13) to obtain distributions of the CO_2 current, $h(x, y, t)$, which can be compared against the observed CO_2 thickness measurements obtained from seismic inversion by Glubokovskikh *et al.* (2020), which are presented in Chapter 4. There are a number of inputs required for application of the numerical scheme to a reservoir setting: an estimate of the geometry of the impermeable caprock beneath which the CO_2 is spreading $d(x, y)$; the permeability $k(x, y)$ and porosity $\phi(x, y)$ of the reservoir; the initial CO_2 saturation in the pore space $s_{CO_2,i}(x, y)$ and residual saturation $s_{CO_2,r}(x, y)$; the density and viscosity of the injected fluid; and the volumetric flux and input location of CO_2 into the reservoir. Each of these input parameters is discussed below.

5.3.1 Model input parameters

Reservoir geometry

The reservoir geometry is constrained by picking the negative amplitude anomaly at 1200 ms two-way travel time (TWTT) in the 2015 baseline survey, which is thought to correspond with the boundary between the top of the PS1 storage formation and the bottom of an extensive, 8 m thick mudstone seal. Waveform modelling of a synthetic reservoir model based on the CRC-2 well log suggests that the high amplitude reflections may be picking out the calcite baffles which overprint the geology and have characteristically high densities and velocities and low porosity and permeability. However, regardless of which horizon the reflection corresponds to, it is a reasonable assumption that the geometries of neighbouring horizons are relatively consistent, particularly as geochemical evidence suggests that these calcite layers form in close proximity to the mudstone seals as they act as the source of the biogenic carbonate (Dutton *et al.*, 2000). Hence, the geometry of the reflection is our best estimate of the reservoir geometry.

The dominant frequency of the source wavelet for the seismic reflection surveys is 40 Hz, which means that the vertical and horizontal resolution is around 20 m. Topographic features below this length scale will not be fully resolved. Comparison of the TWTT of horizons

above the injection zone across time-lapse seismic surveys shows small variations on the order ±1 ms, which suggests the horizon topography is affected by noise on the order ±2 m. This is in line with the error associated with hand picking of the horizons. The seismic survey is binned into 7.5 m × 7.5 m blocks before processing. A median filter with 50 m blocks is applied to the picked surface (Lim, 1990) to mitigate short wavelength noise and remove sharp gradients that could affect the stability of the numerical flow simulations.

The topographic surface of the caprock is converted from two-way travel time to depth below sea-level using a TWTT to depth relationship obtained from vertical seismic profile (VSP) data and well logs (Figure 4.5), and a correction of 50.4 m is applied to convert from metres depth to metres below mean sea level. The TWTT-depth relationship from wells across the fault block varies by ±5 m at a depth of 1500 m, which suggests that there is not significant lateral velocity variations across the fault block (Dance *et al.*, 2012).

Reservoir permeability and porosity

The permeability and porosity for the PS1 formation are estimated using average properties from the CRC-1 and CRC-2 well logs, not including intervals overprinted by the calcite formations. The formation is a deltaic sedimentary package, ranging from clay rich distal mouth bars to high quality distributary channel sandstones. This heterogeneity is reflected in the range of permeabilities (1-1000 mD) and porosities (0.17-0.31) across the formation. The geometric mean permeability across the PS1 formation is 82 ± 7 mD and the average porosity is 0.25±0.04, with the uncertainty range indicating one standard deviation from the mean. The CRC-1 and CRC-2 wells, spaced ~ 150 m apart, show consistent permeability and porosity measurements, suggesting that lateral heterogeneity between wells is limited.

The Naylor South splay fault ~ 200 m from the injection well is assumed to be sealing to across-fault flow. Tenthorey *et al.* (2014) used the shale gouge ratio algorithm to quantify the across-fault flow potential of the splay fault and found that the fault should be sealing to lateral movement of CO_2. The fault-parallel flow properties are harder to quantify and it is likely that a high permeability damage zone exists in the region directly next to the fault (see Section 4.2.3). For these simulations it is assumed that no CO_2 in the vicinity of the

fault leaks through the caprock. However, if the fault damage zone resulted in a 2-3 order of magnitude permeability increase in the caprock, it is possible that CO_2 may start to leak into the overlying formation. Implementing the fault leakage rates estimated in Chapter 3 into the flow simulator is a potential area for future research.

CO_2 saturation

The CO_2 saturation within the plume $s_{CO_2,i}(x, y)$ is difficult to predict due to its spatial variability and the lack of constraining measurements. The pulsed neutron log saturation measurements suggest that the CO_2 saturation varies from $s_{CO_2,i} = 0.2 - 1$ at the injection well. However, it is likely these saturations are larger than the CO_2 saturations further from the injection site. For simplicity, an average saturation is used across the plume in the numerical simulations, which is obtained by comparing the known injected CO_2 mass to the mass of the observed plumes. The observed CO_2 thickness measurements obtained by seismic inversion (Figure 4.32), give an effective volume that the CO_2 occupies. A least squares fitting is used to calculate the average saturation that minimises the misfit between the CO_2 mass in the observed plume and the known injected CO_2 mass, assuming a density for the CO_2 gas mix of $\rho = 348\,\mathrm{kg\,m^{-3}}$ and a reservoir porosity $\phi = 0.25$ (Figure 5.6). The minimum average mass misfit is found at $s_{CO_2,i} = 0.16 \pm 0.03$, with the error reflecting the uncertainty in the plume thickness and any missed CO_2 thickness at the plume edges. It is worth noting that although the model uses a vertically-averaged saturation, the heterogeneous permeability structure means that saturation is likely to vary vertically (see Section 5.2.1 for further discussion).

The residual saturation of $s_{CO_2,r} = 0.13$ is calculated using Land's trapping model (5.11), where the Land's coefficient $C = 1.3$ is calculated using a maximum initial saturation $s_{CO_2,i_{max}} = 0.59$ and maximum residual saturation $s_{CO_2,r_{max}} = 0.33$, obtained from core flood experiments on a sample of Paaratte sandstone (Krevor *et al.*, 2012). As with the initial saturation, it is assumed that the residual saturation is uniform across the plume. In reality, it is likely that residual saturations would be higher close to the injection site where initial CO_2 saturations are also likely to be higher. Estimated values for the initial saturation and residual saturation result in a high trapping fraction $s_{CO_2,r}/s_{CO_2,i} = 0.81$,

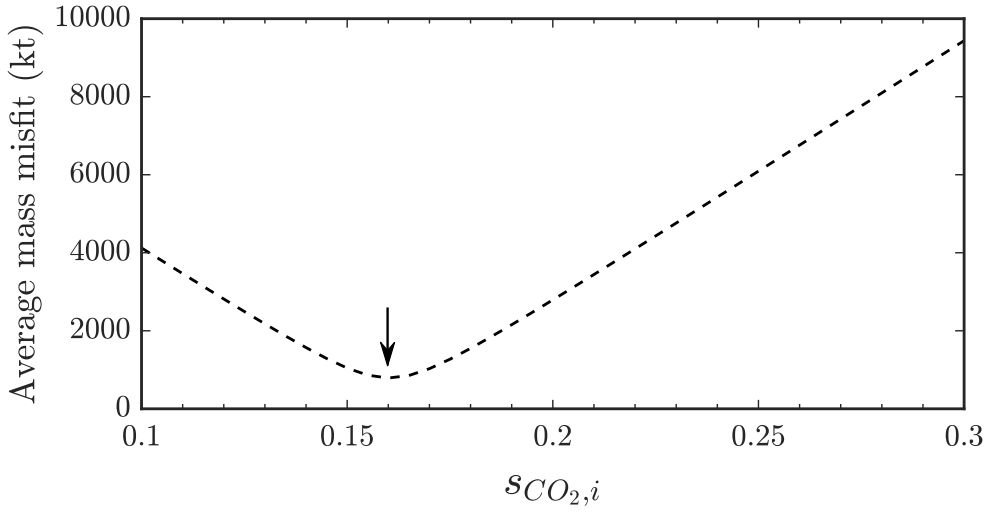

Figure 5.6: Average misfit between the injected CO_2 mass and mass of observed plume as a function of saturation. Average plume saturation $s_{CO_2,i} = 0.16$ gives minimum misfit.

which suggests that fast stabilisation of the plume by residual trapping could be expected.

Fluid properties and injection parameters

A total of 15,006 tonnes of CO_2-rich gas was injected into CRC-2 at an average rate of 120 tonnes a day over the period from 2nd December 2015 to the 4th April 2016 (Figure 5.7). The gas was injected into PS1, Unit A of the Paaratte Formation, over a perforated interval between 1453.1 m and 1464 m TVDss (metres below mean sea level). The injected fluid is a supercritical CO_2-rich gas mixture extracted from the nearby Buttress reservoir with fluid composition 78.7% CO_2, 18.9% CH_4, 1.38% N_2 and 1.04% C_5+ by molar percentage (Watson *et al.*, 2018). The injection rate is measured in standard cubic metres of gas per day (Sm^3/day), where a Sm^3 is a m^3 of gas at 15°C and 1 atm (101.325kPa). To convert the volume flux in Sm^3 to a volume flux at reservoir conditions, I use the GERG 2008 equation of state, which is the ISO standard for calculating the thermodynamic properties of natural gas mixtures (Kunz & Wagner, 2012). The density of a gas mix comprising 78.7% CO_2, 18.9% CH_4, 1.38% N_2 and 1.04% isopentane by molar percentage, is $\rho = 1.65$ kg m^{-3} at 15°C and 101.325kPa and $\rho = 348 \pm 10$ kg m^{-3} at reservoir conditions of 62.4±0.5°C and 14.5±0.1 MPa. For the numerical simulations of the Stage 2C injection, an injection flux of 88475 Sm^3/day, equal to 0.0049 m^3s^{-1} at depth, is used across three discrete injection intervals, lasting 34, 35 and 33 days respectively, shown by the black dashed line in Figure

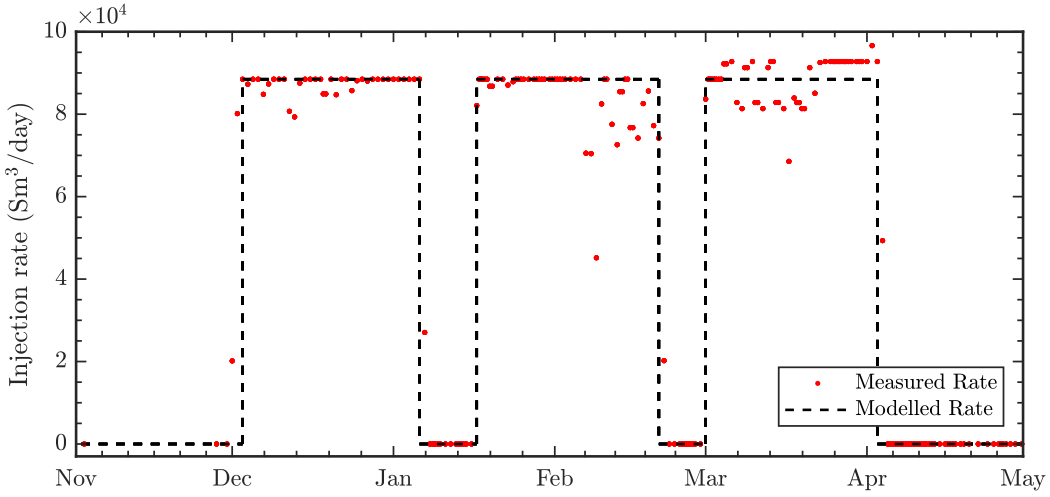

Figure 5.7: Measured and modelled injection rate during the Otway Stage 2C injection. Injection was paused while the TL1 and TL2 seismic surveys were being carried out.

5.7.

The viscosity of the injection mixture is estimated by assuming a gas mix comprising 80% CO_2 and 20% CH_4 by molar percentage. Here, the kinematic viscosity of the mixture ν_{mix} is approximated by the relationship

$$\nu_{mix}^{1/3} = x_{CO_2}\nu_{CO_2}^{1/3} + x_{CH_4}\nu_{CH_4}^{1/3}, \tag{5.15}$$

where x_{CO_2}, x_{CH_4} and ν_{CO_2}, ν_{CH_4} are the mass fractions and kinematic viscosities of CO_2 and CH_4 respectively (Gambill, 1959). Using $\nu_{CO_2} = 8.0 \times 10^{-8}$ m^{2}s^{-1} (Dubacq *et al.*, 2013) and $\nu_{CH_4} = 1.8 \times 10^{-7}$ m^{2}s^{-1} (Gonzalez *et al.*, 1967) calculated at reservoir temperature and pressure, gives a kinematic viscosity for the mixture $\nu_{mix} = 8.6 \times 10^{-8}$ m^{2}s^{-1}, which can be converted into a dynamic viscosity $\mu = 3.0 \times 10^{-5}$ Pa s.

5.3.2 Modelling Results

The CO_2 flow from the Stage 2C injection is simulated and compared against the seismic observations of plume thickness obtained by Glubokovskikh *et al.* (2020) (Figure 5.8). The thickness plotted for the numerical simulations is the total thickness of the active and residually trapped plume (h_{max} in Figure 5.4). It is appropriate to compare the total thickness against the seismically derived thicknesses as the seismic response of the active CO_2 current

and the residually trapped CO_2 is very similar. Here, a uniform permeability for the reservoir of $k = 82\,\text{mD}$ is used, estimated from the CRC-1 and CRC-2 wells.

In general, the simulations using a uniform permeability field do a relatively poor job at matching the overall shape of the plume. At early times, the up-slope extent and thickness around the injection wells agree reasonably well. However, the modelled plume spreads radially, whereas the observed plume forms two distinct lobes. At later times, the modelled plume preferentially propagates towards the east, due to a local topographic high in that area, whereas the observed plume preferentially follows the splay fault towards the southeast.

These results suggest that the uniform parameter inputs used are not sufficient to match the observed CO_2 distribution. In the following sections, uncertainties in the large-scale permeability structure of the reservoir are investigated along with a discussion of the other possible causes for the discrepancy.

5.4 History-Matching the Reservoir Permeability Structure

Post-injection observations of the seismic plumes suggest that the base-case reservoir model used in flow simulations is not representative of the storage reservoir. By comparing results of the numerical simulations to the observations, reservoir models can be retrospectively updated in a process known as history-matching (e.g. Cowton *et al.*, 2018; Nilsen *et al.*, 2017). Due to the computational efficiency of the vertically-integrated flow model, a large number of numerical runs using a range of different bulk parameters for the reservoir can be performed and compared to the seismic observations to see if there are large scale reservoir properties that produce an improved match.

5.4.1 Inversion for uniform permeability structure

A parameter sweep is used to obtain the reservoir permeability that best fits the observed CO_2 distribution. The misfit between the observed plume and the simulated plume is calculated using a least-squares misfit function defined in terms of the thickness of the CO_2

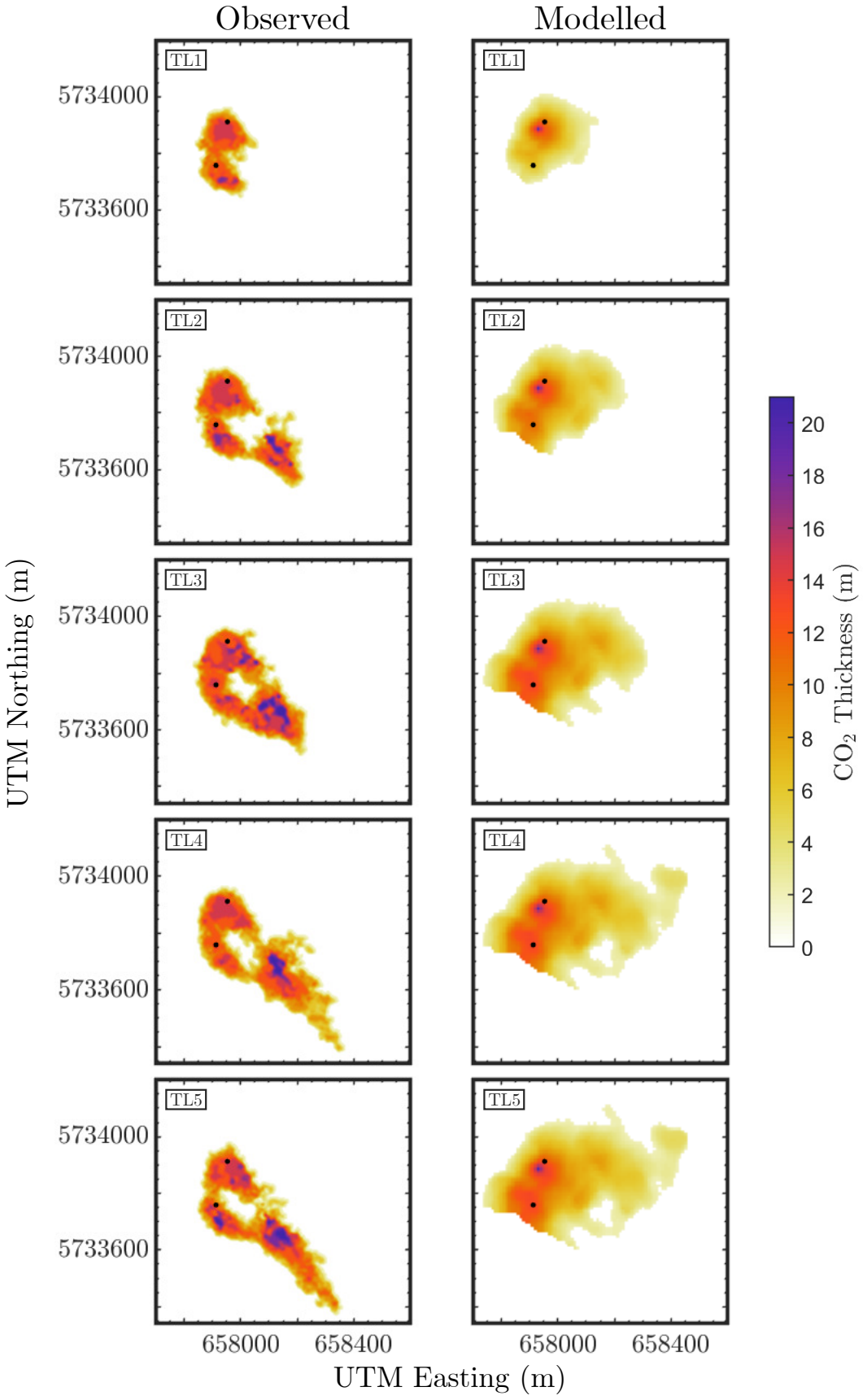

Figure 5.8: Observed (left-hand side) and modelled (right-hand side) CO_2 distribution using a uniform permeability derived from well logs, $k = 82\,\mathrm{mD}$.

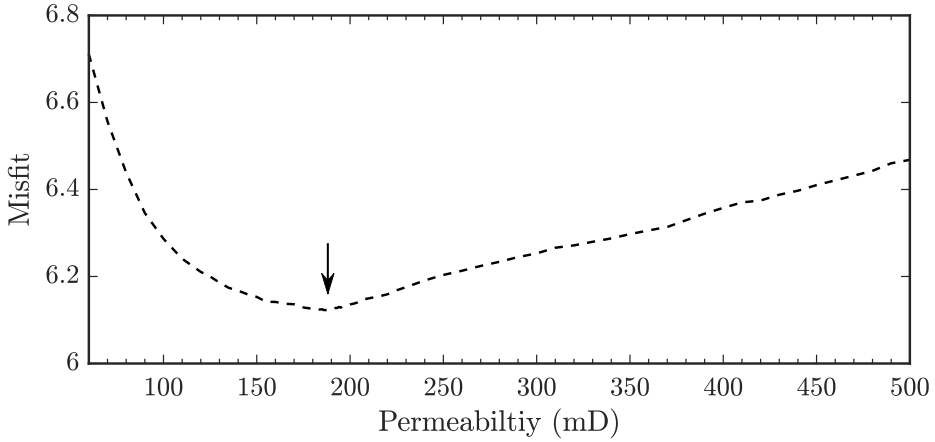

Figure 5.9: Misfit between observed and simulated CO_2 distribution for uniform reservoir permeability simulations. Black arrow shows bulk permeability of 188 mD which corresponds with the minimum misfit.

plume,

$$M = \frac{1}{N_s} \sum_{j=TL1}^{N_s} \left[\frac{1}{N} \sum_{i=1}^{N} (h_{ij}^s - h_{ij}^o)^2 \right], \tag{5.16}$$

where M is the misfit for the simulation, N_s is the number of seismic surveys, j refers to a specific seismic survey in order from time-lapse survey 1 (TL1) to TL5, N is the number of data points in each survey over 2 m thick, i refers to a data point, h^s is the simulated CO_2 thickness and h^o is the observed CO_2 thickness.

The misfit between the observed and simulated CO_2 distributions as a function of bulk reservoir permeability is shown in Figure 5.9. The minimum point in the misfit function is found at $k = 188$ mD. The CO_2 plume distributions for simulations performed at a bulk reservoir permeability of $k = 188$ mD are shown in Figure 5.10. The results of this simulation are very similar to the results from the uniform well log permeability simulations. The discrepancies between the observed and simulated plumes suggest that a bulk permeability structure for the reservoir is not adequate to match the observed CO_2 distribution and that a more complex permeability structure is required.

5.4.2 Large-scale Reservoir Heterogeneity

A likely source of large-scale heterogeneity in the PS1 formation is due to the fault damage zone surrounding the Naylor South fault and splay fault. A simple model for the structure

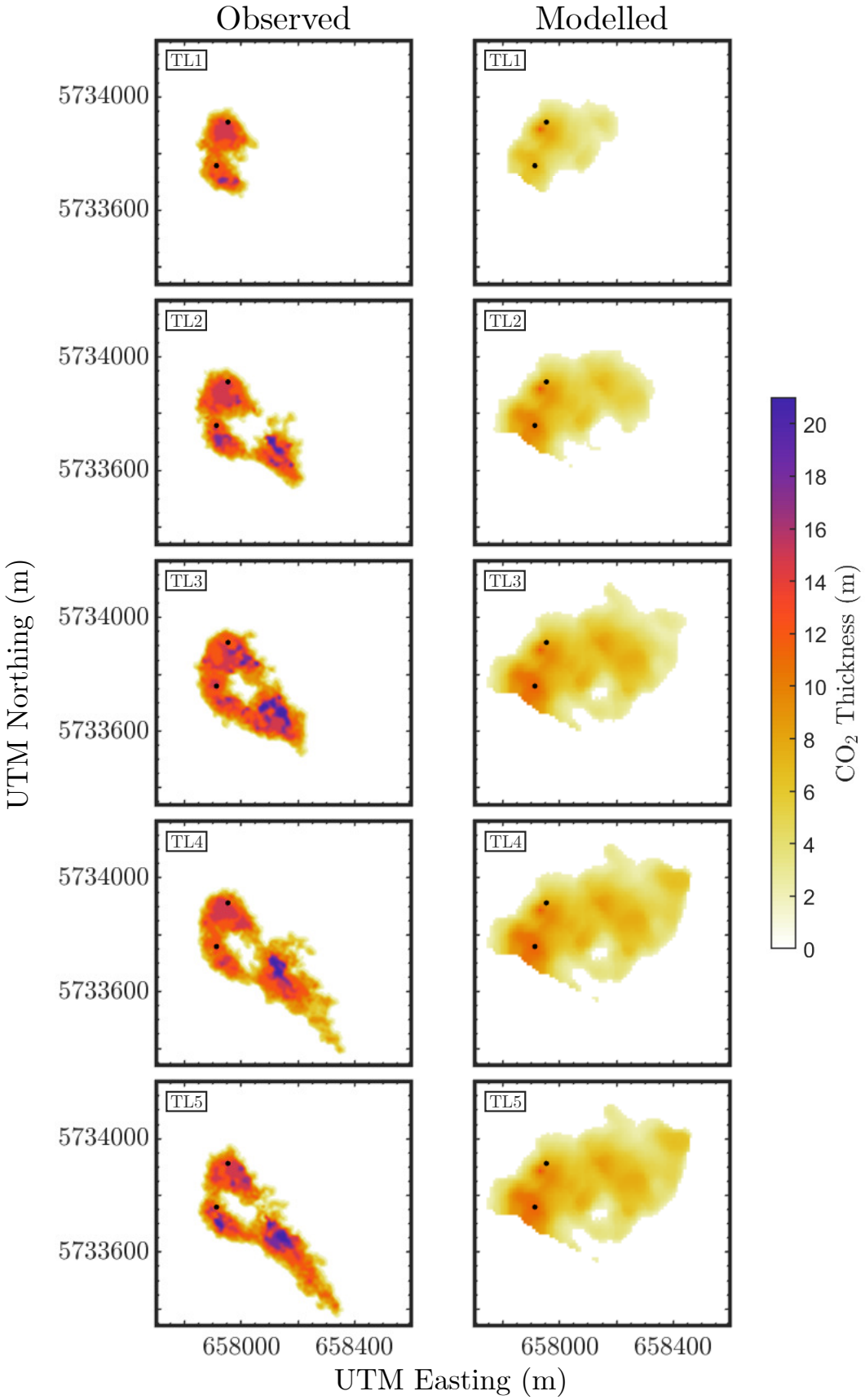

Figure 5.10: Observed (left-hand side) and modelled (right-hand side) CO_2 distribution using uniform permeability obtained by history-matching. $k = 188\,\text{mD}$.

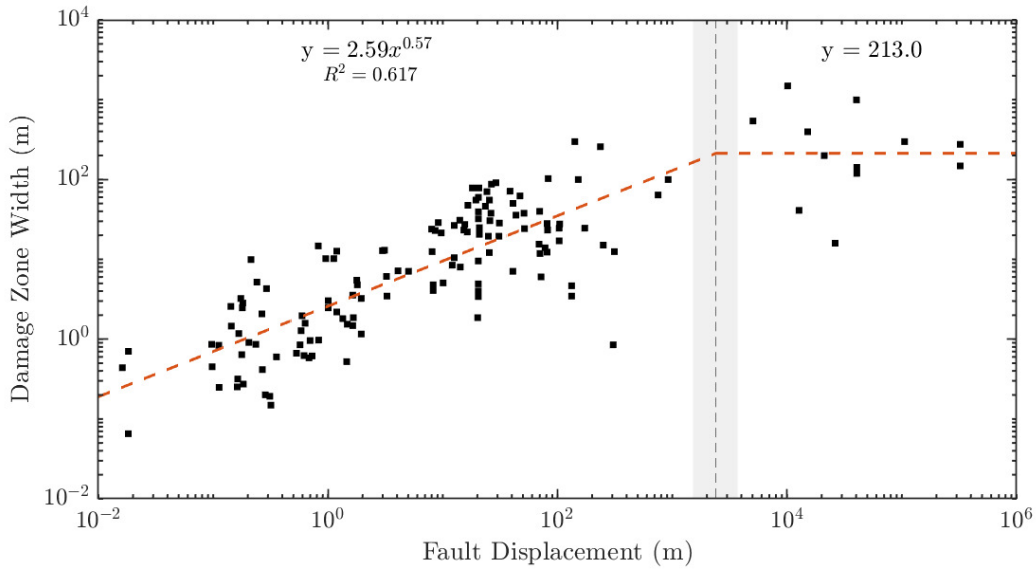

Figure 5.11: Relationship between fault displacement and damage zone width. Grey line marks transition between a power law relationship and constant width. Grey zone is 80% confidence limit on this point. Data collated by Savage & Brodsky (2011) from a range of studies.

of a fault zone is a low permeability fault core surrounded by a zone of intense fracturing, known as the fault damage zone, which decays in intensity away from the fault (Wibberley *et al.*, 2008). Damage zones have enhanced permeabilities due to pervasive fracturing which results in increased flow parallel to the fault. Data collated by Savage & Brodsky (2011) shows that damage zone thickness scales with total fault displacement until around 2400 m displacement, at which point the damage zone grows more gradually (Figure 5.11).

The scaling relationship in Figure 5.11 is used to estimate the damage zone thickness around the Naylor South splay fault and Naylor South fault (Figure 5.12). Here, the displacement across the fault is measured along its length, and a linear fit applied to the data (Figure 5.12b). The scaling relationship between displacement and damage zone thickness is then used to estimate the damage zone width as a function of distance along the fault (Figure 5.12c).

The complex permeability structure of the fault damage zone is simplified to a dual-permeability model for the flow simulations, with the area inside the damage zone assigned a uniform permeability and the rest of the PS1 formation is assigned a lower uniform permeability. Simulations are run for a range of fault and reservoir permeabilities, and the misfit for each

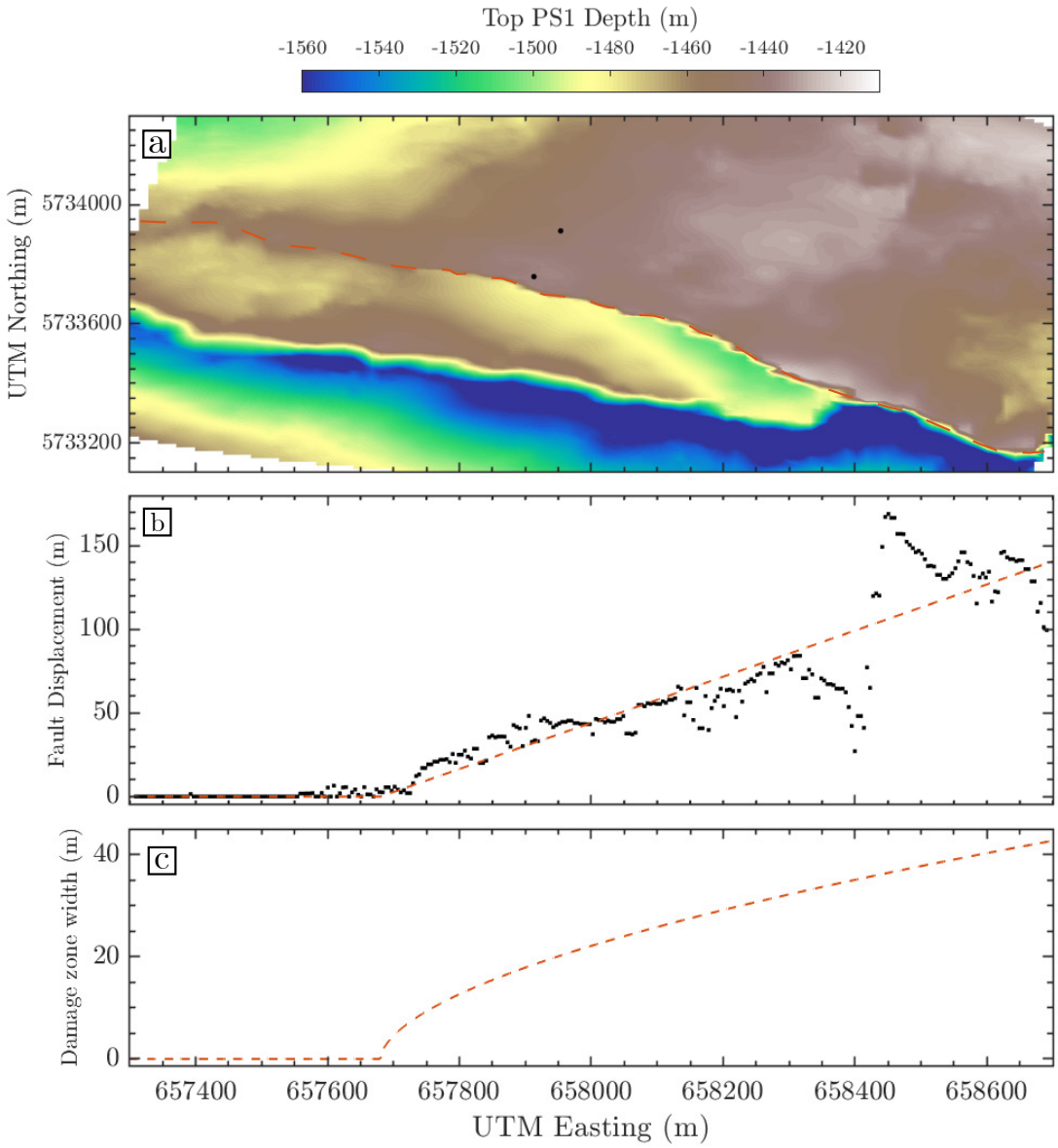

Figure 5.12: (a) Topography of the Top of the PS1 formation. Red dashed line = section fault displacement is calculated along. (b) Displacement across the Naylor South splay fault. Black points = spot displacement measurements. Red dash line = fitted linear function. (c) Estimated damage zone width across the Naylor South splay fault using relationship in Figure 5.11.

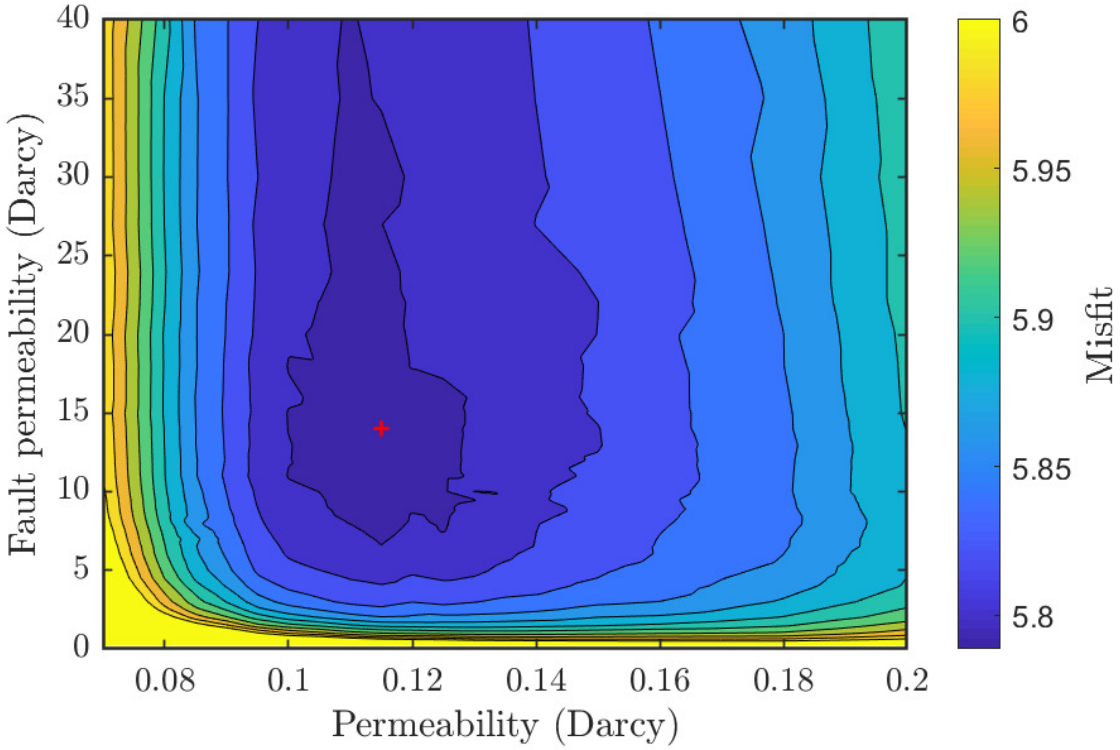

Figure 5.13: Misfit between observed and simulated CO_2 distribution as a function of reservoir permeability and fault damage zone permeability. Red cross shows the misfit low found at a reservoir permeability of $k = 0.11\,\mathrm{D}$ and a fault damage zone permeability of $k_f = 16\,\mathrm{D}$.

run calculated using (5.16) (Figure 5.13). The misfit function is largely insensitive to changes in fault damage zone permeabilities when the permeability is above 5 D, whereas it is more sensitive to changes in the reservoir permeability. Where the fault damage zone permeability is above 5 D, misfit values are lower for the dual-permeability model compared to the bulk permeability model, with the minimum misfit reduced from 6.12 to 5.78. A misfit minimum is found at a reservoir permeability of $k = 0.11\,\mathrm{D}$ and a fault damage zone permeability of $k_f = 16\,\mathrm{D}$. The CO_2 distribution for this simulation is shown in Figure 5.14. A comparison of the misfit function between the bulk permeability model and the dual-permeability model shows that the fit is improved between simulated and observed CO_2 distributions by adding a high permeability damage zone near the fault. However, although more of the CO_2 flow is towards the south-east, there is still a significant fraction of the plume which propagates towards the north-east, which is not seen in the seismic observation. This suggests that a dual-permeability model is not sufficient to explain the observed CO_2 flow, and discussion over the causes for this remaining discrepancy is presented in Section 5.6.

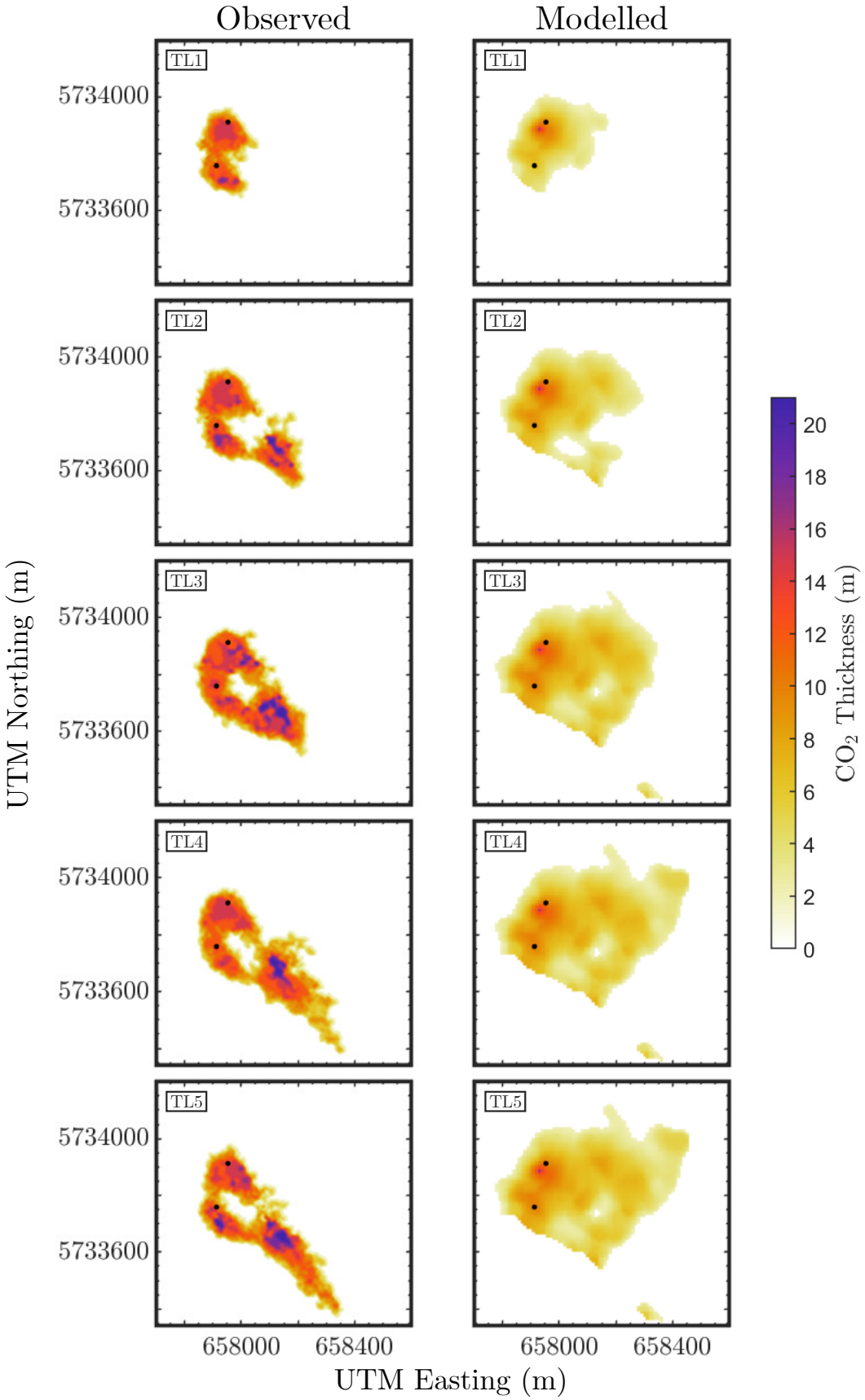

Figure 5.14: Observed (left-hand side) and modelled (right-hand side) CO_2 distribution using a reservoir permeability of $k = 0.11$ D and a fault damage zone permeability of $k_f = 16$ D obtained by history-matching.

5.5 Stabilisation of the CO_2 plume by residual trapping

Although flow simulations using a bulk permeability or dual-permeability model are unable to match the detailed planforms of the observed CO_2 plume, there is agreement on the timescale over which the CO_2 plume stabilises. Simulations are run with a high residual trapping fraction $s_{CO_2,r}/s_{CO_2,i} = 0.81$, meaning that fast stabilisation of the active CO_2 plume due to residual trapping occurs. The similar CO_2 distributions of the simulated plumes in seismic surveys TL4 and TL5, which took place 1 year and 2 years post-injection respectively, signal stabilisation of the active plume, and this is also reflected in the observed CO_2 plumes.

To analyse the effect of residual saturation on time to plume stabilisation more quantitatively, the change in height of the active CO_2 plume is calculated and summed across the entire plume and plotted as a function of time for varying residual trapping fractions $s_{CO_2,r}/s_{CO_2,i}$. (Figure 5.15a). Simulations are performed for a bulk permeability of $k = 188\,\text{mD}$ and assume a uniform initial saturation $s_{CO_2,i} = 0.16$. For larger values of s_r, the volume change of the active plume rapidly decreases as a larger fraction of the CO_2 is being residually trapped, and the active plume stabilises earlier compared to if no residual trapping occurs. For numerical simulations using low residual trapping fractions of $s_{CO_2,r}/s_{CO_2,i} = 0.2$ and 0.4, there is still significant movement of the CO_2 plume at the times of the TL4 and TL5 seismic surveys.

In contrast, for a high residual trapping fraction of $s_{CO_2,r}/s_{CO_2,i} = 0.8$, the volume change by the times of the TL4 and TL5 seismic surveys is greatly reduced, and so the thickness distribution of the resultant plume is similar between the two seismic surveys. This agrees with seismic observations of the plume distributions (Figure 4.32), which show similar plume distribution for the TL4 and TL5 surveys, suggesting that the CO_2 plume has mostly stabilised by the time of the TL5 survey.

By defining a threshold volume change below which the simulated active plume is effectively stable, the time to stabilisation is calculated as a function of the residual trapping fraction (Figure 5.15b). This illustrates the dependency of the time to plume stabilisation on the residual trapping fraction with stabilisation times around five times greater where no residual trapping occurs compared to a 90% trapping fraction. Error bars represent the range of

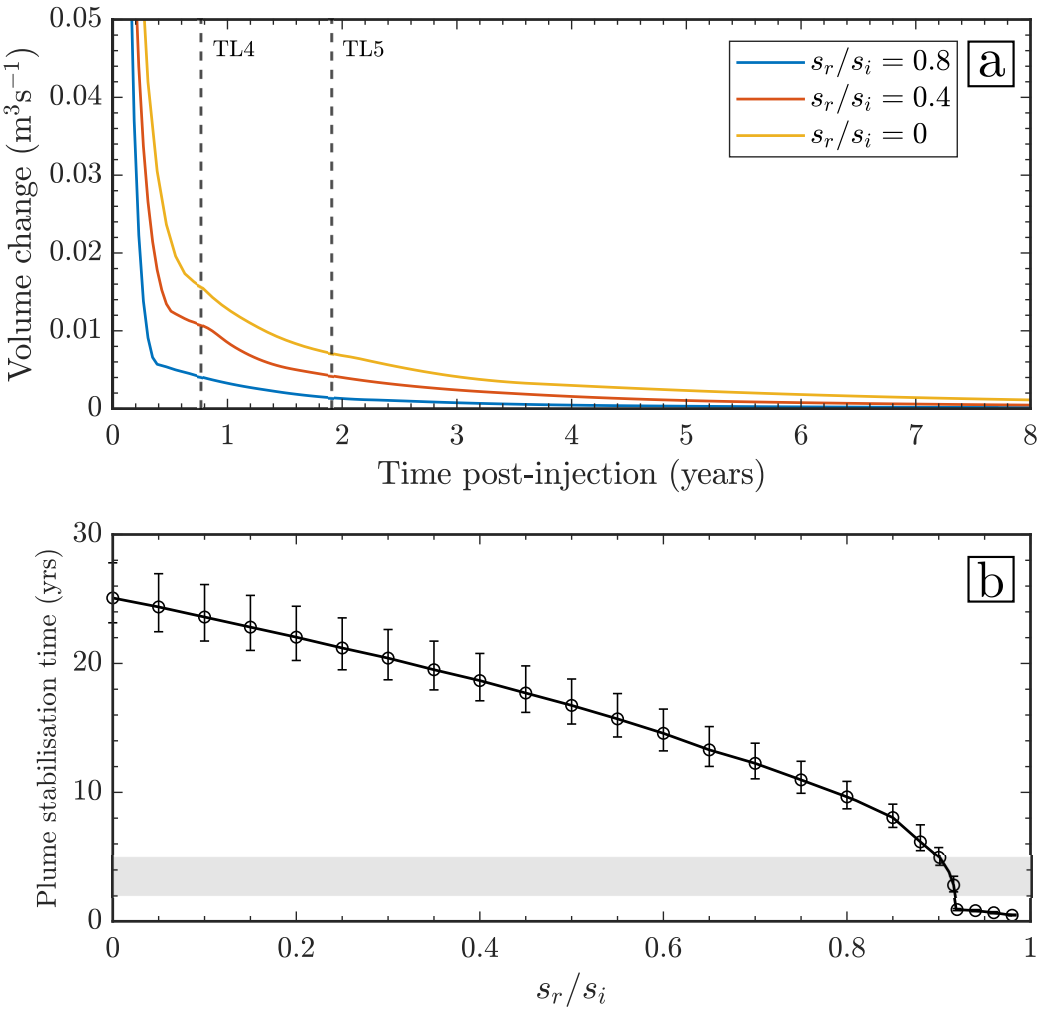

Figure 5.15: (a) Volume change of the CO_2 plume as a function of time for varying residual trapping fractions. Vertical dashed lines show the times of the TL4 and TL5 seismic surveys. (b) Time to plume stabilisation as a function of residual trapping fraction. Stabilisation time is defined as the time at which the volume change in (a) falls below a threshold value of 1×10^{-4} $m^3 s^{-1}$. Error bars illustrate a 20% change in the threshold. The horizontal grey bar represents a plume stabilisation time range of 2-5 years, appropriate for the Otway Stage 2C injection (Watson *et al.*, 2018).

stabilisation times that result from a 20% change in the threshold value. The horizontal grey bar shows the 2-5 year stabilisation time range that is expected for the Stage 2C injection (Dance *et al.*, 2019; Watson *et al.*, 2018). This timescale for stabilisation agrees with simulated plume stabilisation times at high residual trapping fractions, $s_{CO_2,r}/s_{CO_2,i} \approx 0.9$. This suggests that there is a high level of residual trapping in the storage reservoir, and that residual trapping plays an important role in stabilisation of the CO_2 plume.

5.6 Discussion

The vertically-integrated flow simulations capture some aspects of the observed plume behaviour such as the plume thickness and shape at early times and the time to stabilisation by residual trapping. However, there are remaining discrepancies between observed and simulated CO_2 distributions and this section will discuss reason for this, as well as touch upon what we can and cannot infer about the reservoir and flow of CO_2 from the numerical simulations.

The first likely cause for discrepancy is due to uncertainty in the topography of the caprock. The topography of the caprock controls the advective flow of the CO_2. For the simulations performed here, a topographic high towards the north-east of the injection zone drives significant CO_2 flow in that direction, which is not capture by the seismic observations. The numerical simulations for the Stage 2C injection were rerun using the caprock topography from the regional seismic surveys (Dance *et al.*, 2012). A bulk reservoir permeability model was used, and the misfit function between observed and simulated plumes calculated, with a minimum misfit found at a permeability of $k = 134\,\mathrm{mD}$ (Figure 5.16). The simulated plume distributions using this permeability are shown in Figure 5.17. The overall shape of the simulated plumes agree better with the observed plume, especially for the time-lapse surveys TL1-TL3 taken during the injection phase. Simulated CO_2 flow moves preferentially southeast of the injection zone, due to a large scale topographic gradient in this direction. This closer match between observed and simulated plumes is reflected in lower misfit values compared to the bulk permeability simulations performed using caprock topography from the 2015 baseline survey. However, although use of the regional seismic surveys results in a better match, much of this is due to the presence of a high topography channel that runs parallel to the fault (see Figure 4.9b). This is potentially an artifact of the lower resolution seismic acquisition parameters and use of a post-stack time migration during seismic processing, which results in poorer seismic image quality around fault zones.

It is difficult to say exactly what is the cause for the discrepancy between the two seismic surveys, but possible reasons include variations in the acquisition and processing workflows, updated velocity models used in the time-to-depth conversion and different survey resolu-

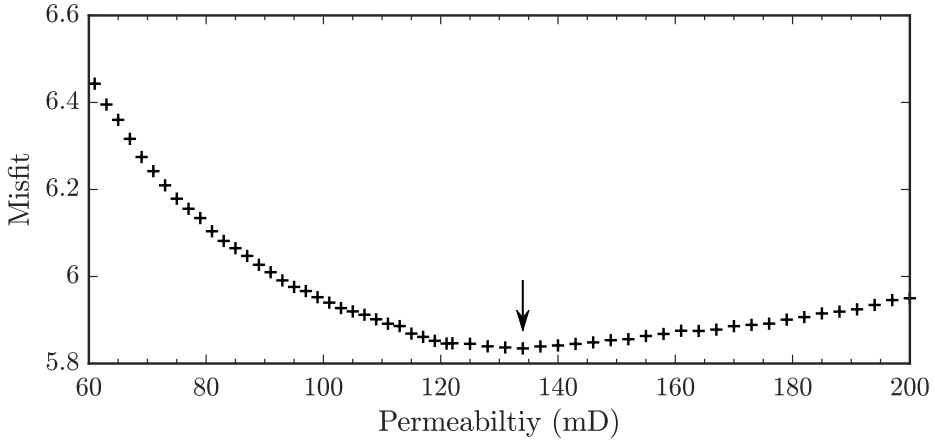

Figure 5.16: Misfit between observed and simulated CO_2 distribution for uniform reservoir permeability simulations with using PS1 caprock topography obtained from regional seismic surveys (Dance *et al.*, 2012). Black arrow shows bulk permeability of 134 mD which corresponds with the minimum misfit.

tions. An important consideration is the extent to which differences between repeat seismic surveys can affect the results of flow simulations. For the Stage 2C injection, looking at the simulations using topographies from different surveys, the planforms have similar shapes and thicknesses at early times, but as the CO_2 moves further into the reservoir there are significant changes in the shapes of the simulated plumes. Accurately determining the causes of discrepancy between repeat seismic surveys at a potential injection site and a quantitative assessment of how this affects the interpreted geological structure and resulting numerical simulations is an important area for future research.

The second likely cause of discrepancy between the simulated and observed CO_2 plumes is due to spatial distribution of permeability in the reservoir. Including a large-scale permeability structure associated with the fault damage zone was not sufficient to match between observed and simulated plumes. Due to the heterogeneous nature of the storage formation, there are likely further spatial variations in permeability, both vertically and laterally, which will affect the flow of CO_2. In particular, the calcite baffles within the reservoir play an important role in governing the flow of CO_2, and uncertainties in their size, position and geometry will translate to uncertainties in the flow models. Modelling a spatially varying permeability structure is not within the scope of this thesis, but results from the numerical simulations performed can be used to infer something about the possible permeability structure of the reservoir.

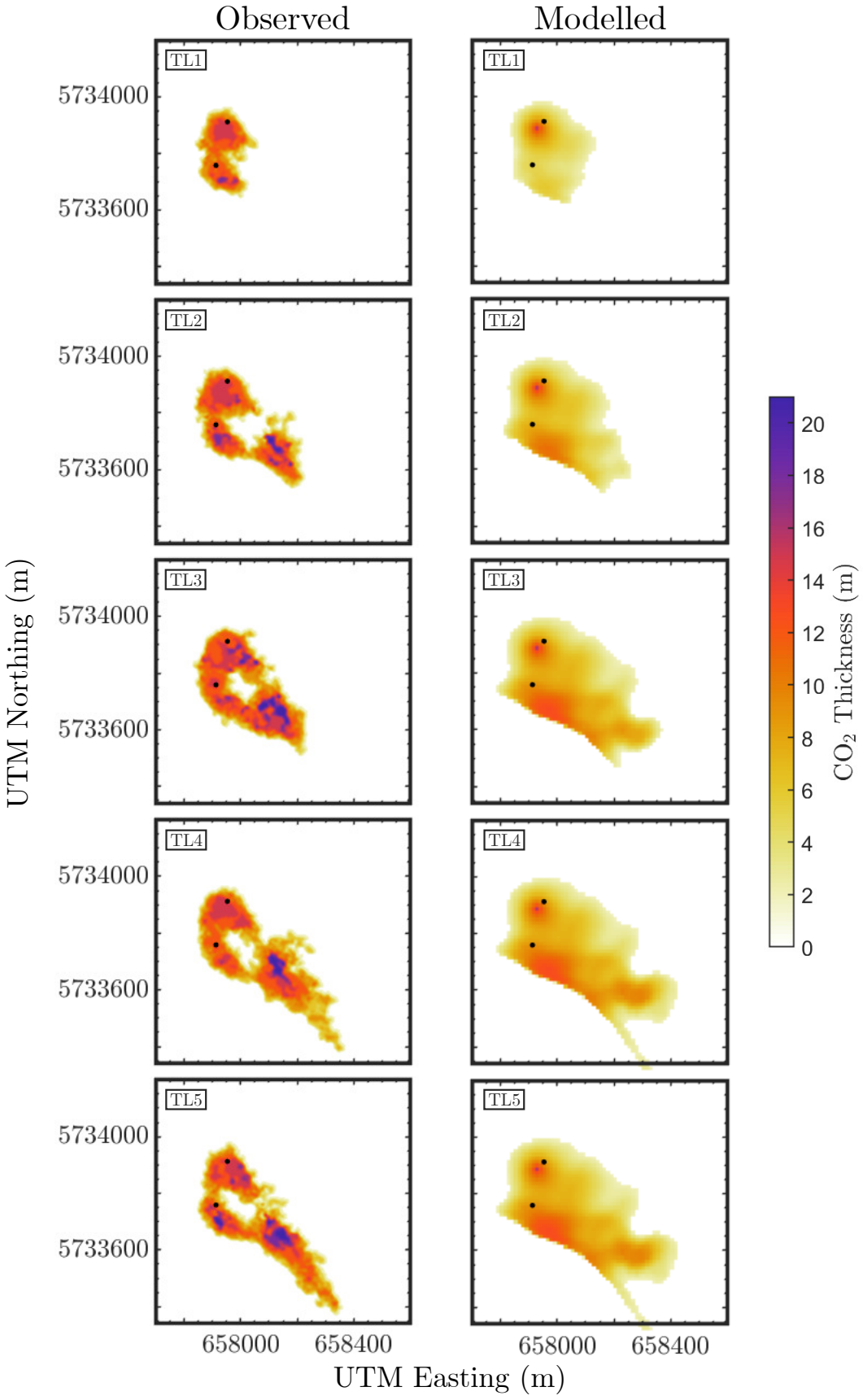

Figure 5.17: Observed (left-hand side) and modelled (right-hand side) CO_2 distribution using uniform permeability obtained by history-matching and topography from Dance *et al.* (2012). $k = 134\,\text{mD}$.

The first discrepancy between the simulated and observed CO_2 plumes that may be a result of spatially varying permeability is the hole seen within the CO_2 plume just to the east of CRC-1. It is likely that there is a low permeability region which is inhibiting flow through this area. Dance *et al.* (2019) speculates that this is due to a further splay fault which inhibits cross-fault flow through the region. It could also be caused by a lower permeability zone due to calcification of the deltaic sandstones. The second discrepancy is the lack of CO_2 in the observed plumes towards the north-east of the area. This could be due to higher permeabilities associated with the fault zone across wider distances than suggested by fault scaling relationships which channel CO_2 flow towards the south-east, or lower permeabilities on a larger-scale towards the north-east of the fault block. However, TWTT-depth relationships for the wells further north suggest there are not significant lateral velocity variations across the fault block (Dance *et al.*, 2012). Another possible explanation is that some CO_2 does move towards the north-east but is not detected by the seismic reflection surveys. Potential evidence to support this are the isolated patches of increased amplitude seen in amplitude difference maps (Figure 4.15), which were thought to be due to noise between seismic surveys but may be due to patches of CO_2. This highlights another important uncertainty associated with the limited resolution of the seismic data.

The third cause of discrepancy between the simulated and observed CO_2 plumes is down to the validity of the gravity current model. The current simulations assume that the flow is unconfined, neglect capillary effects and assume a uniform CO_2 saturation in the plume. Confining forces will govern flow behaviour around the injection zone at early times, and capillary forces will act to rearrange the CO_2 saturation into high permeability layers, as discussed in Section 5.2.1. Vertical permeability structures may also result in significant vertical flow, which is not captured in vertical equilibrium models. However, it is still expected that horizontal flow will still dominate flow behaviour as the aspect ratio of the flow is still large. Incorporating these modifications to the gravity current model are areas for future research.

It is likely that uncertainties in the topography, reservoir permeability structure and simplifications to the gravity current model all contribute towards discrepancies between simulated and observed CO_2 distributions. Differences in the caprock geometry due to variation be-

tween seismic surveys resulted in changes to the simulated plume distribution highlighted by a difference in the misfit function. Similarly, changing from a bulk permeability to dual-permeability model also resulted in a similar reduction in the misfit function, although there was a smaller change in the planform of the CO_2 plume, suggesting that broad scale CO_2 movement is affected more by reservoir geometry. The discrepancies between observed and simulated CO_2 distributions highlights the utility of vertically-integrated simulations combined with history-matching as a means to identify where the reservoir geometry or permeability structure is unknown.

5.7 Summary

In this chapter, I have presented results from flow simulations of the Otway Stage 2C injection. The numerical model used is a vertically-integrated, sharp-interface model which assumes that the CO_2 current is unconfined. It is the first use of a reduced-order modelling approach at the Otway site, and provides an opportunity to assess the use of such models in a heterogeneous storage formation such as the storage interval used in the Otway Stage 2C trial.

I quantitatively assess some of the simplifying assumptions within the model, such as neglecting vertical confinement and capillary effects. I find that although viscous forces due to confinement are likely to play a role in governing the flow behaviour at early times close to the injection well, buoyancy forces should dominate the flow further from the injection well. Due to strong vertical permeability variations across the storage formation, it is likely that capillary effects will play a large role in rearranging the CO_2 saturation in the reservoir, and incorporating multiphase effects such as relative permeability is an important area for future research.

Flow simulations using bulk reservoir and fluid properties from the literature and well log measurements do a relatively poor job at matching the observed CO_2 distributions. Bulk permeability simulations using the best-fit permeability obtained by history-matching reduces the misfit between simulated and observed plumes, but there is still significant disagreement, which suggests the reservoir has a more complex permeability structure.

The damage zone surrounding the Naylor South fault and splay fault which bound the storage formation is a likely source of large-scale heterogeneity. Simulations were run using a dual-permeability model, where the permeability of the fault damage zone and the permeability of the rest of the reservoir were allowed to vary, with the width of the damage zone determined using scaling relationships from the literature between fault displacement and damage zone width. The numerical simulations fit the overall shape of the observed CO_2 better, with more CO_2 flowing along the fault, but there is still significant flow towards a topographic high east of injection well, which is not seen in the seismic images.

Seismic observations of the CO_2 plume at 1 and 2 years post-injection suggest that the plume mostly stabilises within this time. Numerical simulations performed with a high residual trapping fraction of $s_{CO_2,r}/s_{CO_2,i} \approx 0.8$ show stabilisation of the plume within a similar time-frame. It is found that the time to plume stabilisation is around five times greater where no residual trapping occurs compared to a 90% residual trapping fraction.

Possible causes for the remaining discrepancy between observed and simulated CO_2 distributions such as uncertainty in the caprock topography, a spatially variable permeability distribution in the reservoir and simplifications in the gravity current model are discussed. Even though the flow simulations performed are not be able to replicate the observed CO_2 flow, they are valuable in highlighting which aspects of the CO_2 flow cannot be explained with current knowledge of the reservoir geometry and permeability structure.

Chapter 6

Conclusions and Future Work

6.1 Summary and Conclusions

In this dissertation, three important aspects of carbon dioxide (CO_2) storage security in sub-surface geological reservoirs have been investigated through the use of reduced-order analytical and numerical models. These are CO_2 trapping rates due to dissolution in heterogeneous reservoirs, CO_2 leakage rates through fault zones and modelling CO_2 flow for a field-scale carbon storage project with comparison to observations from time-lapse seismic reflection surveys.

The rate of CO_2 dissolution in saline aquifers is the least well-constrained of the secondary trapping mechanisms which enhance the long-term security of geological carbon storage. CO_2 injected into an aquifer with interbedded high and low permeability layers will preferentially be confined to the higher permeability layers, which increases the CO_2-water interfacial area and increases dissolution rates. In Chapter 2, I provide a conservative, first-principles analysis of the quantity of CO_2 dissolved and the rate at which free-phase CO_2 propagates in

layered reservoirs. A horizontally layered reservoir comprising alternating higher and lower permeability layers was modelled. Free-phase, low viscosity CO_2 is confined to the higher permeability layers, and a finite capillary entry pressure impedes the CO_2 from entering the lower permeability layers. The velocity at which CO_2 travels in the reservoir is dominated by the advective input flux at early times and transitions to an intermediate diffusion dominated regime as diffusive loss of CO_2 increases. At late times, the water in the low permeability layers reaches CO_2 saturation, dampening diffusion and resulting in a return to an advection dominated regime. The significance of these regimes is governed by the ratio between the volume available for CO_2 dissolution in the low permeability layers and the volume of CO_2 within the high permeability layers. This ratio also governs the maximum fraction of injected CO_2 dissolved at late times. The model was applied to a real world example of a carbon storage reservoir, and it was found that for characteristic bedding thicknesses of $< 0.1\,\mathrm{m}$, over 10% of the injection CO_2 will dissolve into the water within a few years of injection and propagation distances into the reservoir are reduced by $\sim 10\%$. The tendency of low viscosity supercritical CO_2 to finger and the much more complex flow paths in real reservoirs will likely increase CO_2 dissolution rates above the minimum estimates from this model.

Fault zones have the potential to act as leakage pathways through low permeability structural seals in geological reservoirs. In the case of CO_2 storage, they pose a risk of CO_2 leakage to the surface, as faults can cut through multiple aquifers and caprocks. In Chapter 3, I developed an analytical model to describe the dynamics of leakage through a fault zone cutting multiple aquifers and seals, which was tested against porous media laboratory experiments. It comprises a two-dimensional gravity current in a porous medium, fed by a buoyant plume spreading under a horizontal impermeable baffle. The baffle contains a low permeability fault through which the current leaks. This system constitutes a reduced order model of a faulted caprock, whereby an impermeable fault core is surrounded by a high permeability fracture zone. A set of porous media tank experiments verify the dependence of the fault width, fault height, input flux and input density on leakage rates through the fault as predicted by the model. Crucially, the analysis showed how these parameters control the ratio of fluid flux into the aquifer compared to fluid leaking through the fault, which is significant for storage efficiency. The utility of the model for the assessment of CO_2 storage was demonstrated by application to a naturally occurring CO_2-charged aquifer at Green

River, Utah. I calculated the fluid distribution and leakage rates across multiple vertically stacked aquifers, cross-cut by a fault, and found that if the fault permeability is comparable to or less than the reservoir permeability, the majority of the CO_2 remains trapped within the lowest layer over a roughly 1000 year time scale. This framework can be used for quick assessment of fluid leakage through fault zones, given a set of input parameters relating to properties of the fault, aquifer and fluids, and can be incorporated into basin-scale models to improve computational efficiency.

In Chapter 4, I reviewed the time-lapse seismic reflection surveys and geological information from Stage 2C of the Otway Project, a pilot scale CO_2 sequestration project in Victoria, Australia. 15,000 tonnes of CO_2-rich gas were injected into the Paaratte formation at a depth of 1500 m, accompanied by time-lapse seismic monitoring. Well logs show that the deltaic storage formation is highly heterogeneous. Large variations in porosity and permeability are caused by calcite and dolomite cemented layers. Comparison between the baseline seismic survey and subsequent post-injection surveys show multiple reflections which display an increase in seismic amplitude. This amplitude anomaly spreads out along a bounding fault zone, forming an elongate plume roughly 750 m in length. The areal extent of the anomaly varies depending on the horizon analysed and differencing method use, but all horizons display the same overall behaviour of an increase in plume area during injection followed by a period of steady areal extent with possible decline at later times. Seismic waveform modelling of CO_2 thicknesses in the injection region using a geological model from well log data suggests a linear scaling between the amplitude change and CO_2 thickness. The total volume of CO_2 injection into the reservoir can be used to constrain the exact amplitude-thickness scaling, provided the CO_2 saturation in the plume is known. Saturation logs at the injection well and an observation well suggest that the CO_2 saturation varies from 0.4-1 over the injection interval, with larger variation outside the injection the interval. The lack of further constrains on the CO_2 saturation in the plume mean that amplitude measurements alone cannot be used to estimate the thickness of the CO_2 plume.

Numerical simulations of CO_2 flow are important for testing the suitability of storage sites and identifying potential hazards prior to injection. In Chapter 5, a vertically-integrated reservoir simulator incorporating residual trapping was developed and used to model the

Otway Stage 2C injection. Results of the simulations were compared against CO_2 plume thickness measurements obtained via inversion of vertical changes in acoustic impedance (Glubokovskikh *et al.*, 2020). It is the first attempt at a vertically-integrated modelling approach at Otway, and provides an opportunity to assess the use of such models in a heterogeneous storage formation. Flow simulations performed using a uniform reservoir permeability structure fit the observed CO_2 distribution poorly. The damage zone surrounding the fault that bounds the storage formation is a likely source of large-scale heterogeneity. Simulations were run using a dual-permeability model, which improved the fit but the remaining discrepancy suggests there is further spatial variability in the reservoir permeability. The planform of the simulated plume notably changes when using a caprock topography from old regional seimsic survey. This highlights the need to investigate characteristic errors in reservoir geometry from subsequent seismic surveys. A comparison of the time to plume stabilisation between observed and simulated CO_2 plumes suggests that the residual trapping fraction is high ($s_{CO_2,r}/s_{CO_2,i} \approx 0.8$). Plume stabilisation times are around five times greater when no residual trapping occurs compared to a high residual trapping fraction. Even when flow simulations are unable to match the observed CO_2 distribution precisely, this work highlights their use in identifying unknown aspects of the reservoir geometry and permeability structure.

6.2 Future Work

The analysis presented in this dissertation uses a series of geologically and fluid dynamically informed assumptions to simplify the CO_2-water system and the geological settings. This allows analytical solutions to be obtained, simplifies the numerical modelling, and focuses the understanding on the key physical parameters that affect the behaviour of the system. Future work could look to build on the models developed, so that they incorporate more of the physics that occurs during CO_2 injections into storage reservoirs.

For example, the model for dissolution rates in a horizontally layered system presented in Chapter 2 could be expanded to the three dimensional radial case, to more accurately model CO_2 injection into a three-dimensional reservoir. Assuming a constant injection flux,

the velocity of the front would drop of like $v \sim 1/r^2$, where r is the radial distance from the injection point, without the presence of dissolution, and it would be interesting to see how this affects dissolution rates. Another extension would be to replace the periodically repeating layers with an arbitrary layered reservoir permeability structure, where each layer has a predetermined width and permeability. This would address the current assumption of an infinite capillary entry pressure for the low permeability layers, as CO_2 would be freely allowed to enter all layers, proving the capillary entry pressure was overcome.

Incorporating the effects of mechanical dispersion and viscosity variations between the injected and ambient fluid would act to increase the mixing and hence dissolution of CO_2 in the ambient water. These modifications could also be added to the model for fault leakage presented in Chapter 3. In addition, introducing confinement of the aquifer will mean that flow of the ambient phase is accounted for in the model. This is especially important when the thickness of the CO_2 current becomes comparable with the height of the aquifer. The current model uses a sharp-interface approximation, developed for miscible flows in porous media, but extra multiphase effects such as relative permeability and capillary entry pressures need to be considered when applied to immiscible settings such as CO_2-water systems.

Additional seismic reflection surveys of the Otway CO_2 storage site have been obtained as part of Stage 3 of the Otway Project. Mapping horizons within the Stage 2C storage interval and comparing them to the legacy regional survey and 2015 baseline survey could provide further insight into the differences between subsequent seismic surveys. The sensitivity of the flow of CO_2 in the numerical simulations to these changes in geometry as a result of differences between the seismic surveys could be investigated further. The observed extent of the CO_2 plumes in these subsequent surveys could also be used to test the predictions of the numerical simulations at later times. Five additional wells have also been drilled, and the well log data should provide a more detailed spatial permeability map of the reservoir, as well as an updated velocity model for time to depth conversions. The numerical simulations could be run with a more informed permeability structure, to better understand how permeability variations might affect the flow of CO_2.

Adaptations can be made to the vertically-integrated gravity current model used to simulate the Stage 2C injection in Chapter 5. Incorporating confinement of the aquifer is important

at Otway as the thickness of the plume is comparable to the thickness of the storage interval. This will allow changes in aquifer thickness to influence the flow of CO_2. Analysis of the dominant forces controlling the flow suggests that capillary effects are important in rearranging the CO_2 saturation in the plume due to the heterogeneous nature of the formation. This suggests that multiphase effects such as relative permeability and capillary forces are important and therefore are worthwhile additions to the model. For a homogeneous permeability structure, capillary forces may lead to a lower CO_2 saturation and therefore lower relative permeability. This means the current height profile would need to be steeper in order to drive flow, resulting in a thicker current (Golding *et al.*, 2013). If vertical or lateral permeability variations are introduced, variable capillary entry pressures within the reservoir may mean that there are variations in CO_2 saturations across the reservoir, and hence variations in relative permeability, which will act to disperse the CO_2 flow. Finally, observations of the plume show a possible reduction in areal extent at late times, which could be due to dissolution of CO_2 into the ambient brine. The gravity current model could be adapted to account for the effects of CO_2 dissolution, although benchmarking dissolution rates is difficult as there are limited accurate field measurements of CO_2 dissolution.

Introducing these modifications means that more of the physics observed in CO_2-water systems is captured, which can lead to more accurate results. However, it is important to avoid overcomplicating the problem to maintain an understanding of the key effects controlling the system. This means that the results and knowledge gained can be confidently applied to other CO_2 storage settings.

References

Acton, J. M., Huppert, H. E., & Worster, M. G., 2001. Two-dimensional viscous gravity currents flowing over a deep porous medium, *J. Fluid Mech.*, **440**, 359.

AlNasser, H., Pevzner, R., Tertyshnikov, K., Popik, D., & Urosevic, M., 2017. Application of 4D VSP for monitoring of small-scale supercritical CO_2 injection: Stage 2C of CO2CRC Otway project case study, in *Fourth EAGE Borehole Geophysics Workshop*, vol. 2017, pp. 1–5, European Association of Geoscientists & Engineers.

Amooie, M. A., Soltanian, M. R., & Moortgat, J., 2018. Solutal convection in porous media: Comparison between boundary conditions of constant concentration and constant flux, *Phys. Rev. E*, **98**(3), 033118.

Antonellini, M. & Aydin, A., 1994. Effect of faulting on fluid flow in porous sandstones: petrophysical properties, *AAPG Bull.*, **78**(3), 355–377.

Aradóttir, E. S. P., Sigurdardóttir, H., Sigfússon, B., & Gunnlaugsson, E., 2011. CarbFix: a CCS pilot project imitating and accelerating natural CO_2 sequestration, *Greenh. Gases: Sci. Technol*, **1**(2), 105–118.

Arch, J. & Maltman, A., 1990. Anisotropic permeability and tortuosity in deformed wet sediments, *J. Geophys. Res. Solid Earth*, **95**(B6), 9035–9045.

Arts, R., Eiken, O., Chadwick, A., Zweigel, P., van der Meer, B., & Kirby, G., 2004. Seismic monitoring at the Sleipner underground CO_2 storage site (North Sea), *Geol. Soc. Spec. Publ.*, **233**(1), 181–191.

Audigane, P., Gaus, I., Czernichowski-Lauriol, I., Pruess, K., & Xu, T., 2007. Two-dimensional reactive transport modeling of CO_2 injection in a saline aquifer at the Sleipner site, North Sea, *Am. J. Sci.*, **307**(7), 974–1008.

Avci, C. B., 1994. Evaluation of flow leakage through abandoned wells and boreholes, *Water Resour. Res.*, **30**(9), 2565–2578.

Bachu, S., Bonijoly, D., Bradshaw, J., Burruss, R., Holloway, S., Christensen, N. P., & Mathiassen, O. M., 2007. CO_2 storage capacity estimation: Methodology and gaps, *Int. J. Greenh. Gas Control.*, **1**(4), 430–443.

Baines, S. J. & Worden, R. H., 2004. The long-term fate of CO_2 in the subsurface: natural analogues for CO_2 storage, *Geol. Soc. Spec. Publ.*, **233**(1), 59–85.

Balsamo, F., Storti, F., Salvini, F., Silva, A. T., & Lima, C. C., 2010. Structural and petrophysical evolution of extensional fault zones in low-porosity, poorly lithified sandstones of the Barreiras Formation, NE Brazil, *J. Struct. Geol.*, **32**(11), 1806–1826.

Bandilla, K. W., Celia, M. A., & Leister, E., 2014. Impact of model complexity on CO_2 plume modeling at Sleipner, *Energy Procedia*, **63**, 3405–3415.

Bear, J., 1988. *Dynamics of fluids in porous media*, Courier Corporation.

Bear, J. & Cheng, A. H. D., 2010. *Modeling groundwater flow and contaminant transport*, vol. 23, Springer Science & Business Media.

Benham, G. P., Bickle, M. J., & Neufeld, J. A., 2021. Upscaling multiphase viscous-to-capillary transitions in heterogeneous porous media, *J. Fluid Mech.*, **911**.

Benham, G. P., Bickle, M. J., & Neufeld, J. A., 2021. Two-phase gravity currents in layered porous media, *J. Fluid Mech.*, **922**.

Bennion, B. & Bachu, S., 2005. Relative permeability characteristics for supercritical CO_2 displacing water in a variety of potential sequestration zones, in *SPE Annual Technical Conference and Exhibition*, OnePetro.

Bentham, M. & Kirby, M., 2005. CO_2 storage in saline aquifers, *Oil Gas Sci. Technol.*, **60**(3), 559–567.

Beuttler, C., Charles, L., & Wurzbacher, J., 2019. The role of direct air capture in mitigation of anthropogenic greenhouse gas emissions, *Front. Clim.*, **1**, 10.

Bickle, M. & Kampman, N., 2013. Lessons in carbon storage from geological analogues, *Geology*, **41**(4), 525–526.

Bickle, M., Chadwick, A., Huppert, H. E., Hallworth, M., & Lyle, S., 2007. Modelling carbon dioxide accumulation at sleipner: Implications for underground carbon storage, *Earth Planet. Sci. Lett.*, **255**(1-2), 164–176.

Bickle, M., Kampman, N., Chapman, H., Ballentine, C., Dubacq, B., Galy, A., Sirikitputtisak, T., Warr, O., Wigley, M., & Zhou, Z., 2017. Rapid reactions between CO_2, brine and silicate minerals during geological carbon storage: Modelling based on a field CO_2 injection experiment, *Chem. Geol.*, **468**, 17–31.

Biot, M. A., 1956. Theory of propagation of elastic waves in a fluid-saturated porous solid. II. Higher frequency range, *J. Acoust. Soc. Am.*, **28**(2), 179–191.

Boait, F. C., 2012. *Seismic imaging of sequestered carbon dioxide*, Ph.D. thesis, University of Cambridge.

Boreham, C., Underschultz, J., Stalker, L., Kirste, D., Freifeld, B., Jenkins, C., & Ennis-King, J., 2011. Monitoring of CO_2 storage in a depleted natural gas reservoir: gas geochemistry from the CO2CRC Otway Project, Australia, *Int. J. Greenh. Gas Control.*, **5**(4), 1039–1054.

Bourne, S., Crouch, S., & Smith, M., 2014. A risk-based framework for measurement, monitoring and verification of the quest ccs project, alberta, canada, *Int. J. Greenh. Gas Control.*, **26**, 109–126.

Brie, A., Pampuri, F., Marsala, A. F., & Meazza, O., 1995. Shear sonic interpretation in gas-bearing sands, in *SPE Annual Technical Conference and Exhibition*, OnePetro.

Bunch, M., Daniel, R., Lawrence, M., Browne, G., Menacherry, S., Dance, T., & Arnot, M., 2012. Multi-scale characterisation of the Paaratte Formation, Otway Basin, for CO_2 injection and storage, *The APPEA Journal*, **52**(2), 664–664.

Busch, A., Krooss, B. M., Gensterblum, Y., Bergen, F. V., & Pagnier, H. J. M., 2003. High-pressure adsorption of methane, carbon dioxide and their mixtures on coals with a special focus on the preferential sorption behaviour, *J. Geochem. Explor.*, **78**, 671–674.

Bush, A., 2009. *Physical and chemical hydrogeology of the Otway Basin, southeast Australia*, Ph.D. thesis, University of Melbourne.

Cadogan, S. P., Maitland, G. C., & Trusler, J. P. M., 2014. Diffusion coefficients of CO_2 and N_2 in water at temperatures between 298.15 K and 423.15 K at pressures up to 45 MPa, *J. Chem. Eng. Data*, **59**(2), 519–525.

Caine, J. S., Evans, J. P., & Forster, C. B., 1996. Fault zone architecture and permeability structure, *Geology*, **24**(11), 1025–1028.

Carslaw, H. S. & Jaeger, J. C., 1959. *Conduction of Heat in Solids*, Oxford science publications, Clarendon, Oxford, 2nd edn.

Carter, L. L. & Cashwell, E. D., 1975. Particle-transport simulation with the monte carlo method, Tech. rep., Los Alamos Scientific Lab.

Caspari, E., Pevzner, R., Gurevich, B., Dance, T., Ennis-King, J., Cinar, Y., & Lebedev, M., 2015. Feasibility of CO_2 plume detection using 4D seismic: CO2CRC Otway Project case study—Part 1: Rock-physics modeling, *Geophysics*, **80**(4), B95–B104.

Chadwick, A., Arts, R., Bernstone, C., May, F., Thibeau, S., & Zweigel, P., 2008. *Best practice for the storage of CO_2 in saline aquifers-observations and guidelines from the SACS and CO2STORE projects*, vol. 14, British Geological Survey.

Chadwick, R. A. & Noy, D. J., 2010. History-matching flow simulations and time-lapse seismic data from the Sleipner CO_2 plume, in *Geological Society, London, petroleum geology conference series*, vol. 7, pp. 1171–1182, Geological Society of London.

Chadwick, R. A., Arts, R., & Eiken, O., 2005. 4D seismic quantification of a growing CO_2 plume at Sleipner, North Sea, in *Geological Society, London, Petroleum Geology Conference series*, vol. 6, pp. 1385–1399, Geological Society of London.

Chang, K. W., Minkoff, S. E., & Bryant, S. L., 2008. Modeling leakage through faults of CO_2 stored in an aquifer, in *SPE Annual Technical Conference and Exhibition*, Society of Petroleum Engineers.

Chaudhary, K., Bayani, C. M., Wolfe, W. W., Maisano, J. A., Ketcham, R. A., & Bennett, P. C., 2013. Pore-scale trapping of supercritical CO_2 and the role of grain wettability and shape, *Geophys. Res. Lett.*, **40**(15), 3878–3882.

Class, H., Ebigbo, A., Helmig, R., Dahle, H. K., Nordbotten, J. M., Celia, M. A., Audigane, P., Darcis, M., Ennis-King, J., Fan, Y., Flemisch, B., Gasda, S. E., Jin, M., Krug, S., Labregere, D., Beni, A. N., Pawar, R. J., Sbai, A., Thomas, S. G., Trenty, L., & Wei, L., 2009. A benchmark study on problems related to co_2 storage in geologic formations, *Comput. Geosci.*, **13**(4), 409–434.

Clauser, C. & Kiesner, S., 1987. A conservative, unconditionally stable, second-order three-point differencing scheme for the diffusion—convection equation, *Geophys. J. Int.*, **91**(3), 557–568.

Coates, G. R., Xiao, L., & Prammer, M. G., 1999. *NMR logging: principles and applications*, vol. 234, Haliburton Energy Services Houston.

Cook, P., 2014. *Geologically storing carbon: Learning from the Otway Project experience*, CSIRO Publishing.

Cowton, L. R., 2017. *Monitoring sub-surface storage of carbon dioxide*, Ph.D. thesis, University of Cambridge.

Cowton, L. R., Neufeld, J. A., White, N. J., Bickle, M. J., White, J. C., & Chadwick, R. A., 2016. An inverse method for estimating thickness and volume with time of a thin CO_2-filled layer at the Sleipner Field, North Sea, *J. Geophys. Res. Solid Earth*, **121**(7), 5068–5085.

Cowton, L. R., Neufeld, J. A., White, N. J., Bickle, M. J., Williams, G. A., White, J. C., & Chadwick, R. A., 2018. Benchmarking of vertically-integrated CO_2 flow simulations at the Sleipner Field, North Sea, *Earth Planet. Sci. Lett.*, **491**, 121–133.

Dance, T., 2010. Core and well log analysis from the CRC-2 well, Tech. Rep. CO2CRC Publication Number: RPT10-2221, Cooperative Research Centre for Greenhouse Gas Technologies, Canberra, Australia.

Dance, T., Arnot, M., Brunch, M., Daniel, R., Ennis-King, J., Hortle, A., & Lawrence, M., 2012. Geocharacterisation and static modelling of the lower Paaratte Formation, Tech. Rep. CO2CRC Publication Number: RPT12-3481, Cooperative Research Centre for Greenhouse Gas Technologies, Canberra, Australia.

Dance, T., LaForce, T., Glubokovskikh, S., Ennis-King, J., & Pevzner, R., 2019. Illuminating the geology: Post-injection reservoir characterisation of the co2crc otway site, *Int. J. Greenh. Gas Control.*, **86**, 146–157.

Daniel, R., 2012. Containment/injectivity results from MICP analysis for seals intraformational barriers and reservoir samples, CRC-2, Otway Basin, Tech. Rep. CO2CRC Publication Number: TBN12-3830, Cooperative Research Centre for Greenhouse Gas Technologies, Canberra, Australia.

Davis, T. L., Landrø, M., & Wilson, M., 2019. *Geophysics and geosequestration*, Cambridge University Press.

Delgado, J. M. P. Q., 2007. Longitudinal and transverse dispersion in porous media, *Chem. Eng. Res. Des.*, **85**(9), 1245–1252.

Dooley, J. J., 2013. Estimating the supply and demand for deep geologic CO_2 storage capacity over the course of the 21st century: a meta-analysis of the literature, *Energy Procedia*, **37**, 5141–5150.

Dubacq, B., Bickle, M. J., & Evans, K. A., 2013. An activity model for phase equilibria in the H−2O–CO_2–NaCl system, *Geochim. Cosmochim. Acta*, **110**, 229–252.

Dupuit, J., 1863. *Études théoriques et pratiques sur le mouvement des eaux dans les canaux découverts et à travers les terrains perméabls: avec des considérations relatives au régime des grandes eaux, au débouché à leur donner, et à la marche des alluvions dans les rivières à fond mobile*, Dunod.

Dutton, S. P., Willis, B. J., White, C. D., & Bhattacharya, J. P., 2000. Outcrop characterization of reservoir quality and interwell-scale cement distribution in a tide-influenced delta, Frontier Formation, Wyoming, USA, *Clay Miner.*, **35**(1), 95–105.

Dutton, S. P., White, C. D., Willis, B. J., & Novakovic, D., 2002. Calcite cement distribution and its effect on fluid flow in a deltaic sandstone, Frontier Formation, Wyoming, *AAPG bulletin*, **86**(12), 2007–2021.

Ennis-King, J., LaForce, T., Paterson, L., Black, J. R., Vu, H. P., Haese, R. R., Serno, S., Gilfillan, S., Johnson, G., Freifeld, B., & Singh, R., 2017. Stepping into the same river twice: field evidence for the repeatability of a CO_2 injection test, *Energy Procedia*, **114**, 2760–2771.

Ennis-King, J., LaForce, T., Paterson, L., Dance, T., Jenkins, C., & Cinar, Y., 2017. Interpretation of above zone and storage zone pressure responses to carbon dioxide injection in the 2016 CO2CRC field test, *Energy Procedia*, **114**, 5671–5679.

Ennis-King, J. P. & Paterson, L., 2005. Role of convective mixing in the long-term storage of carbon dioxide in deep saline formations, *SPE Journal*, **10**(03), 349–356.

ETC, 2017. Better Energy, Greater Prosperity, Tech. rep., Energy Transitions Commission.

ETC, 2018. Mission Possible: Reaching net-zero carbon emissions from harder-to-abate sectors by mid-century, Tech. rep., Energy Transitions Commission.

Faulkner, D. R. & Rutter, E. H., 1998. The gas permeability of clay-bearing fault gouge at 20°C, *Geol. Soc. Spec. Publ.*, **147**(1), 147–156.

Faulkner, D. R., Jackson, C. A. L., Lunn, R. J., Schlische, R. W., Shipton, Z. K., Wibberley, C. A. J., & Withjack, M. O., 2010. A review of recent developments concerning the structure, mechanics and fluid flow properties of fault zones, *J. Struct. Geol.*, **32**(11), 1557–1575.

Fine, R. A. & Millero, F. J., 1973. Compressibility of water as a function of temperature and pressure, *J. Chem. Phys.*, **59**(10), 5529–5536.

Forster, R. A., Little, R. C., Briesmeister, J. F., & Hendricks, J. S., 1990. Mcnp capabilities for nuclear well logging calculations, *IEEE Trans. Nucl. Sci.*, **37**(3), 1378–1385.

Francis, A., 2018. A simple guide to depth conversion: Part I, *Geo ExPro*, **15**(2).

Freifeld, B. M., Trautz, R. C., Kharaka, Y. K., Phelps, T. J., Myer, L. R., Hovorka, S. D., & Collins, D. J., 2005. The U-tube: A novel system for acquiring borehole fluid samples from a deep geologic CO_2 sequestration experiment, *J. Geophys. Res. Solid Earth*, **110**(B10).

Furre, A., Kiær, A., & Eiken, O., 2015. CO_2-induced seismic time shifts at Sleipner, *Interpretation*, **3**(3), SS23–SS35.

Furre, A.-K., Eiken, O., Alnes, H., Vevatne, J. N., & Kiær, A. F., 2017. 20 years of monitoring CO_2-injection at Sleipner, *Energy Procedia*, **114**, 3916–3926.

Gambill, W. R., 1959. How to estimate mixtures viscosities, *Chem. Eng.*, **66**(5), 151–152.

Garcia, J. E., 2001. Density of aqueous solutions of CO_2, Tech. rep., Lawrence Berkeley National Lab.

Gasda, S. E., Nordbotten, J. M., & Celia, M. A., 2009. Vertical equilibrium with sub-scale analytical methods for geological CO_2 sequestration, *Comput. Geosci.*, **13**(4), 469.

Gassmann, F., 1951. Elastic waves through a packing of spheres, *Geophysics*, **16**(4), 673–685.

Geistlinger, H., Mohammadian, S., Schlueter, S., & Vogel, H. J., 2014. Quantification of capillary trapping of gas clusters using x-ray microtomography, *Water Resour. Res.*, **50**(5), 4514–4529.

Gershenzon, N. I., R. W. Ritzi, W. R., Dominic, D. F., Soltanian, M., Mehnert, E., & Okwen, R. T., 2015. Influence of small-scale fluvial architecture on CO_2 trapping processes in deep brine reservoirs, *Water Resour. Res.*, **51**(10), 8240–8256.

Ghaderi, A. & Landrø, M., 2009. Estimation of thickness and velocity changes of injected carbon dioxide layers from prestack time-lapse seismic data, *Geophysics*, **74**(2), O17–O28.

Gilfillan, S. M. V., Lollar, B. S., Holland, G., Blagburn, D., Stevens, S., Schoell, M., Cassidy, M., Ding, Z., Zhou, Z., Lacrampe-Couloume, G., & Ballentine, C. J., 2009. Solubility

trapping in formation water as dominant CO_2 sink in natural gas fields, *Nature*, **458**(7238), 614–618.

Gilmore, K. A., Neufeld, J. A., & Bickle, M. J., 2020. CO_2 dissolution trapping rates in heterogeneous porous media, *Geophys. Res. Lett.*, **47**(12), e2020GL087001.

Gilmore, K. A., Sahu, C. K., Benham, G. P., Neufeld, J. A., & Bickle, M. J., 2022. Leakage dynamics of fault zones: experimental and analytical study with application to CO_2 storage, *J. Fluid Mech.*, **931**.

Gislason, S. R. & Oelkers, E. H., 2014. Carbon storage in basalt, *Science*, **344**(6182), 373–374.

Global CCS Institute, 2020. Global status of ccs 2020, Tech. rep., Global CCS Institute.

Glubokovskikh, S., Pevzner, R., Dance, T., Caspari, E., Popik, D., Shulakova, V., & Gurevich, B., 2016. Seismic monitoring of CO_2 geosequestration: CO2CRC Otway case study using full 4D FDTD approach, *Int. J. Greenh. Gas Control.*, **49**, 201–216.

Glubokovskikh, S., Gunning, J., Pevzner, R., Shulakova, V., Popik, D., Proud, C., & Gurevich, B., 2018. Towards Seismic Characterisation of a Small CO_2 Leakage: CO2CRC Otway Project Case Study, in *14th Greenhouse Gas Control Technologies Conference Melbourne*, pp. 21–26.

Glubokovskikh, S., Pevzner, R., Gunning, J., Dance, T., Shulakova, V., Popik, D., Popik, S., Bagheri, M., & Gurevich, B., 2020. How well can time-lapse seismic characterize a small CO_2 leakage into a saline aquifer: CO2CRC Otway 2C experiment (Victoria, Australia), *Int. J. Greenh. Gas Control.*, **92**, 102854.

Godec, M., Kuuskraa, V., Leeuwen, T. V., Melzer, L. S., & Wildgust, N., 2011. CO_2 storage in depleted oil fields: The worldwide potential for carbon dioxide enhanced oil recovery, *Energy Procedia*, **4**, 2162–2169.

Golding, M. J., Neufeld, J. A., Hesse, M. A., & Huppert, H. E., 2011. Two-phase gravity currents in porous media, *J. Fluid Mech.*, **678**, 248–270.

Golding, M. J., Huppert, H. E., & Neufeld, J. A., 2013. The effects of capillary forces on the axisymmetric propagation of two-phase, constant-flux gravity currents in porous media, *Phys. Fluids*, **25**(3), 036602.

Golding, M. J., Huppert, H. E., & Neufeld, J. A., 2017. Two-phase gravity currents resulting from the release of a fixed volume of fluid in a porous medium, *J. Fluid Mech.*, **832**, 550–577.

Gonzalez, M. H., Bukacek, R. F., & Lee, A. L., 1967. The viscosity of methane, *Soc. Pet. Eng. J.*, **7**(01), 75–79.

Green, C. P. & Ennis-King, J., 2014. Steady dissolution rate due to convective mixing in anisotropic porous media, *Adv. Water Resour.*, **73**, 65–73.

Green, D. W. & Southard, M. Z., 2019. *Perry's chemical engineers' handbook*, McGraw-Hill Education.

Haese, R. R., LaForce, T., Boreham, C., Ennis-King, J., Freifeld, B. M., Paterson, L., & Schacht, U., 2013. Determining residual CO_2 saturation through a dissolution test-Results from the CO2CRC Otway Project, *Energy Procedia*, **37**, 5379–5386.

Hansson, A., Anshelm, J., Fridahl, M., & Haikola, S., 2021. Boundary work and interpretations in the IPCC review process of the role of bioenergy with carbon capture and storage (BECCS) in limiting global warming to 1.5°C, *Front. Clim.*.

Herring, A. L., Harper, E. J., Andersson, L., Sheppard, A., Bay, B. K., & Wildenschild, D., 2013. Effect of fluid topology on residual nonwetting phase trapping: Implications for geologic CO_2 sequestration, *Adv. Water Resour.*, **62**, 47–58.

Hesse, M., Tchelepi, H. A., & Orr, F. M., 2006. Scaling analysis of the migration of CO_2 in saline aquifers, in *SPE Annual Technical Conference and Exhibition*, OnePetro.

Hesse, M. A., Tchelepi, H. A., Cantwel, B. J., & Orr, F. M., 2007. Gravity currents in horizontal porous layers: transition from early to late self-similarity, *J. Fluid Mech.*, **577**, 363–383.

Hesse, M. A., Orr, F. M., & Tchelepi, H. A., 2008. Gravity currents with residual trapping, *J. Fluid Mech.*, **611**, 35–60.

Hill, K. A. & Durrand, C., 1993. The western otway basin: an overview of the rift and drift history using serial composite seismic profiles.

Houseworth, J. E., 1984. *Longitudinal dispersion in nonuniform, isotropic porous media*, Ph.D. thesis, California Institute of Technology.

Huang, F., Juhlin, C., Han, L., Kempka, T., Lüth, S., & Zhang, F., 2016. Quantitative evaluation of thin-layer thickness and CO_2 mass utilizing seismic complex decomposition at the Ketzin CO_2 storage site, Germany, *Geophys. J. Int.*, **207**(1), 160–173.

Huang, F., Bergmann, P., Juhlin, C., Ivandic, M., Lüth, S., Ivanova, A., Kempka, T., Henninges, J., Sopher, D., & Zhang, F., 2018. The first post-injection seismic monitor survey at the Ketzin pilot CO_2 storage site: results from time-lapse analysis, *Geophys. Prospect.*, **66**(1), 62–84.

Huang, Y., Ringrose, P. S., & Sorbie, K. S., 1996. The effects of heterogeneity and wettability on oil recovery from laminated sedimentary structures, *SPE Journal*, **1**(04), 451–462.

Huppert, H. E. & Neufeld, J. A., 2014. The fluid mechanics of carbon dioxide sequestration, *Annu. Rev. Fluid Mech.*, **46**, 255–272.

Huppert, H. E. & Woods, A. W., 1995. Gravity-driven flows in porous layers, *J. Fluid Mech.*, **292**, 55–69.

IEA, 2019. Direct CO_2 emissions from selected heavy industry sectors, Tech. rep., International Energy Agency.

IEA, 2020. Direct air capture, Tech. rep., International Energy Agency.

IEA, 2021. Net zero by 2050: A roadmap for the global energy sector, Tech. rep., International Energy Agency.

IEP, 2020. Ecological threat register 2020: Understanding ecological threats, resilience and peace, Tech. rep., Institute for Economics & Peace.

Iglauer, S., Paluszny, A., Pentland, C. H., & Blunt, M. J., 2011. Residual CO_2 imaged with X-ray micro-tomography, *Geophys. Res. Lett.*, **38**(21).

Il'in, A. M., 1969. Differencing scheme for a differential equation with a small parameter affecting the highest derivative, *Math. Notes Acad. Sci.*, **6**(2), 596–602.

Inanc, F., Gilchrist, W. A., & Chace, D., 2009. Physical basis, modeling, and interpretation of a new gas saturation measurement for cased wells, in *SPWLA 50th Annual Logging Symposium*, OnePetro.

IPCC, 2018. Global warming of 1.5°C: An IPCC special report on the impacts of global warming of 1.5°C above pre-industrial levels and related global greenhouse gas emissions pathways, in the context of strengthening the global response to the threat of climate change, sustainable development, and efforts to eradicate poverty., Tech. rep., Intergovernmental Panel on Climate Change.

IPCC, 2021. Climate Change 2021: The Physical Science Basis. Contribution of Working Group I to the Sixth Assessment Report of the Intergovernmental Panel on Climate Change, Tech. rep., Intergovernmental Panel on Climate Change.

Ivanova, A., Kashubin, A., Juhojuntti, N., Kummerow, J., Henninges, J., Juhlin, C., Lüth, S., & Ivandic, M., 2012. Monitoring and volumetric estimation of injected CO_2 using 4D seismic, petrophysical data, core measurements and well logging: a case study at Ketzin, Germany, *Geophys. Prospect.*, **60**(5), 957–973.

Jackson, S. J. & Krevor, S., 2020. Small-scale capillary heterogeneity linked to rapid plume migration during CO_2 storage, *Geophys. Res. Lett.*, **47**(18), e2020GL088616.

Jackson, S. J., Agada, S., Reynolds, C. A., & Krevor, S., 2018. Characterizing drainage multiphase flow in heterogeneous sandstones, *Water Resour. Res.*, **54**(4), 3139–3161.

Jenkins, C., Bagheri, M., Barraclough, P., Dance, T., Ennis-King, J., Freifeld, B., Glubokovskikh, S., Gunning, J., LaForce, T., Marshall, S., Paraschivoiu, E., Paterson, L., Pevzner, R., Tenthorey, E., & Watson, M., 2018. Fit for purpose monitoring - a progress report on the CO2CRC Otway Stage 3 project, in *14th Greenhouse Gas Control Technologies Conference Melbourne*, pp. 21–26.

Jenkins, C. R., Cook, P. J., Ennis-King, J., Undershultz, J., Boreham, C., Dance, T., de Caritat, P., Etheridge, D. M., Freifeld, B. M., Hortle, A., Kirste, D., Paterson, L., Pevzner, R., Schacht, U., Sharma, S., Stalker, L., & Urosevic, M., 2012. Safe storage and effective monitoring of CO_2 in depleted gas fields, *Proc. Natl. Acad. Sci.*, **109**(2), E35–E41.

Journel, A. G. & Alabert, F. G., 1990. New method for reservoir mapping, *J. Pet. Technol.*, **42**(02), 212–218.

Juanes, R., MacMinn, C. W., & Szulczewski, M. L., 2010. The footprint of the CO_2 plume during carbon dioxide storage in saline aquifers: storage efficiency for capillary trapping at the basin scale, *Transp. Porous Media*, **82**(1), 19–30.

Kampitsis, A. E., Kostorz, W. J., Muggeridge, A. H., & Jackson, M. D., 2021. The life span and dynamics of immiscible viscous fingering in rectilinear displacements, *Phys. Fluids*, **33**(9), 096608.

Kampman, N., Bickle, M. J., Maskell, A., Chapman, H. J., Evans, J. P., Purser, G., Zhou, Z., Schaller, M. F., Gattacceca, J. C., Bertier, P., Chen, F., Turchyn, A. V., Assayag, N., Rochelle, C., Ballentine, C. J., & Busch, A., 2014. Drilling and sampling a natural CO_2 reservoir: Implications for fluid flow and CO_2-fluid-rock reactions during CO_2 migration through the overburden, *Chemical Geology*, **369**, 51–82.

Kang, M., Nordbotten, J. M., Doster, F., & Celia, M. A., 2014. Analytical solutions for two-phase subsurface flow to a leaky fault considering vertical flow effects and fault properties, *Water Resour. Res.*, **50**(4), 3536–3552.

Karpyn, Z. T., Piri, M., & Singh, G., 2010. Experimental investigation of trapped oil clusters in a water-wet bead pack using x-ray microtomography, *Water Resour. Res.*, **46**(4).

Keeling, C. D., Piper, S. C., Bacastow, R. B., Wahlen, M., Whorf, T. P., Heimann, M., & Meijer, H. A., 2001. Exchanges of atmospheric CO_2 and $^{13}CO_2$ with the terrestrial biosphere and oceans from 1978 to 2000. I. Global aspects.

Keith, D., Holmes, G., Angelo, D. S., & Heidel, K., 2018. A process for capturing CO_2 from the atmosphere, *Joule*, **2**(8), 1573–1594.

Kochina, I. N., Mikhailov, N. N., & Filinov, M. V., 1983. Groundwater mound damping, *Int. J. Eng. Sci.*, **21**(4), 413–421.

Krassay, A. A., Cathro, D. L., & Ryan, D. J., 2004. A regional tectonostratigraphic framework for the otway basin.

Krevor, S., Blunt, M. J., Benson, S. M., Pentland, C. H., Reynolds, C., Al-Menhali, A., & Niu, B., 2015. Capillary trapping for geologic carbon dioxide storage - from pore scale physics to field scale implications, *Int. J. Greenh. Gas Control.*, **40**, 221–237.

Krevor, S. C. M., Pini, R., Li, B., & Benson, S. M., 2011. Capillary heterogeneity trapping of CO_2 in a sandstone rock at reservoir conditions, *Geophys. Res. Lett.*, **38**(15).

Krevor, S. C. M., Pini, R., Zuo, L., & Benson, S. M., 2012. Relative permeability and trapping of CO_2 and water in sandstone rocks at reservoir conditions, *Water Resour. Res.*, **48**(2).

Kunz, O. & Wagner, W., 2012. The GERG-2008 wide-range equation of state for natural gases and other mixtures: an expansion of GERG-2004, *J. Chem. Eng. Data*, **57**(11), 3032–3091.

LaForce, T., Ennis-King, J., Boreham, C., & Paterson, L., 2014. Residual CO_2 saturation estimate using noble gas tracers in a single-well field test: The CO2CRC Otway project, *Int. J. Greenh. Gas Control.*, **26**, 9–21.

Land, C. S., 1968. Calculation of imbibition relative permeability for two-and three-phase flow from rock properties, *Soc. Pet. Eng. J.*, **8**(02), 149–156.

Land, L. S., Milliken, K. L., & McBride, E. F., 1987. Diagenetic evolution of cenozoic sandstones, gulf of mexico sedimentary basin, *Sediment. Geol.*, **50**(1-3), 195–225.

Lawrence, M., Arnot, M., Browne, G., Bunch, M., Menacherry, S., & Dance, T., 2012. Geological interpretation of Otway Project Well CRC-1 and CRC-2, Tech. Rep. CO2CRC Publication Number: 358, Cooperative Research Centre for Greenhouse Gas Technologies, Canberra, Australia.

Lawrence, M. J. F., Arnot, M., Browne, G. H., Bunch, M., & Dance, T., 2013. Geological interpretation of core and wireline data from Otway Project wells CRC-1 and CRC-2, Tech. Rep. CO2CRC Publication Number: RPT12-3928, Cooperative Research Centre for Greenhouse Gas Technologies, Canberra, Australia.

Lee, K., Zeng, X., McMechan, G. A., Howell, C. D., Bhattacharya, J. P., Marcy, F., & Olariu, C., 2005. A ground-penetrating radar survey of a delta-front reservoir analog in the wall creek member, frontier formation, wyoming, *AAPG Bull.*, **89**(9), 1139–1155.

Leverett, M. C., 1941. Capillary behavior in porous solids, *Trans. AIME*, **142**(01), 152–169.

Li, B. & Benson, S. M., 2015. Influence of small-scale heterogeneity on upward CO_2 plume migration in storage aquifers, *Adv. Water Resour.*, **83**, 389–404.

Lim, J. S., 1990. Two-dimensional signal and image processing, *Englewood Cliffs*.

Lindeberg, E. & Wessel-Berg, D., 1997. Vertical convection in an aquifer column under a gas cap of CO_2, *Energy Convers. Manag.*, **38**, S229–S234.

Lister, J. R., 1992. Viscous flows down an inclined plane from point and line sources, *J. Fluid Mech.*, **242**, 631–653.

Liu, Y., Wang, L., & Yu, B., 2010. Sharp front capturing method for carbon dioxide plume propagation during injection into a deep confined aquifer, *Energy & fuels*, **24**(2), 1431–1440.

Lu, G., Cummer, S. A., Blakeslee, R. J., Weiss, S., & Beasley, W. H., 2012. Lightning morphology and impulse charge moment change of high peak current negative strokes, *J. Geophys. Res. Atmos.*, **117**(D4).

Lyle, S., Huppert, H. E., Hallworth, M., Bickle, M., & Chadwick, A., 2005. Axisymmetric gravity currents in a porous medium, *J. Fluid Mech.*, **543**, 293–302.

MacMinn, C. W., Szulczewski, M. L., & Juanes, R., 2010. CO_2 migration in saline aquifers. Part 1. Capillary trapping under slope and groundwater flow, *J. Fluid Mech.*, **662**, 329–351.

Marsh, R. J., Dance, T., Kim, Y., Chace, D., & Singh, R., 2018. Well-based monitoring of a CO_2 plume in a carbon dioxide storage project, in *SPWLA 59th Annual Logging Symposium*, Society of Petrophysicists and Well-Log Analysts.

Mavko, G., Mukerji, T., & Dvorkin, J., 2020. *The rock physics handbook*, Cambridge university press.

Metz, B., Davidson, O., Coninck, H., Loos, M., & Meyer, L., 2005. IPCC special report on carbon dioxide capture and storage, Tech. rep., Intergovernmental Panel on Climate Change.

Michael, K., Golab, A., Shulakova, V., Ennis-King, J., Allinson, G., Sharma, S., & Aiken, T., 2010. Geological storage of CO_2 in saline aquifers—A review of the experience from existing storage operations, *Int. J. Greenh. Gas Control.*, **4**(4), 659–667.

Mitchell, T. M. & Faulkner, D. R., 2008. Experimental measurements of permeability evolution during triaxial compression of initially intact crystalline rocks and implications for fluid flow in fault zones, *J. Geophys. Res. Solid Earth*, **113**(B11).

Mitchell, T. M. & Faulkner, D. R., 2012. Towards quantifying the matrix permeability of fault damage zones in low porosity rocks, *Earth Planet. Sci. Lett.*, **339**, 24–31.

Myers, M., Stalker, L., LaForce, T., Pejcic, B., Dyt, C., Ho, K., & Ennis-King, J., 2015. Field measurement of residual carbon dioxide saturation using reactive ester tracers, *Chem. Geol.*, **399**, 20–29.

Nakajima, T. & Xue, Z., 2013. Evaluation of a resistivity model derived from time-lapse well logging of a pilot-scale CO_2 injection site, Nagaoka, Japan, *Int. J. Greenh. Gas Control.*, **12**, 288–299.

Neufeld, J. A., Vella, D., & Huppert, H. E., 2009. The effect of a fissure on storage in a porous medium, *J. Fluid Mech.*, **639**, 239.

Neufeld, J. A., Hesse, M. A., Riaz, A., Hallworth, M. A., Tchelepi, H. A., & Huppert, H. E., 2010. Convective dissolution of carbon dioxide in saline aquifers, *Geophys. Res. Lett.*, **37**(22).

Ni, H., Boon, M., Garing, C., & Benson, S. M., 2019. Predicting CO_2 residual trapping ability based on experimental petrophysical properties for different sandstone types, *Int. J. Greenh. Gas Control.*, **86**, 158–176.

Nicol, A., Seebeck, H., Field, B., McNamara, D., Childs, C., Craig, J., & Rolland, A., 2017. Fault permeability and CO_2 storage, *Energy Procedia*, **114**, 3229–3236.

Nijjer, J. S., Hewitt, D. R., & Neufeld, J. A., 2018. The dynamics of miscible viscous fingering from onset to shutdown, *J. Fluid Mech.*, **837**, 520–545.

Nilsen, H. M., Lie, K., & Andersen, O., 2016. Fully-implicit simulation of vertical-equilibrium models with hysteresis and capillary fringe, *Comput. Geosci.*, **20**(1), 49–67.

Nilsen, H. M., Krogstad, S., Andersen, O., Allen, R., & Lie, K.-A., 2017. Using sensitivities and vertical-equilibrium models for parameter estimation of CO_2 injection models with application to Sleipner data, *Energy Procedia*, **114**, 3476–3495.

Nordbotten, J. M. & Celia, M. A., 2006. Similarity solutions for fluid injection into confined aquifers, *J. Fluid Mech.*, **561**, 307–327.

Nordbotten, J. M. & Celia, M. A., 2011. Geological storage of co_2: modeling approaches for large-scale simulation, in *Geological Storage of CO_2: Modeling Approaches for Large-Scale Simulation*, John Wiley and Sons.

Nordbotten, J. M., Celia, M. A., & Bachu, S., 2004. Analytical solutions for leakage rates through abandoned wells, *Water Resour. Res.*, **40**(4).

Nordbotten, J. M., Celia, M. A., & Bachu, S., 2005. Injection and storage of CO_2 in deep saline aquifers: analytical solution for CO_2 plume evolution during injection, *Transp. Porous Media*, **58**(3), 339–360.

Nordbotten, J. M., Kavetski, D., Celia, M. A., & Bachu, S., 2009. Model for co_2 leakage including multiple geological layers and multiple leaky wells, *Environ. Sci. Technol.*, **43**(3), 743–749.

Oda, M., Takemura, T., & Aoki, T., 2002. Damage growth and permeability change in triaxial compression tests of inada granite, *Mech. Mater.*, **34**(6), 313–331.

Partridge, A. D., 2001. Revised stratigraphy of the sherbrook group, otway basin.

Partridge, A. D., 2011. Palynological analysis of core and cuttings samples from the Paaratte Formation in the CRC No.2 well, Otway Basin, Tech. Rep. Report 2011/01, Biostrata Pty Ltd.

Paterson, L., Boreham, C., Bunch, M., Dance, T., Ennis-King, J., Freifeld, B., Haese, R., Jenkins, C., LaForce, T., Raab, M., Singh, R., Stalker, L., & Zhang, Y., 2013. Overview of the CO2CRC Otway residual saturation and dissolution test, *Energy Procedia*, **37**, 6140–6148.

Peaceman, D. W. & Rachford, H. H., 1955. The numerical solution of parabolic and elliptic differential equations, *J. Soc. Ind. Appl. Math.*, **3**(1), 28–41.

Pegler, S. S., Huppert, H. E., & Neufeld, J. A., 2014. Fluid injection into a confined porous layer, *J. Fluid Mech.*, **745**, 592–620.

Pegler, S. S., Huppert, H. E., & Neufeld, J. A., 2014. Fluid migration between confined aquifers, *J. Fluid Mech.*, **757**, 330.

Pentland, C. H., Itsekiri, E., Mansoori, S. K. A., Iglauer, S., Bijeljic, B., & Blunt, M. J., 2010. Measurement of nonwetting-phase trapping in sandpacks, *Spe Journal*, **15**(02), 274–281.

Perkins, S. E., Alexander, L. V., & Nairn, J. R., 2012. Increasing frequency, intensity and duration of observed global heatwaves and warm spells, *Geophys. Res. Lett.*, **39**(20).

Perrin, J.-C. & Benson, S., 2010. An experimental study on the influence of sub-core scale heterogeneities on CO_2 distribution in reservoir rocks, *Transp. Porous Media*, **82**(1), 93–109.

Pevzner, R., Tertyshnikov, K., Shulakova, V., Urosevic, M., Kepic, A., Gurevich, B., & Singh, R., 2015. Design and deployment of a buried geophone array for CO_2 geosequestration monitoring: CO2CRC Otway Project, Stage 2C, in *SEG technical program expanded abstracts 2015*, pp. 266–270, Society of Exploration Geophysicists.

Pevzner, R., Urosevic, M., Popik, D., Shulakova, V., Tertyshnikov, K., Caspari, E., Correa, J., Dance, T., Kepic, A., Glubokovskikh, S., Ziramov, S., Gurevich, B., Singh, R., Raab,

M., Watson, M., Daley, T., Robertson, M., & Freifeld, B., 2017. 4D surface seismic tracks small supercritical CO_2 injection into the subsurface: CO2CRC Otway Project, *Int. J. Greenh. Gas Control.*, **63**, 150–157.

Pevzner, R., Urosevic, M., Tertyshnikov, K., AlNasser, H., Caspari, E., Correa, J., Daley, T., Dance, T., Freifeld, B., Glubokovskikh, S., Greenwood, A., Kepic, A., Popik, D., Popik, S., Raab, M., Robertson, M., Shulakova, V., Singh, R., Watson, M., Yavuz, S., Ziramov, S., & Gurevich, B., 2020. Active surface and borehole seismic monitoring of a small supercritical CO_2 injection into the subsurface: experience from the CO2CRC Otway Project, in *Active Geophysical Monitoring*, pp. 497–522, Elsevier.

Pevzner, R., Isaenkov, R., Yavuz, S., Yurikov, A., Tertyshnikov, K., Shashkin, P., Gurevich, B., Correa, J., Glubokovskikh, S., Wood, T., Freifeld, B., & Barraclough, P., 2021. Seismic monitoring of a small CO_2 injection using a multi-well DAS array: Operations and initial results of Stage 3 of the CO2CRC Otway project, *Int. J. Greenh. Gas Control.*, **110**, 103437.

Pini, R. & Madonna, C., 2016. Moving across scales: a quantitative assessment of x-ray ct to measure the porosity of rocks, *J. Porous Mater.*, **23**(2), 325–338.

Pismen, L. M., 1974. Diffusion in porous media of a random structure, *Chem. Eng. Sci.*, **29**(5), 1227–1236.

Popik, D., V.Shulakova, Tertyshnikov, K., Ziramov, S., Urosevic, M., & Pevzner, R., 2018. Time-lapse surface seismic processing for Stage 2C of CO2CRC Otway Project, *AEGC Extended Abstracts*, **2018**(1), 1–6.

Popik, S., Pevzner, R., Tertyshnikov, K., Popik, D., Urosevic, M., Shulakova, V., Glubokovskikh, S., & Gurevich, B., 2020. 4D surface seismic monitoring the evolution of a small CO_2 plume during and after injection: CO2CRC Otway Project study, *Explor. Geophys.*, **51**(5), 570–580.

Press, W. H., Teukolsky, S. A., Vetterling, W. T., & Flannery, B. P., 2007. *Numerical Recipes: The Art of Scientific Computing*, Cambridge University Press.

Pritchard, D., 2007. Gravity currents over fractured substrates in a porous medium, *J. Fluid Mech.*, **584**, 415.

Pritchard, D. & Hogg, A. J., 2002. Draining viscous gravity currents in a vertical fracture, *J. Fluid Mech.*, **459**, 207.

Pritchard, D., Woods, A. W., & Hogg, A. J., 2001. On the slow draining of a gravity current moving through a layered permeable medium, *J. Fluid Mech.*, **444**, 23.

Riaz, A., Hesse, M., Tchelepi, H. A., & Orr, F. M., 2006. Onset of convection in a gravitationally unstable diffusive boundary layer in porous media, *J. Fluid Mech.*, **548**, 87–111.

Ringrose, P. S., Mathieson, A. S., Wright, I. W., Selama, F., Hansen, O., Bissell, R., Saoula, N., & Midgley, J., 2013. The In Salah CO_2 storage project: lessons learned and knowledge transfer, *Energy Procedia*, **37**, 6226–6236.

Ringrose, P. S., Furre, A.-K., Gilfillan, S. M. V., Krevor, S., Landrø, M., Leslie, R., Meckel, T., Nazarian, B., & Zahid, A., 2021. Storage of carbon dioxide in saline aquifers: Physicochemical processes, key constraints, and scale-up potential, *Annu. Rev. Chem. Biomol. Eng.*, **12**, 471–494.

Roberts, J. J., Gilfillan, S. M. V., Stalker, L., & Naylor, M., 2017. Geochemical tracers for monitoring offshore CO_2 stores, *Int. J. Greenh. Gas Control.*, **65**, 218–234.

Ryan, H., 1994. Ormsby, Klauder, Butterworth — a choice of wavelets, *Can. Soc. Explor. Geophys. Record*, **19**(7), 8–9.

Saadatpoor, E., Bryant, S. L., & Sepehrnoori, K., 2010. New trapping mechanism in carbon sequestration, *Transp. Porous Media*, **82**(1), 3–17.

Sævik, P. N. & Nixon, C. W., 2017. Inclusion of topological measurements into analytic estimates of effective permeability in fractured media, *Water Resour. Res.*, **53**(11), 9424–9443.

Saffman, P. G. & Taylor, G. I., 1958. The penetration of a fluid into a porous medium or Hele-Shaw cell containing a more viscous liquid, *Proc. R. Soc. A: Math. Phys. Eng. Sci.*, **245**(1242), 312–329.

Sahu, C. K. & Flynn, M. R., 2015. Filling box flows in porous media, *J. Fluid Mech.*, **782**, 455–478.

Sahu, C. K. & Neufeld, J. A., 2020. Dispersive entrainment into gravity currents in porous media, *J. Fluid Mech.*, **886**.

Sathaye, K. J., Hesse, M. A., Cassidy, M., & Stockli, D. F., 2014. Constraints on the magnitude and rate of CO_2 dissolution at Bravo Dome natural gas field, *Proc. Natl. Acad. Sci.*, **111**(43), 15332–15337.

Savage, H. M. & Brodsky, E. E., 2011. Collateral damage: Evolution with displacement of fracture distribution and secondary fault strands in fault damage zones, *J. Geophys. Res. Solid Earth*, **116**(B3).

Sayag, R. & Neufeld, J. A., 2016. Propagation of viscous currents on a porous substrate with finite capillary entry pressure, *J. Fluid Mech.*, **801**, 65–90.

Serno, S., Johnson, G., LaForce, T. C., Ennis-King, J., Haese, R. R., Boreham, C. J., Paterson, L., Freifeld, B. M., Cook, P. J., Kirste, D., Haszeldine, R. S., & Gilfillan, S. M. V., 2016. Using oxygen isotopes to quantitatively assess residual CO_2 saturation during the CO2CRC Otway Stage 2B Extension residual saturation test, *Int. J. Greenh. Gas Control.*, **52**, 73–83.

Shipton, Z. K., Evans, J. P., Robeson, K. R., Forster, C. B., & Snelgrove, S., 2002. Structural heterogeneity and permeability in faulted eolian sandstone: Implications for subsurface modeling of faults, *AAPG bulletin*, **86**(5), 863–883.

Shipton, Z. K., Evans, J. P., & Thompson, L. B., 2005. The geometry and thickness of deformation-band fault core and its influence on sealing characteristics of deformation-band fault zones, *Am. Assoc. Petroleum Geol. Memoir*.

Shulakova, V., Pevzner, R., Dupuis, C. J., Urosevic, M., Tertyshnikov, K., Lumley, D. E., & Gurevich, B., 2015. Burying receivers for improved time-lapse seismic repeatability: CO2CRC Otway field experiment, *Geophys. Prospect.*, **63**(1), 55–69.

Simpson, G., Guéguen, Y., & Schneider, F., 2001. Permeability enhancement due to microcrack dilatancy in the damage regime, *J. Geophys. Res. Solid Earth*, **106**(B3), 3999–4016.

Smith, T. M., Sondergeld, C. H., & Rai, C. S., 2003. Gassmann fluid substitutions: A tutorial, *Geophysics*, **68**(2), 430–440.

Snippe, J., Kampman, N., Bisdom, K., Tambach, T., March, R., Maier, C., Phillips, T., Inskip, N. F., Doster, F., & Busch, A., 2021. Modeling of long-term along-fault flow of CO_2 from a natural reservoir, *Proceedings of the 15th Greenhouse Gas Control Technologies Conference 15-18 March 2021*.

Soltanian, M. R., Amooie, M. A., Dai, Z., Cole, D., & Moortgat, J., 2016. Critical dynamics of gravito-convective mixing in geological carbon sequestration, *Sci. Rep.*, **6**(1), 1–13.

Spiteri, E. J., Juanes, R., Blunt, M. J., & Orr, F. M., 2008. A new model of trapping and relative permeability hysteresis for all wettability characteristics, *SPE Journal*, **13**(03), 277–288.

Suzanne, K., Hamon, G., Billiotte, J., & Trocme, V., 2003. Experimental relationships between residual gas saturation and initial gas saturation in heterogeneous sandstone reservoirs, in *SPE Annual Technical Conference and Exhibition*, OnePetro.

Tanase, D. & Tanaka, J., 2021. Progress of CO_2 injection and monitoring of the Tomakomai CCS Demonstration Project, *Proceedings of the 15th Greenhouse Gas Control Technologies Conference 15-18 March 2021*.

Taylor, T. P., , Pennell, K. D., Abriola, L. M., & Dane, J. H., 2001. Surfactant enhanced recovery of tetrachloroethylene from a porous medium containing low permeability lenses: 1. experimental studies, *J. Contam. Hydrol.*.

Teng, H. & Yamasaki, A., 1998. Solubility of liquid CO_2 in synthetic sea water at temperatures from 278 K to 293 K and pressures from 6.44 MPa to 29.49 MPa, and densities of the corresponding aqueous solutions, *J. Chem. Eng. Data*, **43**(1), 2–5.

Tenthorey, E., Dance, T., Cinar, Y., Ennis-King, J., & Strand, J., 2014. Fault modelling and geomechanical integrity associated with the CO2CRC Otway 2C injection experiment, *Int. J. Greenh. Gas Control.*, **30**, 72–85.

Thiem, G., 1906. *Hydrologische Methoden: Dissertation zur Erlangung der Würde eines Doktor-Ingenieurs durch die Königliche Technische Hochschule zu Stuttgart*, Ph.D. thesis, JM Gebhardt's verlag.

Trenberth, K. E., 2011. Changes in precipitation with climate change, *Clim. Res.*, **47**(1-2), 123–138.

Vella, D. & Huppert, H. E., 2006. Gravity currents in a porous medium at an inclined plane, *J. Fluid Mech.*, **555**, 353–362.

Virnovsky, G. A., Friis, H. A., & Lohne, A., 2004. A steady-state upscaling approach for immiscible two-phase flow, *Transp. Porous Media*, **54**(2), 167–192.

Walden, A. T. & White, R. E., 1998. Seismic wavelet estimation: A frequency domain solution to a geophysical noisy input-output problem, *IEEE Trans. Geosci. Remote Sens.*, **36**(1), 287–297.

Watson, M., Cinar, T., Dance, T., Pevzner, R., Tenthorey, E., Caspari, E., Ennis-King, J., Shulakova, V., Bunch, M., Urosevic, M., Singh, R., Gurevich, B., Paterson, L., Jenkins, C., Hortle, A., & Raab, M., 2012. Vertification of CO_2 storage in a saline formation (Paaratte) using time-lapse seismic, Tech. Rep. CO2CRC Publication Number: RPT12-4109, Cooperative Research Centre for Greenhouse Gas Technologies, Canberra, Australia.

Watson, M., Pevzner, R., Dance, T., Gurevich, B., Ennis-King, J., Glubokovskikh, S., Urosevic, M., Tertyshnikov, K., Force, T. L., Tenthorey, E., Bagheri, M., Paterson, L., Cinar, Y., Freifeld, B., Singh, R., & Raab, M., 2018. The Otway Stage 2C Project - End to end CO_2 storage in a saline formation, comprising characterisation, injection and monitoring, in *14th Greenhouse Gas Control Technologies Conference Melbourne*, pp. 21–26.

Watson, M. N., Boreham, C. J., & Tingate, P. R., 2004. Carbon dioxide and carbonate cements in the otway basin: implications for geological storage of carbon dioxide, *The APPEA Journal*, **44**(1), 703–720.

White, D., Harris, K., Roach, L., Roberts, B., Worth, K., Stork, A., Nixon, C., Schmitt, D., Daley, T., & Samson, C., 2017. Monitoring results after 36 ktonnes of deep CO_2 injection at the Aquistore CO_2 storage site, Saskatchewan, Canada, *Energy Procedia*, **114**, 4056–4061.

White, J. C., Williams, G., Chadwick, A., Furre, A.-K., & Kiær, A., 2018. Sleipner: The ongoing challenge to determine the thickness of a thin CO_2 layer, *Int. J. Greenh. Gas Control.*, **69**, 81–95.

Wibberley, C. A. J. & Shimamoto, T., 2003. Internal structure and permeability of major strike-slip fault zones: the median tectonic line in mie prefecture, southwest japan, *J. Struct. Geol.*, **25**(1), 59–78.

Wibberley, C. A. J., Yielding, G., & Toro, G. D., 2008. Recent advances in the understanding of fault zone internal structure: a review, *Geol. Soc. Spec. Publ.*, **299**(1), 5–33.

Wilkinson, M., Haszeldine, R. S., Fallick, A. E., Odling, N., Stoker, S. J., & Gatliff, R. W., 2009. CO_2–mineral reaction in a natural analogue for CO_2 storage—implications for modeling, *J. Sediment. Res.*, **79**(7), 486–494.

Wilkinson, M., Mouli-Castillo, J., Morgan, P., & Eid, R., 2017. Time-lapse gravity surveying as a monitoring tool for CO_2 storage, *Int. J. Greenh. Gas Control.*, **60**, 93–99.

Williams, G. & Chadwick, A., 2012. Quantitative seismic analysis of a thin layer of CO_2 in the Sleipner injection plume, *Geophysics*, **77**(6), R245–R256.

Williams, G. A. & Chadwick, R. A., 2017. An improved history-match for layer spreading within the sleipner plume including thermal propagation effects, *Energy Procedia*, **114**, 2856–2870.

Williams, G. A., Chadwick, R. A., & Vosper, H., 2018. Some thoughts on Darcy-type flow simulation for modelling underground CO_2 storage, based on the Sleipner CO_2 storage operation, *Int. J. Greenh. Gas Control.*, **68**, 164–175.

Willis, B. J., Bhattacharya, J. P., Gabel, S. L., & White, C. D., 1999. Architecture of a tide-influenced river delta in the frontier formation of central wyoming, usa, *Sedimentology*, **46**(4), 667–688.

Wooding, R. A., 1963. Convection in a saturated porous medium at large rayleigh number or peclet number, *J. Fluid Mech.*, **15**(4), 527–544.

Woods, A., Hesse, M., Berkowitz, R., & Chang, K. W., 2015. Multiple steady states in exchange flows across faults and the dissolution of CO_2, *J. Fluid Mech.*, **769**, 229–241.

Woods, A. W., 2015. *Flow in porous rocks*, Cambridge University Press.

Woods, A. W. & Farcas, A., 2009. Capillary entry pressure and the leakage of gravity currents through a sloping layered permeable rock, *J. Fluid Mech.*, **618**, 361–379.

Woollands, M. A. & Wong, D., 2001. Petroleum atlas of Victoria, Australia, Tech. rep., The State of Victoria, Department of Natural Resources and Environment.

Zhang, S. & Tullis, T. E., 1998. The effect of fault slip on permeability and permeability anisotropy in quartz gouge, *Tectonophysics*, **295**(1-2), 41–52.

Zhang, S., Tullis, T. E., & Scruggs, V. J., 2001. Implications of permeability and its anisotropy in a mica gouge for pore pressures in fault zones, *Tectonophysics*, **335**(1-2), 37–50.

Zhang, Y., Freifeld, B., Finsterle, S., Leahy, M., Ennis-King, J., Paterson, L., & Dance, T., 2011. Single-well experimental design for studying residual trapping of supercritical carbon dioxide, *Int. J. Greenh. Gas Control.*, **5**(1), 88–98.

Zhu, J., Lines, L., & Gray, S., 1998. Smiles and frowns in migration/velocity analysis, *Geophysics*, **63**(4), 1200–1209.

Appendix A

Late Time Behaviour of the Current Horizontal Extent

Assuming that changes to the shape of the current are small at late times, the time derivative of (3.30) is

$$\phi\kappa\frac{d}{dt}[h_0 x_N] \approx q - q_F \tag{A.1}$$

where κ represents the dimensionless volume of the current (e.g. $\kappa = 1/2$ in the case of a triangle) and the leakage flux

$$q_F = \frac{\zeta q}{h_f}(h_0 + h_f), \tag{A.2}$$

with $\zeta = \frac{d_f \phi_f k_f g'}{\nu q}$. From (3.29a), we obtain the relationship

$$-\frac{kg'}{\nu}h_0\frac{\partial h}{\partial x}\bigg|_{x=0} = q - q_F. \tag{A.3}$$

At late times, we can approximate

$$\left.\frac{\partial h}{\partial x}\right|_{x=0} \approx -\frac{h_0}{x_N}. \tag{A.4}$$

At the equilibrium point where $q_F \to q$, the thickness of the current at $x = 0$

$$h_0 \to h_f \left(\frac{1}{\zeta} - 1\right) = h_{0\infty}, \tag{A.5}$$

which is obtained from (A.2). We consider the current thickness at $x = 0$,

$$h_0 = h_{0\infty} - \delta(t), \tag{A.6}$$

where $\delta(t) \ll h_{0\infty}$ is a small perturbation. On equating (A.1) and (A.3) and applying the relationships (A.4) and (A.6),

$$\phi\kappa \frac{d}{dt}[(h_{0\infty} - \delta(t))x_N] \approx \frac{kg'}{\nu x_N}(h_{0\infty} - \delta(t))^2. \tag{A.7}$$

By considering the leading order terms, we find that

$$x_N \approx \left(\frac{kg' h_{0\infty}}{\phi\kappa\nu} t\right)^{1/2}, \tag{A.8}$$

which indicates that the current extent follows a $t^{1/2}$ power law relationship at late times.